Low Coronal Signatures of Coronal Mass Ejections

Coronal "waves" and dimmings

Gemma Diana Ruth Attrill

Mullard Space Science Laboratory
Department of Space and Climate Physics
University College London

A thesis submitted to University College London
for the degree of Doctor of Philosophy

July 2008

I, Gemma Diana Ruth Attrill, confirm that the work presented in this thesis is my own. Where information has been derived from other sources, I confirm that this has been indicated in the thesis.

Much of the work undertaken during study for this PhD can be found in the following articles:

• **Attrill, G. D. R.**, van Driel-Gesztelyi, L., Démoulin, P., Zhukov, A. N., Steed, K., Harra, L. K., Mandrini, C. H. and Linker, J.: The recovery of CME-related dimmings and the ICME's enduring magnetic connection to the Sun. 2008, *Sol. Phys.*, 252, 349.

• van Driel-Gesztelyi, L., **Attrill, G. D. R.**, Démoulin, P., Mandrini, C. H. and Harra, L. K.: Why are CMEs large-scale events: nature or nurture? 2008, *Ann. Geophys.*, Special Issue: SOHO 20 Transient Events on the Sun and in the Heliosphere, 26, 3077.

• **Attrill, G. D. R.**, Harra, L. K., van Driel-Gesztelyi, L. and Démoulin, P.: Coronal "wave": Magnetic footprint of a coronal mass ejection? 2007, *ApJ*, 656, L101.

• **Attrill, G. D. R.**, Harra, L. K., van Driel-Gesztelyi, L. and Démoulin, P.: Coronal "wave": A signature of the mechanism making CMEs large-scale in the low corona? 2007, *Astron. Nachr.*, 328, 760.

• **Attrill, G. D. R.**, Harra, L. K., van Driel-Gesztelyi, L., Williams, D. R. and Alexeev, I. V.: Study of the physical properties of coronal "waves" and associated dimmings. 2007, *ASP Conference Series, Hinode* First Results Meeting, 397, 126.

• Baker, D., van Driel-Gesztelyi, L. and **Attrill, G. D. R.**, Evidence for interchange reconnection between a coronal hole and an adjacent emerging flux region. 2007, *Astron. Nachr.*, 328, 773.

• Green, L. M., Kliem, B., Török, T., van Driel-Gesztelyi, L. and **Attrill, G. D. R.**: What are transient soft X-ray sigmoids? 2007, *Sol. Phys.*, 246, 365.

• Harra, L. K., Crooker, N. U., Mandrini, C. H., van Driel-Gesztelyi, L., Dasso, S., Wang, J., Elliott, H., **Attrill, G. D. R.**, Jackson, B. V. and Bisi, M. M.: How does large flaring activity from the same active region produce oppositely directed magnetic clouds? 2007, *Sol. Phys.*, 244, 95.

• Harra, L. K., Hara, H., Imada, S., Young, P. R., Williams, D. R., Sterling, A. C., Korendyke, C. and **Attrill, G. D. R.**: Coronal dimming observed with *Hinode*: outflows related to a coronal mass ejection. 2007, *Publ. Astron. Soc. Japan*, 59, S801.

• Mandrini, C. H., Nakwacki, M. S., **Attrill, G. D. R.**, van Driel-Gesztelyi, L., Démoulin, P., Dasso, S. and Elliott, H.: Are CME related dimmings always a simple signature of interplanetary magnetic cloud footpoints? 2007, *Sol. Phys.*, 244, 25.

• Zhang, Y., Wang, J., **Attrill, G. D. R.**, Harra, L. K., Yang, Z. and He, X.: Coronal magnetic connectivity and EUV dimmings. 2007, *Sol. Phys.*, 241, 329.

• **Attrill, G. D. R.**, Nakwacki, M. S., Harra, L. K., van Driel-Gesztelyi, L., Mandrini, C. H., Dasso, S. and Wang, J.: Using the evolution of coronal dimming regions to probe the global magnetic field topology. "Unidentical Twins": A new interpretation of the 12th May 1997 event. 2006, *Sol. Phys.*, 238, 117.

• **Attrill, G. D. R.**, Narukage, N., Shibata, K. and Harra, L. K.: Magnetic fields and intensity changes in coronal dimming regions. 2005, *Proceedings of the International Scientific Conference on Chromospheric and Coronal Magnetic Fields*, ESA SP-596.

Abstract

Coronal mass ejections (CMEs) are vast eruptions of magnetised plasma that explode from the solar atmosphere. This thesis focuses on understanding the nascent stages of CMEs, and their magnetic development as they expand into the interplanetary space of our solar system. This is an important part of our effort to understand the space weather environment that we live in, and increasingly interact with through satellite communications technologies. Predominantly through combining extreme ultra-violet imaging and magnetogram data, two low coronal signatures of CMEs, namely coronal waves and dimmings, are studied.

A comprehensive list of observational properties of EIT coronal waves is compiled and potential counterparts in radio, Hα, soft X-rays and He II wavelengths are also discussed. New observational constraints on EIT coronal waves are presented, most notably diffuse coronal waves are shown to have a magnetic nature.

Finding that many observational constraints are not satisfactorily explained by current theories, a new model for understanding the physical nature of diffuse coronal waves is developed. The new model interprets diffuse coronal "wave" bright fronts to be the low coronal magnetic footprint of CMEs. Implications for developing our understanding of *how* CMEs become large-scale in the low corona are discussed.

Application of the model demonstrates how an understanding of the formation of complex global-scale coronal dimmings can be derived. For the first time it is shown that study of the evolution and magnetic nature of coronal dimming regions can be used to probe the *post-eruptive* evolution of the CME. Finally, a study is presented regarding why and how CME-related dimmings recover, despite the "open" magnetic connectivity of the ejecta to the Sun being maintained as indicated by electron heat flux measurements at 1 AU.

Acknowledgements

First and foremost, I would like to thank my supervisors, Louise Harra and Lidia van Driel-Gesztelyi.

Louise, thankyou for introducing me to the world of solar physics research and for providing me with the opportunity to undertake a PhD within the solar group. You identified a research area where, with your guidance and supervision, I could make a real contribution. Through your support and encouragement I have been able to enjoy so many wonderful opportunities that have really enriched my experiences as a student. None of this would have been possible without you. Thankyou so much!

Lidia, your enthusiasm, teaching and unwavering patience have provided me with so much, that I simply cannot put my gratitude into words. Thankyou from the bottom of my heart for all the many, many discussions. I hope that these continue for years to come! You are a huge inspiration and I would not have completed these studies without your guidance and encouragement.

Pascal Démoulin, thankyou for all the hundreds of emails (no seriously, I checked!), for your teaching and many valuable, enjoyable discussions.

Cristina Mandrini, for showing me how to overhaul an article (your sharp scissors!) - I am learning...

All of you have been strong reference points for me, each in different ways and I would not have got as far as I have without you. I am very, *very* grateful.

Len Culhane, Alphonse Sterling, Carl Foley and Nigel Meredith, thankyou for encouraging me to study for a PhD in solar physics at MSSL. Shibata-sensi, Kamio-san, Isobe-san, Okamoto-san, Miyagoshi-san and everyone at Kwasan and Hida observatories, for welcoming me into your group so warmly for the summer of 2005. In particular, Narukage-san, thankyou so much for your patient teaching and many discussions. I learnt such a lot from my time in Japan with you. Sergio Dasso and Soledad Nackwacki - the Argentinian MC crew! Jingxiu Wang and Yuzong Zhang for an introduction to studying coronal dimmings and helpful discussions during the steep learning curve that followed. Jon Linker and everyone at the SHINE meeting, summer 2007, for your interest in this work and the challenging discussions! Tibor Török and Lucie Green for many patient and detailed explanations. Also for sharing stories of your own and for listening to mine - you have no idea how supportive you have been! Elena Podladchikova, for your teaching and discussions, the discovery of a great colleague and good friend too :o) Andrei Zhukov for some great debates (sure more to come!), your teaching and your willingness to work together.

The website of Frédérick Auchére, `http://www.ias.u-psud.fr/eit/movies/`, which provides an incredibly useful quick-look resource for original and running difference movies of all SOHO/EIT data.

The "gang" in GO1, ever-changing over the years: *huge* thanks to Dave Williams and Chris Goff for the endless pestering in the first years! You taught me so much and always made the time to help me when I was stuck. Jian Sun for help with technical/IDL-related questions, Laura Bone and Michelle Murray for many "can I just check this makes sense with you" conversations and for

the warnings/advice regarding writing! Alison Wallace, Kimberley Steed and Deb Baker for giving me the opportunity to explain things and helping me realise I *do* know some things! Also, Deb for listening patiently to my rabbiting through various stages and for your support, advice, friendship and attempts to educate me in things American...!

The wider solar group members, both past (Maria Madjarska, Urmila Mitra-Kraev) and present (Sarah Matthews, Giulio Del Zanna, Ken Phillips, Bob Bentley, Khalid Al-Janabi, Kevin Benson, Louisa Bradley), for ad hoc explanations here and there and for generally making the MSSL solar group a very pleasant place to work.

My friends: Sam Thomas, Jon Rutter, Dorian Pascoe, Gareth Turner - for *still* patiently listening to me and for all the encouragement. Jo Bartlett and Paul Henderson, for being great mates and making up one fabulous PhD intake back in 2004! Ilya Alexeev for patiently dealing with the tears of frustratation, as well as excited explanations of a days developments. For your teaching in aspects of IDL, physics and maths and for many long discussions! Sam Oates, Andy Walsh, Glyn Collinson, Rebecca Smith, Andy Fenny, Yasir Soobiah, Chris Copperwheat, Pat Schady, Hazel Kenyon, Gethyn Lewis and Matt Whillock for being one fab bunch of mates :o) Huw Bennett for your encouragement and support to get over the last hurdles and for keeping me sane with a life outside writing!

My wonderful Family for giving me the space and time to write quietly, the endless supply of tea and support, interest and encouragement - love to you all!

List of Abbreviations

Abbreviation	Details
2-D/3-D	Two/Three Dimensional
3DP	3-Dimensional Plasma Experiment
AC	Alternating Current
ACE	Advanced Composition Explorer
AIA	Atmospheric Imaging Assembly
AR	Active Region
AU	Astronomical Unit (1.5×10^{11}m)
CCD	Charge-Coupled Device
CDS	Coronal Diagnostic Spectrometer
CME	Coronal Mass Ejection
COR	Coronagraph
CSHKP	Carmichael, Sturrock, Hirayama, Kopp and Pneuman
GOES	Geostationary Operational Environmental Satellites
EESA(-H)	(High) Energy Electron Electrostatic Analyser
EIS	Extreme ultra-violet Imaging Spectrometer
EIT	Extreme ultra-violet Imaging Telescope
ESA	European Space Agency
EUV	Extreme Ultra-Violet
EUVI	Extreme Ultra-Violet Imager
GMT	Greenwich Mean Time
GSE	Geocentric Solar Ecliptic
HMI	Helioseismic and Magnetic Imager
ICME	Interplanetary Coronal Mass Ejection
IMF	Interplanetary Magnetic Field
ISAS	Institute of Space and Astronautical Science
LASCO	Large Angle Spectroscopic Coronagraph
LCP	Left Circulary Polarised
MAG	Magnetometer
MC	Magnetic Cloud
MCP	Micro Channel Plate
MDI	Michelson Doppler Imager
MFI	Magnetic Fields Investigation
MHD	Magnetohydrodynamic(s)
MV	Miniumum Varience
NASA	National Aeronautics and Space Administration
NOAA	National Oceanic and Atmospheric Administration
NRH	Nobeyama Radioheliograph
PEA	Post-Eruptive Arcade
QS	Quiet Sun
QSL	Quasi-Separatrix Layer
$R_\odot$	Solar radius (6.96×10^8m)
R_E	Earth radius (6.38×10^6m)
RCP	Right Circularly Polarised
RHESSI	Reuven Ramaty High Energy Solar Spectroscopic Imager
SAA	South Atlantic Anomaly
SDO	Solar Dynamics Observatory
SECCHI	Sun Earth Connection Coronal and Heliospheric Investigation
SOHO	Solar and Heliospheric Observatory
SOI	Solar Oscillations Investigation
SPIRIT	Spectrographic X-ray Imaging Telescope
STEREO	Solar Terrestrial Relations Observatory
SXI	Solar X-ray Imager
SXT	Soft X-ray Telescope
TCH	Transient Coronal Hole
TEQ	Trans-Equatorial
TRACE	Transition Region And Coronal Explorer
UT	Universal Time
XBP	X-ray Bright Point
XRT	X-ray Telescope

Contents

Chapter 1

Introduction

1.1 The Sun

Our Sun is situated near the centre of the main sequence of nearby stars when shown on a plot of luminosity versus effective temperature (see Figure 1.1, the Hertzsprung-Russell diagram). The Sun is a relatively average star, of mass $\sim 1.99\times10^{30}$ kg and is about 4.6×10^{9} years old, approximately halfway through its lifetime. Essentially a massive ball of ionised gas, the Sun spins with a differential rotation (rotating faster at the equator than at the poles). A complete solar rotation at the equator takes about 25 days, and this increases to 28.6 days at a latitude of $\pm$ 40°. The rotation rate Ω (in μrads^{-1}), as a function of latitude ϕ, is best fit by: $\Omega(\phi)$ = 2.9 - 0.4 $\sin^2\phi$ - 0.4 $\sin^4\phi$ (Komm *et al.*, 1993). The Sun's chemical composition (by number of atoms) is $\sim$ 90% hydrogen (H), nearly 10% helium (He), with trace amounts of heavier elements. The abundances of these elements in the Sun broadly reflect those of a second-generation star, i.e. one created from the coalescence of material left over from first-generation stars that underwent supernova explosions in our Galaxy (Phillips *et al.*, 2008). When viewing images of the Sun, two of the traditional compass points are reversed, such that east is west, and west is east. This convention is used throughout this thesis.

The Sun has many secrets, two of which, coronal waves and dimmings, are the focus of this thesis. A comment by Aschwanden *et al.* (2001) captures the essence of studying our nearest star: "The Sun is at once intriguing and daunting in its complexity" (see Figure 1.2).

1.1.1 The Solar Surface

When observing the Sun in optical light with the naked eye, we essentially see the photosphere (Greek for "light"). The photosphere can loosely be regarded as the Sun's surface, (it is actually a thin layer $\sim$ 100 km thick). Determination of the base of the photosphere depends on the wavelength of the radiation. The universally accepted definition is where the optical depth τ, is unity for radiation of wavelength 5000 Å, written $\tau_{5000} = 1$ (Phillips *et al.*, 2008). This means that the gas becomes opaque when the optical depth becomes unity. The opacity of the photosphere is due mainly to H^- ionisation. The extra electron associated with the hydrogen atom means that

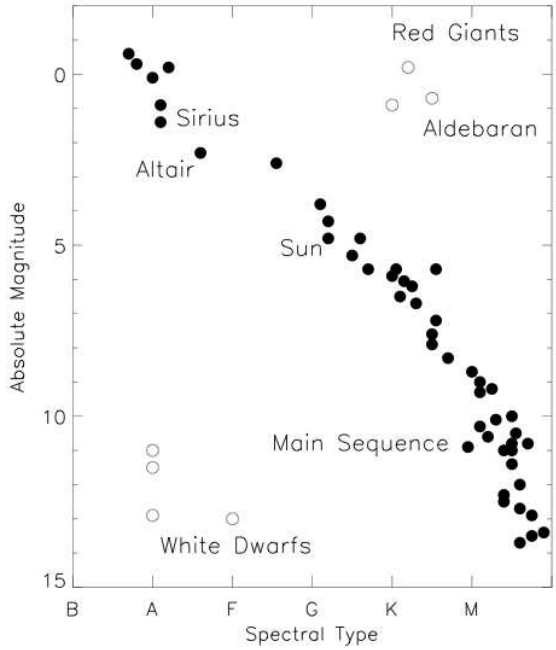

Figure 1.1: Hertzsprung-Russell diagram for stars in the neighbourhood of the Sun. The figure shows the spectral type (related to effective temperature) as a function of absolute magnitude (related to stellar luminosity). The main sequence is the name given to the broad clustering of stars running from upper left to lower right (solid black dots). Evolved stars on the red giant branch and white dwarf stars (open black dots) are also plotted. Figure from Phillips *et al.* (2008). Permission to reproduce this figure has been granted by Cambridge University Press.

H^- effectively absorbs photons. The average temperature at the base of the photosphere where $\tau_{5000} = 1$ is $\sim$ 6400 K (Phillips, 1992; Harra and Mason, 2004). The radius of the photosphere is known as the solar radius, $R_\odot = 6.96\times10^8$m.

1.1.2 The Solar Interior

Regions progressively deeper than the photosphere constitute the solar interior and are characterized by increasing densities where there are continual interactions between atoms, ions and radiation. At its core, the Sun is dense and hot enough to allow thermonuclear reactions to occur. The core extends from the centre of the Sun to $\sim 0.25R_\odot$, and has a temperature of 1.5×10^7K (Priest, 1982). The energy that we observe radiating from the photosphere is generated in the Sun's core by nuclear reactions, in particular fusion of four protons to form ^{4}He nuclei. The energy (in the form of high energy gamma ray photons) is transferred to the layer of dense plasma above the core, where radiation dominates out to $0.667R_\odot$. The high density of the plasma in the radiation zone prevents the photons from travelling straight to the solar surface in a few seconds. Instead, many collisions between the photons and the dense plasma send the photons on a "random walk" through the radiative zone. On average, it is estimated to take $\sim$ 100 thousand years for a photon to make its way to the surface. The many collisions mean that the photons that originated from the core as gamma rays lose more than 99.999% of their energy, finally emerging as visible light at the top of the radiation zone. From this point, the temperature becomes too cool to allow continued radiative energy transport and massive convective currents take over as the dominant energy transport process to the photosphere. The convective currents create and sustain two major conspicuous cellular patterns (called granulation and supergranulation, with typical length scales

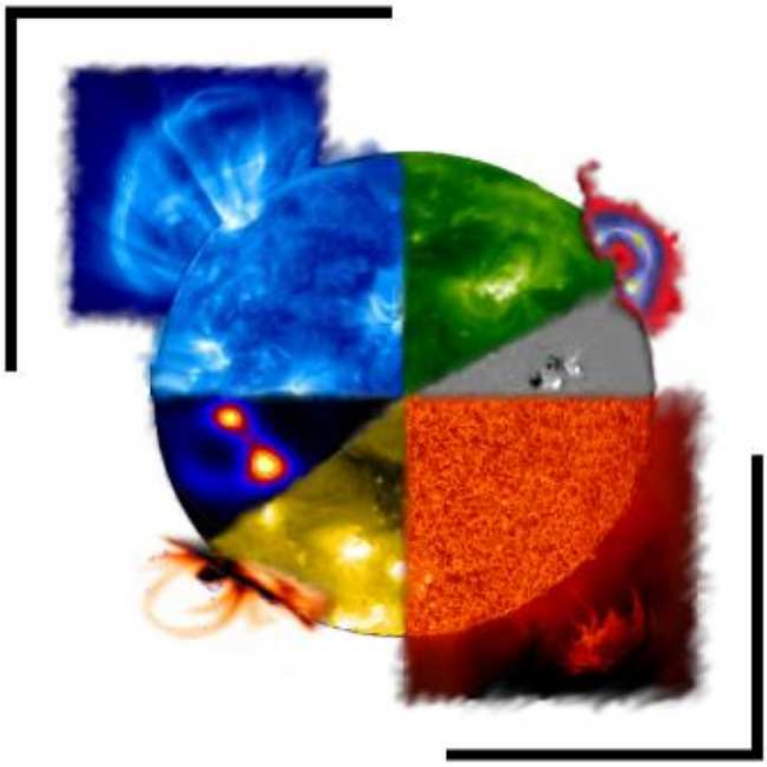

Figure 1.2: Our Sun viewed at many different wavelengths. Clockwise from top center: solar corona viewed in SOHO/EIT Fe XII 195 Å data; a false colour soft X-ray intensity image of the "Masuda flare", overlaid with hard X-ray contours; SOHO/MDI line-of-sight magnetogram; chromosphere/transition region showing an erupting prominence viewed in SOHO/EIT He II 304 Å data; solar corona viewed in SOHO/EIT Fe XV 284 Å data; coronal loop system viewed in TRACE data; RHESSI hard X-ray source; solar corona viewed in SOHO/EIT Fe IX 171 Å data.

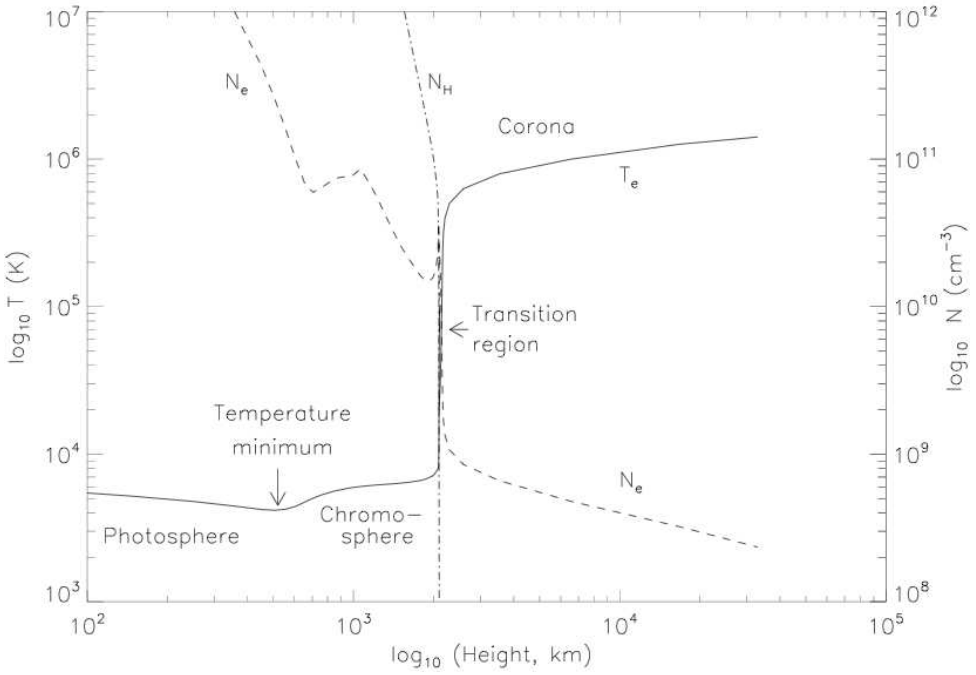

Figure 1.3: One-dimensional model calculations which show the variation of temperature with height in the solar atmosphere (solid curve). In such one-dimensional models the transition region is a relatively thin layer where the temperature rises dramatically from $\sim$ T=10^4 - 10^6 K. (Variations in the number densities of neutral H atoms and electrons are also shown by dot-dash and dash curves, respectively). Figure from Phillips *et al.* (2008). Permission to reproduce this figure has been granted by Cambridge University Press.

$\sim 10^3$ km and $\sim 3{\times}10^4$ km, respectively) with a rise, cooling and subsequent fall of the plasma in a cyclic motion.

1.1.3 The Solar Atmosphere

The solar atmosphere may be broadly defined as "that part of the Sun ... where energy generated at the Sun's core begins to escape into space as radiation" (Phillips *et al.*, 2008). It is expected that the temperature of the Sun should continuously decrease with increasing distance from the energy source at the Sun's core. In fact, above the photosphere, the temperature actually rises. Figure 1.3 shows the variation of temperature with height in the solar atmosphere. The temperature minimum (4400K) is reached at a height of $\sim$ 500 km above the base of the photosphere. Above this temperature minimum up to where the temperature is $\sim$ 20,000K, lies a region known as the chromosphere (Greek for "colour").

The photosphere and lower chromosphere are largely made up of neutral H atoms. In the upper chromosphere, where the temperature increases beyond about 10,000 K, the H atoms begin to be ionised so that there are large numbers of free protons and electrons as well as neutral atoms of H and He. Higher still, both H and He are almost completely ionised, so that the composition is free protons and electrons and He nuclei, with much smaller numbers of ions, including those of heavier elements. The corona has a very low density compared to the chromosphere, and is nearly isothermal with an electron temperature, T_e, between $1.0{\times}10^6$ K and $1.4{\times}10^6$ K. However, features such as coronal holes and active regions do differ from this general description (discussed in more detail in §1.2.3).

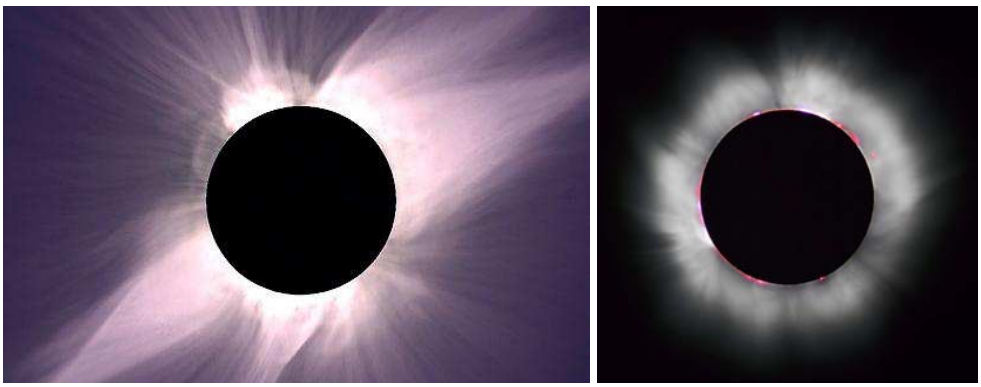

Figure 1.4: White-light images of the Sun taken during solar eclipses. The black disk is the moon, and the tenuous pinkish-white light is the hot plasma of the solar corona. The corona is far too faint to be seen against the blinding brightness of the photosphere (maximum brightness ratio $\sim 10^{-6}$, Golub and Pasachoff, 1997), but becomes visible during times of total solar eclipses when the photosphere is obscured by the Moon, as in these photographs. The image on the left was taken by a group from the High Altitude Observatory at Mauna Kea, Hawaii during the total solar eclipse of 1991 (near solar maximum). On the right is a white-light image of the 1999 solar eclipse taken in the rise phase of the solar cycle (photo by Luc Viatour). Bright red features can be seen above the solar limb - these are prominences and appear red because their temperature of $\sim$ 10,000 K means that they emit most strongly in the Hα line at 6563 Å, at the red end of the visible spectrum. Prominences are discussed in more detail in §1.5.1.

The transition region (in solar atmospheric models) is a thin $\sim$ 200 km layer that separates the dense, relatively cool chromosphere and tenuous, hot corona. In the transition region, the temperature dramatically rises from $\sim 10^4$ - 10^6 K. Due to the extreme temperatures, the bulk of the electromagnetic radiation from the corona has photon energies between 10 eV-100 eV, corresponding to wavelengths between $\sim$1000 Å and $\sim$ <100 Å. The solar chromosphere and corona are therefore strong emitters of radiation with wavelengths between the ultraviolet and soft X-ray range.

Traditionally the solar atmosphere has been described in terms of stratification (photosphere, temperature minimum, chromosphere, transition region, corona). However during total solar eclipses where the overpowering light from the photosphere is obscured by the Moon, the tenuous white-light corona can actually be observed due to Thomson scattering of photospheric light by the fast-moving free electrons in the high-temperature corona (see Figure 1.4). Such white-light images show the corona to be highly non-uniform. The Skylab mission taught us that the corona is dynamic (e.g. Gosling *et al.*, 1974) and modern solar observations provided, in particular, by *Yohkoh*, SOHO, TRACE, *Hinode* and STEREO in extreme ultra-violet and X-rays show the corona not only to be dynamic, but also that it is made up of many different structures spanning multiple spatial, temporal and temperature scales (Aschwanden *et al.*, 2001). As such, the solar corona is now recognised as being inhomogeneous. In view of such observations, Phillips *et al.* (2008) notes that model atmospheres (such as the one-dimensional model shown in Figure 1.3), while useful in describing the way in which temperature rises (and density decreases) with height, have limitations in that the high degree of structure and temporal variation in the chromosphere and corona is not properly reproduced and the true nature of the transition region may also be substantially different.

1.2 The Magnetic Sun

Just before noon on Thursday 1st September 1859, Richard Carrington was at work in his solar observatory near Redhill in Surrey, making observations of the forms and positions of sunspots. Carrington (1859) reported the following unusual event: suddenly at 11:18 GMT, he witnessed the occurrence of striking brightenings associated with a large group of sunspots. By 11:23 GMT, the two bright patches had disappeared, having travelled about 35,000 miles across the sunspot. At Kew, variations of the three geomagnetic vector components were recorded, showing a "moderate but very marked disturbance" that took place at about 11:20 GMT on the same date. That night, around 04:00 GMT, a great magnetic storm occurred. Not one to jump to conclusions, it was recorded (in an editorial addition to the report) that "while the contemporary occurrence may deserve noting, [Carrington] would not have it supposed that he even leans towards hastily connecting them [the magnetic disturbance with the event he had observed on the surface of the Sun]." In fact, these observations were the first indication of a direct link between solar activity and magnetism. Today, it is acknowledged that magnetic fields are of fundamental importance in the physics of the Sun.

1.2.1 Regeneration of the Solar Magnetic Field

The Sun is believed to have formed from the contraction of a gas cloud. It is possible that a "primordial" magnetic field was dragged in with this gas, and is still maintained today in the solar interior. Through the combined actions of convection (α) and differential rotation (Ω), the Sun operates as an α - Ω dynamo where the seed magnetic field is being constantly regenerated, amplified and sustained. A dynamo can convert the kinetic energy of an electrically conducting medium into magnetic energy. The convective motion of the medium, $\mathbf{v}$, across the magnetic field $\mathbf{B}$, induces an electric field $\mathbf{v} \times \mathbf{B}/c$ that drives a current, $\mathbf{j}$ to generate $\mathbf{B}_{alpha}$ (Hoyng, 1992). When $\mathbf{B}_{alpha}$ reinforces the original magnetic field, $\mathbf{B}$, a dynamo is created. This dynamo is believed to be located at the bottom of the convection zone in the tachocline, the interface between the radiative interior and differentially rotating convection zone. Starting with a north-south poloidal dipole field, differential rotation effectively stretches the magnetic field and winds it around the Sun generating two east-west zones of toroidal magnetic flux, oppositely orientated in each hemisphere of the convection zone (see Figure 1.5). This is referred to as the Ω-effect. The α-effect is due to the interaction of convection and solar rotation. The α-effect takes the east-west toroidal magnetic field generated by the Ω-effect and transforms it back into a north-south poloidal magnetic field. Meridional circulation then carries this field poleward and down to the base of the convection zone.

The global solar magnetic field, driven by this regenerative dynamo undergoes an oscillation between north-south poloidal and east-west torroidal components. This oscillation is known as the solar cycle and is of approximately 11.1 years duration (Phillips *et al.*, 2008). It takes two solar cycles for the same pattern of magnetic polarities to reappear. Magnetic flux tubes emerge from the toroidal flux layer, and when they become buoyant enough, rise through the convection zone. The flux tube can break through the photosphere forming loops which create bipolar concentrations of magnetic field (called active regions, illustrated by N1, N2, S1 and S2 in Figure 1.5. Also see §1.2.3.2). The first breakthroughs of the magnetic field occur at high latitudes ($\pm \sim 30°$). As the Ω-effect winds the magnetic field increasingly tighter, such breakthroughs drift toward the solar equator. For a summary of observations and theoretical advances on the large-scale emergence and

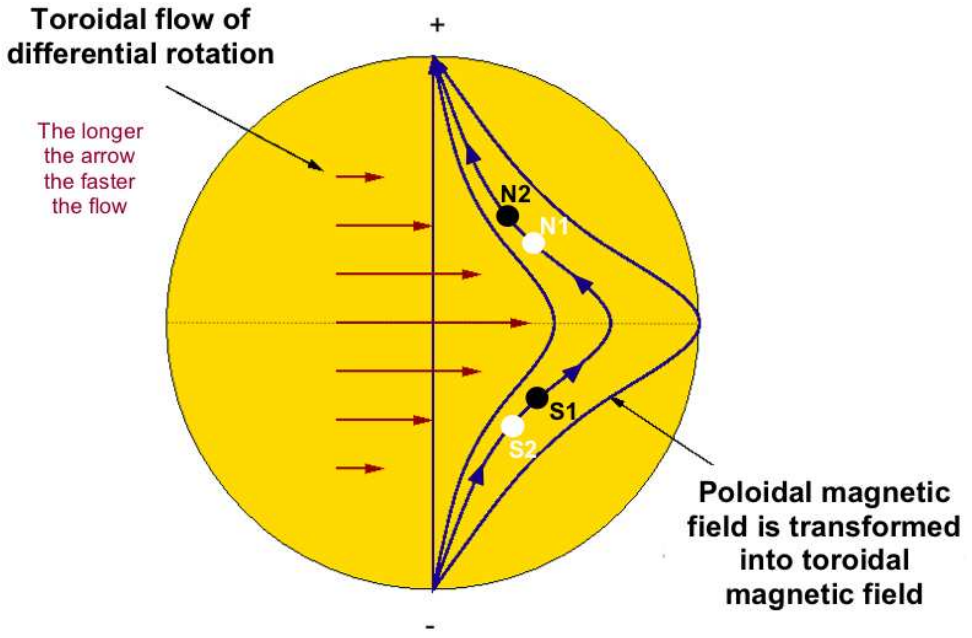

Figure 1.5: Illustration of the Ω dynamo effect, where the north-south poloidal solar magnetic field is stretched by differential rotation generating two zones of toroidal magnetic flux, oppositely directed in each hemisphere of the convection zone. White (black) dots indicate concentrations of positive (negative) active region magnetic field polarity appearing at the intersection of the emerged flux tube with the photosphere. Figure adapted from `http://www.cora.nwra.com/~werne/eos/images/omega.gif`

decay which forms and dominates the magnetic field patterns that we observe on the Sun, see the review by van Driel-Gesztelyi (2002).

The Coriolis force acts on the rising and expanding flux tube, inducing a bipole tilt, making the most equatorward part of the magnetic flux tubes (N1 and S1) lead the poleward part (N2 and S2, as shown in Figure 1.5). This tilt (known as Joy's Law) plays a part in the neutralisation and subsequent reversal of the poloidal field as follows. On each hemisphere, turbulent diffusion and small-scale reconnection events lead to the cancellation of 99% of flux (Schrijver and Zwaan, 2000). However a remnant part of the bipole survives. Eventually the leading polarities of the remnant bipoles, (N1 and S1), which have opposite polarities in the two hemispheres (Hale's Law), cancel at the equator and $< 1\%$ of the remnant following polarities (N2 and S2) make it to the poles. At the poles, the remnant following polarities first neutralise the existing field and then replace the flux by the new polarity. A near-poloidal field is restored, with all polarities reversed. The cycle then begins again. Such a model of the 22-year solar cycle was first described by Babcock (1961) and successfully describes why the solar magnetic field reverses its magnetic polarity regularly. This "Babcock model" also explains the observed pattern and behaviour of sunspots (concentrations of active region magnetic field) during the solar cycle (see Figure 1.6). Although many observed features are successfully described, it should be noted that the Sun can misbehave - e.g. non-Hale (reversed polarity) active regions can emerge. Such reversed polarity regions may be caused by deformation of the flux tube by vortices in the convection zone, or kink deformation due to high internal twist during emergence (López Fuentes *et al.*, 2003; van Driel-Gesztelyi *et al.*, 2000).

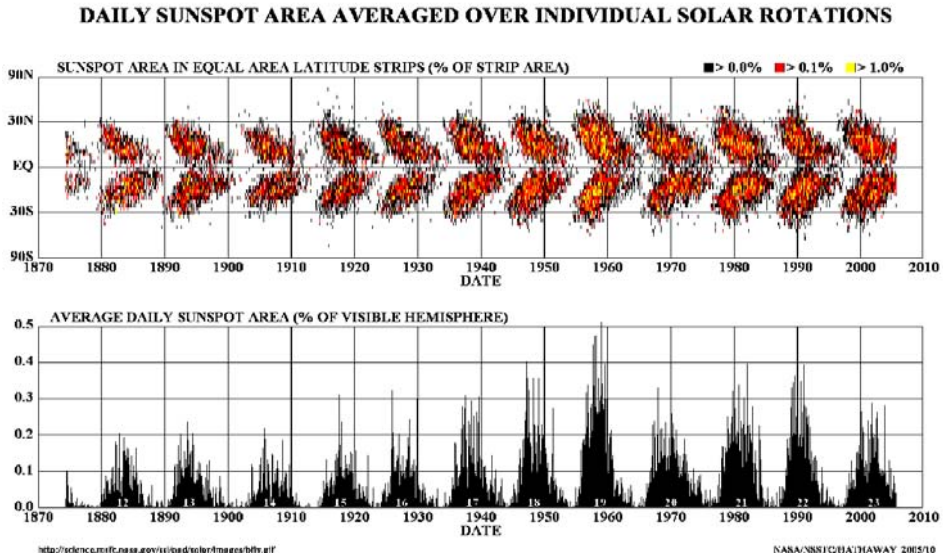

Figure 1.6: Diagram showing the variation of the spatial location (top panel) and area (bottom panel) occupied by sunspots (concentrations of active region magnetic field) observed on the photosphere. A plot of the spatial variation of the sunspots with time (top panel) is known as a Butterfly diagram. Figure courtesy Marshall Space Flight Center, NASA.

1.2.2 Measurement of the Solar Magnetic Field

Solar magnetic flux density is measured in the c.g.s. unit of Gauss (G) (1 Gauss = 10^{-4} Tesla) and magnetic flux is measured in the c.g.s. unit of Maxwells (Mx) (1 Maxwell = 10^{-8} Weber). In a magnetic field strength of one Gauss, one Maxwell is the total flux across a surface of one square centimeter perpendicular to the magnetic field:

$$F_M = \int_S \mathbf{B} \cdot \mathbf{dS} \tag{1.1}$$

where F_M is the magnetic flux (Mx), $\mathbf{dS}$ is a vector normal to the surface, S. Typical solar magnetic field strengths are of the order of 10 - 1000 G. For comparison, Earth's magnetic field strength varies between $\sim$ 0.3 - 0.6 G.

It is possible to measure the photospheric magnetic field using "Zeeman spectropolarimetry".

An electron orbiting an atom is equivalent to a current which induces a magnetic field. When an external magnetic field is applied, it exerts a torque on the magnetic field of the electron, which depends on the alignment (θ) between the electron's magnetic field and the external magnetic field. The electron acquires an additional potential energy, which may be positive, zero, or negative, depending on the angle θ. The stronger the external magnetic field, the greater the added or subtracted potential energy.

As a result, there are two σ components of the spectral line, displaced to either side of the unperturbed central component (see Figure 1.7).

Light is composed of electromagnetic waves. By convention, the electric field vector is described,

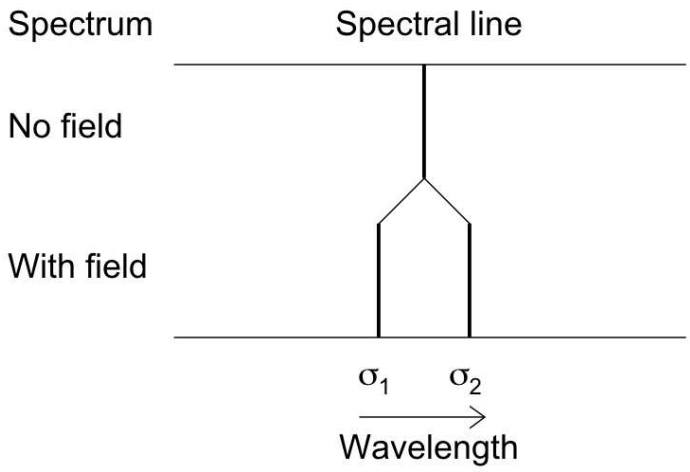

Figure 1.7: The patterns of Zeeman-split spectral lines when viewed along the direction of the external magnetic field. The spectral line is split into two σ components. Figure adapted from Phillips (1992). Permission to reproduce this figure has been granted by Cambridge University Press.

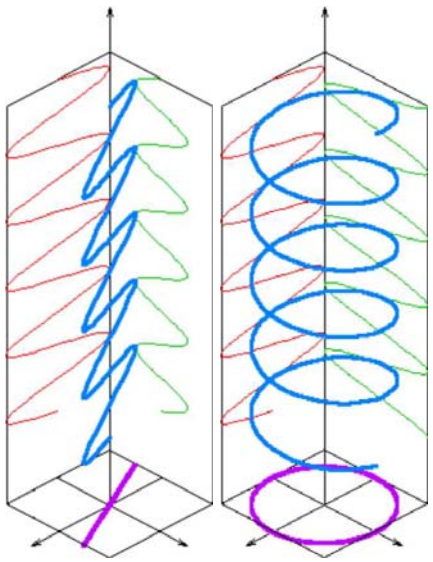

Figure 1.8: Left: Linear polarisation, where the orthogonal components of the electric field vector are in phase. Right: Circular polarisation, where the two orthogonal components have exactly the same amplitude and are exactly 90° ($\lambda/4$) out of phase. Figures from `http://en.wikipedia.org`.

with the magnetic field being directed perpendicular to the direction of propagation, as well as being proportional to it. The shape traced in a fixed plane by the electric field vector (see Figure 1.8) of such a plane wave is known as a "Lissajous figure" and the plane wave can be described as being linearly polarised. Circular polarisation exists where the two orthogonal components have exactly the same amplitude and are exactly 90° ($\lambda/4$) out of phase, so the x-component can be either 90° ahead of or behind the y-component. The direction of rotation of the electric field depends on which component leads the 90° phase-shift and the different directions are described as right-hand circular polarisation (RCP) or left-hand circular polarisation (LCP). The two σ components arising from the Zeeman effect are circularly polarised in opposite directions.

The effect of the Zeeman splitting means that the circularly polarised σ components are displaced in wavelength to either side of the unperturbed central component by an amount propor-

tional to the strength of the external magnetic field:

$$\triangle\lambda_B = 4.7 \times 10^{-13} g_l \lambda^2 B \tag{1.2}$$

where λ_B is the shift in wavelength (the magnitude of the splitting), B is the strength in Gauss of the magnetic field being measured and λ is the wavelength (Å) in which the splitting is being observed (Zirin, 1992). g_l is the Landé g-factor:

$$g_l = 1 + \frac{j(j+1) - l(l+1) + s(s+1)}{2j(j+1)} \tag{1.3}$$

where l is the orbital angular momentum, s is the spin angular momentum and j is the total angular momentum of the electron and is a constant for each spectral line. Lines having a large g_l are the most sensitive to external magnetic fields.

The direction along the line-of-sight (so the sense of the magnetic polarity) is determined by the circular polarisation of the shifted lines. Electrons with angular momentum aligned with (against) the magnetic field will emit and absorb light that is circularly polarised in the same (opposite) direction.

It is, however, much more difficult to measure the magnetic field in the corona. The atoms in an emitting gas have a distribution of velocities. Each photon emitted will be red or blue shifted by the Doppler effect depending on the velocity of the atom relative to the observer. The higher the temperature of the gas, the wider the distribution of velocities in the gas. Since the spectral line is the combination of all of the emitted radiation, the higher the temperature of the gas, the broader will be the spectral line emitted from that gas. The extremely high temperature in the corona means that the Zeeman splitting is nearly obscured by the thermal broadening. However, due to the λ^2 term in Equation 1.2, infrared spectral lines can be used to make coronal magnetic field measurements (Tomczyk *et al.*, 2008, and references therein). Magnetic field strength and direction in the corona can also be determined from radio emission. Furthermore, we can infer the coronal magnetic field strength by creating mathematical models using the measured photospheric magnetic field as a boundary condition.

1.2.3 Structure of the Solar Magnetic Field

The structure of the solar magnetic field is largely indicated by the three major components of the corona that are observed: coronal holes, where the average electron temperature drops to 0.7-1.3$\times10^6$ K (although a weak high temperature component is also detected); active regions where the average magnetic field strength and heat input are much greater, with temperatures of 1-8$\times10^6$ K, rising to 10-20$\times10^6$ K during explosive activity; and the quiet Sun, confined by closed magnetic fields with temperature averages around 1-2$\times10^6$ K (Phillips *et al.*, 2008).

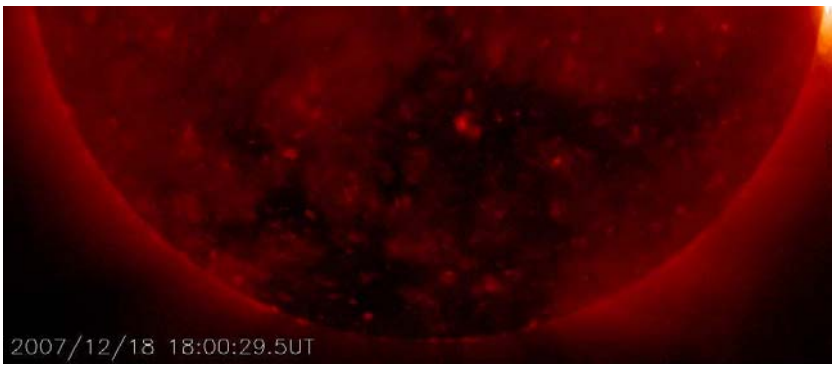

Figure 1.9: *Hinode*/XRT image of the south polar coronal hole. Within the coronal hole, small loop structures and X-ray bright points are evident.

1.2.3.1 Coronal Holes

Extensive coronal holes (seen in EUV and X-ray images as regions of decreased emission) are often located at the solar poles. These polar coronal holes are most substantial at solar minimum. Low-latitude coronal holes may also exist, away from the poles, nearer the solar equator. These occur nearer solar maximum when the magnetic field of the Sun is at its most complex (§1.2.1). The magnetic field in coronal holes can be described as being "open". "Open" magnetic field is understood to be connected to the Sun at one end, extending far out into the interplanetary space, eventually connecting to the interplanetary magnetic field. From the point of view of the corona, the magnetic field *appears* to be connected to the Sun only at one end, hence the usage of "open". Coronal holes appear dark because the plasma in these "open" field regions is not constrained to the corona, but can escape along the field lines, so being evacuated out into the interplanetary space. They therefore have a low density $\sim 10^7$ - 10^8 cm^{-3}. The constant outflow from coronal holes is known as the "fast solar wind" and has an average velocity of about 800 km s^{-1}. Coronal holes are dominated by either positive or negative polarity magnetic field, but do not exclusively consist of one polarity. Mixed magnetic field, most evidently in the form of small bipoles also exists within coronal holes. Cancellation of opposite magnetic polarity photospheric fragments has been linked to the occurance of coronal X-ray bright points (e.g. Parnell *et al.*, 1994). Such X-ray bright points are dynamically illustrated by observations recently obtained by the *Hinode*/X-Ray Telescope (see Figure 1.9).

1.2.3.2 Active Regions

Active regions can be described as areas of magnetic complexity and strong magnetic field, often associated with sunspots. In contrast to the "open" magnetic description applicable to coronal holes, active regions constitute areas of closed magnetic field, in the form of loops (see Figure 1.10). The photospheric field strength in sunspots can be high, 3000-4000 G, but even values up to 6100 G have been recorded (Livingston *et al.*, 2006). The total flux of a large sunspot is typically 10^{22} Mx (Hoyng, 1992). In comparison, the total flux of a large active region may be a few times 10^{22} Mx. The electron density of plasma in an active region may typically be of order $\sim 10^9$ - 10^{10} cm^{-3}.

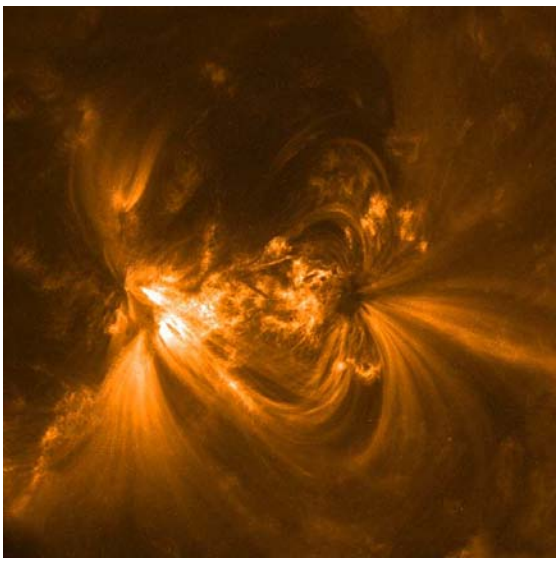

Figure 1.10: TRACE EUV image of an active region showing closed magnetic loops.

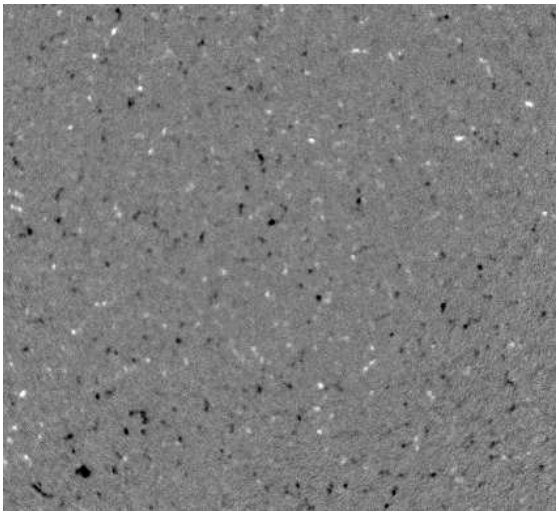

Figure 1.11: SOHO/MDI magnetic map of a quiet Sun region near solar disk centre. Note the mixed polarity "salt and pepper" magnetic field distribution.

1.2.3.3 Quiet Sun

The quiet Sun can be described as a mixed polarity "salt and pepper" magnetic field, consisting of a mixture of relatively small-scale, randomly orientated closed coronal loops, as well as scattered "open" field lines. Figure 1.11 shows a SOHO/MDI magnetogram (a magnetic map) of a region of quiet Sun. Black indicates magnetic field directed into the Sun (negative polarity), while white indicates a direction out of the Sun (positive polarity). Feldman *et al.* (1999) analysed TRACE EUV images and found that: "Observations of quiet-region morphology indicate that the $\sim 4{\times}10^4$ - $1.4{\times}10^6$ K temperature domain of the solar upper atmosphere consists of a hierarchy of isothermal looplike emission structures... The hotter looplike structures are the largest among the quiet-Sun loop structures ... they form a canopy over the lower temperature loop structures." In agreement with this work, recently Matsuzaki *et al.* (2007) analysed data obtained with the

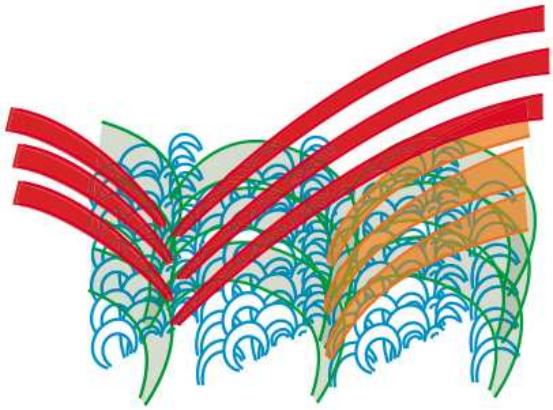

Figure 1.12: A schematic of the temperature components of the coronal loop structures in a quiet Sun region (Matsuzaki *et al.*, 2007). Blue represents the cooler network loops with green, through orange to red representing loops at progressively higher temperatures. Permission to reproduce this figure has been granted by the Astronomical Society of Japan.

Hinode/Extreme ultra-violet Imaging Spectrometer (EIS) instrument and have shown that "ubiquitous high-temperature components, consisting of a collection of loops at temperatures of $\sim 1{\times}10^6$ K and $\sim 2{\times}10^6$ K are superposed in the line of sight, and a mottled low-temperature component ($\sim 4{\times}10^5$ K)." They also observe longer closed loops at higher temperatures. Matsuzaki *et al.* (2007) conclude that the drastic difference in morphology between the low and high temperature components arises because the low component originates in loops within a super-granule cell, whilst the hotter component originates in larger, overlying loops connecting different super-granule cells or in "open" magnetic fields. Figure 1.12 shows a schematic of the temperature components of the coronal loop structures in a quiet Sun region.

In addition, Feldman *et al.* (1999) measured electron densities in an equatorial quiet Sun coronal region. They found that, on average, electron densities in quiet Sun regions are higher by a factor 2 to 3 compared to electron densities in coronal holes. The origin of the slow-speed solar wind, with velocities of about 400 km s^{-1} is less clear than the origin of the fast solar wind, although it is believed to originate mainly in quiet Sun regions. Typical magnetic field strength of network elements constituting the quiet Sun is $\sim 10^{18}$ Mx (Hoyng, 1992).

1.3 Magnetohydrodynamics (MHD)

We have discussed that a dynamo can convert the kinetic energy of an electrically conducting medium into magnetic energy (§1.2.1). MHD processes can generate and convert magnetic energy into kinetic energy.

For a physically consistent description of magnetic features on a macroscopic scale, it is necessary to solve the MHD equations which are comprised of equations of continuity, motion, energy, the equation of state, a simplified form of Maxwell's equations and Ohm's Law. In §1.3.5, Ohm's Law and Maxwell's equations are manipulated to derive Alfvén's Frozen Flux theorem. A quantity known as the plasma beta is introduced in §1.3.8. The magnetic Reynold's number, R_M, gives an idea of the degree of the coupling between the plasma flow in a region and the ambient magnetic field and is described in §1.3.9.

In MHD, processes which convert energy into other forms can be distinguished as either ideal or non-ideal (Priest and Forbes, 2000). Ideal processes (e.g. ideal kink instability, §1.5.1) convert magnetic energy into kinetic energy without magnetic dissipation. Non-ideal processes (e.g. magnetic reconnection §1.4) can convert magnetic energy into kinetic energy and heat.

Magnetohydrodynamics (MHD) can be described as the study of the interaction between a magnetic field and the flow of an electrically conducting fluid (a plasma).

1.3.1 Description of a Plasma

Given the extreme temperatures of the Sun (particularly of the solar atmosphere) and the importance of the magnetic field, a realistic description of the solar environment necessarily demands consideration of a magnetised plasma.

A plasma is a highly ionized gas. When the temperature of a gas exceeds a certain threshold, the thermal energy of the particles becomes so great that it overwhelms the electrostatic forces which bind electrons to atomic nuclei. As a result, plasmas have a very high electrical conductivity. Plasmas are most precisely described by particle distributions, which evolve according to kinetic equations where each particle has a time-dependent position, $\mathrm{x}_i(\mathrm{t})$ and velocity $\mathrm{v}_i(\mathrm{t})$ (Baumjohann and Treumann, 1997). The Maxwellian velocity distribution shown below, *f(v)*, is generally used for a collisionless plasma:

$$f(v) = n\left(\frac{m}{2\pi k_B T}\right)^{3/2} exp\left(-\frac{mv^2}{2k_B T}\right) \tag{1.4}$$

where n = particle number density, m = particle mass, k_B = Boltzmann's constant and T = temperature. To express the speeds of the particles rather than their velocities, Equation 1.4 must be multiplied by $4\pi v^2$ (Spitzer, 1962).

To describe the generic properties of a plasma, we need to determine the spatial and temporal development of macroscopic moments of the distribution for each particle species, such as density (ρ), velocity (v) and temperature (T), which depend only on position (x) and time (t). The distribution function, *f(v)*, may be integrated with respect to velocity (v) to obtain these moments.

$$Moment_i(x,t) = \int f(v,x,t)v^i d^3v \tag{1.5}$$

The i = 0 moment is the density, ρ and takes the form: $\rho = \int f(v)d^3v$. The i = 1 moment is the bulk flow velocity, v_b and takes the form: $v_b = \frac{1}{\rho}\int v f(v)d^3v$. In the same way, the i= 2 and i = 3 moments correspond to pressure, P, and temperature, T.

1.3.2 Fluid Equations

1.3.2.1 The Equation of Mass Continuity

The equation of mass continuity results from the zeroth-order (i = 0) moment of equation 1.5. It couples the plasma density (ρ) to the fluid velocity ($\mathbf{v}$).

$$\frac{\partial \rho}{\partial t} + \nabla \cdot (\rho \mathbf{v}) = 0 \tag{1.6}$$

states that if mass flows with velocity, $\mathbf{v}$ into a region then there is a concentration of mass ($\nabla \cdot (\rho \mathbf{v}) < 0$)), and the plasma density (ρ increases ($\frac{\partial \rho}{\partial t} > 0$). On the other hand, if the mass flux diverges, then the density decreases. There is no creation or destruction of matter - mass flux is conserved during the motion of the fluid.

Equation 1.6 can be expanded and written as:

$$\frac{\partial \rho}{\partial t} + (\mathbf{v} \cdot \nabla) n + n(\nabla \cdot \mathbf{v}) = 0 \tag{1.7}$$

1.3.2.2 The Equation of Motion

The equation of motion results from the first-order (i = 1) moment of equation 1.5. It relates the fluid velocity $\mathbf{v}$, to the plasma density ρ, and to the electromagnetic Lorentz force acting on the charges in the fluid. The equation of motion may be expressed as:

$$\rho \frac{\partial \mathbf{v}}{\partial t} + \rho(\mathbf{v} \cdot \nabla)\mathbf{v} = -\nabla p + \mathbf{j} \times \mathbf{B} + q\mathbf{E} + \rho \mathbf{g} + \mathbf{F} \tag{1.8}$$

where $-\nabla p$ is the plasma pressure gradient, $\mathbf{j}$ is the current density, $\mathbf{B}$ is the magnetic induction (usually referred to as the magnetic field, although technically this is $\mathbf{H} = \mathbf{B}/\mu$, where μ is the magnetic permeability), $\mathbf{j} \times \mathbf{B}$ is the Lorentz force which accelerates the fluid and couples the fluid equations to the electromagnetic equations, q is the charge density, $\mathbf{E}$ is the electric field strength, $\rho \mathbf{g}$ is the gravitational force and $\mathbf{F}$ indicates additional forces, such as the effect of viscosity.

Neglecting velocity variations with respect to time, and equating the left-hand side of the equation of motion with the magnetic force (in order of magnitude), gives the Alfvén speed, v_A:

$$v_A = \frac{B}{(\mu \rho)^{1/2}} \tag{1.9}$$

The Alfvén speed is the maximum velocity to which magnetic forces can accelerate the plasma, and the speed at which magnetic disturbances travel along the magnetic field.

For the quiet Sun lower corona v_A is ~ 700 km s^{-1}, where $\rho \sim 10^9$ cm^{-3} and B ~ 10 G (Phillips *et al.*, 2008).

1.3.2.3 The Energy Equation

The equation of energy conservation results from the second-order (i = 2) moment of equation 1.5 and expresses that the heat increases or decreases as the net effect of energy sources and sinks, as the plasma moves in space. It may be expressed as:

$$\frac{\partial p}{\partial t} + \mathbf{v}\cdot \nabla p + \gamma p \nabla \cdot \mathbf{v} = E_\ell \tag{1.10}$$

where E_ℓ is the total energy loss function and γ is the ratio of specific heat at constant pressure to specific heat at constant volume (normally taken as 5/3). Energy loss can result from e.g. radiative cooling, conduction, and energy gain may be the result of e.g. MHD wave dissipation, joule heating, heating due to friction.

1.3.2.4 Equation of State

For a plasma that behaves as an ideal gas, the equation of state relates pressure (p) and temperature (T) by:

$$p = \frac{k_B}{\bar{m}} \rho T \tag{1.11}$$

where p is the gas pressure, k_B is the Boltzmann constant, $\bar{m}$ is the mean particle mass, ρ is the gas density and T is the temperature.

By assuming an equation of state for the pressure, it becomes possible to close the system of fluid equations.

1.3.3 Electromagnetic Equations

1.3.3.1 Maxwell's Equations

Ampére's Law:

$$\nabla \times \mathbf{B} = \mu \mathbf{j} + \frac{1}{c^2} \frac{\partial \mathbf{E}}{\partial t} \tag{1.12}$$

where c is the speed of light in a vacuum (3×10^8 ms^{-1}) and $\partial\mathbf{E}/\partial t$ is the displacement current. Equation 1.12 means that either currents or time-varying electric fields may produce magnetic fields.

Solenoidal condition:

$$\nabla \cdot \mathbf{B} = 0 \tag{1.13}$$

Equation 1.13 indicates that there are no magnetic monopoles.

Faraday's Law states that a time-varying magnetic field induces an electric field:

$$\nabla \times \mathbf{E} = -\frac{\partial \mathbf{B}}{\partial \mathbf{t}} \tag{1.14}$$

Gauss' Law for **E**, implying charge conservation:

$$\nabla \cdot \mathbf{E} = \frac{\rho_e}{\epsilon} \tag{1.15}$$

where ρ_e is the charge density and ϵ is the permittivity of free space.

1.3.3.2 Ohm's Law

A simplified Ohm's law is used:

$$\mathbf{j} = \sigma(\mathbf{E} + \mathbf{v} \times \mathbf{B}) \tag{1.16}$$

since plasma moving with a velocity, **v** across a magnetic field is subject to an electric field described by $\mathbf{v} \times \mathbf{B}$. There may also be an electric field, **E** acting on the plasma even when it is at rest. σ is the electrical conductivity, assumed constant. This form of Ohm's law couples the electromagnetic equations to the plasma fluid equations through **v**, the plasma velocity.

1.3.4 The MHD Approximation

The fundamental equations (given below) use these assumptions (Priest, 1982):

- Quasi-neutrality of the plasma is assumed, so local electric charge densities are neglected since $\rho_{electrons} = \rho_{ions}$. As a result, the concept of charge conservation is irrelevant. In this case, $qE \rightarrow 0$ under the MHD approximation and Gauss's Law for **E** (Equation 1.15) becomes $\nabla \cdot \mathbf{E} = 0$.
- An inertial (not accelerating or rotating) frame of reference is used.
- The plasma is treated as a single fluid system. This assumes that both electrons and ions are collision-dominated so that a given particle remains reasonably close to its neighbours during timescales of interest. Then, the plasma may be divided into small, identifiable fluid elements. The characteristic lengthscale is greater than internal plasma lengths (e.g. ion gyroradius and the mean free path length).
- The characteristic timescale is greater than internal plasma timescales (e.g. ion gyrofrequency and mean free path time). The plasma is therefore assumed to be in thermodynamic equilibrium with distribution functions close to Maxwellian (Equation 1.4).
- In solar physics, the bulk plasma flow speed, sound speed and Alfvén speed are assumed to be much less than c, so relativistic effects can be ignored. As a result, the displacement current in Equation 1.12 is neglected.
- μ and ϵ are assumed to be constant and (for solar plasmas) have the vacuum values $\mu_0 = 4\pi \times 10^{-7}$ Hm^{-1} and $\epsilon_0 = 8.854 \times 10^{-12}$ Fm^{-1}.

These assumptions result in the fundamental MHD Equations:

$$\frac{\partial \rho}{\partial t} + \nabla \cdot (\rho \mathbf{v}) = 0 \tag{1.17}$$

$$\rho \frac{\partial \mathbf{v}}{\partial t} + \rho(\mathbf{v} \cdot \nabla)\mathbf{v} = -\nabla p + \mathbf{j} \times \mathbf{B} + \rho \mathbf{g} + \mathbf{F} \tag{1.18}$$

$$\frac{\partial p}{\partial t} + \mathbf{v} \cdot \nabla p = -\gamma p \nabla \cdot \mathbf{v} + E_\ell \tag{1.19}$$

$$p = \frac{k_B}{\bar{m}} \rho T \tag{1.20}$$

$$\nabla \times \mathbf{B} = \mu_0 \mathbf{j} \tag{1.21}$$

$$\nabla \cdot \mathbf{B} = 0 \tag{1.22}$$

$$\nabla \times \mathbf{E} = -\frac{\partial \mathbf{B}}{\partial \mathbf{t}} \tag{1.23}$$

$$\mathbf{j} = \sigma(\mathbf{E} + \mathbf{v} \times \mathbf{B}) \tag{1.24}$$

In the *ideal* MHD approximation, the electrical conductivity of the gas, σ, is assumed to be extremely high, so that is can be treated as a perfect conductor. Therefore ideal MHD describes the interaction of inviscid fluids of low electrical resistivity with magnetic and gravitational fields.

Further simplifications to the MHD approximation may be made, including:

- The plasma is assumed to be incompressible so that the density does not change with time and Equation 1.17 reduces to $\nabla \cdot \mathbf{v} = 0$.
- The plasma is assumed to be inviscid, so viscous forces can be neglected and the equation of motion (Equation 1.18) is simplified.
- The system is assumed to vary adiabatically, without energy loss so the energy equation (Equation 1.19) is simplified.

1.3.5 Alfvén's Frozen Flux Theorem

In this section, Ohm's Law and Maxwell's Equations are manipulated to derive Alfvén's Frozen Flux theorem, which has fundamental consequences for the physics of the solar corona.

Rearranging Ohm's Law (Equation 1.24) for $\mathbf{E}$ and substituting into Equation 1.23 gives:

$$\frac{\partial \mathbf{B}}{\partial t} = -\left(\nabla \times \frac{\mathbf{j}}{\sigma}\right) + \nabla \times (\mathbf{v} \times \mathbf{B}) \tag{1.25}$$

Rearranging Ampére's Law (Equation 1.21) for $\mathbf{j}$ and substituting into Equation 1.25 gives:

$$\frac{\partial \mathbf{B}}{\partial t} = -\nabla \times \left(\frac{\nabla \times \mathbf{B}}{\mu_0 \sigma}\right) + \nabla \times (\mathbf{v} \times \mathbf{B}) \tag{1.26}$$

Using the following triple vector product identity:

$$\nabla \times (\nabla \times \mathbf{A}) = \nabla(\nabla \cdot \mathbf{A}) - (\nabla \cdot \nabla)\mathbf{A} \tag{1.27}$$

Equation 1.26 can be expressed as:

$$\frac{\partial \mathbf{B}}{\partial t} = -\frac{1}{\mu_0 \sigma}(\nabla(\nabla \cdot \mathbf{B}) - \nabla^{\mathbf{2}}\mathbf{B}) + \nabla \times (\mathbf{v} \times \mathbf{B}) \tag{1.28}$$

From Equation 1.13, the divergence of the magnetic field is zero ($\nabla \cdot \mathbf{B} = 0$). Inserting this into Equation 1.28 gives the Induction Equation:

$$\frac{\partial \mathbf{B}}{\partial t} = \frac{\nabla^2 \mathbf{B}}{\mu_0 \sigma} + \nabla \times (\mathbf{v} \times \mathbf{B}) \tag{1.29}$$

The induction equation links the evolution of the magnetic field to the plasma in resistive (non-ideal) MHD. $\nabla^2\mathbf{B}/\mu_0\sigma$ is a diffusion term (the magnetic diffusivity, $\eta_0 = 1/\mu_0\sigma$, is assumed to be constant), and $\nabla \times (\mathbf{v} \times \mathbf{B})$ is an advective term. The induction equation therefore expresses that change of the magnetic field can be due to diffusion and/or advection. In the corona however, the conductivity, σ is extremely high. This means that the diffusion term is usually negligible, leaving the evolution of the magnetic field to be described by the advective term so that the plasma and the magnetic field are constrained to move together. This result is known as Alfvén's Frozen-Flux Theorem and has considerable implications for the solar corona, as will be discussed in Section 1.4.

1.3.6 Magnetic Pressure and Magnetic Tension

The Lorentz force, $\mathbf{j} \times \mathbf{B}$ is the effect of the magnetic pressure and magnetic tension on a conducting MHD fluid. Using Ampére's Law (Equation 1.21), and taking the cross-product with the magnetic field $\mathbf{B}$:

$$\mathbf{j} \times \mathbf{B} = \frac{1}{\mu_0}(\nabla \times \mathbf{B}) \times \mathbf{B} \tag{1.30}$$

using the vector identity:

$$\nabla(\mathbf{A} \cdot \mathbf{A}) = 2\mathbf{A} \times (\nabla \times \mathbf{A}) + 2(\mathbf{A} \cdot \nabla)\mathbf{A} \tag{1.31}$$

the following understanding of the Lorentz force is obtained:

$$\mathbf{j} \times \mathbf{B} = -\nabla \left(\frac{B^2}{2\mu_0} \right) + \frac{(\mathbf{B} \cdot \nabla)\mathbf{B}}{\mu_0} \tag{1.32}$$

The first term on the right hand side is a magnetic pressure term, P_B, and the second term is a magnetic tension term, T_B. The magnetic pressure force acts to distribute the magnetic field uniformly. The magnetic tension force acts if the magnetic field lines are curved, exerting a force perpendicular to the magnetic field.

1.3.7 MHD Waves

The basic modes of wave motion in hot astrophysical plasmas consist of the following (van Driel-Gesztelyi, 2004):

1.3.7.1 Sound (acoustic) waves

Driven by perturbations in the plasma pressure, acoustic waves travel at the sound speed c_s:

$${c_s}^2 = \frac{\gamma p_0}{\rho_0} = \frac{\gamma k_B T_0}{m} \tag{1.33}$$

where γ is the polytropic index (ratio of specific heat at constant pressure to the specific heat at constant volume), p_0 is the gas pressure, ρ_0 is the gas density, T_0 is the plasma temperature and k_B is Boltzmann's constant. Equation 1.33 shows that sound wave speeds for the solar atmosphere are approximately the most probable thermal speed, which for protons in the quiet Sun corona is ~ 200 km s^{-1} (Phillips *et al.*, 2008).

1.3.7.2 Alfvén waves

Alfvén waves are another type of plasma wave and consist of oscillations of the magnetic field (Alfvén, 1942). Shear Alfvén waves and their energy propagate parallel to $\mathbf{B}$. They are driven by the restoring force of the magnetic tension, T_B (Equation 1.32). They are not density perturbations, but are purely transverse waves and are non-dispersive. They propagate at the Alfvén speed, v_A (Equation 1.9).

1.3.7.3 Magnetoacoustic waves

This type of wave can exist when the magnetic pressure, P_B (Equation 1.32) and plasma pressure act together. They can therefore be described as hybrids of Alfvén and sound (acoustic) waves. There are two modes: fast and slow. Fast mode magnetoacoustic waves travel at nearly the Alfvén speed, v_A, whilst slow magnetoacoustic waves travel at approximately the ion sound speed, c_s.

The phase speed of individual magnetoacoustic waves is given by the following dispersion relation:

$$v_{fast,slow}{}^2 = \frac{\omega}{k} = \left[\frac{1}{2}(c_s^2 + v_A^2) \pm \frac{1}{2}\sqrt{c_s^4 + v_A^2 - 2c_s^2 v_A^2 cos2\Theta_B}\right]^{1/2} \tag{1.34}$$

where Θ_B is the angle between the magnetic field, **B**, and wave vector, **k**. The solutions to equation 1.34 depend on whether $v_A > c_s$, or vice versa. As discussed above for the quiet Sun lower corona, $v_A \sim 700$ km s$^{-1} > c_s \sim 200$ km s^{-1}.
Therefore, for $v_A > c_s$:
For propagation of the wave vector along the magnetic field, $\Theta_B = 0$, $v_{fast} = v_A$ and $v_{slow} = c_s$.
For propagation of the wave vector across the magnetic field, $\Theta_B = \pi/2$, $v_{fast} = ({c_s}^2 + {v_A}^2)^{1/2}$ and $v_{slow} = 0$.

Therefore, the fast magnetoacoustic mode is the only MHD wave mode that can propagate perpendicular to **B**.

We note that the derivation of the dispersion relation (Equation 1.34) is made using the linear approximation, where we assume that the amplitude of the waves is small and the MHD equations are linearised about an equilibrium, assuming the initial state is static. Plane wave solutions are determined, assuming that the pertubations vary as $e^{i(k \cdot r - \omega t)}$.

1.3.7.4 Fast and Slow Shocks

Both fast and slow magnetoacoustic waves can evolve to large amplitudes, thus steepening to become fast and slow shocks. Shocks develop when the plasma fluid velocity exceeds the magnetosonic speed, c_{ms}:

$$c_{ms}^2 = c_s^2 + v_A^2 \tag{1.35}$$

Shock speeds may be given in terms of a magnetosonic Mach number: $M_{ms} = v_{shock}/c_{ms}$, or an Alvénic Mach number: $M_A = v_{shock}/v_A$.

Across a shock transition, the plasma pressure always increases when progressing from the unshocked to the shocked medium. So both fast and slow mode shocks are compressive, with the downstream density higher than the upstream one. In addition, heated plasma exists following the shock. As a result, enhanced emission (e.g. in EUV and soft X-rays) is expected following a shock. However, there are differences between fast and slow shocks (Baumjohann and Treumann, 1997). Across a fast shock, the Alfvén speed and correspondingly the magnetic pressure parallel to the shock surface, increases. Across a slow shock, the inverse occurs and the magnetic pressure

decreases. In addition, across fast shocks, the magnetic field strength increases and is tilted toward the shock surface, whilst across slow shocks, it decreases and bends toward the shock normal.

1.3.8 Plasma Beta, β

The MHD equations allow a description of the interaction between the magnetic field and the solar plasma. A useful parameter is the plasma β, defined by the ratio of the gas pressure to the magnetic pressure:

$$\beta = \frac{P_{gas}}{P_{mag}} = \frac{2\mu_0 p}{B^2} \tag{1.36}$$

When $\beta < 1$, the magnetic field is the dominating influence. The following examples are given by Phillips *et al.* (2008): At the base of the photosphere, where T = 6400 K and B = 1000 G, β = 3, so the magnetic field is moved around by the motions of the convective granular cells as the magnetic field is not dominant there. However, in the quiet solar corona, where $T_e \sim 1.4 \times 10^6$ K and B $\sim$ 10 G, the plasma $\beta = 0.1$. So in the solar corona, the low plasma β tells us that the magnetic field is the dominant influence.

1.3.9 Magnetic Reynold's Number, R_M

The magnetic Reynold's number, R_M, is another way to indicate the degree of coupling between the plasma flow in a region and the ambient magnetic field. If v_0 is a typical velocity scale for the flow under consideration, and l_0 is the length scale over which the magnetic field varies, then the timescales associated with the two terms on the right hand side of Equation 1.29 are (i) the diffusion timescale:

$$\tau_d = \frac{{l_0}^2}{\eta} \tag{1.37}$$

and (ii) the advection timescale:

$$\tau_a = \frac{l_0}{v_0} \tag{1.38}$$

The ratio of these two timescales gives the Magnetic Reynold's number:

$$R_M = \frac{\tau_d}{\tau_a} = \frac{v_0 l_0}{\eta} \tag{1.39}$$

A much-used concept is that of a magnetic *field line*, which is defined as a path tangent to the local direction of the magnetic field. Plasmas with a low ($\ll 1$) R_M diffuse across magnetic field lines, those with a high ($\gg 1$) R_M are tightly bound ("frozen") to the magnetic field lines (because diffusion is relatively unimportant on the considered length scale l_0).

In the solar corona, the typical velocity scale is the Alfvén velocity, $v_A = 10^3$ kms^{-1}. A typical length scale over which the magnetic field varies is of the order 10^7 m. The resistive magnetic diffusion in the solar corona is typically expressed as a function of temperature, T(K) so that $\eta \sim 10^9 \mathrm{T}^{-1.5}$ m^{2}s^{-1} (Spitzer, 1962). As previously described, the temperature of the quiet solar corona is $\sim 1.4\times10^6$ K. Using these values in Equation 1.39 gives R_M of the order 10^{10}. Thus the coronal magnetic field has $R_M \gg 1$, and the magnetic field is considered frozen into the plasma. Diffusion is negligible, since the timescale associated with evolution of the plasma in the corona (using the values above) is extremely large and is given by $\tau_d \sim 10^6$ years.

The process of diffusion may be described as the dissipation of energy (Emslie, 1992). However, the diffusion timescale, τ_d of the solar corona derived above is many orders of magnitude larger than observed energy release timescales ($\sim$ 100 s for a solar flare). Somehow, the magnetic energy released must be dissipated rapidly on observable timescales. The solution suggested by Sweet (1958) (to quote Parker, 1957): "... gives a means of altering quickly the configuration of magnetic fields in ionized gases, allowing a stable field to go over into an unstable configuration, subsequently converting much of the magnetic energy into kinetic energy of the fluid."

1.4 Magnetic Reconnection

1.4.1 Sweet-Parker Solution

The "Sweet-Parker" solution to making such considerable energy release occur rapidly, was to significantly reduce the length scale over which the magnetic field varies. This solution effectively brings two oppositely directed magnetic fields into close proximity. At the boundary between the two oppositely directed magnetic fields, a steep magnetic field gradient is created. Following from Ampére's law (Equation 1.21), a strong current sheet is expected to form all the way along the interface where the direction and/or magnitude of the magnetic field suddenly changes. This current sheet is assumed to be of thickness w and length $2L$ (see Figure 1.13). In the current sheet, diffusion dominates so there is little coupling between the magnetic field and the plasma (Equation 1.29). Plasma is assumed to diffuse into the current layer, along its whole length $2L$, at some relatively small inflow velocity, v. The plasma is accelerated along the layer, and eventually expelled from its two ends at some relatively large exit velocity, v_x.

The Sweet-Parker model therefore converts inflowing magnetic energy into bulk kinetic energy, heat and fast particle energy via resistive diffusion. Typical energy release rates in solar explosions can exceed 10^{30} erg s^{-1} (1 erg = 1 10^{-7}J). The Sweet-Parker reconnection model yields energy release rates of $\sim 10^{24}$ erg s^{-1}. Therefore, although providing a means by which to rapidly convert stored magnetic energy into kinetic energy of the fluid, the energy release rate using the Sweet-Parker model is still several orders of magnitude too low to account for observations.

1.4.2 Petschek Reconnection

Petschek (1964) pointed out that most of the magnetic energy can be converted into plasma thermal energy and kinetic energy as a result of shock waves being set up in the plasma, in addition to

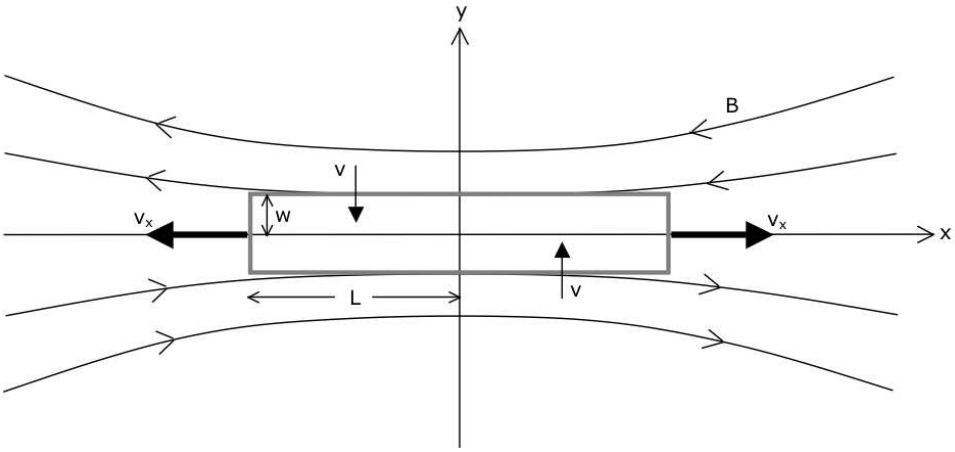

Figure 1.13: Sketch of the Sweet-Parker model. The magnetic field reverses direction along the line x=0. Material advects inward along the y-direction toward y=0 with velocity v and is ejected outward along the x-axis with a relatively large exit velocity v_x. The grey box indicates the current sheet of length $2L$. Note that the width of the current sheet, w, is very much smaller than the length. Figure adapted from Emslie (1992).

the conversion due to the action of resistive diffusion. In Petschek's model, the length-scale of the current sheet, L, is orders of magnitude smaller than the one assumed by Sweet-Parker.

Under an incompressible regime, the volume of a plasma element with dimensions Δx, Δy, must be conserved. So as the plasma element is advected toward the current sheet, because $\Delta y \rightarrow 0$, Δx must $\rightarrow \infty$. Because of the frozen-in condition, B_x must also $\rightarrow \infty$ as $\Delta y \rightarrow 0$. However, it is not physically possible to satisfy these requirements. As a result, standing shocks (denoted **S** in Figure 1.14) are formed. At the shocks, the density changes, so the velocity flow of the plasma changes abruptly from a gradual inflow v to a rapid outflow $v_x \sim v_A$, converting most of the magnetic energy to kinetic energy and heat. The shocks remove the requirement for all the flow having to pass through the small diffusion region at the current sheet. In addition, the connectivity of the magnetic field lines is actually changed: the red and blue oppositely directed field lines (see Figure 1.14) reconnect in the current sheet (grey box), forming the green field lines. This is true "magnetic *reconnection*" as opposed to just dissipation. It is the strong magnetic tension force of these newly formed green field lines, directed along the x-axis that propels the frozen-in plasma at $\sim v_A$. Therefore most of the magnetic energy is converted into kinetic energy of this outflowing material. Magnetic reconnection is currently thought to be the main way in which magnetic energy is released in highly conducting plasmas.

Priest and Forbes (2002) review the work that followed that of Sweet, Parker and Petschek, as well as the development from 2-D to 3-D reconnection theory.

1.4.3 Separatrices and Quasi-Separatrix Layers

The Sweet-Parker model of reconnection is purely 2-D. Magnetic reconnection occurs at the boundary where the two oppositely directed magnetic fields come into contact. Such an interface where the two components of the oppositely directed magnetic field vanish is termed an "X-type neutral/null point" or "X-point" for short. The limiting field lines (shown as heavy black lines in Figure 1.15) which link to the X-point are known as *separatrices*. Separatrices are surfaces of zero

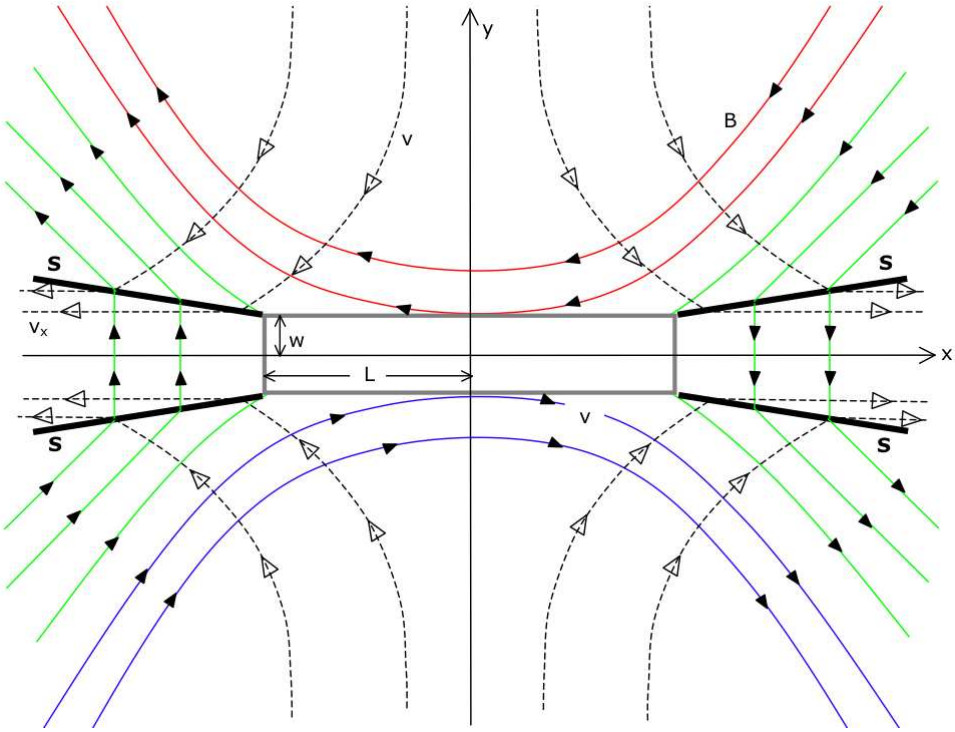

Figure 1.14: Sketch of the Petschek reconnection topology. Similar to the Sweet-Parker model, material advects inward toward y=0. However, in the Petschek regime, there are standing shocks **S** (heavy black solid lines), which dramatically increase the velocity of the material. In addition, the connectivity of the magnetic field lines is actually changed: red and blue oppositely directed field lines reconnect in the current sheet (grey box), forming the green field lines. This is true "magnetic *reconnection*". Figure adapted from Emslie (1992).

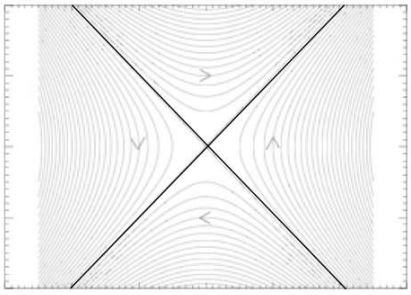

Figure 1.15: Figure showing a two-dimensional x-type neutral point. The limiting field lines through the origin (heavy black lines) identify the magnetic separatrices. Figure courtesy C. Parnell.

thickness where the mapping (linkage) of the magnetic field lines is discontinuous. Separatrices intersect in field lines called separators. Current sheets form all along the separatrices, where reconnection can occur, as described.

In 2.5-D (where invariance along one of either x, y, z, is maintained) and 3-D, separatrices exist when there is a null point (field lines tangent to the boundary which enclose the volume under consideration). However, in 3-D it is not necessary to have null-points for reconnection to occur (Priest and Démoulin, 1995). Instead, reconnection may occur at "quasi-separatrix layers" (QSLs). QSLs are sheets of finite thickness where ideal MHD can break down, so that the variation in field line linkage changes rapidly. In QSLs, the magnetic connectivity is continuous but still has very sharp gradients over squashed volumes (Aulanier *et al.*, 2005) so that current sheets can be generated and dissipated. QSLs can intersect in tube-like quasi-separators (Démoulin *et al.*, 1996; Démoulin, 2005, 2006). QSLs are identified by (i) enclosing the region of plasma being considered by a boundary, (ii) mapping the field lines to the boundary and (iii) determining where there is a steep (very much larger than normal) gradient in the magnetic field line mapping.

1.4.4 Connectivity and Topology

We note here that the term "connectivity" should be used to refer to magnetic field connections, whilst "topology" should be restricted to describing connectivity domains of the magnetic field (defined by separatrices). These two terms are often used interchangeably, but they are *not* the same. The connectivity is set by the topology of the magnetic field.

1.5 Large-Scale Eruptive Phenomena

The most dynamic aspects of the corona involve rapid, large-scale destabilisation of the magnetic field. Observational indicators of large-scale eruptive phenomena include prominence/filament eruptions, flares and coronal mass ejections (CMEs). They are all the result of magnetic reorganisation and can occur separately and together, in any combination (Aschwanden *et al.*, 2001). As discussed in §1.4, magnetic reconnection rapidly releases phenomenal quantities of magnetic energy into thermal energy, radiation, accelerated energetic particles and magnetic ejecta.

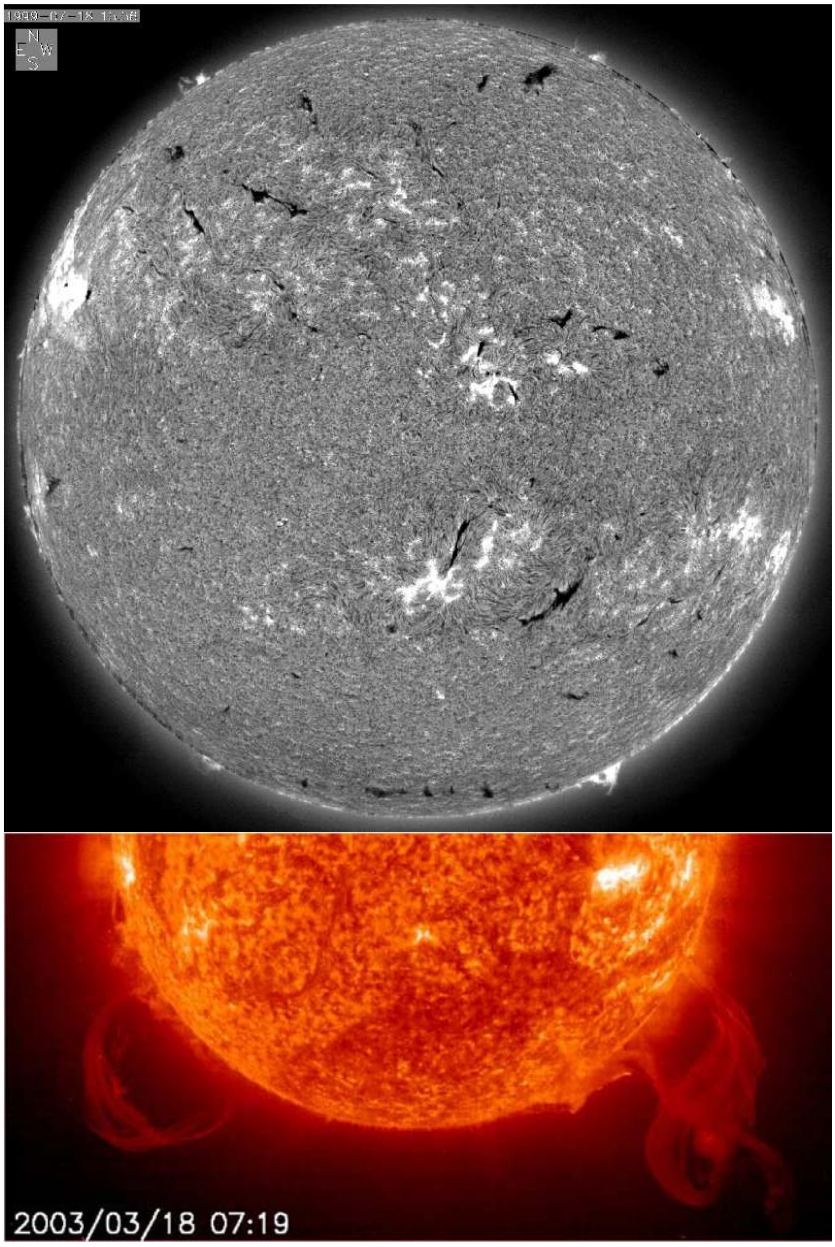

Figure 1.16: Top: A full-disk heliogram taken in the Hα 6563 Å chomospheric spectral line at the Big Bear Solar Observatory, California. Hα images show dense, relatively cool features called filaments (dark features when seen against the solar disk) and prominences (bright features when seen on the solar limb). Bottom: A SOHO/EIT He II 304 Å image showing two huge erupting prominences.

1.5.1 Prominence/Filament Eruptions

Figure 1.16 shows a full-disk image of the Sun taken in the Hα spectral line. The Hα line is associated with neutral hydrogen and has a wavelength of 6563 Å. Hα images show layers of the Sun up to 1700 km above the photosphere and are used to observe prominences and filaments. Prominences and filaments actually describe the same feature, but they are called prominences when seen on the solar limb (appearing as bright features because they are hot with respect to the cold darkness of space). They are called filaments when seen against the solar disk (appearing as dark features because the filament is relatively cool ($\sim$ 10,000 K) compared to the surrounding

hot corona and because the filament scatters incident photons in all directions, weakening the photospheric radiation). Both prominences and filaments can be identified in the Hα image shown in Figure 1.16. Prominences/filaments that are associated with quiet Sun (as opposed to active regions) are termed "quiescent" prominences/filaments. Prominences/filaments are denser ($\sim 10^{11}$ cm^{-3}) than the surrounding corona ($\sim 10^{9}$ cm^{-3}) and so they must somehow be held up amidst the lower density corona. Several magnetic field configurations have been proposed to fulfil this role, where magnetic field lines support the prominence/filament material against gravity. Work comparing 3-D models with observations (e.g. Aulanier and Demoulin, 1998, and references therein) strongly favours the configuration of a magnetic flux rope (a 3-D helical spiral of magnetic field, with a geometry not unlike that of a corkscrew), with the prominence/filament material cradled in the base of the helical field lines.

Whilst quiescent prominences/filaments can exist for several solar rotations, their smaller active region-related counterparts have shorter lifetimes. Suddenly, prominences/filaments can erupt, in either failed or successful ejections from the Sun. How such eruptions occur is an active area of research, but the loss of equilibrium may be due to instability or catastrophe. Two possibilities for eruption drivers are the ideal MHD helical kink and torus instabilities. The helical kink instability sets in if a certain threshold of critical twist (2.5π for line-tied flux ropes) is reached (e.g. Török and Kliem, 2005). At this critical threshold, twist becomes converted to writhe during the eruption, deforming the flux rope into a helical kink shape. Figure 1.17 shows snapshots from an MHD simulation of the helical kink instability. Another type of ideal MHD instabilty is the torus instability (Kliem and Török, 2006), which does not require a pre-eruption highly-twisted flux rope. The torus instability requires (i) a sufficiently steep poloidal field decrease and (ii) an (approximately) semi-circular flux rope shape. Both the helical kink and torus instabilities may be responsible for driving prominence/filament eruptions (see bottom panel, Figure 1.16). When such eruptions are ejective, the prominence/filament material is expelled into the interplanetary space.

1.5.2 Flares

Phillips *et al.* (2008) describes solar flares as "the most energetic (10^{29} - 10^{32} erg) and rapid (down to milliseconds) releases of energy in the solar corona", following re-arrangement of the solar magnetic field. Flare temperatures range from 10^4 K to 3×10^7 K (Priest and Forbes, 2002). In the initial stages of a solar flare, a sheared or twisted coronal arcade (in most cases, but not necessarily containing a prominence/filament) rises slowly during the preflare phase, in a succession of equilibrium states. Suddenly, there is a rapid eruption and the production of fast particles and flare loops. The development of flares is therefore marked by a very rapid impulsive phase near the onset consisting of short pulses ($\sim$ second) of hard X-ray (wavelengths $\sim$ 0.6 Å, photon energies 20 keV), ultraviolet and radio-wave emission, lasting for a minute or so. Soft X-ray emission may begin at or a little before the impulsive stage and peak a few minutes after it. Figure 1.18 (top right) shows an example of typical hard (solid line) and soft (dashed line) X-ray time profiles. The radiant energy from flares is often from all regions of the electromagnetic spectrum, from gamma-rays to km-wavelength radio emission. The bright flare emission (see Figure 1.18) is due to hot plasma contained in magnetic loops which are low-lying in the initial flare development but rise with time. Flares are most commonly associated with active regions, however a similar eruptive process can also occur when a large quiescent prominence erupts. Because the magnetic field strength outside of active regions is much lower, the kinetic energy and heating associated

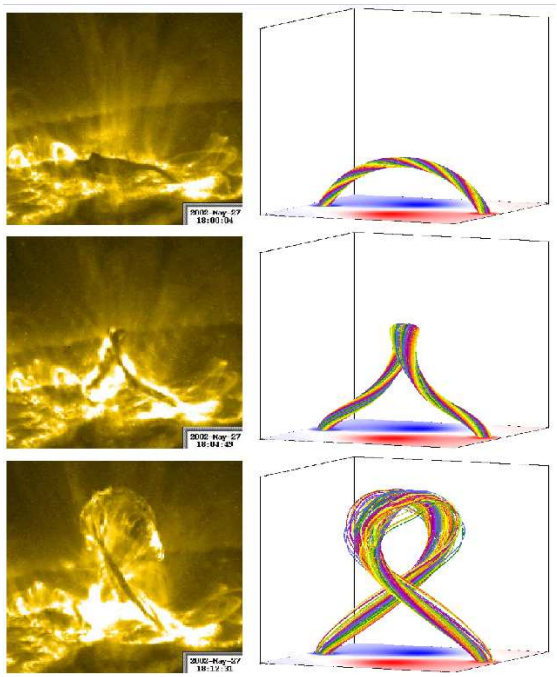

Figure 1.17: Left: TRACE EUV 195 Å images of a failed filament eruption on 27th May 2002. Right: Magnetic field lines outlining the core of the simulated ideal MHD kink-unstable flux rope. Figure from Török and Kliem (2005). Permission to reproduce this figure has been granted by the American Astronomical Society.

with such flares is also weaker.

In the so-called "CSHKP standard flare model", (Carmichael, 1964; Sturrock, 1966; Hirayama, 1974; Kopp and Pneuman, 1976), an instability or loss of equilibrium causes a flux rope to rise, "opening" the magnetic field, bringing the oppositely orientated field lines rooted in the footpoints of the loop into close proximity (see top left panel, Figure 1.19). A current sheet forms at their interface and magnetic reconnection (§1.4) occurs along the current sheet high in the corona. The magnetic reconnection changes the connectivity of the magnetic loop, creating a plasmoid at the top of the loop which becomes disconnected from the newly reconnected magnetic field lines that shrink down at the base of the loop (red loop feature in top left panel, Figure 1.19). Several key observations can be understood in the context of the standard flare model: (i) flare loops consist of cooler loops (reconnected earlier and so cooling) nested below the hotter ones, which are more recently reconnected (see Figure 1.18) (ii) during the course of a flare, the separation between the flare footpoints increases, as field lines rooted further away from the magnetic inversion line reconnect, which also causes (iii) the loops to grow larger with time.

According to the classical "thick-target model" (e.g. Brown, 1971) non-thermal electrons are accelerated in the corona in the reconnection event and then descend along the flare loop legs. When they reach the footpoints of the coronal loop they are stopped by the dense plasma in the chromosphere resulting in hard X-ray emission by collisional bremsstrahlung. The dumping of energy at the loop footpoints by the non-thermal electrons gives rise to turbulent motions in the chromosphere (observed as soft X-ray line broadening) and an evaporation, or convection of the heated plasma up the loop legs (observed as a Doppler shift of rising material), causes the bright thermal soft X-ray emission seen as the flare. In this model, the nature and location of the acceleration site are considered to be irrelevant.

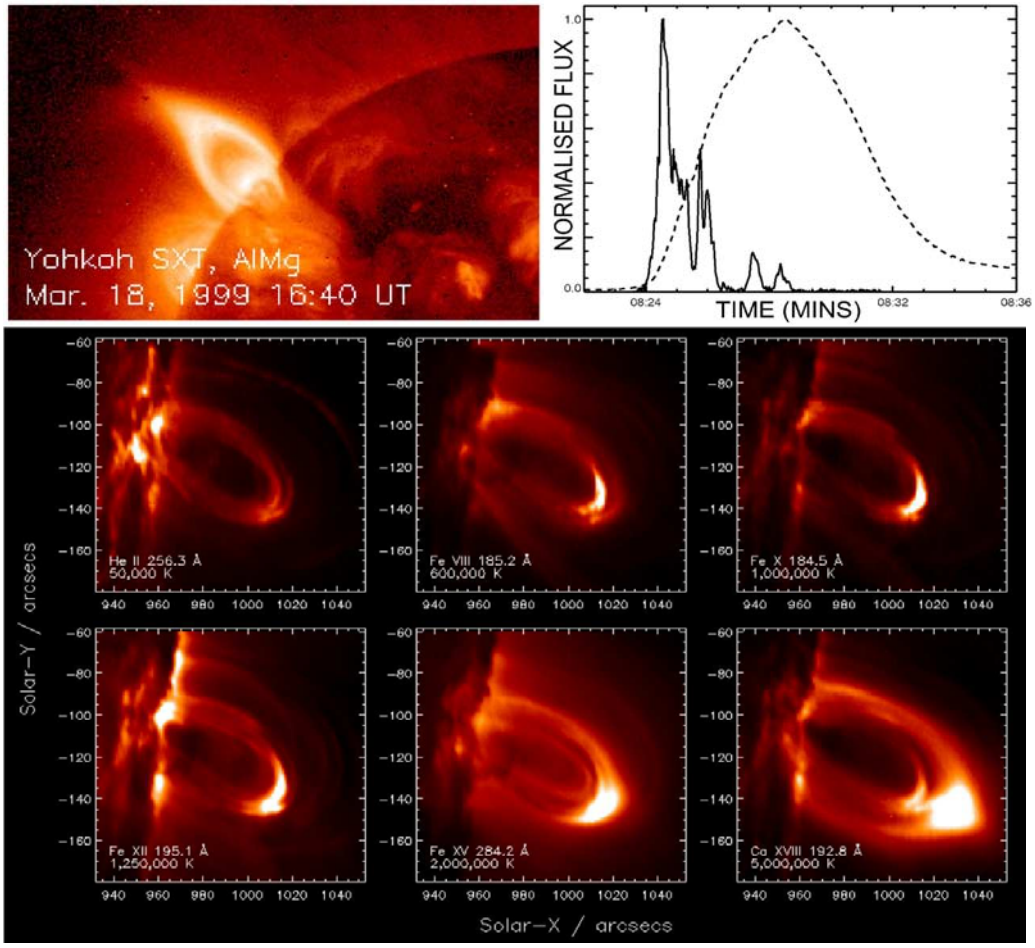

Figure 1.18: The top left image shows *Yohkoh*/SXT data of a flare on the solar limb on 18th March 1999. Top right shows the impulsive phase of a typical flare. Solid curve shows the hard X-ray time profile, and dotted curve the soft X-rays. (Figure from a RHESSI nugget on 04/02/2008 by L. Fletcher and H. Hudson). The bottom images show a system of coronal loops observed at the west limb of the Sun on 17th December 2006 by the *Hinode*/Extreme ultra-violet Imaging Spectrometer. Each image was taken simultaneously by EIS and shows the region in different spectral emission lines. In the hottest line (Ca XVII 192.8) a bright knot of emission is seen above the loops - a feature which is characteristic of intense solar flares. (Figure by P. Young). This EIS observation shows an *atypical* event because there was barely any impulsive hard X-ray radiation observed for this flare (L. Bone, private communication). See also Hara *et al.* (2008).

Very recently, it has been proposed by Fletcher and Hudson (2008) that large-scale reconfiguration of the coronal field launches a torsional Alfvén wave pulse through the low β corona and into the chromosphere, as well as a fast-mode wave pulse (see Figure 1.19). The Alfvén wave can lead to electron acceleration in the corona of energies on the order of 10 keV and above. This acceleration is driven by field-aligned electric currents which occur in the presence of strong spatial gradients of density and temperature (as expected between the corona and chromosphere). The fraction of the Alfvén wave energy that survives into the chromosphere can also lead to stochastic acceleration there. The wave will be partially reflected from the steep gradients of density and temperature in the chromosphere (not shown in bottom panel of Figure 1.19) and re-enter the corona. This will also accelerate electrons by turbulence. In this model, energy is transported via the Poynting flux, $\mathbf{S} = \mathbf{E} \times \mathbf{B}$ and both the nature and location of the particle acceleration leading to the observed mildly relativistic (10-100 keV) electrons, are specified.

1.5.2.1 Flare classification

Flare magnitude is classified through the amount of soft X-ray emission that is detected in the 1-8 Å spectral band of the Earth-orbiting Geostationary Operational Environmental Satellites (GOES), operated by the U.S. National Oceanic and Atmospheric Administration (NOAA). Flares having peak fluxes in the 1-8 Å band of 10^{-8}, 10^{-7}, 10^{-6} , 10^{-5} , and 10^{-4} W m^{-2} are assigned increasing X-ray importances: A1, B1, C1, M1, and X1 respectively.

1.5.2.2 Flares in the quiet Sun

Phillips *et al.* (2008) note that over the past 20 years, it has become increasingly evident that even what is generally known as the quiet solar atmosphere is extremely dynamic, with flows, oscillations, transient brightenings, and explosive phenomena occurring throughout. This is independent of the solar activity in the form of active regions and flares. Nearly all these phenomena are related to the Sun's magnetic field which pervades the entire solar atmosphere. Small magnetic concentrations, particularly prominent in regions of the Sun devoid of active regions, are subject to flaring like larger active regions. Flares from them are correspondingly small. Indeed, some models (e.g. Pauluhn and Solanki, 2007) assume that all quiet-Sun EUV emission is due to microflares (10^{25-26} ergs; Krucker and Benz, 1998) and nanoflares (10^{24} ergs; Parker, 1988). X-ray bright points (XBPs) can be observed in coronal holes (as mentioned §1.2.3.1), but they are also observed amongst old, disintegrating active regions as well as profusely in quiet Sun regions. Brightness variations in XBPs have been identified as small flares, created during reconnection between pre-existing magnetic field and a newly emerged bipole impinging on the pre-existing magnetic domain (e.g van Driel-Gesztelyi *et al.*, 1996). This interaction between previously disparate magnetic domains is a strong focus of the work presented throughout this thesis and will be discussed and explained in greater detail in Chapters 4, 5 and 6.

1.5.3 Coronal Mass Ejections (CMEs)

Often accompanying large flares and prominence/filament eruptions, but sometimes independent of them, are coronal mass ejections (CMEs). CMEs can be described as large-scale ejections of mass (typically 10^{15-16}g) and magnetic flux (10^{20-22}Mx) from the lower corona into the interplanetary

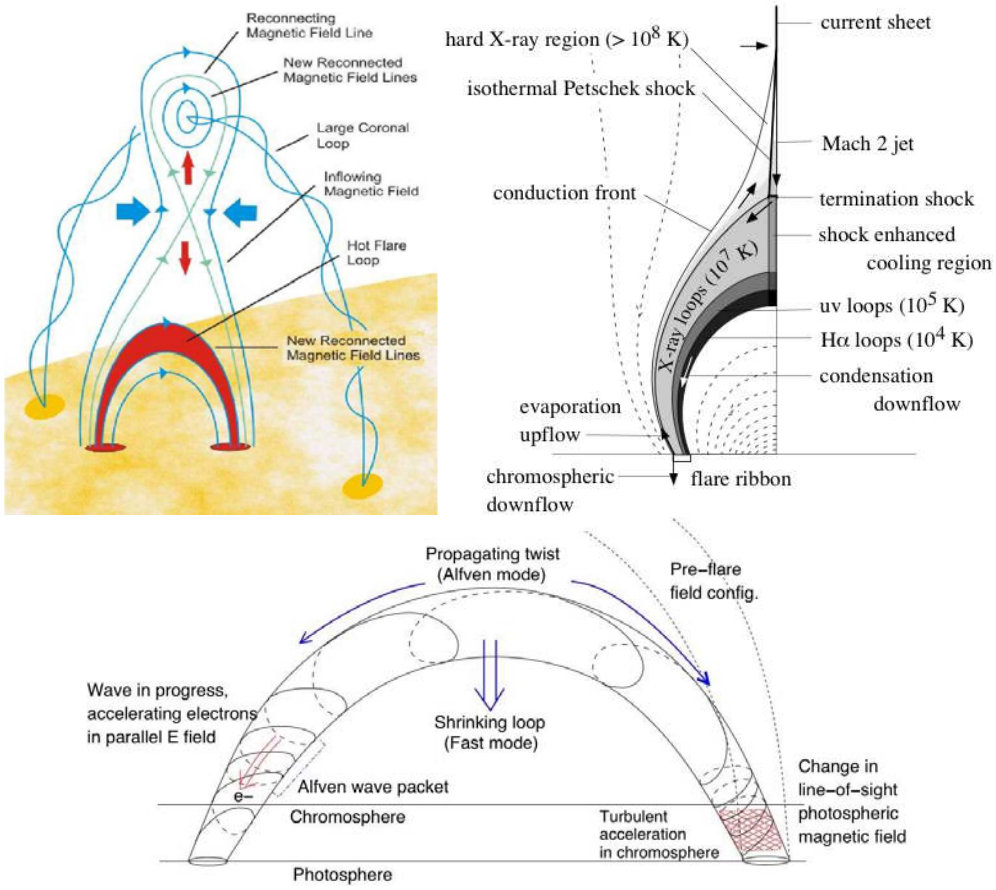

Figure 1.19: Top left: CSHKP standard model of solar flares. Figure by G. Holman, Solar Physics Division Summer School 2006, adapted from Shibata *et al.* (1995). Top right: Schematic diagram of a flare loop system formed by reconnection. Figure from Priest and Forbes (2002). Bottom: Alternative model where the energy to drive chromospheric evaporation is specified to arrive via the Poynting flux, as shown. The particle acceleration takes place in or near the chromosphere, where the Alfvén waves damp. Figure from Fletcher and Hudson (2008). Permission to reproduce these figures has been granted by Springer Science and Business Media and the American Astronomical Society.

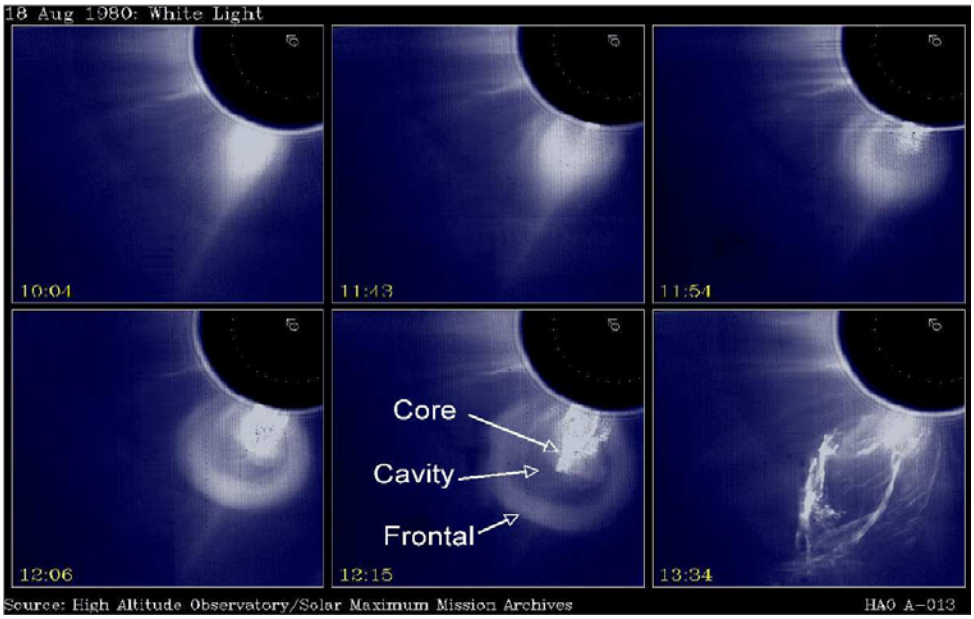

Figure 1.20: A 3-part CME in progress, captured by the Solar Maximum Mission white-light coronagraph.

medium, with velocities ranging from < 100 to > 3000 km s^{-1} (Gosling *et al.*, 1976; Williams *et al.*, 2005). Indeed, prominence/filament eruptions have long been associated with CMEs (e.g. Hildner *et al.*, 1975). CMEs are observed most completely in spacecraft-borne coronagraphs (essentially artificial eclipses, see Chapter 2), often as a bubble-shaped ejection of coronal material (Crooker *et al.*, 1990, and see Figure 1.20). CMEs were first discovered in 1973 with a coronagraph on-board the Orbiting Solar Observatory OSO-7, and further observations were made by Skylab also in 1973 (MacQueen *et al.*, 1974). A typical amount of energy associated with a CME is 10^{32} erg. The frequency of CMEs exhibits a relationship with the solar cycle, ranging from one every $\sim$ two days at solar minimum to ~ 3 CMEs per day at solar maximum (St. Cyr *et al.*, 2000). From white-light coronal images obtained by the Solar Maximum Mission, Hundhausen *et al.* (1984) define a CME to be "an observable change in coronal structure that i) occurs on a time scale of a few minutes and several hours and ii) involves the appearance (and outward motion) of a new, discrete, bright, white-light feature in the coronagraph field-of-view".

Some CMEs (though not all), exhibit a so-called "3-part structure" (e.g. as shown in Figure 1.20). The 3-part structure consists of a dense, cool core that has a relatively strong magnetic field (n $\sim 10^{17}$ m^{-3}, T $\sim$ 8000 K, B $\sim 10^{-3}$ T). In some cases, it has been shown that the core corresponds to ejected prominence/filament material (Schmieder *et al.*, 2002) cradelled in the erupting flux rope. In some CMEs, no prominence/filament material is visible. However failure to observe such material does not remove the possibility that a magnetic flux rope is still ejected. Indeed, the core is surrounded by a cavity (n $\sim 10^{13}$ m^{-3}, T $\sim 2\times10^{6}$ K, B $\sim 10^{-4}$ T), which is sometimes identified as the magnetic flux rope. Both the core and cavity are preceeded by a hot frontal lobe, or "outer shell" (n $\sim 10^{14}$ m^{-3}, T $\sim 2\times10^{6}$ K, B $\sim 10^{-4}$ T).

Forbes *et al.* (2006) give a recent overview of current efforts in the theory and modeling of CMEs. The details of the CME initiation process currently remain undetermined, but a CME is initiated when the magnetic energy stored in the solar corona is rapidly turned into kinetic energy as a result of instability or loss-of-equilibrium.

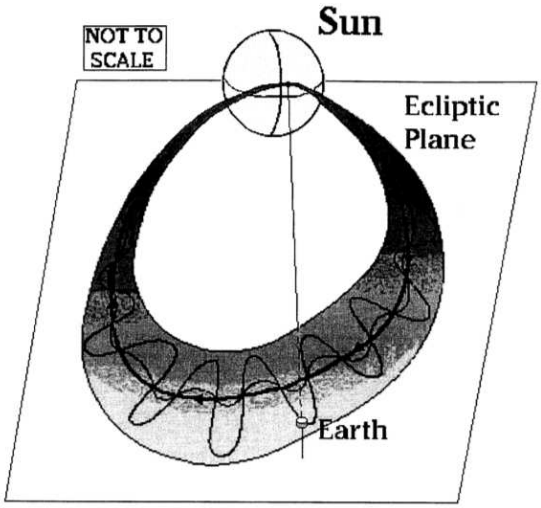

Figure 1.21: Sketch showing a CME expanding out into the interplanetary space. The footpoints of the ICME remain connected to the Sun. The ICME has a fluxrope (3-D spiral) structure. Figure from Webb *et al.* (2000). Permission to reproduce this figure has been granted by the American Geophysical Union.

1.5.3.1 Interplanetary Coronal Mass Ejections (ICMEs)

CMEs observed in the interplanetary space are called interplanetary CMEs (ICMEs). ICMEs are observed *in situ* as transients with certain changes in various physical parameters including:
- an enhanced magnetic field strength
- a higher density and
- a lower temperature than the surrounding solar wind.

In addition, the abundance of elements and their charge states tend to rise within ICMEs, which is characteristic of a plasma with hot origins like the Sun. As a result the plasma composition of ICMEs is very different to that of the surrounding solar wind plasma.

Spacecraft such as the Advanced Composition Explorer (ACE, `http://www.srl.caltech.edu/ACE/`) and *Wind* (`http://www-istp.gsfc.nasa.gov/istp/wind/`) carry instruments (some of which are described in detail in Chapter 2) that make single point measurements of various physical parameters of the magnetic field and plasma *in situ*. In some cases, when the core of an ICME can be unambiguously identified, the term "Magnetic Cloud" (MC) is used (Burlaga *et al.*, 1981). An ICME must exhibit certain criteria to be termed a MC including:
- an enhanced magnetic field $> 10^{-9}$ T with respect to ambient values (Hirshberg and Colburn, 1969),
- a smooth and large rotation of the magnetic field vector (Klein and Burlaga, 1982),
- a proton temperature decrease (Gosling *et al.*, 1973) and
- a low plasma β (Equation 1.36).

ICME identification can be considered something of an art, given the dependence on single-point measurements and the fact that not every ICME/MC has all the identified properties and that the boundaries of the different properties do not always match. Questions over whether a MC is truly a different physical class of ICME or is simply an observational selection effect have been raised (e.g. Marubashi, 1997), since it has been shown that the same event can be seen by one

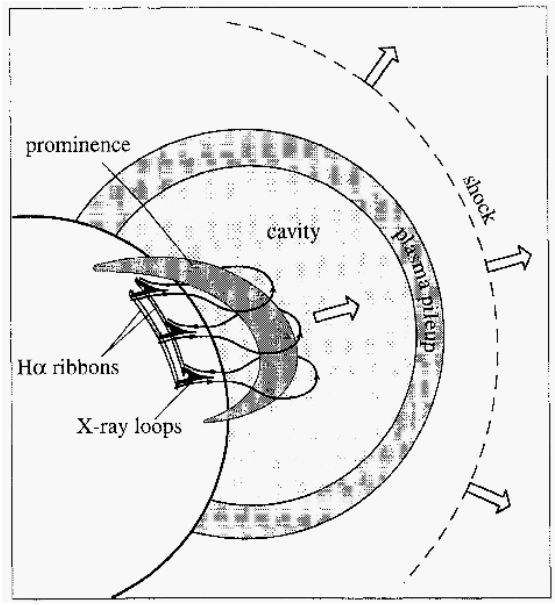

Figure 1.22: Schematic diagram showing the relationship between various features associated with a CME. Figure from Forbes (2000). Permission to reproduce this figure has been granted by the American Geophysical Union.

spacecraft as a non-flux rope ICME while at another it can appear as a MC (Jian *et al.*, 2006). In any case, it is important to understand precisely how a CME evolves in the interplanetary medium (see Démoulin, 2008, for a review of current methods used to quantitatively link CMEs and MCs).

1.5.4 Relationship between Large-Scale Eruptive Phenomena

The precise relationship between prominence/filament eruptions, flares and CMEs remains elusive, although it is known that strong X-ray flares and large CMEs usually occur closely related in time (Švestka, 2001), and it is thought that both flares and CMEs are a coronal response to a common underlying magnetic cause (Harrison, 2003). Zhang *et al.* (2001, 2004) showed that the impulsive acceleration phase of a CME coincides with the flare's rise phase and that the end of the acceleration of a CME coincides with the peak of the corresponding soft X-ray flare. A possible relationship between the various features associated with a CME is shown in Figure 1.22.

Further cause for thought is the apparent contradiction between small-scale source regions of, and large-scale coronal response to, CMEs. This has been highlighted by Klimchuk (2001): "Coronagraph observations suggest that the horizontal scale of the opened field can be many times greater than that of the reconnection arcade and this may be difficult to reconcile with the geometry of the [existing] model[s]." (Figure 1.23 illustrates this quandary). van Driel-Gesztelyi *et al.* (2008) give a review on the current status of work concerning this question. CMEs may be viewed as (i) *inherently* large-scale events, so that their energy supply, initiation and final angular width all originate from a large-scale region (e.g. Zhang *et al.*, 2007; Wang *et al.*, 2007; Zhukov and Veselovsky, 2007) or (ii) starting small-scale and *evolving* to become large-scale events due to interaction between the expanding magnetic structure of the CME and other low-coronal magnetic structures (e.g. Maia *et al.*, 1999; Pohjolainen *et al.*, 2001; Attrill *et al.*, 2007a; Mandrini *et al.*, 2007; Moore *et al.*, 2007). We discuss this issue further in Chapter 4.

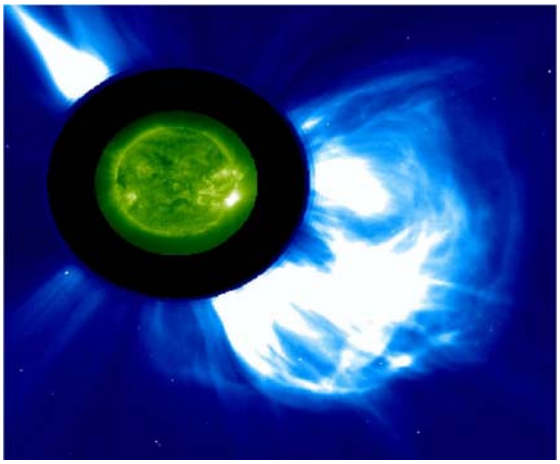

Figure 1.23: Composite EIT 195 Å low corona (green) and LASCO/C2 white light coronagraph (blue) image, illustrating the quandary described by Klimchuk (2001) where the horizontal scale of the CME is many times greater than that of the reconnection arcade (seen as the bright feature on the limb of the EIT image).

1.5.5 Space Weather

Prominence/filament eruptions, flares and CMEs contribute intermittently to the outflow from the Sun, potentially impacting our near-Earth space environment. For example, energetic particles that are accelerated in solar flares and escape into the interplanetary space could potentially kill a space-walking astronaut. Additionally, CME-driven shocks are believed to accelerate charged particles to high energies (Reames, 1999). CMEs when directed at Earth are called "halo" CMEs. The first detection of such an event was made by Howard *et al.* (1982). Upon interaction with the Earth's magnetic shield (magnetosphere), ICMEs have the potential (if there is a southward component to the magnetic field vector) to bring strong solar magnetic fields into the near-Earth magnetic environment through magnetic reconnection, producing intense geomagnetic storms (e.g. Howard *et al.*, 1982; Srivastava and Venkatakrishnan, 2004). The significance of CMEs for the Earth was initially revealed in a study by Gosling *et al.* (1974). These geomagnetic disturbances create the beautiful aurora, but they can also disrupt and destroy satellite communications (e.g. instrumentation in orbiting satellites can be degraded and damaged by high-energy particle impacts). Work directed toward predicting when and how such solar storms occur is clearly a priority in our modern technologically dependent world. As well as the derivation of ICME physical properties (§1.5.3.1), understanding the topology and evolution of these gigantic magnetic structures is also of fundamental interest for space weather forecasting, since their geoeffectiveness depends to a large extent on their magnetic orientation. The sources and effects of space weather are further discussed in Matthews (2004).

1.5.6 Low Coronal Signatures associated with CMEs

EUV observations of the lower corona reveal two (often global-scale), dynamic phenomena closely linked to the origins of CMEs: "coronal waves" and "dimmings" (Zhukov and Auchère, 2004). These particular low-coronal signatures of CMEs are studied in detail in the work presented in this thesis.

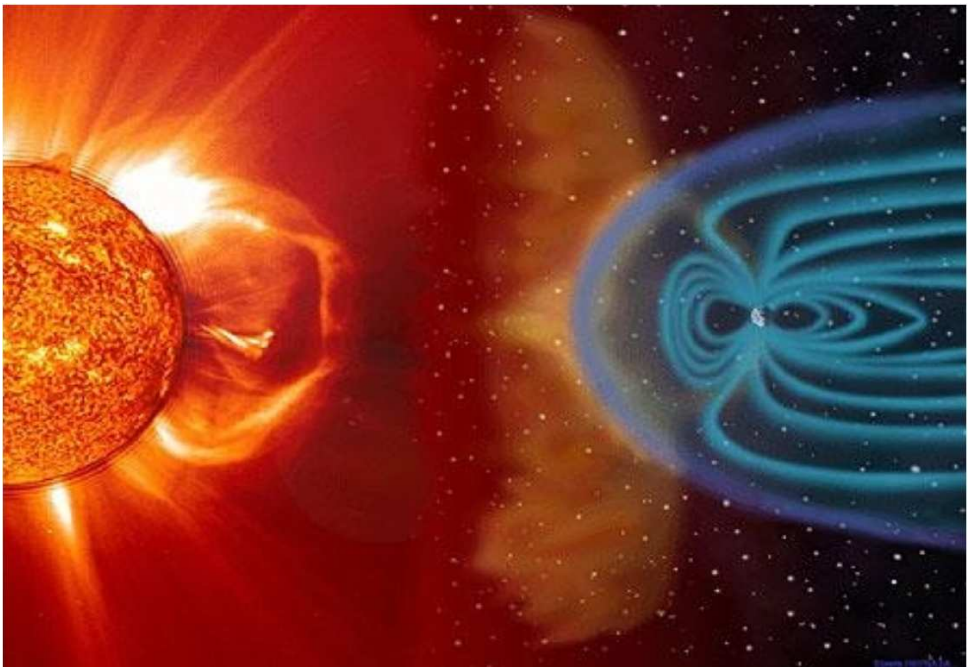

Figure 1.24: Figure illustrating the Sun-Earth coupled environment.

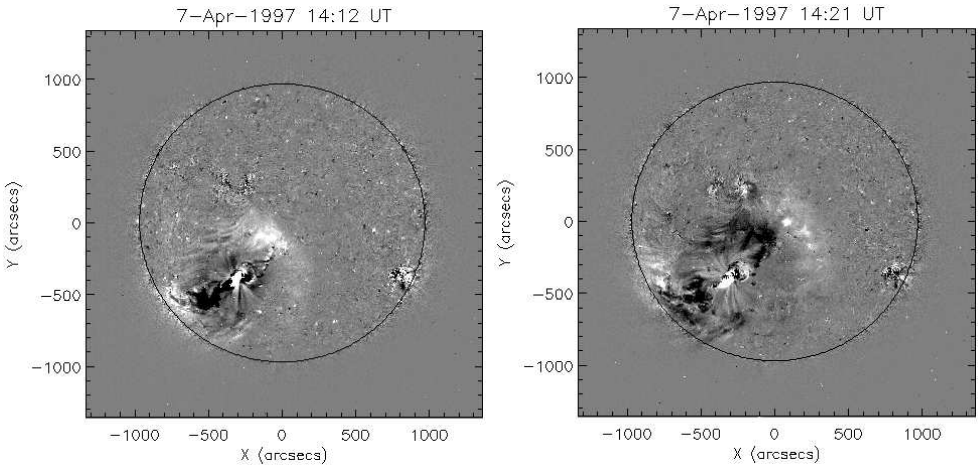

Figure 1.25: Running difference images from SOHO/EIT 195Å heliograms showing the "EIT coronal wave" event on 7th April 1997.

1.6 Coronal Waves

1.6.1 EUV data

The first direct observations of large-scale transient coronal wave-like phenomena related to flares and CMEs were made by SOHO/EIT (Delaboudinière *et al.*, 1995), hence their colloquial name: "EIT waves". They appear as a bright front of enhanced EUV emission, propagating quasi-radially away from a source region (see Figure 1.25). Processed images are used to study coronal waves because they are too subtle to easily detect in raw data. "Running difference" images may be used to show the extent of a disturbance (where each image has the previous frame subtracted),

whilst "base difference" images (where a pre-event image is subtracted from all subsequent images) must be used to show real enhancements (brightenings) and depletions (dimmings) in intensity. These disturbances can cover the diameter of the solar disk in tens of minutes. Despite much work, more than a decade after their initial discovery, a comprehensive understanding of coronal waves continues to elude researchers. What EIT coronal waves actually *are* is hotly debated, with theories ranging from fast-mode MHD waves to non-wave explanations where the bright front is due to electric currents and pressure increases. The full range of possibilities currently under consideration are discussed in more detail in Chapter 3. We contribute our own understanding in Chapter 4.

Due to the somewhat limited cadence of EIT (one full-disk image at 195 Å is made every $\sim$ 12 - 17 minutes), EIT waves are typically only caught in one, maybe two or three frames at most. The recently launched STEREO and *Hinode* missions are already starting to address this somewhat frustrating situation. The contribution from SDO/AIA, which will provide full-disk observations in 10 different wavelengths (6 in the EUV), at 10 *second* cadence is eagerly anticipated! However, right now, our current understanding of the physical nature of coronal waves is strongly shaped by related observations made in other spectral ranges that have a higher time cadence.

1.6.2 Related observations in other spectral ranges

In order to be able to discuss the relationship of such multi-wavelength observations to EIT coronal waves (Chapter 3), the next sections constitute an introduction to the various types of data used to study phenomena related to large-scale waves in other spectral bandpasses.

1.6.2.1 Radio data

Non-thermal radio emission occurs at the fundamental plasma frequency, f and/or its first harmonic, $2f$. The plasma frequency can be used to determine the density, n_e, of the plasma according to the relationship $\mathrm{f} = 9\sqrt{n_e}$. As a result, radio emission with lower frequencies comes from greater heights in the solar atmosphere since plasma density strongly decreases with height. There are various classes of radio emission, we discuss type I, type II, type III, type IV bursts and direct radio imaging.

Type I radio bursts are produced by supra-thermal electrons and are also referred to as "noise storms". Meter wavelength activity is often observed in close spatial and temporal association with CMEs and in the absence of flares (Pick, 2006). The origin of the noise storm non-thermal activity is believed to be due to emerging magnetic loops interacting with overlying loops and leading to magnetic reconfiguration.

Type II radio bursts are narrow-band emission, which show a drift from higher to lower frequencies (so from higher to lower densities) and are understood to be signatures of shock waves travelling outwards through the solar corona (Wild and McCready, 1950; Nelson and Melrose, 1985). Applying a suitable coronal density model, the velocity (typically 500-2000 km s^{-1}) is inferred from the drift rates of the radio bursts. Shock waves can accelerate electrons, exciting plasma oscillations known as Langmuir waves. Langmuir waves are electrostatic waves at the electron plasma frequency which can interact with other waves (e.g. ion acoustic waves) or particles,

or they may coalesce giving harmonic emission. The resulting electromagnetic radiation can escape the corona in the form of radio waves (Melrose, 1985). It is worth emphasising that radio spectra do not show the coronal disturbance directly since the type II burst only traces the part of the shock segment that excites the radio emission (Vršnak, 2005). In this respect, type II radio burst data shows a sudden increase in brightness, allowing recognition of the moment the wave is converted into a shock (Hudson *et al.*, 2003).

There is debate in the literature as to the driver of the type II bursts. There are generally two explosive processes capable of launching large-scale coronal shocks; ejections in various forms and flares (Vršnak and Lulić, 2000a). The expansion of CMEs from the solar corona can be followed through their non-thermal radio emissions, from microwaves to metric and decimetric wavelengths (Kaufmann *et al.*, 2003). Cliver *et al.* (2004) report a strong correlation with CMEs, in that 93% of CMEs are associated with metric type IIs (private communication with N. Gopalswamy 2003). According to Cliver *et al.* (2004), although the type II burst source tends to be located at or near the CME front leading edge, there is also evidence where it occurs at the flanks of the CME (Gergely *et al.*, 1984). Cliver *et al.* (1999) note that many type IIs are associated with relatively weak flares which have fast CMEs and that the vast majority of flares do not have associated type II bursts. (E.g. 12th May 1997 event studied in detail in this thesis was accompanied by a $\sim$ 15 minute type II burst, whilst the flare was only GOES class C.2). So there is a strong case for association of type II bursts with CMEs. However, since type IIs were detected long before the discovery of CMEs, traditionally they were strongly associated with flares. This association is by no means relegated to the history books however. Magdalenić *et al.* (2008) recently convincingly demonstrated that a coronal shock wave, detected by the presence of type II radio bursts, was not driven by the accompanying CME, but rather by a relatively weak flare. Temporally, type II bursts have been observed to coincide with the peak of the flare impulsive phase (White and Thompson, 2005). Spatially, Klassen *et al.* (2000) estimate that the type II bursts are generated between 0.35 - 0.63 $R_\odot$ whilst Cliver *et al.* (2004) estimate the nominal height range of type II bursts to range from 1.1 - 2.5 $R_\odot$.

Type III bursts show a very fast drift from higher to lower frequencies, indicating that the emission moves out to lower density plasma very quickly. Type III bursts are understood to be due to electron beams along "open" magnetic field lines moving at near-relativistic velocities ($\sim 0.3c$). Aurass *et al.* (1999) studied the timing of the early stages of CME formation for two long-duration flare-CME dimming events. In one case, an "opening" of coronal structures is observed in EIT and LASCO/C1 data. A faint group of metric type III radio bursts accompanies this restructuring. In another case where the overlying structure in LASCO/C1 data remained closed, no metric type III burst was observed.

Type IV radio bursts have a broadband nature, covering a wide frequency range, and are due to emission from non-thermal electrons trapped in a magnetic structure. There can be a continuum of Type IV emission and/or moving Type IV bursts, in which case the magnetic structure is likely to be the bubble of an expanding CME. Recent work with Type IV radio bursts by Wen *et al.* (2006) showed that they are observed to occur successively, tending to appear at the fronts of diffuse coronal waves observed in EUV data, preceding the expansion of EUV dimmings. Because the locations of the radio bursts later dim, they are interpreted as the result of magnetic reconnection leading to the "opening" and restructuring of the coronal magnetic field. The radio bursts that match the extension of the dimming are weak and are detected at 164 MHz. Type IV bursts occur in conjunction with type II emission.

Direct radio imaging can be used to produce (i) 2-D mapping of radio bursts, so imaging the location and extent of the bursts and (ii) radio images of the corona (e.g. Bastian *et al.*, 2001). At metric wavelengths (e.g. 327 MHz), the emission is sensitive to large-scale structures of the corona, such as coronal holes, loops, and the streamer belt. For events associated with flaring regions located behind the limb, faint emission can be detected over the solar limb, and directly compared to white light coronagraph emissions (Pick, 2006). The radio emission is non-thermal gyrosynchrotron and comes from electrons with energies of a few MeV (e.g. 164 MHz).

1.6.2.2 Hα data: Chromospheric Moreton Waves

Moreton waves (Moreton, 1960; Moreton and Ramsey, 1960) are disturbances in the chromosphere directly imaged in the wings of the Hα I 6562 Å line. Moreton waves appear first in absorption in the +0.8 Å red-shifted wing, then in emission in the -0.8 Å blue-shifted wing (Dodson and Hedeman, 1968). This down-up swing reflects the response of the chromosphere due to compression from a sudden pressure jump in the corona. The blue-shift is *not* believed to be related to matter ejection (as stated in Delannée *et al.*, 2007), but rather to the relaxation of the chromosphere following the compression. Indeed, Warmuth *et al.* (2004b) specifically emphasise that "the down-up swing of the chromosphere indicates that the travelling disturbance is a wave, and not ... propagating ejected matter." However, Moreton waves can disturb filaments, causing them to oscillate (Smith and Harvey, 1971, known as "winking") or to be ejected. In the case of ejection, the filament erupts in the direction of the associated Moreton wave event, as found to be the case for *all* events observed by Hida observatory (Narukage *et al.*, 2004). Ejected filament material is expected to generate a blue-shift, although this would still be distinct from that of the Moreton wave blue-shifted signature.

Moreton waves are generally accepted to be closely associated with flares, although this view has been debated with Cliver *et al.* (1999) arguing that fast CMEs may be the root cause of Moreton waves. More recently Balasubramaniam *et al.* (2007) suggest that Moreton waves may be caused by a removal of coronal material due to a CME, arguing that Moreton waves must have a significant coronal component because they disturb filaments which are located in the corona. In a similar vein, Delannée *et al.* (2007) support the view that Moreton waves are closely associated with CMEs.

Moreton waves are usually observed in Hα data for only about 3-6 minutes, extending over a limited arc 60″ - 120″ (Balasubramaniam *et al.*, 2007). They propagate away from the flare site and perpendicular to it at high velocities of $\sim$ 1000 km s^{-1} (Moreton, 1960), becoming fainter until they can no longer be distinguished from the background (Warmuth *et al.*, 2004a). However, a recent observation reported by Warmuth *et al.* (2005) and Balasubramaniam *et al.* (2007), describes a wide-angle Moreton wave, propagating away from the flare site with both north and south components. This unusual event on 29th October 2003 lasted for $\sim$ 12 minutes. Another exceptional Moreton wave is the so-called "tsunami" event, observed on 6th December 2006 (see Figure 1.26), associated with a white-light flare. The semi-isotropic and diffuse nature of the bright front is also an unusual feature of this event.

Moreton waves are observed to avoid strong magnetic field regions (e.g. active regions > several 100 G), instead propagating through regions of weak magnetic field (e.g. quiet Sun < 100 G) and across magnetic neutral lines (e.g. Liu *et al.*, 2006; Balasubramaniam *et al.*, 2007). Temmer *et al.* (2005) find distinct differences in the propagation of the Moreton wave in different

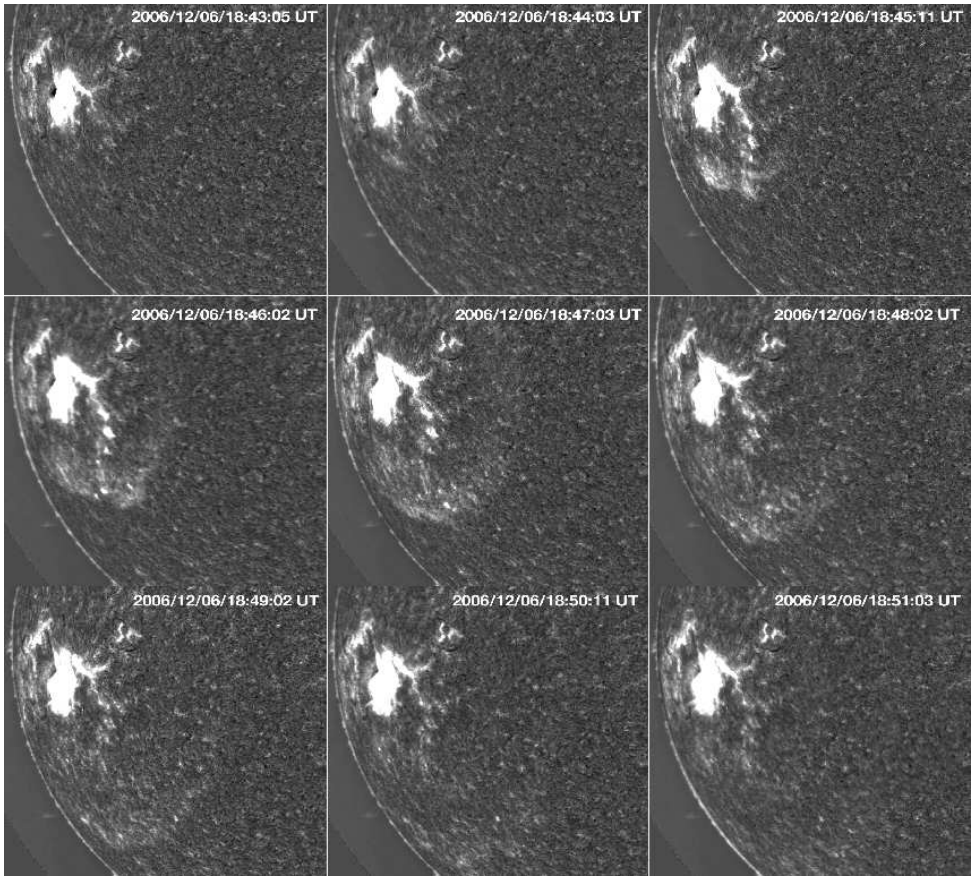

Figure 1.26: A composite of 9 still frames in Hα (6563 Å) on 6th December 2006 shows a tsunami-like wave spreading from a white-light flare erupting from AR 10930. Figure from the Optical Solar Patrol Network at the National Solar Observatory in New Mexico. Credit: `http://www.nso.edu/press/tsunami`.

directions. They relate the differences to the presence of a coronal hole. Hα Moreton wave fronts are deformed by low-lying obstacles (Warmuth *et al.*, 2002) and they are observed only when the speed of the disturbance is supersonic. Narukage *et al.* (2004) and Balasubramaniam *et al.* (2007) report that the Moreton wave disappears when it slows to magnetosonic Mach 1 and Mach 2 speeds, respectively. Moreton waves are also observed to decelerate, with the magnitude of the deceleration weakening with increasing time and distance from the source (Warmuth *et al.*, 2004a).

Interpretation of Moreton Waves

Because characteristic speeds in the chromosphere (c_s, v_A) are of the order of 10 km s^{-1}, the existence of wave modes that could account for the observed speeds of Moreton waves is prohibited. If Moreton waves were chromospheric waves, they would have Mach numbers > 10 and would dissipate strongly, instead of remaining reasonably coherent over large distances (Warmuth, 2007). So instead of interpreting Moreton waves directly as waves, Uchida (1968, 1974) treated them as an acoustic wave generated by refraction of a coronal fast-mode shock wave at the intersection of the wave with the chromosphere. In this so-called "sweeping-skirt" hypothesis, the Moreton wave constitutes the surface track of a weak fast-mode MHD shock wave generated in the corona by a flare (known as the "blast-wave" scenario). Fast-mode waves in the corona are expected to refract because their Alfvén velocity should increase with height, due to the exponential decrease of density (Uchida, 1968). The refraction concentrates energy down into the chromosphere, creating the compression and down-up wave motion. Using numerical simulations, Uchida (1970) showed that the shock wave is refracted away from regions of high Alfvén velocity (regions of strong magnetic field) and enhanced in regions of low Alfvén velocity, consistent with observations as described above.

It was well known in the late 1960s that Moreton waves are accompanied by type II bursts and flares (e.g. Moreton, 1964). Since then, more recent observational studies have also highlighted the close association between Moreton waves and type II bursts (e.g. Kai, 1970; Harvey *et al.*, 1974; Klassen *et al.*, 1999; Khan and Aurass, 2002; Warmuth *et al.*, 2004b). Khan and Aurass (2002) analyse an event where type II bursts were imaged and found to be co-spatial with a Moreton wave. Pohjolainen *et al.* (2001) also indicate an association between the two features. More recently, Liu *et al.* (2006) studied the unusual 29th October 2003 event and found the Moreton wave fronts in different directions to be spatially correlated with type II radio bursts. For the powerful 28th October 2003 event, Pick *et al.* (2005) report that the Moreton wave front appears to bound the emissions seen in radio, with the projected positions of type III bursts tracing the same pattern as part of the Moreton wave front. Naturally linking these two phenomena, Uchida (1974) understood Moreton waves and metric type II bursts to be two different aspects of the same driving agent, namely a coronal MHD fast-mode shock. As with the type II radio bursts, Hα data do not show the coronal disturbance directly since the Hα Moreton wave is only a surface imprint of the disturbance.

1.6.2.3 X-ray data

Coronal wave features have also been observed in X-ray data, first by *Yohkoh*/SXT (Khan and Hudson, 2000; Hudson *et al.*, 2003; Narukage *et al.*, 2002, 2004; Warmuth *et al.*, 2004a) and more recently by GOES/Solar X-ray Imager (SXI) (Warmuth *et al.*, 2005) and *Hinode*/XRT (Asai *et al.*, 2008). SXT coronal waves are thought to form high in the corona, due to the $\sim 3{\times}10^6$ K formation temperature of the SXT-observed plasma. Khan and Hudson (2000) report the first discovery of

large-scale X-ray waves as the result of purposeful searching of the SXT data, motivated by the discovery of EIT waves. SXT waves had not previously been found because it is generally very difficult to see the ambient corona in SXT flare-mode observations as the instrument switches to automatic short exposures. (The appendices in Hudson *et al.*, 2003, detail factors that make X-ray wave detection with *Yohkoh* difficult). From an observational point of view, it is difficult to distinguish a wave from an expanding loop in SXT data alone (e.g. Pohjolainen *et al.*, 2005). Indeed, there is even some disagreement when looking at EIT data! As pointed out by Hudson *et al.* (2003), Khan and Aurass (2002) describe the 3rd November 1997 event at $\sim$ 09:00 UT and identify the corresponding bright front seen in EIT as a coronal wave (as do Thompson and Myers, 2009), but Delannée *et al.* (2000) identify the same feature as a loop.

SXT waves are observed to become more diffuse and wider as they expand. Hudson *et al.* (2003) analyse an SXT wave and conclude that the event can be interpreted as a flare-induced blast-wave. The wave is observed to refract as it approaches the chromosphere (becoming increasingly tilted to the magnetic field), consistent with the expectation from Uchida's 1968 model corona where v_A increases with height. Using filter-ratio methods, Narukage *et al.* (2002) and Hudson *et al.* (2003) showed that the intensities of the SXT wavefronts were consistent with those expected to be generated by fast-mode shocks. More recently, large-scale X-ray coronal waves have also been observed by GOES/SXI (a full disk telescope with a 4 minute cadence at $\sim$ 3 $\times 10^6$ K, and 8 minute cadence at 4-5 $\times 10^6$ K Lemen *et al.*, 2004). Asai *et al.* (2008) report *Hinode*/XRT and EIS observations of a faint, strongly blueshifted coronal wave feature, with an Alfvénic Mach number of 1.4. They conclude that the XRT feature is identifiable as a weak MHD fast-mode shock.

1.6.2.4 He I data

The formation of the He I 10830 Å optically thin absorption line is complex since it is affected by processes in the upper chromosphere, transition region and low corona (Vršnak *et al.*, 2002). In He I images the quiet Sun is characterised by a weak background and darker patches (known as "mottles") which reproduce the Hα network and photospheric magnetic field concentrations. He I data show diffuse, patchy, stationary brightenings due to a weakening of absorption. These brightenings are relatively long-lived ($>$ 2 hours) and are morphologically similar to dimming observed in EUV data. This is interpreted to be due to a removal of overlying coronal material (Vršnak *et al.*, 2002; de Toma *et al.*, 2005).

The range of speeds for waves observed in He I data is $\sim$ 200 - 600 km s^{-1} (Gilbert *et al.*, 2004). The propagation of He I events is modified by the presence of magnetic features like active regions and the disturbances are observed in quiet Sun regions, free from filaments and plage.

Vršnak *et al.* (2002) report wave phenomena in He I data, consisting of a main perturbation (described as a diffuse but uniform disturbance, which is observed to be co-spatial with, but morphologically different from, an Hα Moreton wave) and a forerunner which is observed to move *ahead* of the associated Moreton wave front. The forerunner can be described as a diffuse and patchy disturbance, with the brightenings corresponding to He I mottles, suggesting the importance of the magnetic field in creating this forerunner (Vršnak *et al.*, 2002). Vršnak *et al.* (2002) invoke the passage of a shock wave to increase densities and temperatures in the transition region. These conditions lead to more collisions which enhances the He I absorption in the main He I perturbation. An inclination of the shock wave (since v_A increases with height far from active regions), would mean that higher parts of the shock wave intersect the magnetic field connected to surface areas

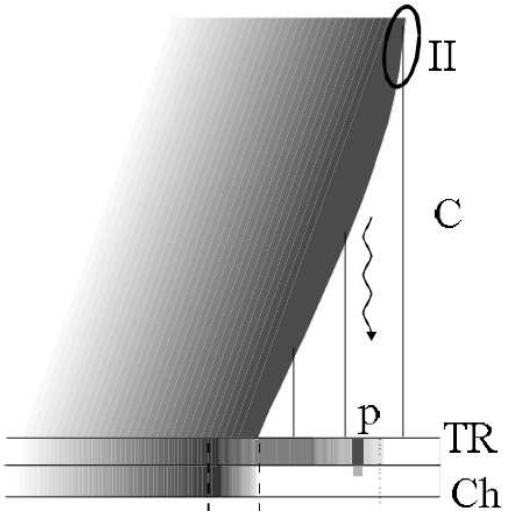

Figure 1.27: Schematic presentation of the fast-mode MHD shock passage through the corona (C) and its signatures in the transition region (TR) and chromosphere (Ch) as suggested by Vršnak *et al.* (2002) for producing the He I waves. Thin vertical lines represent magnetic field lines and the wavy arrow indicates the agent causing the He I forerunner. The shading behind the shock front above the TR illustrates the density and temperature enhancement in the shock downstream region. The type II burst source is indicated (II) in the quasi-perpendicular segment of the shock. Figure adapted from Vršnak *et al.* (2002). Permission to reproduce this figure has been granted by Astronomy and Astrophysics.

ahead of the shock at the base of the corona, allowing some "signal" to propagate down along the magnetic field, creating the forerunner (see Figure 1.27). Possible causes of the "signal" are considered by Vršnak *et al.* (2002) as either (i) a thermal conduction front, enhancing the collisional processes in the transition region, upstream of the intersection with the shock or (ii) fast non-thermal electrons accelerated at the quasi-perpendicular part of the shock and directed along the magnetic field, leading to an increased collision rate.

1.7 Coronal Dimmings

Another feature that can be observed when a CME occurs is a phenomenon known as coronal dimming.

1.7.1 What are Dimmings?

Transient dimming of coronal intensity, or in short "dimmings", are most often observed as decreases in intensity in soft X-rays (Hudson *et al.*, 1996; Sterling and Hudson, 1997) and extreme ultra-violet (EUV) data (Thompson *et al.*, 1998), and can appear relatively suddenly, on timescales of minutes. Dimmings were first observed at optical wavelengths in ground-based coronagraph data (Hansen *et al.*, 1974), with the first space-based observation being made in soft X-rays by the Skylab mission (1973-74; Vaiana *et al.*, 1977). These dimmings were referred to as "transient coronal holes" (TCHs; Rust, 1983), since the intensity of these regions was observed to be similar to that of established coronal holes. More recently, dimmings have been identified in ground-based observations made in the He I 1083 nm line, where they appear as brightenings which are co-spatial and co-temporal with EUV dimmings. The brightenings are believed to be induced by a decrease in

the overlying coronal radiation (de Toma *et al.*, 2005).

The cause of coronal dimmings has been much debated in the literature. At present, there appear to be two generally accepted possibilities. The dimming may be due to a density depletion caused by an evacuation of plasma (Hudson *et al.*, 1996). Such an effect may be caused by the eruption of the local magnetic field, leading to considerable expansion of magnetic loops into interplanetary space. The expansion creates a larger volume, leading to a region of decreased plasma density as a result. Supporting this interpretation is the study of plasma Doppler motions using SOHO/Coronal Diagnostic Spectrometer (CDS; Harrison *et al.*, 1995) data by Harra and Sterling (2001). They found strong, direct evidence of blue-shifted mass motion in coronal dimming regions, concluding that the dimming is indeed due to plasma evacuation. Harrison and Lyons (2000) came to a similar conclusion based on work that focused on density depletion in coronal dimming regions, emphasising that the dimming is mainly caused by a loss of plasma at a temperature of $1{\times}10^6$ K. Work by Zarro *et al.* (1999), compared *Yohkoh*/SXT and SOHO/EIT observations, establishing that similar co-spatial dimmings exist simultaneously at different wavelengths, thus strengthening the theory that the dimmings could indeed be caused by a decrease in coronal density. More recently, data obtained by the *Hinode*/Extreme ultra-violet Imaging Spectrometer (EIS; Culhane *et al.*, 2007) have shown detection of Doppler blueshifted plasma outflows of velocity ≈ 40 km s^{-1} corresponding to a coronal dimming (Harra *et al.*, 2007b). Imada *et al.* (2007) find that *Hinode*/EIS data of a dimming shows a dependence of the outflow velocity on temperature, with hotter lines showing a stronger plasma outflow (up to almost 150 km s^{-1}). These works collectively support the interpretation of coronal dimmings as being due to plasma evacuation.

Although plasma evacuation is a widely accepted interpretation of the dimming signature, it should be noted that a decrease in intensity in coronal plasma may be caused by cooling as well as by density depletion (e.g. Thompson *et al.*, 1998; Chertok and Grechnev, 2003). Differences observed between images in different emission lines suggest that some secondary temperature variations may also be responsible for the appearance of dimmings. However, Hudson *et al.* (1996) showed that the timescale of the dimming formation observed in *Yohkoh*/SXT data is much faster than corresponding conductive and radiative cooling times, which suggests that the dimmings are primarily a result of density depletion rather than a temperature effect. Finally, we note that in addition to these two possibilities, Gopalswamy and Thompson (2000) suggest that part of the dimming may be caused by reconnection inflow.

1.7.2 The Link with CMEs: How are coronal dimmings related to interplanetary observations?

Although coronal dimming has long been closely associated with CMEs (e.g. Rust and Hildner, 1976) and dimmings are now widely acknowledged as a reliable indicator of front-side CMEs (e.g. Thompson *et al.*, 2000a; Hudson and Cliver, 2001), the CME-dimming association was only confirmed recently using a statistical analysis (Bewsher *et al.*, 2008). In classical "double dimming" events (e.g. 7th April 1997, 12th May 1997), it was suggested that the dimmings mark the position of the foot-points of an erupted flux rope that makes up the core magnetic field of the associated CME (Hudson and Webb, 1997; Sterling and Hudson, 1997; Webb *et al.*, 2000). Upon eruption of the flux rope (which makes up the core field of the associated CME), the magnetic loops rooted in the dimming regions greatly expand to heights much larger than the gravitational scale-height of the plasma. As a result, the plasma can escape the corona and the dimming regions are believed to

exhibit a decrease in intensity as the plasma is evacuated along the "open" field lines (Thompson *et al.*, 2000a).

Assuming that the CME is mostly rooted in the dimmings, several properties derived from the study of dimmings can be used to obtain information about the associated CME. Firstly, calculations of the emission measure and estimates of the volume of dimmings can give a proxy for the amount of plasma making up the CME mass (Sterling and Hudson, 1997; Wang *et al.*, 2002; Zhukov and Auchère, 2004). Although large uncertainties are associated with estimates of coronal mass loss (due to the dependence of calculations on the emission measure distribution, which is not well known, and uncertainties in estimating the volume of the dimming regions; Hudson and Webb, 1997), the results do suggest that at least part of the CME mass comes from coronal dimming regions. Indeed, Harrison and Lyons (2000) conclude that the mass evacuated from the dimming regions may account for much of the mass of the outer shell of the CME. For the 12th May 1997 event, Zhukov and Auchère (2004) calculate that 50% of the mass of the CME comes from TCHs, and the other 50% from a more extended region. Secondly, the spatial extent of coronal dimmings can give information regarding the angular extent of the associated CME (Thompson *et al.*, 2000a; Attrill *et al.*, 2007b). Thirdly, quantitative measurement of the magnetic flux through dimmings can be compared to the magnetic flux of modelled magnetic clouds (MC) at 1 AU (Webb *et al.*, 2000; Mandrini *et al.*, 2005; Attrill *et al.*, 2006; Qiu *et al.*, 2007), see Démoulin (2008) for a review. Fourth, as we will show in chapter 5, studying the evolution of the dimmings, particularly during their recovery phase can give information about the evolution of the CME *post-eruption* (Attrill *et al.*, 2006). Finally, study of the distribution of the dimmings, their order of formation and measurement of their magnetic flux contribution to the associated CME enabled Mandrini *et al.* (2007) to derive an understanding of the CME interaction with its surroundings in the low corona for the case of the complex 28th October 2003 event.

Interplanetary observations can also be used to derive physical parameters of the associated interplanetary CME (ICME). Solar energetic particles, such as bi-directional electron heat fluxes, can be utilized as diagnostic tracers of the large-scale structure and topology of the interplanetary magnetic field embedded within ICME/MC events (Malandraki *et al.*, 2005). In the context of a closed field configuration, bidirectional flows are understood to result from particle circulation and reflection; the absence of electron heat fluxes is interpreted as a full disconnection; whilst in an "open" field configuration (where the ICME/MC is connected to the Sun only at one end), the expectation is to observe uni-directional electron heat fluxes (Richardson *et al.*, 1991; Shodhan *et al.*, 2000). However, it should be noted that the enhanced magnetic field regions associated with CME-driven shocks can act to mirror the energetic particles and hence can also produce bidirectional flows (Malandraki *et al.*, 2005). Although this "connectivity indicator" is applied in general, intermittency can be present in the electron flux distribution with many abrupt, discontinuous dropouts in electron fluxes (see e.g. Larson *et al.*, 1997; Shodhan *et al.*, 2000). It has been suggested that these dropouts may be due to disconnection of the interplanetary magnetic field from the corona (McComas *et al.*, 1989). Larson *et al.* (1997) noted that the disconnections "presumably result from magnetic reconnection near the Sun". If so, then the heat flux dropouts might correspond to the regions of "open" field lines in the dimming which have become closed in the corona during the recovery of the dimming. Whilst there are uncertainties associated with using electron heat flux distributions as indicators of magnetic connectivity (Riley *et al.*, 2004), for the purposes of the work in chapters 5 and 6, we adopt the interpretation of the general "connectivity indicator" described above.

Given the close relationship between the manifestation of coronal dimming regions and CMEs,

the drive to understand the magnetic nature of CMEs naturally requires investigation of the magnetic nature of dimming regions. This magnetic nature is studied in detail in chapters 5 and 6.

1.8 Aim of Thesis

Understanding what triggers a CME's initiation, its development from an initial point into a global disturbance, its evolution during expansion into interplanetary space and crucially, its magnetic orientation, are clearly of interest given their potential geoeffectiveness and impact on human space activites. The research presented in this thesis predominantly combines EUV imaging and measurements of the solar magnetic field. It is the first work to demonstrate that study of the evolution of dimmings and coronal wave bright fronts can be integrated with magnetic field measurements to build an understanding of the global structure and evolution of the associated CME. This thesis aims to contribute new and original scientific research on the subjects of coronal waves and coronal dimmings.

1.9 Outline of Following Chapters

Chapter 2 comprises a description of the various solar telescopes and *in situ* instruments that provided data used in this work. Chapter 3 comprehensively reviews previous work on coronal waves and provides a historical context for our current understanding. Multi-wavelength observations and the various existing EIT wave models are described. Chapter 4 presents our new results posing an interesting challenge to previously widely-accepted theory and a new model for the generation of EIT coronal "waves" is described and applied to several case studies. Chapter 5 describes work on the early-stage recovery of coronal dimmings, showing for the first time how careful study of the evolution of coronal dimmings can be used to probe the global magnetic field connectivity of an ICME. Chapter 6 focuses on the late-stage recovery of coronal dimmings, tackling the question of how dimmings recover. It is quantitatively demonstrated that a model of reconnection between "open" magnetic field and small coronal loops is a strong candidate for the mechanism facilitating the recovery of coronal dimmings. Chapter 7 discusses the collective contribution of this work to the fields of study of coronal waves and coronal dimmings. Possibilities for future work are also considered.

Chapter 2

Instrumentation

The data used in the work presented in this thesis comes from both solar telescopes and *in situ* instruments. The solar instrumentation includes extreme ultra-violet and soft x-ray imagers, white light coronagraphs and a magnetograph. The *in situ* instrumentation includes fluxgate magnetometers and an electrostatic plamsa analyser. Such a range of instrumentation is required because coronal waves and dimmings are low-coronal signatures of coronal mass ejections (CMEs). To understand the connection between the low-coronal signatures and their ejective counterpart, the evolution of the CME as it traverses the interplanetary space is also studied. This necessitates a coupled solar-*in situ* approach to the data analysis. First the solar instrumentation is described, followed by an outline of the *in situ* instruments.

2.1 Extreme Ultra-Violet Imagers

2.1.1 SOHO/Extreme ultra-violet Imaging Telescope (EIT)

The Solar and Heliospheric Observatory (SOHO, Domingo *et al.*, 1995) is a joint mission of co-operation between the U.S. National Aeronautics and Space Administration (NASA) and the European Space Agency (ESA). The SOHO spacecraft was built in Europe by an industry team led by prime contractor Matra Marconi Space (now EADS Astrium) under overall management by ESA. NASA was responsible for the launch and is now responsible for mission operations. Mission control is based at Goddard Space Flight Center in Maryland. SOHO was successfully launched aboard an Atlas IIAS rocket on 2nd December 1995 at 08:08 UT from the Cape Canaveral Air Force Station, Florida. SOHO flies in a fully sunlit "halo" orbit near the L1 Lagrangian Point. The L1 Lagrangian point is located about 148.5 million km from the Sun and about 1.5 million km from the Earth and is the point at which the gravitational and centripetal accelerations of the Earth balance those of the Sun.

The relationship between the orbits of two bodies is described by Kepler's Third Law:

$$\frac{{P_1}^2}{{P_2}^2} = \frac{{R_1}^3}{{R_2}^3} \tag{2.1}$$

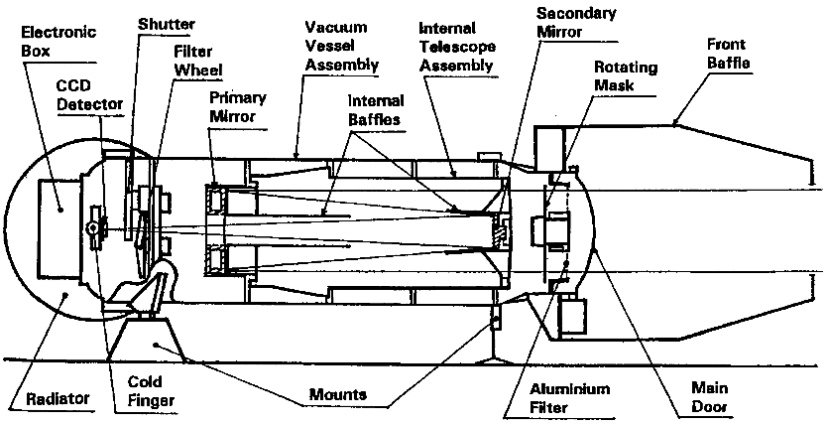

Figure 2.1: Schematic of the EIT indicating its major substystems. Figure from Delaboudinière *et al.* (1995). Permission to reproduce this figure has been granted by Springer Science and Business Media.

This law implies that the period (P) for a planet to orbit the Sun increases rapidly with the radius (R) of its orbit. For the Sun-Earth system, a spacecraft moving around the Sun in an orbit smaller than the Earth's will overtake the Earth, so it will not remain at a fixed position relative to the Sun-Earth line. However, if the spacecraft is placed at L1, the Earth's gravity acts on the spacecraft, cancelling some of the gravitational attraction from the Sun, so the spacecraft maintains its position, requiring a slower orbital period to do so, and so appears "fixed" with respect to the Sun-Earth line. Although such an orbit is unstable, positioning commands are sent to SOHO, correcting and maintaining the orbit. The L1 location also allows data to be taken continually, uninterrupted by earth occultations and the Moon's shadow that occur in observations taken from spacecraft in low Earth orbit.

SOHO carries 12 instruments on board, data from several of which are used extensively in this thesis. The Extreme ultra-violet (EUV) Imaging Telescope (EIT; Delaboudinière *et al.*, 1995) is designed to study the dynamics and evolution of coronal structures over a wide range of time scales, sizes and temperatures. EIT is a normal incidence telescope with an effective focal length of 1652 mm (Moses *et al.*, 1997). EIT returns EUV images of the corona and transition region on the solar disk and up to 1.5 $R_\odot$ above the solar limb with a $45' \times 45'$ square field of view. EIT has a maximum spatial resolution, imaging 1024×1024 pixels of $2.63''$ each, although on-chip binning reducing the resolution by half to improve the cadence (imaging 512×512 pixels of $5.26''$ each) is also commonly used (Moses *et al.*, 1997).

The main body of the EIT telescope is comprised of two mirrors mounted on each end of an aluminium cylinder (see Figure 2.1), which is attached to the main telescope structure by a central flange to avoid thermal stresses. The optical cylinder is wrapped with thermofoil heaters so that the spacing between the mirrors can be maintained by adjustment of the temperature using active thermal control. A rotating mask illuminates only one quadrant of the telescope at a time with sunlight. The image from the selected quadrant is focused on a back-illuminated, EUV enhanced sensitivity charge-coupled device (CCD), which comprises a 1024×1024 array of 21 μm square pixels.

CCDs are photon-detecting pixel arrays that make use of intrinsic photoconduction (Culhane, 2004). CCDs have a layer of semiconductor material (a commonly used element is silicon) beneath an insulating layer (typically a metal oxide). On top of the insulating layer is an electrode. When

a positive voltage is applied to the electrode, all of the negatively charged electrons are attracted to the area immediately under the electrode. Any positive charges are repelled from the area around the electrode. This separation of charges forms a"potential well". The absorption of an incoming photon whose energy is greater than the band gap of the material (1.12 eV for silicon) will lift an electron into the conduction band of the semiconductor, creating a hole in the so-called depletion region. The electrons are collected in the potential wells, with the number of electrons collected being proportional to the number of photons that fall on each pixel. For read-out of the accumulated charge, a positive voltage is applied to the semiconductor, transferring the electrons in the potential wells to a register. The charges are converted to a voltage and then digitally encoded. (Further detail on the principles of operation of CCDs is given by Mackay, 1986).

Back-illuminated CCDs have exceptional quantum efficiency at EUV wavelengths compared to front-illuminated CCDs. A back-illuminated CCD is where the CCD chip is thinned - down to only 15 μm thick - then it is mounted upsidedown. Since the back of the CCD has no electrodes on it, the surface is clear of obstruction so the incoming light has access straight to the pixel wells and the CCD is therefore more sensitive. As mentioned, back-illuminated CCDs are more sensitive to blue wavelengths of light, which makes them especially suitable for detecting ultra-violet wavelengths. Front-illuminated CCDs must be much thicker than their back-illuminated counterparts because red photons must penetrate further than blue photons before they are absorbed into the silicon (Mackay, 1986). The CCD is cooled by a cold finger attached to a passive radiator directed toward deep space. The temperature is regulated to about -80° C by a small heater. This cooling reduces noise, minimising dark current (the relatively small electric current that flows through a photosensitive device such as a CCD even when no photons are entering the device), and mitigates against radiation damage from cosmic ray hits by preventing the read noise level being permanently raised. In addition, EIT is fully baffled to prevent contamination and fake readings from charged particles entering the front aperture of the telescope and reaching the CCD.

The flat-field calibration, necessary to perform meaningful analysis with EIT images, was obtained by illuminating the CCD with a beam of monochromatic EUV radiation. By obtaining several images with the CCD placed at different positions in the beam, variations in CCD response can be detected. The resulting flat-field image is then normalised to unity. The raw images from the EIT are then divided by the flat-field image to remove spatial non-uniformities associated with the CCD. After the launch of EIT, in-flight images were carefully scrutinised to establish spatial variations of the instrument response across the field of view. No change of the intrinsic CCD flat-field was detected in in-flight images during EIT's first year in space (Moses *et al.*, 1997). Over time, radiation-induced ageing degrades the CCD response so that the calculated flat-field becomes distorted by strong residuals of solar activity. CCD "bakeouts" (heating the CCD to $\sim$ +16 °C) can partly cure the damage, but the degree of recovery is variable over the field of view. Bakeouts evaporate condensated contamination, which would otherwise contribute to a decline in CCD performance. The major radiation-induced factor contributing to CCD degradation is contamination from cosmic/solar energetic particle radiation. Also known as displacement damage, it is caused when energetic particles impart enough energy to an atom, displacing it from its lattice site. The vacancy created becomes a trap, collecting the electrons before the charge makes it to the CCD, so impeding the signal and reducing the charge collection efficiency. Bakeout anneals the electron traps in order to maintain the performance of the instrument. Ultimately the EIT instrument operations team aim to build a consistent model of the radiation damage, in order to maximise the accuracy of the reconstructed data. Work on such a model, as well as analysis of regular in-flight images to check the flat-field is ongoing throughout the lifetime of the mission.

EIT has four spectral emission line bandpasses centred on the intense emission lines at: Fe IX (171 Å), Fe XII (195 Å), Fe XV (284 Å) and He II (304 Å). These four spectral emission lines cover temperatures ranging from 6×10^4 K to 3×10^6 K. Fe XII 195 Åalso includes a hot ($\sim 10{\times}10^6$ K) Fe XXIV line emitted during flares. By dividing the telescope mirrors into quadrants, the emissions from narrow temperature ranges can be isolated by "tuning" the coatings of each quadrant to the desired wavelength. EIT's normal incidence multi-layer coated EUV optics (Spiller *et al.*, 1994) consist of alternating layers of molybdenum and silicon. The four separate multilayer coatings are deposited on the matching quadrants of both the primary and secondary (tiltable) mirrors. Interference effects arising in the different multilayer coatings define the selection of the four spectral emission lines so that the quadrants of the EIT mirrors reflect light at the four different wavelength bands specified above. Because of the high contrast and high sensitivity to quiet Sun structures, the principal waveband for studying coronal evolution is Fe XII 195 Å. Fortunately for our field of study, 195 Å is also the waveband in which coronal waves have been most clearly observed, and as such, most of the data analysis presented in this thesis comes from the Fe XII 195 Å waveband. Apart from the Fe XXIV line, the peak temperature of the Fe XII 195 Å emission line is at 1.6×10^6 K, and this spectral line is particularly suited to observations of the quiet corona outside of coronal holes. In addition to observations of coronal material, EIT 195 Å images can also show chromospheric and prominence material in absorption (Zarro *et al.*, 1999).

The brightness variations of individual pixels in the images of the corona are due to changes in emission measure of the relevant line:

$$\xi = \int n^2 A \, ds \tag{2.2}$$

where the integration is along the line of sight in s, A is the pixel size and the density, n, refers to the plasma in the specified temperature range (Benz and Krucker, 2001).

EIT can be used to provide limited field of view study of the Sun with higher time resolution, by only reading out sub-arrays of pixels (32×32 pixels), while discarding the rest of the CCD field. However, the subjects of coronal waves and dimmings in this thesis are global-scale events, and thus we only use the full-Sun images. These tend to be taken during EIT's "CME Watch" programme, which takes full-disk 195 Å data continuously, at 12-17 minute intervals.

2.1.2 STEREO/Extreme Ultra-Violet Imager (EUVI)

The Solar Terrestrial Relations Observatory (STEREO, Driesman *et al.*, 2008) is the third mission in NASA's Solar Terrestrial Probes programme. STEREO was launched on a Boeing Delta II 7925-10L rocket at 00:52 UT on 26th October 2006, from Cape Canaveral Air Force Station. STEREO consists of two identically instrumented spacecraft in heliocentric orbits, drifting away from Earth in opposite directions (one ahead "A" and one behind "B") at $\sim 22°$ per year. The two observatories will provide stereoscopic imaging of the Sun as their separation angle increases. STEREO is designed to study the flow of energy and matter from the Sun to the Earth, in particular revealing the three-dimensional structure of CMEs to help explain their genesis and evolution. The mission is managed by the Goddard Space Flight Center and the operations are implemented from the John Hopkins University Applied Physics Laboratory in Maryland.

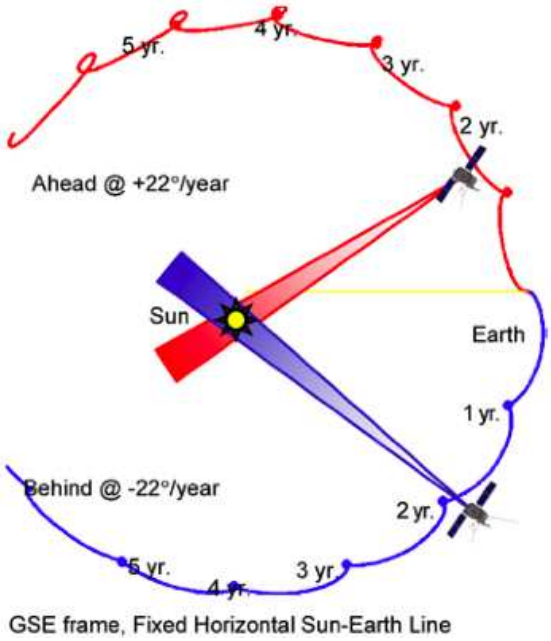

Figure 2.2: The orbits of the two STEREO spacecraft, projected onto the ecliptic plane with a fixed Sun-Earth line. The drifts of the observatories, separating by $\sim 22°$ each year are shown. Figure from Driesman *et al.* (2008). Permission to reproduce this figure has been granted by Springer Science and Business Media.

The identical EUV Imaging (EUVI, Wuelser *et al.*, 2004) telescopes on the two STEREO spacecraft are designed to study the structure and evolution of the solar corona in three dimensions, and specifically to focus on the initiation and early evolution of CMEs. The EUVI is a part of the Sun Earth Connection Coronal and Heliospheric Investigation (SECCHI) instrument suite, which comprises five telescopes covering a broad range of fields of view, starting at the solar surface and extending all the way to the interplanetary space between the Sun and Earth. The EUVI's 2048 x 2048 pixel CCD detectors (13.5 μm square pixels) have a field of view out to 1.7 $R_{\odot}$, and observe in four spectral channels (deliberately chosen to match those of SOHO/EIT) spanning a temperature range of 1×10^5 K to 2×10^7 K. In addition to its view from two vantage points, the EUVI therefore provides a substantial improvement in image resolution and image cadence over its predecessor SOHO/EIT (EUVI can be run at $\sim$ 2 minute cadence).

Since the basic EUVI instrument design (normal incidence telescope with thin metal filters to suppress most of the non-EUV radiation, quadrant multilayer MoSi coated mirrors, tiltable secondary mirror and a back-thinned CCD detector) build on and are similar to those of SOHO/EIT, we do not reproduce the EUVI instrument schematic here, but refer the reader to Wuelser *et al.* (2004). EUVI uses a graphite/cyanate metering tube (lined with aluminium foil as a contamination barrier) as the main telescope structure. The stiffness and low coefficient of thermal expansion are desirable qualities of this composite, eliminating the need for a focusing mechanism. The CCD is cooled to about -60° C by a cold finger attached to a passive radiator directed toward deep space. EUVI has two main modes of operation: the first (synoptic) program schedules every observation by time, is identical on both observatories, and occupies about 80% of the available telemetry. The second (campaign) program is more flexible, allowing higher data rates for limited periods of time.

The unique design of STEREO allowed the two observatories, which had drastically different orbital requirements, to be launched on a single launch vehicle. A series of seven propulsive

manoeuvers were used to adjust the trajectories of the two spacecraft onto specific phasing orbits which allowed the required lunar swing-by distances and subsequent trajectories to be achieved. The first lunar swing-by allowed observatory A to gain sufficient energy to be ejected from the Earth-Moon system, achieving the required heliocentric orbit after spending 52 days in Earth orbit. This first swing-by also imparted enough energy to observatory B to place it in a higher elliptical orbit. Observatory B re-encountered the Moon for a second lunar swing-by 38 days after the first lunar swing-by event. This second lunar swing-by event ejected observatory B into its heliocentric orbit with a larger semimajor axis and therefore a drift rate lagging the Earth. Observatory B was ejected into its final orbit on 24th January 2007. The data from STEREO's observatory B used in this thesis were taken at $\sim$ 07:00 UT on 25th January 2007. So this thesis and the accompanying paper Attrill *et al.* (2007b) analyse the very first EUVI scientific data on coronal waves and dimmings obtained from STEREO's observatory B.

2.2 Soft X-ray Imager

2.2.1 *Yohkoh*/Soft X-ray Telescope (SXT)

The Solar-A mission Ogawara *et al.* (1991) (christened *Yohkoh* meaning "*Sunbeam*" after the spacecraft completed its first orbit), was launched by the Japanese Institute of Space and Astronautical Science (ISAS) from Kagashima Space Center on 30th August 1991. *Yohkoh* was a collaborative project between Japan, the United States and the United Kingdom. During the solar eclipse of 14th December 2001, *Yohkoh* lost its pointing and the batteries discharged. The spacecraft operators were unable to command the satellite to point back toward the Sun. During its very successful operations, *Yohkoh* occupied a quasi-circular orbit about Earth at an altitude of $\sim$ 600km, with a period of 97 minutes. The orbit was inclined at 31° to the ecliptic plane, and as a result *Yohkoh* passed into the Earth's shadow for about 40 minutes each orbit. During this time, known as "spacecraft night", no solar data can be taken. For most of the orbit, *Yohkoh* was located beneath the Earth's radiation belts, but during passage over the south Atlantic, the offset of the Earth's magnetic axes with respect to its axis of rotation means that the radiation belts are at an anomalously low altitude. This region is known as the South Atlantic Anomaly (SAA), and passage through this region exposes spacecraft to high fluxes of energetic particles. To combat potential damage to the instruments, the spacecraft high voltage power supplies are switched off during crossing of the SAA.

Yohkoh carried four instruments: The Soft X-ray Telescope (SXT), the Hard X-ray Telescope, the Bragg Crystal Spectrometer and a Wide Band Spectrometer. This thesis uses data from the SXT (Tsuneta *et al.*, 1991). Although the primary objective of SXT was to study solar flares, in this thesis the capability of SXT to image the entire Sun in soft X-rays is exploited. In particular, because SXT imaged the emitting plasma that is confined by magnetic fields (see Section 1.1.3), SXT images allow indirect observation of the magnetic field connectivity. This capability is also used to infer information about the global magnetic field connectivity (Chapter 5).

SXT was a fixed-focus grazing incidence telescope with a focal length of 1500 mm. Figure 2.3 shows a schematic diagram of the layout. X-rays are difficult to focus because an X-ray beam striking a mirror head-on passes right through it. However, an X-ray beam hitting a mirror at a very oblique glancing angle is reflected at the same angle, with only a small part of the beam

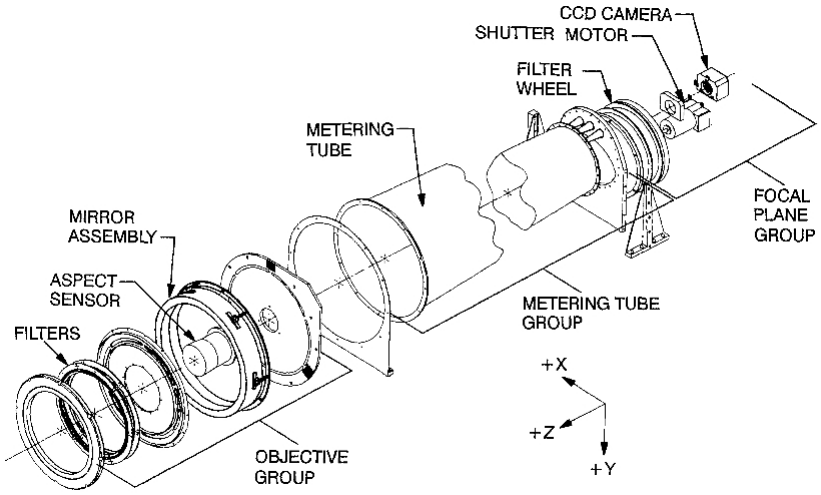

Figure 2.3: Schematic diagram of the SXT with sub-assemblies identified. Figure from Tsuneta *et al.* (1991). Permission to reproduce this figure has been granted by Springer Science and Business media.

Table 2.1: Summary of the filters used in SXT. Data from Tsuneta *et al.* (1991).

Commanded Position	Front Filter	Rear Filter
1	Open	Open
2	30 Å at 4310 Å	Al 1265 Å
3	CCD Flood Lens	Al/Mg/Mn composite
4	Opal-glass diffuser	Be 119 μm
5	140 Å at 4580 Å	Al 11.6 μm
6	8.05% mesh	Mg 2.52 μm

passing through the mirror or being absorbed by it. Mirrors using this principle are called "grazing incidence" optics.

The CCD field of view comprised $42' \times 42'$, with a pixel size of $2.45''$. Full-disk, full-resolution images could be obtained, but often telemetry restrictions required that only parts of the CCD and/or binned images (to half-resolution $4.9''$, or quarter-resolution $9.8''$) were transmitted.

SXT used various combinations of two filters to image the solar plasma from $<1\times10^6$K to $>50\times10^6$K over a wide range of intensities. A summary of the various filters is given in Table 2.1. The different filters transmitted various passbands and were therefore sensitive to different temperature plasmas. The sensitivity for the different filters as a function of temperature is shown in Figure 2.4. The well-defined absorption edges of the analysis filters emphasise different spectral lines. This feature of SXT provides rudimentary spectral (and therefore temperature) discrimination. Figure 2.4 shows that there are two thick filters (Al 11.6 μm and Be 119 μm), which are most suitable for studying flare temperature plasma. In the work presented in this thesis, data from the thinner filters (Al 1265 Å, Al/Mg/Mn composite and Mg 2.52 μm) is used, since these are most sensitive to non-flare temperature plasmas.

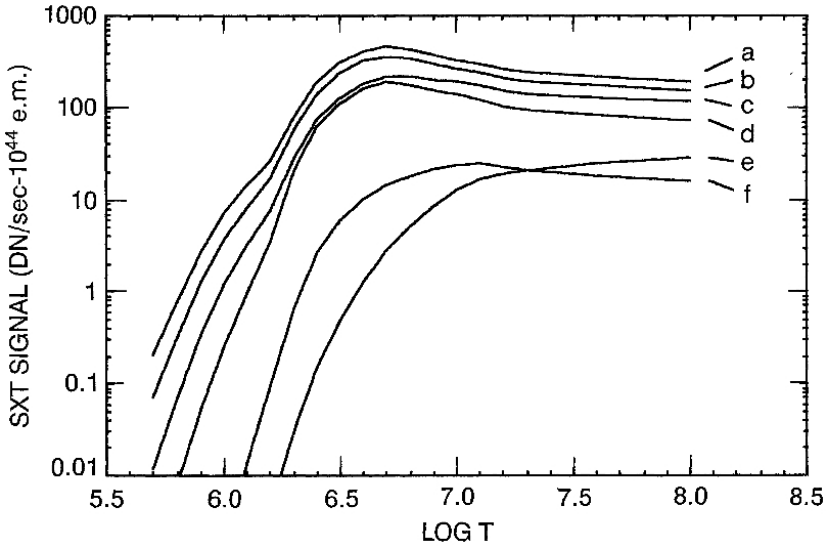

Figure 2.4: The total SXT signal as a function of temperature for the open filter (a) and the SXT analysis filters: (b) Al 1265 Å (c) Al/Mg/Mn, (d) Mg 2.52 μm, (e) Al 11.6 μm, (f) Be 119 μm. Figure from Tsuneta *et al.* (1991). According to the *Yohkoh* analysis guide (1994, pg. 55), the filters (e) and (f) are mis-labelled in this plot and should be exchanged so that (e) actually indicates the Be 119 μm filter and (f) actually indicates the Al 11.6 μm filter. Permission to reproduce this figure has been granted by Springer Science and Business Media.

2.3 Coronagraph

2.3.1 SOHO/Large Angle Spectroscopic Coronagraph (LASCO)

Observations of the tenuous white-light corona other than during a solar eclipse are made possible using a coronagraph (invented by Bernhard Lyot, 1930) to block out the intense photospheric surface light of the Sun. Coronagraph observations from space are limited by the scattered light generated within the instrument. As well as inhomogeneities within the lenses, the main contributions of scattered light in an ordinary objective lens telescope come from diffraction at the aperture of the lens and "ghost" solar images from multiple reflections in the objective lens. The coronagraph is designed to reduce the scattering from these processes.

The SOHO/Large Angle Spectroscopic Coronagraph package (Brueckner *et al.*, 1995) has 3 coronagraphs, C1, C2 and C3, imaging the solar corona from 1.1-3 $R_\odot$, 1.5-6$R_\odot$ and 3.7-30 $R_\odot$ respectively. C1 was an internally-occulted mirror Lyot coronagraph, whilst C2 and C3 are externally occulted instruments. (C1 was internally occulted because given the spacecraft dimension constraints, it was not possible to build a sufficiently long externally occulted coronagraph to observe the innermost corona with the required high spatial resolution). Since the work in this thesis is focused on the low corona, data from the C2 instrument is used (i) because the lateral extent of CMEs is easily viewed directly in C2 data and (ii) the C1 coronagraph did not take data after June 1998.

Figure 2.5 shows the optical layout of the C2 coronagraph. The role of the external occulter is to completely shadow the entrance aperture from direct sunlight. The objective lens, O1, images the corona (out to 6.0 $R_\odot$ for C2) onto the field stop, A2. Here, where a CCD would usually record the image in an ordinary objective lens telescope, an occulting spot (focal plane mask) is

placed instead. The role of this occulting spot it to absorb most of the light from the center of the field of view, leaving only light from the central source concentrated around the edges of the telescope aperture. This remaining light forms rings around the edge of the aperture A1 image. The objective lens, O1, also images the external occulter onto an internal occulter D2, just behind the coronal image stop A2. The internal occulter, D2, intercepts residual diffracted light from the edges of the external occulter. The field lens (O2) collimates the primary corona image, and images the entrance aperture (A1) as well as its diffraction pattern onto the Lyot stop (A3). The Lyot spot intercepts the diffracted light from the edges of A1 (residual diffracted light from the external occulter, imaged on the spot as "ghost-images" by inter-reflections in the O1 objective lens) and prevents it from reaching the focal plane where the CCD is located. Finally, a relay lens (O3, which also has a Lyot spot) re-images and magnifies the primary coronal image seen through O2 onto the 1024×1024 pixel, front-side illuminated CCD camera. Two plane mirrors (coated with an anti-reflection coating to reduce their polarisation to a few percent) fold the optical path in order to limit the overall length of the instrument. The shutter and filter wheel are mounted as close as possible to O3, being just in front of, and behind this final pupil, respectively. The polariser wheel is located just in front of the CCD camera.

Two additional components further improve the performance of the coronagraph. A heat rejection mirror collects all direct sunlight entering the instrument and focuses the solar image in between the external occulter and the A0 aperture, rejecting the image outside this space. Second, the light-tube itself prevents single or double reflections on the tube from falling inside the A1 aperture.

The C2 images are produced using various filters to select different nominal bandpasses: Blue (420-520 nm), Orange (540-640 nm), Light Red (620-780 nm), Deep Red (730-835 nm) and H-alpha (2nm at 656.3 nm). The efforts undertaken to minimise scattered light within the instrument have successfully resulted in both the C2 and C3 coronagraphs having stray light levels at least an order of magnitude below the anticipated coronal signal from the Sun.

2.4 Magnetograph

2.4.1 SOHO/Michelson Doppler Imager (MDI)

The Michelson Doppler Imager (Scherrer *et al.*, 1995), part of the Solar Oscillations Investigation (SOI) on board SOHO is the first spaceborne solar magnetograph. Although the primary scientific objective of SOI is to measure the internal stratification and dynamics of the Sun using helioseismology, MDI also makes non-helioseismic measurements, essential for understanding solar dynamics. Several times each day, polarizers are inserted to measure the line-of-sight component of the magnetic field. It is this particular capability to make magnetic field measurements that is used in the work presented in this thesis. MDI obtains high-quality synoptic observations of the full-disk line-of-sight magnetic field every 96 minutes. The full-disk field of view comprises $34' \times 34'$ with $4''$ resolution. As well as full-disk observations, MDI can operate in a higher resolution mode, comprising a $1.25''$ resolution ($\times$ 3 magnification) $11' \times 11'$ field of view centred about $160''$ north of the solar equator, to allow observation of active regions. The field of view is selected by the shutter. Because the subjects of study are the global phenomena of coronal waves and dimmings, the full-Sun magnetograms are used in the work presented in this thesis.

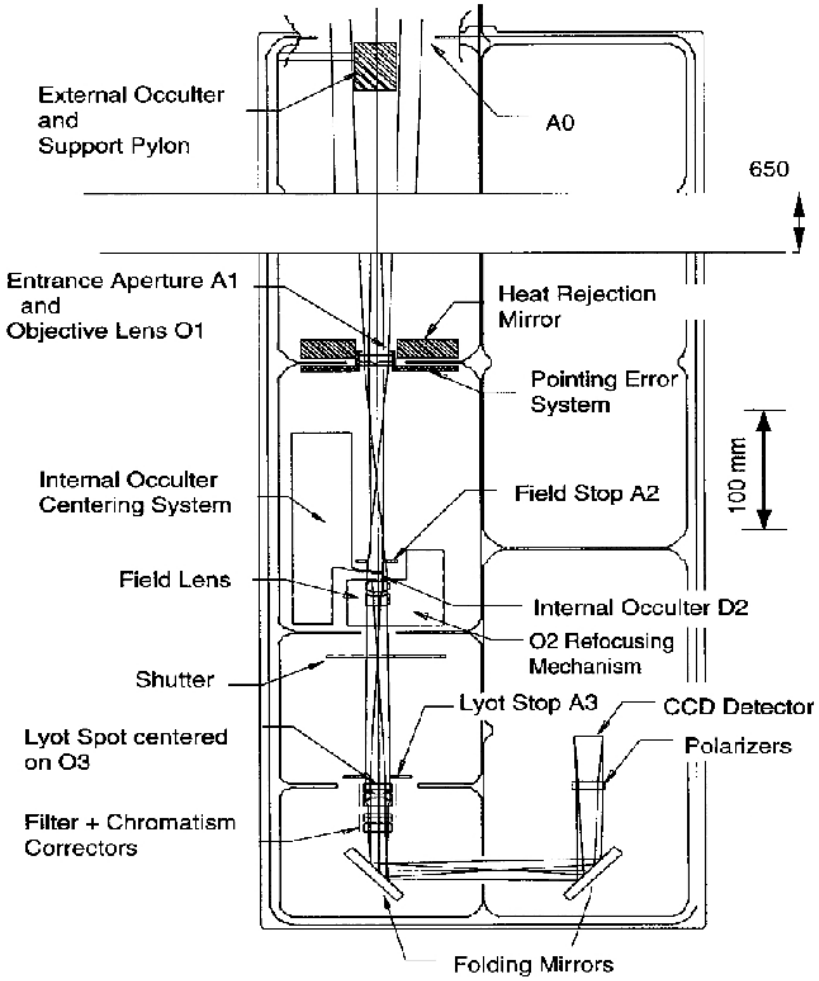

Figure 2.5: The optical layout of the externally occulted C2 coronagraph: front aperture A0, external occulter D1, entrance aperture A1, objective lens O1, internal occulter D2, field lens O2, Lyot stop A3, relay lens with Lyot spot O3, filter/polarizer wheels, and focal plane at the CCD detector. Figure from Brueckner *et al.* (1995). Permission to reproduce this figure has been granted by Springer Science and Business Media.

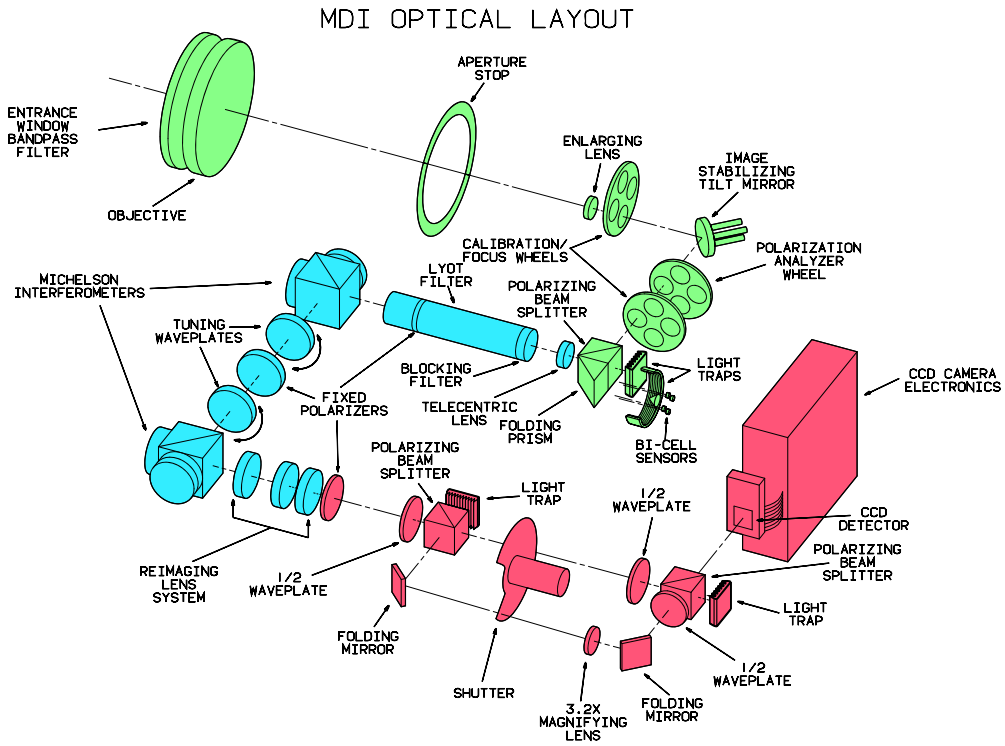

Figure 2.6: Schematic of MDI's optical layout, showing the light path and the primary optical components. Green highlights the imaging optics, blue the filter system and pink the camera system. Figure from Scherrer *et al.* (1995). Permission to reproduce this figure has been granted by Springer Science and Business Media.

MDI uses a refracting telescope to feed sunlight through a cascade of increasingly narrow spectral filters onto a passively cooled 1024 × 1024 pixel CCD camera. Figure 2.6 is a schematic showing MDI's optical layout. The green shaded components highlight the imaging optics. After passing through the entrance window and enlarging lens, waveplates in the polarisation analyser wheel convert the input (i.e. right circularly polarised, RCP; or left circularly polarised, LCP) sunlight into vertically plane polarised light.

A wave plate may be made of birefringent (anisotropic, directionally dependent) crystal and works by shifting the phase of the electromagnetic wave between the two perpendicular polarization components. Over the thickness of the waveplate, one component (parallel to the optical axis of the waveplate) may propagate slightly slower than the perpendicular component, thus increasing the phase shift between the two components. A quarter-wave plate creates a 90° phase shift and can change linearly polarized light to circular and vice versa. Similarly, a half-wave plate retards one component of the polarised light by 180°. After this conversion, the image stabilisation system (ISS) beam splitter sends the vertically plane polarised component through the instrument. For magnetic measurements, the polarisation analyser wheel alternately selects RCP and LCP positions between filtergrams.

The imaging optics consist of two lenses: the primary "objective" (tiltable) lens and the secondary "enlarging" lens. Together they form a telescope with an effective focal length of 1867 mm. The optical path of the light is folded by the ISS tilt mirror and then split by the polarising beam splitter (prism), projecting two primary images: a p-wave (longitudinal component) and s-wave (transverse component). The s-component image plane lies inside the filter oven containing the temperature sensitive filters. The p-component falls onto four orthogonal detectors of the limb sensor assembly, used to determine the instrument relative pointing, which can be adjusted over $\sim 13'$. A quarter-wave plate (not shown) mounted between the beamsplitter and the filter oven directs undesired reflections back through the beam splitter and onto a light trap. The quarter-wave plate circularly polarises the light in the observing beam, so only half the light passes through the linear entrance polariser of the Lyot filter.

The filter system is the heart of the MDI instrument and is shaded blue in Figure 2.6. The telecentric lens makes the angular distribution of light passing through the subsequent filters identical for each image point. The filter system consists of the front window, the blocker, the Lyot and the two tuneable Michelson interferometers. Fixed filters transmit light only near the Ni I 6768 Å line, formed in the mid-photosphere and have a combined full-width-half-maximum of 454 mÅ. Filtergrams in the vicinity of this solar spectral line can be obtained by tuning the Michelsons' peak transmission (see Figure 2.7). The Michelson interferometers have free spectral ranges of 377 mÅ and 189 mÅ. The tuning is accomplished by rotating the half-wave plates mounted between the interferometers, so altering the phase shift and the resulting selected wavelength of the light.

The pink shaded components of Figure 2.6 highlight the MDI camera system. The lens system re-images the primary focus onto the detector. The following beamsplitters and folding mirrors separate the full-disk and high-resolution light paths, with the shutter selecting which beam falls on the CCD. The CCD is a front-illuminated 1024×1024 array with 21μm square pixels.

Longitudinal line-of-sight magnetograms are constructed by measuring the Doppler shift separately in RCP and LCP light. The difference of the Doppler shift between these two polarisations is a measure of the Zeeman splitting (see Chapter 1) and is roughly proportional to the net magnetic flux density (i.e. the line-of-sight component of the magnetic field averaged over the pixel field of

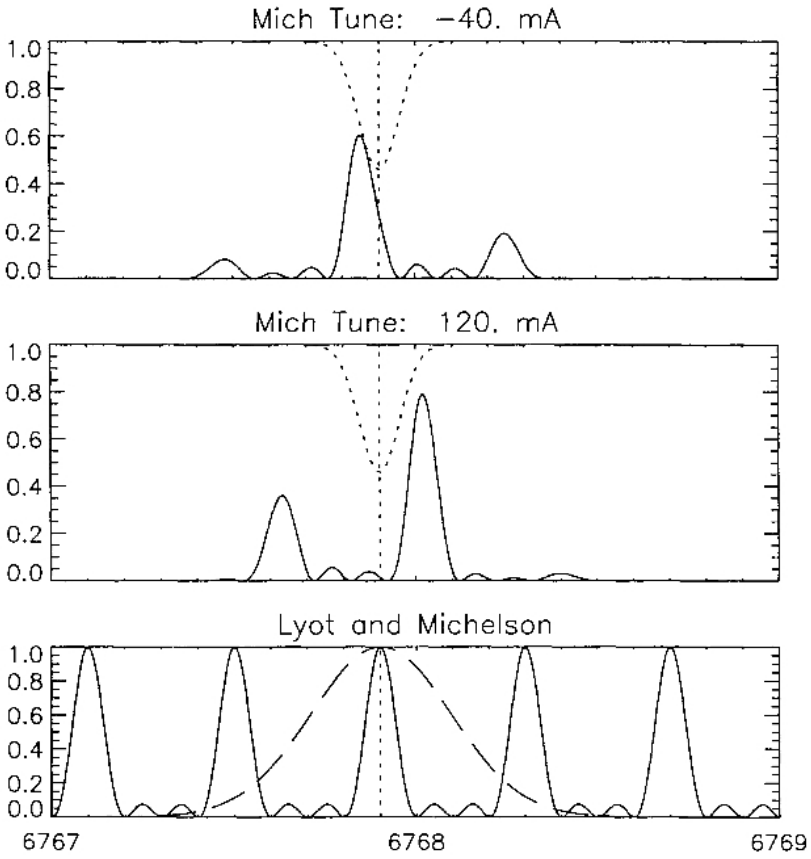

Figure 2.7: MDI's principle of operation. The lower panel shows both the profiles of the Lyot filter (dashed line) and the spectrum of both Michelsons in series (solid line). The upper panels illustrate two of the four nominal Doppler tunings. The solid line represents the resulting instrument transmission profile with respect to the 6768 Å line profile (dotted line). Figure from Scherrer *et al.* (1995). Permission to reproduce this figure has been granted by Springer Science and Business Media.

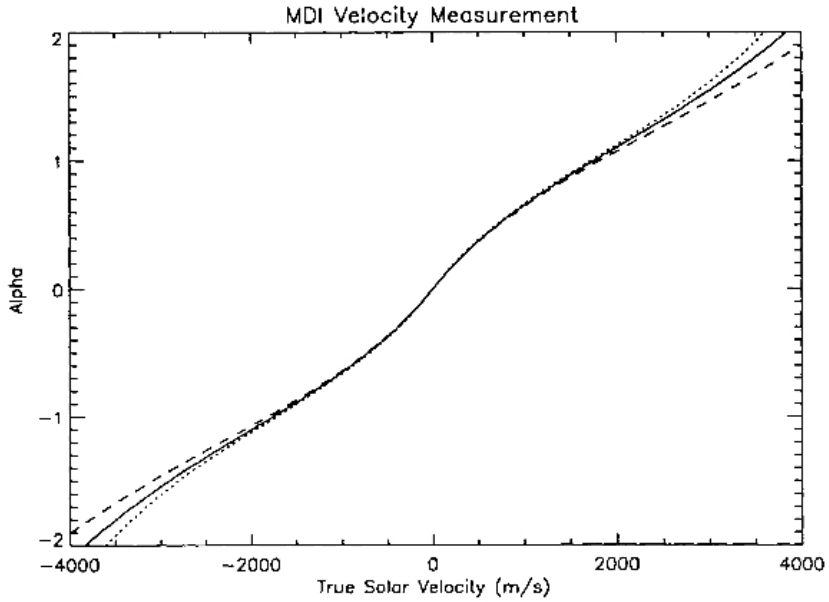

Figure 2.8: Relation between α and Doppler velocity calculated for a nominal line profile (solid) and for lines 25% broader (dashed) and narrower (dotted). Figure from Scherrer *et al.* (1995). Permission to reproduce this figure has been granted by Springer Science and Business Media.

view). Pixel size of MDI data is $\sim 2''$.

The primary observable of MDI is the line-of-sight Doppler velocity. MDI records filtergrams (images of the photosphere in five well-defined narrow wavelength bands and polarisation states), at different positions along the Ni I 6767.8 Å absorption line. These filtergrams therefore have the characteristics of mono-chromatic images of a given solar spectral line, even though the filters do not perfectly isolate a single narrow band of the spectrum. As a result, the filtergrams can be treated like intensities at single wavelengths. The Doppler velocity is estimated from a ratio, α, between sets of five filtergrams, equally spaced by 75 mÅ, where F_0 is nearly continuum, F_1 and F_4 are centered on the wings of the profile, and F_2 and F_3 are centered about the core of the center-of-disk Ni line. Errors in measurements of the longitudinal magnetic field are estimated to be ± 20 G.

If numerator > 0 then:

$$\alpha = \frac{(F_1 + F_2 - F_3 - F_4)}{(F_1 - F_3)} \tag{2.3}$$

Or, if numerator ≤ 0 then:

$$\alpha = \frac{(F_1 + F_2 - F_3 - F_4)}{(F_4 - F_2)} \tag{2.4}$$

The image processor computer then calculates the corresponding Doppler velocity from α using a look-up table shown in Figure 2.8. The lookup table is constructed from synthetic line profiles and measured filter transmission profiles.

2.5 *In-Situ* Measurements

2.5.1 *Wind*/Magnetic Field Investigation (MFI)

Wind (Figure 2.9) is the first spacecraft of NASA's Global Geospace Science program, which is part of the International Solar-Terrestrial Physics (ISTP) Science Initiative, a collaboration between several countries in Europe, Asia, and North America. The aim of this initiative is to understand the behaviour of the solar-terrestrial plasma environment in order to predict how the Earth's atmosphere will respond to changes in solar wind conditions. *Wind* measures the properties of the solar wind before it reaches the Earth. *Wind* was launched on 1st November 1994 by a Delta rocket from Cape Canaveral. For the first two years of operation, *Wind* was positioned in a sunward orbit with a maximum apogee of 250 R_E, undergoing two lunar swingbys to boost its speed. This allowed *Wind* to gradually approach its final station of a "halo" orbit at the Sun-Earth L1 Lagrangian point, providing *Wind* with a prime view of the solar wind, interplanetary magnetic field and energetic particles. At the end of 1997, *Wind* rounded the L1 Lagrangian point and headed back toward the Earth. On 8th April 1998 *Wind* moved to a complicated "petal" orbit that brings it as close as 10 R_E and as far as 80 R_E from our planet. This orbit takes *Wind* to an angle of 60° from the ecliptic plane. The variations in *Wind*'s orbit mean it moves through different plasma environments including the solar wind, magnetosheath and magnetosphere.

One of the nine instruments on-board *Wind*, the Magnetic Fields Investigation (MFI; Lepping *et al.*, 1995) is designed to investigate the large-scale structure and fluctuation characteristics of the interplanetary magnetic field, which influence the transport of energy and the acceleration of particles in the solar wind as well as generating dynamic processes in the Earth's magnetosphere.

The magnetometers of the MFI measure the dynamic behaviour of the vector interplanetary magnetic field up to 44 times a second. MFI also measures interplanetary shocks, waves, and other features that govern the acceleration and transport of energetic particles. The magnetometers are mounted on a 12-meter boom (see Figure 2.9), with the outer one being mounted at the end of the boom and the inner one mounted about halfway along it, so placing the magnetometers at different radial distances from the main spacecraft body. The data processing and control unit is situated within the body of the spacecraft. This configuration is used to reduce contamination from spacecraft-generated magnetic fields. This is important because the interplanetary magnetic field (IMF) is very weak (about $\frac{1}{10{,}000}$ the Earth's surface field) and the magnetic fields produced by electric currents on the spacecraft are strong enough to disturb observation of the IMF.

The fluxgate magnetometer was originally designed and developed for use from low-flying aircraft as a submarine detection device during World War II. The first magnetic field measurements made in space were conducted by the triaxial fluxgate magnetometer aboard the U.S.S.R.'s Sputnik III, launched on 15th May 1958. MFI has two such triaxial flux-gate magnetometers (this full redundancy emphasises the critical nature of the magnetic field measurements for the science goals of the *Wind* mission).

One possible setup of a fluxgate magnetometer in which two parallel bars of a ferromagnetic material are placed closely together is illustrated in the left hand panel of Figure 2.10. In a ferromagnetic metal (e.g. iron), the magnetic axes of its atoms point in random directions. When a current flows in a coil wrapped around such a metal, an electromagnet is created, and the magnetic field generated by the current aligns all the atoms in the metal, adding to the magnetic

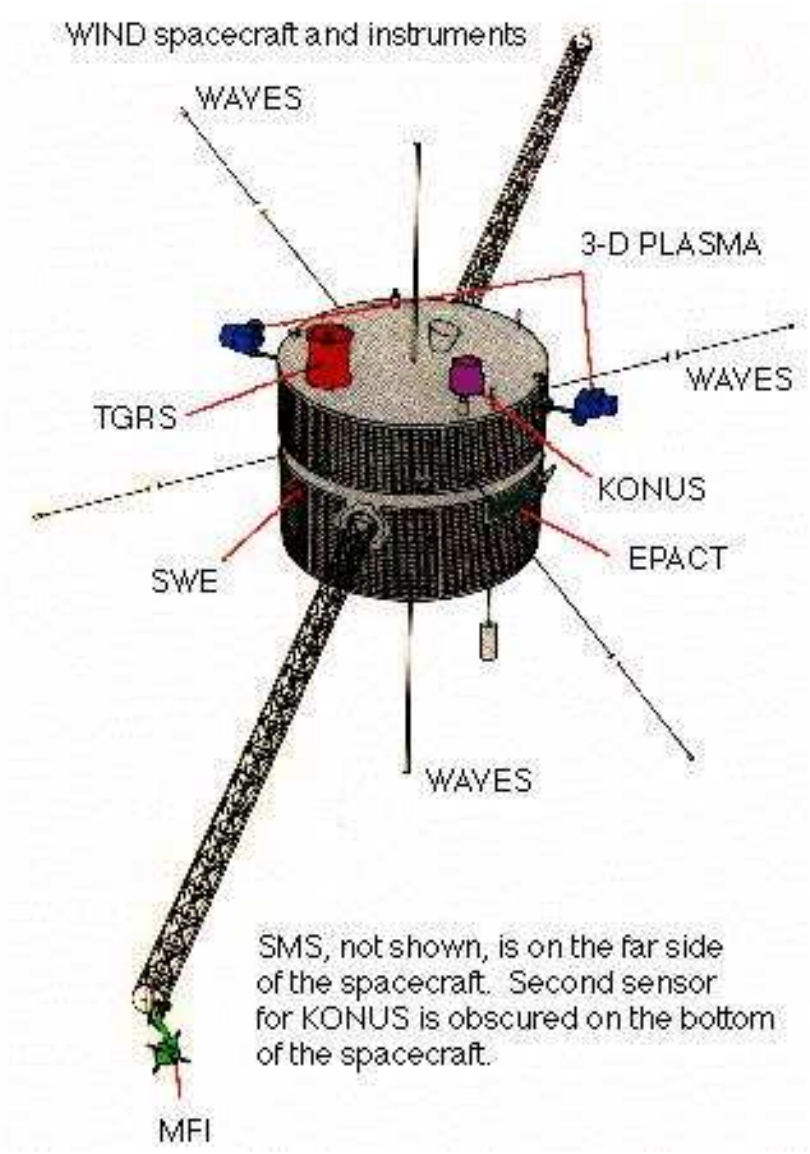

Figure 2.9: The *Wind* spacecraft diagram from ISTP's Spacecraft and Instruments Summary webpage. Note the locations of the Magnetic Field Investigation (MFI) and the 3-D Plasma analysers at the ends of the booms.

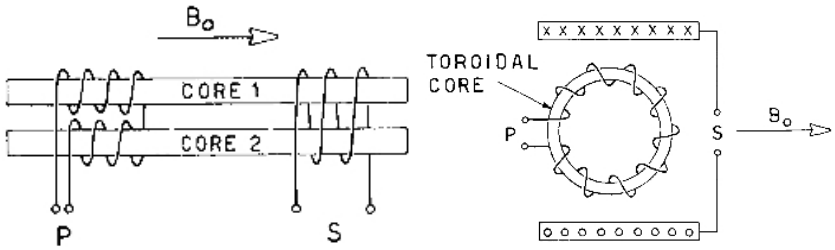

Figure 2.10: Two possible geometries of saturable core sensing elements for a fluxgate magnetometer. Left shows a two-core bar arrangement. Right shows a ring-core arrangement as used in the *Wind*/MFI and ACE/MAG instruments. Figure from Ness (1970). Permission to reproduce these figures has been granted by Springer Science and Business Media.

field generated by the current. When the magnetic field strength (H) reaches a critical point, all the atoms are lined up, so the magnetic flux density (B) no longer increases and the metal is said to be saturated. If the current in the coil is increased further, the magnetic field only increases by the amount due to the electric current, with no further contribution from the core.

Each bar is wound with a primary coil, with the coils wound in opposite directions. The input signal, an alternating current (AC), is applied through the primary winding on each core, creating a large varying magnetic field in each coil, where the core's magnetic polarity flips back and forth with the cycle. In this situation, saturation occurs in each half of the cycle in a symmetric manner. The magnetic field induced in each core has the same magnetic field strength, but opposite orientation at any given time during the AC cycle.

If such an electromagnet is subject to an external magnetic field, of intensity dH, one component of this field will be directed along the axis of the core metal. This distorts the symmetry since as the current in the coil increases, the magnetic field due to the coil will be *opposite* to that of the external magnetic field in one bar, so saturation is delayed because the sum of the coil and external magnetic fields is weaker than that of the core alone. In the other bar, the magnetic field will be *parallel* to that of the external field, thus increasing the total magnetic field and advancing the onset of saturation. The resultant magnetic flux density is obtained by following the B-H hysteresis loop (see Figure 2.11). This resultant magnetic flux density induces a voltage potential in a secondary coil, wrapped around both the two bar cores and the primary coil (Figure 2.10). This voltage can be measured using an Ampére meter and is proportional to the strength of the magnetic field aligned along the axes of the bars. The measurement of the vector magnetic field therefore requires the use of three monoaxial fluxgate magnetometers. These analog signals are then digitized and processed by a microprocessor controlled data system. MFI actually uses a ring-core fluxgate magnetometer arrangement (right panel, Figure 2.10), although the principle of operation is the same as for the two-core bar arrangement described here. The MFI fluxgate magnetometers are capable of detecting a wide range of magnetic field strengths from ± 0.001 nT to ± 65,536 nT.

2.5.2 ACE/Magnetometer (MAG)

The Advanced Composition Explorer (ACE) was built by John Hopkins University/Applied Physics Laboratory and launched on a McDonnell-Douglas Delta II 7920 launch vehicle on 25th August 1997 from the Kennedy Space Center in Florida. The mission is managed by NASA. ACE

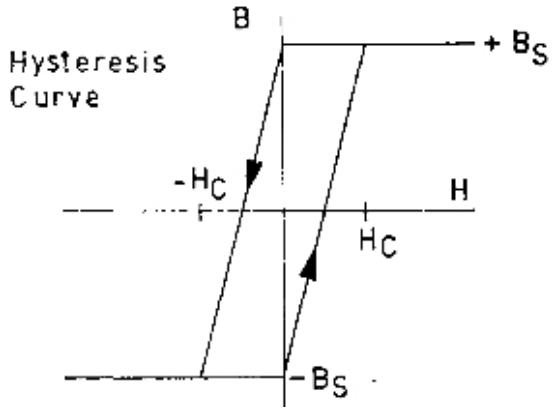

Figure 2.11: A theoretical parallelogram magnetic hysteresis loop for a saturable core of a fluxgate magnetometer showing the relation between the magnetic field strength (H) and the magnetic flux density (B). Figure from Ness (1970). Permission to reproduce this figure has been granted by Springer Science and Business Media.

uses six high-resolution sensors to measure and compare the elemental and isotopic composition of the solar corona, the nearby interstellar medium and the Galaxy, and to study particle acceleration processes that occur in a wide range of environments. ACE also carries three instruments that provide the heliospheric context for ion composition studies by monitoring the state of the interplanetary medium. ACE also orbits the L1 Lagrangian point, but occupies a modified "halo" orbit which can be described as a complicated Lissajous-like path about L1 with a major axis of about 150,000 km and a minor axis of about 75,000 km. The magnetometer (MAG; Smith *et al.*, 1998) is one of the three instruments that monitors the state of the interplanetary medium. MAG is actually the reconditioned flight spare of the magnetometer instrument (MFI) flown on *Wind*. The only changes made to the unit were to accommodate the ACE data bus and to change the sampling rate of the instrument, so it better met the reduced telemetry requirements for ACE. As a result, the instrument description remains the same as for *Wind*/MFI as described in the preceeding subsection.

2.5.3 *Wind*/3-Dimensional Plasma Experiment (3DP)

The 3-Dimensional Plasma (3DP) and energetic electron experiment on-board *Wind* is designed to measure the full 3-dimensional distribution of suprathermal electrons and ions at energies from a few eV to over several hundred keV. In conjunction with other *Wind* instruments, the 3DP (Lin *et al.*, 1995) studies where these energetic particles come from, how they are accelerated and transported, and what effects they have on the Earth's interplanetary space environment. The experiment consists of three detector systems: solid state telescopes, electron electrostatic analysers (EESA), and ion electrostatic analysers. The data from energetic electrons used in this thesis are obtained by the EESA high energy analyser (EESA-H). To avoid effects of the spacecraft potential on the energetic particle detection, and to provide a clear field of view, the EESA analysers are mounted on the end of a short 0.5 m boom (Figure 2.9).

EESA-H is a "spherical-sector electrostatic analyser" with a 360° field of view, tangent to the spacecraft surface. The instrument consists of two conductive hemispheres that are arranged concentrically so that there is a small gap (0.6cm) between the two conductors (see Figure 2.12). A variable electric field is applied over the gap, which selectively determines the energy that the

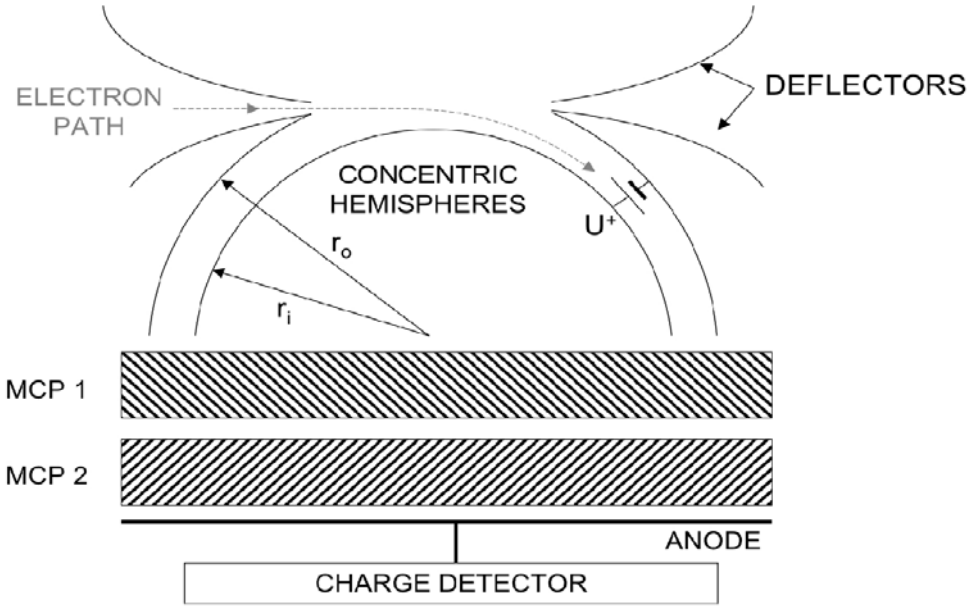

Figure 2.12: Schematic of a hemispherical electrostatic plasma analyser.

incoming electrons must have in order to pass between the hemispheres without colliding with the walls. The use of an electrostatic analyser with curved conducting plates means that both centripetal and electric forces are at work on the incoming electrons:

$$q\frac{U}{(r_o - r_i)} = \frac{2m_e v^2}{(r_o + r_i)} \tag{2.5}$$

where q is the charge of the electron, U is the difference in potential between the two conducting hemispheres, r_o and r_i are the radii of the outer and inner hemispheres respectively, m_e is the mass of the electron, and v is the velocity of the electron.

The EESA-H field of view is divided into six 60°, 1 mm thick micro-channel plate (MCP) detectors, forming a 360° ring. The selected electrons that follow a path between the concentric hemispheres enter a chevron pair of MCPs. When an energy-selected electron strikes the surface of an MCP pore, it causes further electrons to be emitted from the MCP surface. These electrons bounce down the walls of the MCP creating progressively more electrons, thus the initial impacting electron is effectively multiplied, giving an electron multiplication gain of $\sim 2{\times}10^6$ at the base of the MCP. Since the plasma analyser accepts electrons from all directions, by accumulating electrons only for a fraction of the spacecraft spin at a time, the directional information is preserved. Additionally, the field of view can be electrostatically deflected into a cone up to $\pm$ 45° out of its normal plane by voltage applied to curved plates placed at the analyser entrance aperture (see Figure 2.12). The deflectors allow the analyser field of view to follow the magnetic field as the spacecraft spins.

The EESA-H detector is swept through logarithmically spaced energy channels ranging from 100 eV up to 30 keV. The EESA instruments are essentially particle counters that are sampled 1024 times per spacecraft spin, giving a sampling period of $\sim$ 3 ms. Moments (density, velocity, pressure tensor, electron heat flux) are computed on-board, and three dimensional distributions

with various energy and angular resolutions, as well as pitch-angle distributions (like the ones used in this thesis) are downloaded from the spacecraft. Further information on particle measurement techniques in space plasmas can be found in Pfaff *et al.* (1998).

Chapter 3

Understanding Coronal Waves

The very first observation of an EIT coronal wave was reported by Dere *et al.* (1997) during SOHO's first "CME watch" observing programme. They observed a limb coronal wave event on 23rd December 1996, which was associated with a large-scale CME, spanning 70° in LASCO/C2 data. Dere *et al.* (1997) described the event: "a weak large-scale wave passes across the solar disk. Although the signature is not especially distinct, it appears to originate near the site of the CME and travel outward as a slight brightening." The velocity of this event was measured to be ~ 200 km s^{-1} in EIT and LASCO/C1 data.

Since SOHO's launch in 1996, several hundred EIT waves have now been observed (e.g. Figure 3.1). In order to answer the question of what an EIT coronal wave actually *is*, a review of the observational data available that shapes our understanding is helpful. Since EIT coronal waves were first discovered in EUV data, so we begin with a review of observations made in EUV bandpasses. Signatures of large-scale disturbances in the solar atmosphere seen in data from different spectral ranges were discussed in §1.6. The relationship of these observations to EUV coronal waves is considered in this chapter. Following our summary of the observational characteristics, a review of existing models is presented in §3.5. Potential generation mechanisms for driving EIT coronal waves are also discussed within the context of the various proposed models.

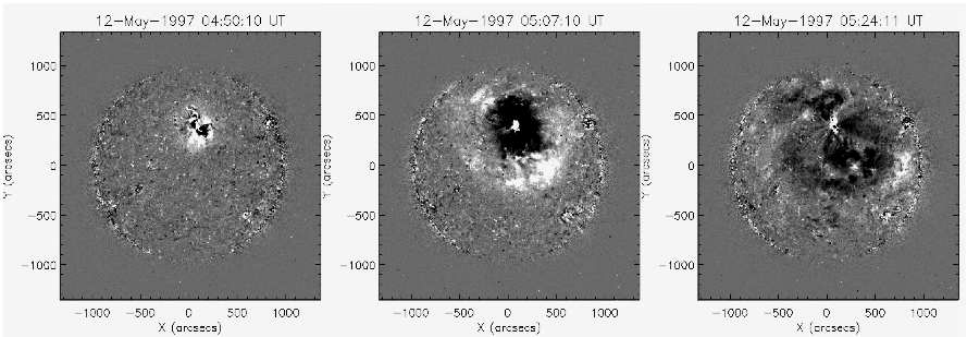

Figure 3.1: EIT 195 Å running difference images showing a classical diffuse coronal wave event observed on the solar disk on 12th May 1997.

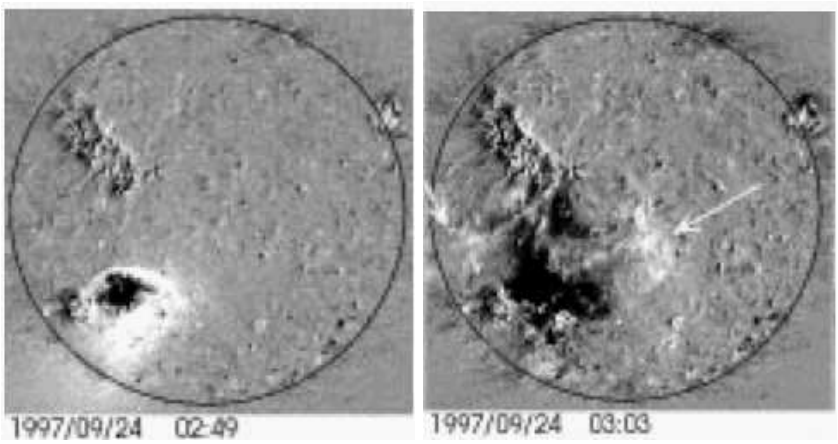

Figure 3.2: Base difference EIT 195 Å images for an EIT coronal wave event on 24th September 1997. Left panel shows an "S-wave", well-defined and located close to the source flaring active region. Right panel shows a "classical" patchy and diffuse semi-isotropic coronal wave bright front. (Figure from Thompson *et al.*, 2000a). Permission to reproduce this figure has been granted by Springer Science and Business Media.

3.1 Two types of EIT coronal wave?

Gradually, a consistent and generally accepted picture seems to be emerging in the literature of two distinct types of EIT wave, based mainly on observed morphology (Vršnak, 2005). In $\sim 7\%$ of EIT wave events, the bright front appears as a well-defined, sharp feature (Biesecker *et al.*, 2002), see left panel of Figure 3.2. These "brow waves" (Gopalswamy *et al.*, 2000) or **"S-waves"** (Biesecker *et al.*, 2002) often have high velocities ($>$ several hundred km s^{-1}) and have a restricted arc-like angle of propagation. However, by far the majority of EIT wave events may be described as having a more **diffuse** bright front (e.g. Thompson *et al.*, 1998, 1999). Figure 3.1 and the right panel of Figure 3.2 show examples of diffuse EIT waves, in which the bright front is not a coherent feature (Moses *et al.*, 1997; Podladchikova and Berghmans, 2005a), but rather tends to have a semi-isotropic, patchy morphology. We use "semi-isotropic" to describe the existence of the bright front in approximately all directions surrounding the source region. Diffuse EIT waves also move at slower speeds (although this may be an artifact of the relatively low time cadence of EIT, as most recently argued by Long *et al.*, 2008, with higher time cadence results from STEREO/EUVI). S-waves are always observed to be located close to the source active region. Diffuse bright fronts on the other hand, can be observed at distances from the source region on the scale of $R_\odot$. The distinction between S-waves and diffuse bright fronts will be important during the discussion in this chapter.

3.2 Observational characteristics of EUV coronal waves

The following list describes the various observations of EIT waves, their behaviour, morphology and physical characteristics. The observations are numbered for ease of referral throughout this chapter and in chapter 4, but the ordering is of no special significance.

1. **Huge range of coronal wave velocities**, with average speeds ranging between 25 - 438 km s^{-1} (Wills-Davey *et al.*, 2007), based on a sample of 160 events from a catalogue by

Thompson and Myers (2009). From a sample of 21 events, Klassen *et al.* (1999) measure an average EIT wave velocity $\sim$ 271 km s^{-1}. Recent work by Long *et al.* (2008) using all 4 passbands of STEREO/EUVI data shows that the cadence of observations can have a very strong influence on measured velocities, suggesting that due to the relatively low cadence of EIT's 195 Å filter data, EIT wave velocities may previously have been underestimated.

2. **The bright front becomes broader, more diffuse and less intense as it expands further from the source region** (e.g. Dere *et al.*, 1997; Klassen *et al.*, 2000; Podladchikova and Berghmans, 2005a). On average, the intensity enhancement constituting the bright front changes from 25% to 20% to 14% in successive EIT images (Thompson *et al.*, 1999).

3. **Coronal waves are observed to deflect magnetic features** such as filaments (Okamoto *et al.*, 2004), and they can directly instigate kink-mode loop oscillations where the loop is bodily displaced, but the footpoints remain fixed (Wills-Davey and Thompson, 1999; Harra and Sterling, 2003; Hudson and Warmuth, 2004).

4. **Diffuse coronal waves can rotate** (Podladchikova and Berghmans, 2005a). Almost a decade after its initial discovery, the much-studied 12th May 1997 coronal wave bright front (Figure 3.1) was shown to have a systematic angular displacement in time counterclockwise. This observation demonstrates that the coronal wave not only propagates radially but also rotates as it expands.

5. **There is no close association between coronal waves and the magnitude of flares** (Delannée and Aulanier, 1999; Cliver *et al.*, 2005; Chen, 2006).

6. **Every coronal wave is associated with a CME**, but not every CME has an associated coronal wave (Biesecker *et al.*, 2002).

7. **Coronal waves are observed primarily in the ambient quiet Sun corona** (e.g. Thompson *et al.*, 1999; Veronig *et al.*, 2006).

8. **Coronal waves do not traverse active regions or propagate into coronal holes** (Thompson *et al.*, 1999; Wills-Davey and Thompson, 1999; Veronig *et al.*, 2006; Tripathi and Raouafi, 2007).

9. **Coronal waves have a 3-D nature**, such that the bright front and dimming of the transients can be observed extending beyond the limb of the Sun (Thompson *et al.*, 1999).

10. **The brightening is a transitory phenomenon**. The intensity of the bright front returns to its pre-eruption level (or lower) by the time of the next EIT 195 Å image, typically 12 - 17 minutes (Thompson *et al.*, 1999).

11. **Coronal waves decelerate as they expand** (Warmuth *et al.*, 2004a,b). Warmuth *et al.* (2004a) report observing the largest deceleration in the first 200 seconds of a coronal wave event.

12. **Velocity of coronal wave and velocity of CME in same directions are proportional**. Based on analysis of five events by Hata (2001) (in Japanese, findings summarised in Uchida *et al.*, 2001), the velocity of the coronal wave (corrected for projection effects) and that of the CME are found to be proportional to each other for respective directions. Thompson *et al.* (1998) and Plunkett *et al.* (1998) report lateral expansion velocities of $\sim$ 250 km s^{-1} for the diffuse coronal wave and CME, respectively, on 12th May 1997.

13. **There is a weak trend for EIT wave quality (high rating = clearly defined bright front) to increase with CME speed.** (Biesecker *et al.*, 2002). However, the correlation is not statistically significant.

14. **There is a definite trend for CME-EIT wave association to increase with increasing CME speed** (Cliver *et al.*, 2005). They find that CMEs with speeds from 700 - 800 km s^{-1} were accompanied by EIT waves $\sim$ 30% of the time. From 800 - 1000 km s^{-1}, the association increased to $\sim$ 50%. For CMEs with speeds $>$ 1000 km s^{-1} a further increase to 60%. (We note that this point is somewhat in contradiction to point 13 above, however Biesecker *et al.* (2002) focus on the association with CME speed as a function of wave quality, whilst Cliver *et al.* (2005) consider waves of any quality in their study).

15. **CME width is an important factor for EIT wave formation/detection** (Cliver *et al.*, 2005). The median width of 25 fast ($>$ 700 km s^{-1}) CMEs that were associated with EIT waves was 165°. The median width of 31 such CMEs that lacked EIT waves was 60°.

16. **Coronal dimmings manifest following the expanding bright front** in most cases (see e.g. Thompson *et al.*, 1998, 2000a; Delannée *et al.*, 2000; Delannée, 2000; Gopalswamy and Thompson, 2000; Harra and Sterling, 2003; Zhukov and Auchère, 2004; Veronig *et al.*, 2006). Coronal dimming is seen as a region of decreased emission at EUV wavelengths. It is primarily considered to be due to the evacuation of coronal plasma (Hudson *et al.*, 1996; Harra and Sterling, 2001; Harra *et al.*, 2007b) during the "opening" of previously closed magnetic structures. (Dimming will be discussed further in chapters 5 and 6). However, Zhukov and Auchère (2004); Warmuth *et al.* (2004a); Grechnev *et al.* (2005) point out that there are discrepancies because, in some events it appears that the bright front expands to a larger distance than the dimming (e.g. 12th May 1997 event, although we will show in chapter 4 that a weak dimming does, in fact, manifest following the expanding bright front). Coronal dimmings are rather inhomogeneous, and they remain long after the coronal waves have vanished, slowly returning to their pre-event brightness on a timescale of tens of hours. Podladchikova and Berghmans (2005a) demonstrate that there is a strong connection between the structure of the EIT wave bright front and the dimmings.

17. **Stationary/persistent bright fronts** are sometimes found at coronal hole boundaries (e.g. Thompson *et al.*, 1998; Veronig *et al.*, 2006) and between active regions in the quiet Sun, at separatrices and QSLs formed in the large-scale magnetic topology (Delannée and Aulanier, 1999; Delannée, 2000; Delannée *et al.*, 2007).

18. **Coronal waves are observed in many different EUV bandpasses**. Most commonly observed in 195 Å data (due to EIT's high cadence "CME watch" campaign with this filter), observations of coronal waves identifiable with the same feature at 195 Å have also been made at 171 Å as well as at 284 Å (Zhukov and Auchère, 2004). In addition, TRACE observations of coronal waves have been made almost simultaneously at 195 Å and 171 Å (Wills-Davey and Thompson, 1999; Delannée, 2000). More recently, SPIRIT (Zhitnik *et al.*, 2002) 175 Å data have also been used to detect coronal waves (Grechnev *et al.*, 2005). Observations of coronal waves can also be made at 304 Å (e.g. Long *et al.*, 2008), but we consider that the dramatically changing background granulation seen in He II introduces a lot of noise and largely obscures the subtle coronal wave bright front. We note that out of all the EUV bandpasses typically used, coronal waves are consistently preferentially observed at 195 Å.

19. **A diffuse coronal wave has similar kinematics in four different EUV bandpasses**. This result comes from recent high-cadence STEREO/EUVI data, showing the coronal wave

bright front to be co-spatial at different wavelengths (Long *et al.*, 2008).

Some additional observations pertinent to EIT waves that are derived from the multi-wavelength data to be described in the following subsections are also added to our list of observations from EUV data:

20. **Bright front: due to density or temperature enhancement?** Exactly what physical mechanism causes the bright front observed in EUV is difficult to specify and this lack of clarity contributes to the mystery surrounding EIT coronal waves. It is difficult to separate density and temperature effects from a single narrow bandpass (such as 195 Å used by EIT) because intensity increases can theoretically be caused by density and/or temperature increases. A statement by Delannée *et al.* (2008) captures the problem: "there exists no observation yet that would clearly show whether a density enhancement or a heating process is responsible for the appearance of wave fronts." However, by studying the response functions of the TRACE 171 Å and 195 Å passbands for an event on 13th June 1998, Wills-Davey and Thompson (1999) claim strong evidence of heating of the bright front material since an increase of temperature in the range of 1 - 1.4 $\times 10^6$ K would create an enhancement in 195 Å emission and a drop in 171 Å emission, as they observe. Gopalswamy and Thompson (2000) report observation of a bright front that appears different in EIT data at 171 Å and 195 Å, suggesting that the difference may be due to the temperature structure of the ejecta. On the other hand, Grechnev *et al.* (2005) comment that "no direct indications of strong temperature dependence for coronal waves have been found so far." Wills-Davey (2006) also study the 13th June 1998 event using automated methods and find evidence for density perturbations. They consider the case where a structure unambiguously observed in two different narrow passbands is assumed to be isothermal. Under this simplifying assumption the emission measure becomes a function of electron density, so brightenings are subscribed to density enhancements.

    In radio data, bright features may be reliably ascribed to density enhancements and not temperature effects because the optically thin thermal free-free (bremstrahlung) emission does not have a very strong temperature dependence (it is proportional to $T^{-0.5}$). Therefore, White and Thompson (2005) conclude (for the S-wave event they studied) that "both the EUV and radio emission arise from a density increase in the low corona." Warmuth *et al.* (2005) note that the comparable brightness increase over the range from 1.5 $\times 10^6$ K (EIT 195 Å) to 4 $\times 10^6$ K (GOES/SXI), implies that the coronal disturbance must be compressive, and not solely due to temperature changes. The six EIT waves in their study all have the diffuse type of bright front.

    This controversy is just a small part of the problem with identifying what a large-scale EIT coronal wave actually *is*. A study is currently being run by *Hinode*/EIS in the hope of capturing spectroscopic information that can be used to derive temperature and density diagnostics so that we can better understand this aspect of EIT coronal waves.

21. **Formation altitude of coronal waves**.
    - Solar limb features make it clear that 195 Å coronal emission features are confined to the first $\sim 0.5 R_\odot$ (350 Mm) above the visible surface, so Thompson *et al.* (1999) surmise that most of the transient increase in 195 Å emission during a coronal wave event must occur relatively close to the surface.
    - TRACE 171 Å data shows that the propagating front affects only the large tenuous overarching coronal loops; lower-lying field structures, such as coronal bright points, are "passed

over". Wills-Davey and Thompson (1999) estimate that the largest unaffected structures are $\sim 40''$ in height, so that the front would have to travel at a minimum propagation height of at least 0.02 $R_\odot$ (15 Mm) above the photosphere, resulting in negligible effects on the sub-coronal layers. (We note that this result is derived from a study of the 13th June 1998 event where we consider that overlying transequatorial loops complicate the interpretation of the data. This cautionary comment is justified in detail in §3.6).
- EIT waves observed at the solar limb can extend up to more than 0.14 $R_\odot$ (100 Mm) (Warmuth *et al.*, 2004a), although they state that "the majority of the emission increase occurs relatively close to the surface".
- Coronal waves are between one and two scale heights in altitude (Wills-Davey *et al.*, 2007). (One scale height is ~ 0.07 $R_\odot$ (50 Mm) at $\sim 1{\times}10^6$K).
- A diffuse coronal wave event, observed on the limb with SXI data showed the bulk of the emission to reside below ~ 0.07 $R_\odot$ (50 Mm), but that it could reach up to ~ 0.14 $R_\odot$ (100 Mm) (Warmuth *et al.*, 2005).
- The centroid of broadband radio emission associated with a diffuse coronal wave was observed to vary between 0 - 0.29 $R_\odot$ (0 - 200 Mm) above the solar limb (Vršnak *et al.*, 2005).

3.3 The relationship between observations from other spectral ranges and EIT coronal waves

As mentioned in chapter 1, due to the somewhat limited cadence of EIT (one full-disk image at 195 Å is made every $\sim$ 12 - 17 minutes), EIT coronal waves are typically only caught in one, maybe two or three frames at most so our current understanding of their physical nature is strongly shaped by related observations made in other spectral ranges that have a higher time cadence. It is natural (and a scientific necessity) to place new discoveries in the context of existing knowledge and experience. Therefore, in order to develop a comprehensive understanding of EIT coronal waves, we must first consider how EIT coronal waves are related to large-scale disturbances observed in other spectral bandpasses.

3.3.1 EIT coronal waves and radio data

90% of type II radio bursts (19 out of 21 events) have an associated coronal wave (Klassen *et al.*, 2000). However, despite this striking correspondence, the velocity of the radio bursts ~ 740 km s^{-1} (Mann *et al.*, 1999) is, on average, three times larger than the coronal wave velocity ~ 271 km s^{-1} (Klassen *et al.*, 1999). Klassen *et al.* (2000) also note that the best pronounced coronal waves are observed if the type II bursts are accompanied by strong type IV emission. Interestingly, given the work of Klassen *et al.* (2000) described above, Biesecker *et al.* (2002) found that only 29% of their sample of 173 EIT waves have associated type II radio bursts. This suggests that far from all EIT waves are associated with coronal shocks, since a shock is required to create a type II burst (§1.6.2.1). However, it is noteworthy that all five S-waves that Biesecker *et al.* (2002) studied had an associated type II burst. Gopalswamy *et al.* (2000) showed an example of an S-wave ("brow wave") that was found to be spatially coincident with a metric type II burst (see Figure 3.3). Gopalswamy and Thompson (2000) conclude that "one may infer that the EIT wave, especially the brow type (S-wave) is a manifestation of the MHD shock wave responsible for the type II burst."

Aurass *et al.* (2002) were the first to report observations of a radio feature that moved in the same direction as a weak EIT wave disturbance on 2nd April 1997, but the radio feature

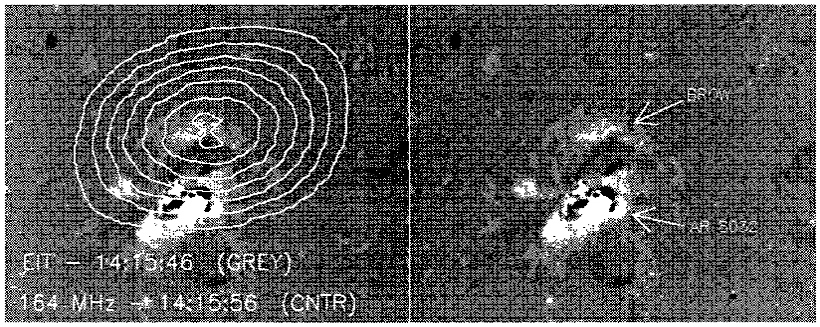

Figure 3.3: Superposition of 164 MHz type II burst contours on an EIT difference image. The EIT "brow" (S-wave) can be clearly seen to the north of AR 8032. Figure from Gopalswamy *et al.* (2000). Permission to reproduce this figure has been granted by the Astronomical Society of the Pacific.

was not directly coincident with the EIT wave. White and Thompson (2005) observed a coronal wave in radio data from the Nobeyama radioheliograph (NRH) at 17 and 34 GHz on 24th September 1997, which was related to an S-wave in EIT data. The same event was also studied by Thompson *et al.* (2000b); Warmuth *et al.* (2004a). The "radio wave" moved at a speed of 835 km s^{-1} and showed no deceleration during the $\sim$ 4 minutes (= 240s) it was observable in radio data. We note that this result is in contradiction to Warmuth *et al.* (2004a) who examined EIT data (including the 24th September 1997 event) and report observing the largest deceleration in the first 200 seconds of a coronal wave event (No. 11). White and Thompson (2005) describe the radio emission from these waves as being "weak and difficult to detect." They note that the radio brightness temperature decreased as the wave propagated during this event. Vršnak *et al.* (2005) report a broadband radio source ("NRH wave") propagating co-laterally with a diffuse EIT wave and an Hα Moreton wave (see next section). They also link these data with type II bursts higher in the corona. They note that the NRH wave emission is considerably weaker than the flare-related type IV bursts and weakened dramatically with increasing time and distance. For the event they studied (3rd November 2003), Vršnak *et al.* (2005) observed a deceleration of the diffuse EIT wave, Hα Moreton wave and the NRH wave. Vršnak *et al.* (2005) interpret the radio emission of this event as optically thin gyrosynchrotron emission excited by the passage of a coronal fast-mode shock.

3.3.2 EIT coronal waves and Moreton waves

The Uchida (1968) model identifies the Moreton wave as the sweeping skirt on the chromosphere of a weak MHD fast-mode shock that propagates in the corona (§1.6.2.2). A crucial point relevant to our current understanding of coronal waves, is that the Uchida (1968) model *predicts the existence of a coronal couterpart of the chromospheric Moreton wave.*

In order to understand what coronal waves are, it is important to understand whether EIT coronal waves and Moreton waves are distinct phenomena or counterparts of the same physical disturbance as predicted by Uchida. This has proved to be a difficult quandary to resolve, but the new high-cadence observations from *Hinode*, STEREO/EUVI and SDO/AIA should further help to tackle this question.

In the literature, Neupert (1989) is cited as reporting the first observation of a moving source of weak EUV emission along the trajectory of an erupting filament, coincident with Moreton wave Hα emission. This observation was interpreted as strong evidence for a coronal

EUV counterpart of the chromospheric Moreton wave. Much more recently, Thompson *et al.* (2000b); Warmuth *et al.* (2001); Pohjolainen *et al.* (2001); Khan and Aurass (2002); Warmuth *et al.* (2004a); Temmer *et al.* (2005); Warmuth *et al.* (2005); Vršnak *et al.* (2005); Veronig *et al.* (2006) all report observations of cospatial SOHO/EIT and Moreton waves. We note that all of these observations (with the exception of one on the 3rd November 2003 Warmuth *et al.*, 2005; Vršnak *et al.*, 2005) show co-spatiality of S-waves and Moreton waves, strongly implying that at least the EIT S-waves are the coronal counterpart to Moreton waves as predicted by Uchida (1968). Warmuth *et al.* (2004a) review 12 coronal wave events with multi-wavelength (Hα, EUV, He I, soft X-ray and 17 GHz radio) data and demonstrate the similarity of coronal waves and Moreton waves by showing that for all eight events where there is EIT data, they both lie on closely associated kinematical curves (their Figure 9). They state that "this supports the hypothesis that Hα and EIT waves are signatures of the same physical disturbance." However, their sample is automatically biased toward fast events, which they acknowledge and describe as "a sub category of flare waves", since they started their search by looking for prominent Moreton wave events and then checked other wavelength data corresponding to Moreton waves. In all eight events where EIT data was available, the early frames show an S-wave whilst the later observations show the diffuse type of EIT wave.

Also supporting a link between coronal waves and Moreton waves, Delannée *et al.* (2007) examine stationary brightenings in EUV and Hα data associated with coronal waves and Moreton waves, showing them to be located at separatrices present in the large-scale magnetic topology. They conclude for an event on 2nd May 1998 that EIT and Moreton waves are "certainly different parts of the same wavelike structure because they are almost cospatial".

On the other hand, Eto *et al.* (2002) and Okamoto *et al.* (2004) study events with diffuse EIT coronal waves and conclude that they are physically distinct from Moreton waves. Eto *et al.* (2002) studied a filament oscillation which they believe could not have been initiated by the EIT wave because it hadn't reached the filament location at the start of the winking. A time-distance extrapolation plot of the Moreton wave (with an approximately constant velocity) indicates that it could have initiated the winking, even though it could no longer be observed at that time. Because the Moreton wave preceeded the EIT wave, they conclude that "the diffuse EIT wave is not the coronal counterpart of the Moreton wave." Eto *et al.* (2002) noted that although the filament started winking before the EIT wave reached its location, there was a drastic change in brightness of the filament in the central Hα image at the same time the EIT wave reached the filament location. So the EIT wave also interacted with the filament, but distinct from the interaction with the Moreton wave. Warmuth *et al.* (2004a) counter this argument, suggesting that the wave may be inclined to the surface, so that the wave progresses further at higher altitudes (since v_A increases with height far from active regions). They suggest that at high altitudes, the EIT wave cannot be observed as such, although it still exists and could match the Moreton wave. Okamoto *et al.* (2004) report a filament oscillation (first down, then up) instigated by a diffuse EIT wave on 10th April 2001. They conclude that the oscillation could not be triggered by a Moreton wave in this event, because no Moreton wave was observed to exist.

3.3.2.1 The so-called "velocity discrepancy" between coronal waves and Moreton waves

If the distinction between S-waves and diffuse EIT waves is not made, then comparison with Moreton waves leads to discrepancies where the average speed of the EUV and Hα waves

and the distances over which they are observed are noteably different. Thompson *et al.* (1999) give a range of 200-600 km s^{-1} for typical EIT wave average velocities. Wills-Davey *et al.* (2007) quote the average range (from Thompson and Myers, 2009) as 25 - 438 km s^{-1}. We emphasise that both estimates include velocities derived dominantly from diffuse, but also from S-wave events. As described, Moreton waves on the other hand have much faster velocities $\sim$ 1000 km s^{-1}. On spatial scales, EIT waves are generally observed to cover a major fraction of the solar disk during their semi-isotropic expansion whereas Moreton waves typically extend over a restricted arc not exceeding 120° and tend to vanish before extending to global distances.

Warmuth *et al.* (2001) have shown that this so-called "velocity discrepancy" can be resolved by showing that both EIT waves and Moreton waves decelerate. Because Moreton waves are observed primarily during their early, strong acceleration phase, and EIT waves (due to the cadence of EIT) are observed later, during a slower-moving phase, higher average velocity measurements for Moreton waves are naturally expected. Recent work by Long *et al.* (2008) using all 4 passbands of STEREO/EUVI data shows that the cadence of observations can have a very strong influence on measured velocities, suggesting that due to the relatively low cadence of EIT's 195 Å filter data, EIT wave velocities may previously have been underestimated.

In summary then, there is good evidence for co-spatiality of Moreton waves with S-type EIT waves. There is not such strong evidence linking Moreton waves with diffuse EIT waves, although Thompson *et al.* (2000b); Warmuth *et al.* (2004a); Warmuth (2007) suggest that since S-wave events also display diffuse bright fronts at a later stage (e.g. Figure 3.2), and because both S-waves and the diffuse bright fronts both exhibit deceleration (Warmuth *et al.*, 2004a), these observations are consistent with the decay of a single perturbation. In this case, both the S-waves and the diffuse bright fronts may be connected with Moreton waves and can be understood as the result of a single driver.

3.3.3 EIT coronal waves and X-ray waves

Bearing in mind the possibilities for confused interpretation(s) (outlined in §1.6.2.3), Khan and Aurass (2002) reported the first observations of a simultaneous SXT and Moreton wave, on 3rd November 1997 at $\sim$ 09:00 UT. They concluded that the "SXT wave is the coronal counterpart of a Moreton wave, analogous to EIT waves." The propagating disturbance observed in SXT data that they report is described as the first confirmed direct observation of a coronal shock wave seen in soft X-rays. Narukage *et al.* (2002) report an on-disk observation of an SXT wave and a Moreton wave also on 3rd November 1997, but at $\sim$ 04:30 UT. They identify the X-ray wave as the coronal counterpart of the Moreton wave, and verify that the "observed properties of the X-ray wave are consistent with the X-ray wave interpreted as a coronal MHD weak shock." They also note that the SXT wave is observed to be "somewhat decelerating." Narukage *et al.* (2004) report observations of an SXT wave on the limb, which propagated into the outer corona, associated with a Moreton wave that propagated on the solar disk. These two waves did not spatially overlap in 2-D, but the two disturbances are shown to be linked if the 3-D dome expansion of a shock wave is considered. In this case, they firmly establish that the SXT X-ray wave is the coronal counterpart of the Moreton wave. The wave is shown to be a fast-mode MHD shock with a magnetosonic Mach number of 1.13 - 1.31, which is consistent with Uchida's expectation of a weak fast-mode MHD shock (Uchida, 1968, see §1.6.2.2). They find the SXT wave in this event to also show deceleration.

Some authors (e.g. Khan and Aurass, 2002; Delannée *et al.*, 2008) take the view that More-

ton waves, EIT coronal waves and SXT coronal waves are all associated and are different manifestations of the same physical disturbance, since they all "show approximately the same behaviour". This has, to our knowledge, been demonstrated so far for only two events, those of 3rd November 1997 at $\sim$ 04:30 UT and $\sim$ 09:00 UT, where in both cases an SXT wave was shown to be closely associated with both a Moreton wave and an EIT S-wave (Narukage *et al.*, 2002; Warmuth *et al.*, 2004a) and (Khan and Aurass, 2002; Warmuth *et al.*, 2004a), respectively. However as mentioned previously, Delannée *et al.* (2000) identify the EIT wave in this same event at $\sim$ 09:00 UT as a loop.

Warmuth *et al.* (2005) show that six "SXI waves" were observed to match their EIT counterparts and to decelerate to comparable mean speeds. Corresponding Hα disturbances were also studied and in three of the six SXI wave events where data was available from SXI, EIT and Hα, the kinematics of the disturbances in all the different wavelengths were found to lie on the same kinematic curves. Following Warmuth *et al.* (2004a), Warmuth *et al.* (2005) interpret this as being "consistent with a single physical disturbance causing the different signatures". Asai *et al.* (2008) find the extrapolated position of the XRT coronal wave (identified as a weak MHD fast-mode shock) to be located $\sim 50''$ ahead of the EIT wave. Future study of this association between Moreton waves, X-ray coronal waves and EIT waves will be important in clarifying our understanding of the physical relationship between these features. Even given the limited number of studies so far, it seems to be strongly established that SXT waves are indeed the coronal counterpart of Moreton waves, as predicted by Uchida (1968). It also seems promising that S-waves and SXT waves are closely related, although exactly how the diffuse SXI and EIT waves fit/do not fit into this understanding requires further clarification.

3.3.4 EIT coronal waves and He I waves

Vršnak *et al.* (2002) interpret EIT S-waves as fast-mode MHD shock waves because in one event, where EIT, He I and Hα data were all available, the disturbances in all three wavelengths were shown to have closely associated kinematic curves. Gilbert *et al.* (2004) also examine chromospheric He I 10830 Å data, as well as coronal Fe XII 195 Å data for two events. They find for both events that the chromospheric (He I) and coronal (Fe XII) waves are cospatial. Gilbert *et al.* (2004) conclude that the He I signatures are chromospheric "imprints" of the MHD waves propagating through the corona. Therefore the He I signatures are not interpreted as waves themselves, but are the track of a compressive disturbance in the corona. If the He I disturbance was also a wave, then it would lag behind the EIT counterpart, rather than being cospatial with it, due to the characteristic speed being much lower in the chromosphere. In this "imprint" interpretation of the formation of the He I signature, the disturbance in the corona does not necessarily have to have steepened into a shock, and there is no inclination of the front at low heights (as required in Vršnak *et al.*, 2002). Instead, the mechanism suggested as being mainly responsible for increased He I absorption is photoionization-recombination, where the coronal radiation ionises the helium. The subsequent recombination serves to populate the lower level of the He I 10830 Å line. Atoms in this metastable state absorb photospheric continuum radiation, producing the He I absorption line. In the work of Gilbert *et al.* (2004) and Gilbert and Holzer (2004), only chromospheric line formation by photoionization-recombination is considered and collisional excitation in the lower transition region is ignored because in the quiet Sun (in the absence of filaments and plage), the He I 10830 Å line is formed almost entirely in the upper chromosphere so the contribution from the lower transition region is negligible.

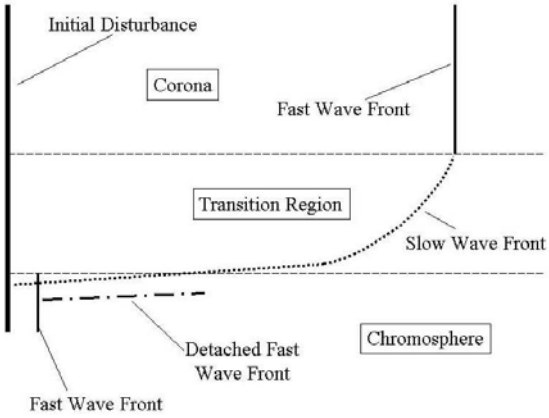

Figure 3.4: Schematic showing how a vertical (magnetic field aligned) initial disturbance (which propagates perpendicularly to the magnetic field lines) extending through the corona, transition region, and chromosphere may evolve. A fast-mode wave front emanating from this disturbance is shown in the schematic (a short time after the initiation of the disturbance) with the following assumptions: a large, constant (with height) fast-mode speed in the corona, a small, constant fast-mode speed in the chromosphere, and a linearly varying fast-mode speed through the transition region. Figure from Gilbert and Holzer (2004). Permission to reproduce this figure has been granted by the American Astronomical Society.

Gilbert and Holzer (2004) re-analyse the same two events as in Gilbert *et al.* (2004), and note the occurence of multiple waves existing in close proximity to each other, propagating away from the same localised flare site. They note the "very diffuse signals of the wave fronts." Velocity data in He I show a bright feature leading a darker feature. The bright (dark) feature indicates a downward (upward) motion of the upper chromosphere. The velocity signature is delayed slightly ($\sim$ 30 seconds) with respect to the intensity signature. Gilbert and Holzer (2004) interpret this as being a consequence of a slow-mode wave compression followed by a slow-mode wave rarefaction. They suggest that a vertical (propagating perpendicular to **B**) coronal fast-mode wave (constant fast-mode speed) refracts in the transition region (linearly varying fast-mode speed), rapidly becoming nearly horizontal (see Figure 3.4). In the chromosphere the wave is once again vertical, but with a much-reduced (constant) fast-mode speed. Because the fast-mode wave in the transition region is nearly horizontal, it will not be able to impact the chromosphere causing a compression, so will not produce a vertical velocity signal. However, the base of the fast-mode wavefront in the corona will be a source of downward-propagating slow-mode waves that impact the chromosphere. Increases in pressure behind the leading fast-mode wave in the corona will generate successive slow-mode compressions propagating down to the chromosphere.

3.4 Discussion and Summary of observational data

We have reviewed observational characteristics of EUV coronal waves and their potential counterparts in radio, Hα, X-ray and He I data. We find that there do indeed appear to be two distinct types of EUV coronal wave; (i) those with a clear chromospheric Moreton wave signature (S-waves) which also have close relationships to transients observed in other spectral ranges (X-ray, He I and 17 GHz radio data, as well as metric type II bursts), and (ii) the diffuse semi-isotropic type. We stress that these coronal transients *appear* to fall into two different morphological categories, and their differing physical nature is strongly suggested by multi-wavelength observations. However this issue will not be fundamentally resolved until high cadence observations can determine the origin and evolution of these two (apparently distinct) phenomena conclusively. From EIT observations, (e.g. Figure 3.2) sometimes the

sharp S-wave is observed in the same event as the diffuse EIT wave bright front. Harra and Sterling (2003) and Zhukov and Auchère (2004) suggest that different physical mechanisms may be responsible for the two different observed morphologies, whilst Thompson *et al.* (2000b), Warmuth *et al.* (2004a,b) and Warmuth (2007) argue that in events where there is a prominent Moreton wave, even the more common diffuse EIT wave can be created by the same physical disturbance. In this case the two types may reflect a strongly driven and then freely propagating stage of one common driver, since the observed deceleration of the waves resolves the "velocity discrepancy" between Moreton waves and coronal waves (§3.3.2.1).

3.5 Models for coronal waves

We now discuss the various existing models for EIT coronal waves. Potential generation mechanisms are also discussed within the context of the various proposed models.

3.5.1 Fast-mode magnetoacoustic MHD wave/shock

Historically, and until very recently, by far the most successful model for describing the observed characteristics of EIT coronal waves was as a fast-mode MHD wave/shock (Dere *et al.*, 1997; Thompson *et al.*, 1998, 2000b; Wills-Davey and Thompson, 1999; Wang, 2000; Klassen *et al.*, 2000; Gopalswamy and Thompson, 2000; Wu *et al.*, 2001; Ofman and Thompson, 2002; Vršnak *et al.*, 2002; Warmuth *et al.*, 2004b; Gilbert and Holzer, 2004; Ballai *et al.*, 2005; Warmuth *et al.*, 2005; Vršnak *et al.*, 2005; Veronig *et al.*, 2006).

The theory of fast-mode magnetoacoustic MHD waves and shocks was discussed in Chapter 1 (§1.3.7.3).

3.5.1.1 Confronting theory with observations

A recent summary of the main observational signatures that lend themselves to interpretation within the fast-mode framework is given by Warmuth (2007). We supplement this summary with examples from observations. We also highlight the difficulties associated with the fast-mode wave/shock interpretation of EIT waves.

Two key properties of fast-mode waves is that they travel at speeds $\geq v_A$ and can move in a direction perpendicular to the magnetic field. It is clear that EIT waves expand across the quiet Sun and the mean velocity of this expansion ($\sim$ 250 km s^{-1}) is comparable to estimates of v_A in the quiet Sun low corona (200-600 km s^{-1}, e.g. Narukage *et al.*, 2002). Although compressional Alfvén waves also propagate perpendicular to the magnetic field, they cannot produce the necessary compression to be seen as an intensity enhancement in EUV data (Wills-Davey *et al.*, 2007). Some EUV coronal waves are observed to have speeds of $\sim$ 1000 km s^{-1} (Thompson *et al.*, 2000b), so to be explained within the fast-mode context, they must initially be considered as shocked fast-mode waves. Since the minimum fast-mode speed is constrained by the Alfvén speed, any EIT wave must travel faster than v_A for a fast-mode MHD solution to be valid. Clearly this is not the case for many EIT waves (Vršnak, 2005; Wills-Davey *et al.*, 2007, No. 1), although EIT wave velocities may have been underestimated due to the low image cadence of EIT (Long *et al.*, 2008). (We note that Uchida *et al.* (2001) alternatively suggested that an EIT wave may be a trapped MHD wave with a long wavelength, whose horizontal group velocity is much less than the fast-mode speed. This interpretation may perhaps explain the lower velocities, but work concerning this interpretation has not been pursued, so we do not mention it further here.)

Observations of deceleration, broadening and weakening of the bright front with time are consistent with interpretation as the decay of a shock formed from a large-amplitude simple MHD wave. An example from radio data supporting these properties is that the radio brightness temperature decreased as the wave propagated during the S-wave event studied by White and Thompson (2005). The decrease in radio brightness temperature may be interpreted as the decreasing amplitude of a disturbance (Warmuth *et al.*, 2001, 2004a) which is consistent with a shock wave scenario, where the trailing edge of the shock wave has a small amplitude and so moves with a linear fast-mode speed whereas the leading edge propagates super-magnetosonically. This leads to a broadening of the wave's profile. The broadening leads to a drop in the perturbation amplitude, slowing down the disturbance and so the shock decays to a linear wave at fast-mode speed. However White and Thompson (2005) actually interpret this amplitude decrease as *opposing* a shock scenario. They argue that the amount of material swept up and compressed by a shock would *increase* with time, producing increasing radio emission, whereas they observe decreasing radio emission. It is conceiveable that the disturbance was initially a shock that then decelerated into a fast-mode wave, but the White and Thompson (2005) radio event is observed during the first 200 seconds of its lifetime when it should presumeably still be forming into a shock. Indeed, Vršnak *et al.* (2002) note that the location of the sharp bright waves (EIT, Hα, X-ray and He I) always being remote from the source active region is consistent with a simple MHD wave needing time to steepen into a shock. However, Gilbert and Holzer (2004) highlight that there is currently no direct observational evidence that waves at the base of the corona have steepened into shocks, because it is currently impossible to evaluate the characteristic parameters for a coronal shock because the magnetic geometry remains unknown.

Additional arguments in favour of interpretation of EIT waves as fast-mode waves concern their velocity, since the velocity at which fast-mode waves propagate is determined by the properties of the ambient medium. At large distances, EIT waves are observed to decelerate to comparable mean velocities, as calculated from two different samples of events, yielding mean velocities of 311 ± 84 km s^{-1} (derived from EIT data; Warmuth *et al.*, 2004a) and 320 ± 120 km s^{-1} (from six "SXI wave" events; Warmuth *et al.*, 2005). The agreement in velocity from separate samples implies that in the late phase of the event, the velocity is not determined by the perturbation of the individual event, but rather "reflects the characteristic speed of the ambient medium" (Warmuth *et al.*, 2005). If this is the case and the ambient medium is responsible for the velocity of the EIT waves, as expected in the fast-mode interpretation, then it becomes very difficult to explain the dramatically different velocities of seven EIT waves observed from 1st - 3rd May 1998, which over just a 36 hour period showed mean speeds ranging from 85 - 435 km s^{-1}. The waves all travelled through the same region of ambient quiet Sun. We note that the speed of the coronal waves (Thompson and Myers, 2009) varies somewhat erratically, neither systematically increasing or decreasing for successive events. As Wills-Davey *et al.* (2007) assert: "explaining each of these wave fronts as fast-modes would require that the quiet Sun fast-mode speed change globally on time-scales shorter than a few hours. Since EIT waves are strongly associated with CMEs, it may be that CMEs corresponding to EIT waves produce large-scale topology changes which then affect the global fast-mode speed. However, the lack of global changes shown by difference images suggests that this is unlikely".

Warmuth (2007) additionally note that in observations in the various spectral ranges, the wavefront is often described as an enhancement of existing structures. This is consistent with activation by a passing wave disturbance, affecting a large area simultaneously. Regarding the morphology of EIT waves, Warmuth *et al.* (2004a) argue that "the retention of a basic

circular curvature over large distances is a strong indication of the wave-like nature of the disturbances." We will return to this point in chapter 4, showing that in the light of our work, the observation of a semi-isotropic coronal wave shape can actually be argued as support for a non-wave interpretation.

3.5.1.2 Results from numerical simulations

Veronig *et al.* (2006) consider that observations of EIT waves avoiding active regions (No. 8), stopping at the boundaries of coronal holes and at separatrices (No. 17) have been successsfully reproduced in numerical simulations by treating EIT waves as fast-mode MHD waves. It was shown by Uchida (1974); Ofman and Thompson (2002) that when a fast magnetoacoustic wave encounters an active region it undergoes strong reflection and refraction and does not traverse the active region. The stopping of the wave at the boundary of a coronal hole was numerically simulated by Wang (2000) and Wu *et al.* (2001). As the wave approaches the region of high magnetosonic speed it is refracted away and the wave propagation is halted. Due to the plasma β being relatively low in the coronal hole region compared to the source region, the plasma mass motion is constrained by the magnetic field at the coronal hole (Wu *et al.*, 2001) and the plasma literally piles up when the wave encounters the coronal hole boundary. (In the work presented in chapters 4 and 5 we provide evidence for alternative explanations of brightenings observed at coronal hole boundaries). On stationary brightenings, Warmuth (2007) note that an MHD wave or shock is actually capable of triggering a localised energy release when it crosses pre-existing coronal structures. This energy release would cause localised heating and a stationary emission enhancement, as successfully simulated in the work of Ofman and Thompson (2002). Although stationary/persistent bright fronts found at coronal hole and active region boundaries are successfully reproduced in fast-mode models, they are also found in the quiet Sun (which fast-mode models cannot explain), and at separatrices and QSLs identified in the pre-existing large-scale magnetic topology (Delannée and Aulanier, 1999; Delannée *et al.*, 2007). Considering that in a quiet Sun environment coronal waves expand semi-isotropically, the observation of patches of stationary brightening in this relatively uniform ambient medium is a difficulty that even the localised heating argument described above struggles to explain, since energy releases should surely occur throughout the passage of the coronal wave, all over the quiet Sun and not just in discrete patches.

Coronal waves are also observed to deflect magnetic features (No. 3). This property has been successfully reproduced in simulations by (Ofman and Thompson, 2002), where the coronal wave is modelled as a fast-mode MHD wave.

With regard to the formation altitude of coronal waves, Mann *et al.* (1999); Klassen *et al.* (2000) assume a formation and propagation height of $0.08R_{\odot}$ above the photosphere. The simulations of Wang (2000) initiate the wave at a height of 35,000 km ($0.05\ R_{\odot}$). Comparison with observations concerning the altitude of coronal waves (No. 21) shows that these assumptions are consistent with observations.

Recent simulations by Pomoell *et al.* (2008) show that an erupting flux rope is surrounded by a shock front, which is strongest near the leading edge of the erupting mass, but also shows compression near to the solar surface. For rapidly accelerating filaments, the shock front in the simulation is observed to form in the low corona. Although the speed of the driver is less than the Alfvén speed near the top of the atmosphere, the shock is observed to survive in this region as well, but as a freely propagating wave. Perhaps the results of these simulations seem to be somewhat at odds with observations, since Biesecker *et al.* (2002) find only a "very weak correlation" between CME speed and observation of an EIT wave (No.

13). Although on the other hand, Cliver *et al.* (2005) report a "definite trend for EIT wave association to decrease with decreasing CME speed" (No. 14).

Finally, the velocity of EIT waves modelled as fast-mode waves in simulations is apparently independent of the speed or magnitude of the associated initiating impulse (Ofman and Thompson, 2002), so that the velocity is dependent on the medium through which the disturbance propagates. As discussed, this is a property expected for fast-mode waves.

An additional issue with regard to numerical simulations of EIT coronal waves is the theoretical assumptions of a large β corona. E.g. Wu *et al.* (2001) use a plasma β much larger than unity, which they deduce from the measured photospheric magnetic field strength. In their simulations, as a result of the large plasma β, the "magnetic field is not stiff and is easily moved around to generate detection of the EIT waves." They consider that EIT waves are "MHD fast waves propagating on a global scale in a large plasma β medium which is dominated by the acoustic mode." Assumptions of a large plasma β tend to be considered grossly unrealistic for a description of the quiet Sun corona.

3.5.1.3 Additional difficulties with the fast-mode interpretation

Despite interpretation as fast-mode waves/shocks being really very successful at explaining some of the properties of EIT coronal waves, we have identified observations that the fast-mode interpretation fails to explain adequately, if at all. The work presented in chapter 4 adds to these challenges for the fast-mode wave interpretation, but here we discuss some existing inconsistencies.

Coronal Dimming: The fast-mode wave theory does not naturally produce coronal dimming, so often observed in association with coronal wave events (No. 16). It has been suggested that an alternative interpretation may be that the dimmings are rarefied regions that manifest behind the waves (as in Wu *et al.*, 2001), since a rarefaction shock develops at the trailing part of a large-amplitude perturbation (Landau and Lifshitz, 1987). However, Cliver *et al.* (2005); Delannée *et al.* (2007) discount this because dimmings formed by such a mechanism would be short-lived, with a duration on Alfvén timescales, contrary to observations (No. 16). Therefore White and Thompson (2005) argue that coronal dimmings are unexplained in MHD wave models, because the coronal material is compressed in place and is not transported by the wave. On the other hand, Warmuth (2007) point out that the launch of a CME and a fast-mode wave are not mutually exclusive. The launch of a CME would naturally explain the dimming, as a result of the significant expansion.

Kinematic argument: Plots showing that disturbances in the different wavelengths (i.e. Hα, He I, soft X-rays, EUV - both S-waves and diffuse waves) all lie on the same kinematic curve are often interpreted as evidence that a single physical disturbance is responsible for causing the different signatures (Vršnak *et al.*, 2002; Warmuth *et al.*, 2004a,b, 2005; Vršnak *et al.*, 2005; Veronig *et al.*, 2006). Where this is restricted to S-waves, which have been shown to have a strong co-spatial and morphological association with Moreton waves, He I waves and soft X-ray waves, this is a reasonable argument (e.g. three instances in Warmuth *et al.* (2004a,b) and Veronig *et al.* (2006)). However, we do not find the extension of this argument to diffuse EIT waves (eight events in Warmuth *et al.* (2004a,b), Vršnak *et al.* (2002); Warmuth *et al.* (2005); Vršnak *et al.* (2005)) sufficient or acceptable "evidence" that a single physical disturbance is at work. We qualify and explain our objection as follows:

Firstly, Warmuth (2007) consider the excellent timing association between metric type IIs and Moreton waves with the impulsive flare phase (e.g. Klassen *et al.*, 1999; Khan and Aurass, 2002, respectively) to be "ambiguous" results since the CME impulsive acceleration phase is

often synchronised with the impulsive energy release of the associated flare (e.g. Zhang *et al.*, 2001). Secondly, with regard to the early-stage evolution of CMEs, Warmuth (2007) note that the flanks of a CME remain fixed during much of the later phase of eruption, which implies they have had to decelerate between launch of the CME and the later phase of the eruption. They also state that "the kinematical behaviour of CME flanks is presently not well understood." Warmuth (2007) also acknowledge "it is possible that more than one process is working in a single event". Combining these points, we assert that although Moreton waves, X-ray waves, S-waves and diffuse EIT waves can be shown to lie on the same kinematic curve, this is *not* enough to validate that they are necessarily generated by the same physical disturbance.

Similar kinematics in different EUV bandpasses: Long *et al.* (2008) reported STEREO/EUVI observations showing a diffuse coronal wave to have similar kinematics in all four EUVI passbands (No. 19). Specifically, they showed that the bright front moves with a similar speed and acceleration in all four passbands (304, 171, 195 and 284 Å). This result is difficult to interpret within a fast-mode wave context, because the characteristic speed of the wave changes with the density of the ambient medium. A fast-mode wave in a denser region would be expected to lag behind its counterpart in a more rarefied region, not be co-spatial with it.

Although the 304 Å passband is dominated by He II with a peak temperature of 8.0×10^4K, providing observations of the chromspheric network, Long *et al.* (2008) note that this passband also contains a strong contribution from Si XI at 303.32 Å with a peak formation temperature of $\sim1.6\times10^6$K. Therefore 304 Å emission may also contain a coronal component, so care must be taken when interpreting narrow bandpass observations. Further multi-wavelength results on coronal waves are likely to provide clarification on this issue.

3.5.1.4 Are coronal waves flare-initiated or CME-driven?

If EIT coronal waves are really MHD fast-mode waves (as indeed seems to be the case for S-waves), then what causes these waves? Both flares and other large-scale ejecta are capable of creating large-scale, large-amplitude MHD perturbations which can sweep through the corona. Warmuth (2007) emphasise that small-scale ejecta (e.g. in the form of flare sprays, X-ray jets and erupting loops) may also be the root cause of coronal waves and shocks. In the classic blast-wave scenario (Steinolfson *et al.*, 1978), a flare produces an initial pressure pulse which works as a temporary piston (Vršnak and Lulić, 2000a), creating a large-amplitude disturbance in the ambient plasma, which then propagates freely through the corona as a fast-mode wave. This perturbation can steepen to become a fast-mode shock (e.g Vršnak and Lulić, 2000a,b).

In the CME-driven mechanism (Cliver *et al.*, 1999), the wave is continuously supplied with energy. Two different types of situation can occur with this mechanism. If ambient plasma cannot flow into the region behind the CME as it expands, then the mechanism is described as a piston-driven shock. (The speed of the driving piston does not necessarily have to exceed c_s or v_A to form a shock (Vršnak and Lulić, 2000a)). In this case the shock wave (formed at the leading edge of the perturbation) moves faster than the driving piston so that the distance between the driver and the shock increases. Alternatively, if the plasma can flow past the driver, then both the driver and shock propagate at the same speed. This situation is called a bow shock and in this case, the driver has to be super-magnetosonic and super-Alfvénic in order to drive the shock. Vršnak (2005) suggest that in the initial phase, the CME may piston-drive a shock, which later becomes a bow shock. If the energy driving the shock is exhausted, then the shock may continue in a freely propagating manner, as in the case of a

blast-wave.

When EIT waves were first observed, Dere *et al.* (1997); Thompson *et al.* (1999) suggested that they could be the coronal counterpart of the chromospheric flare-induced Moreton fast-mode shock wave (Moreton, 1960; Moreton and Ramsey, 1960), that had been predicted by Uchida (1968) (§1.6.2.2). However, Plunkett *et al.* (1998) considered that EIT waves are actually strongly associated with CMEs. More recently, statistical studies (Biesecker *et al.*, 2002; Cliver *et al.*, 2005) have confirmed this initial suggestion, showing EIT waves to be more closely associated with CMEs than with flares (Nos. 4 & 5). Okamoto *et al.* (2004) searched for coronal waves associated with flares larger than GOES M-class. For 358 flare events they found only 33 EIT waves. Moses *et al.* (1997) report for the first five observed EIT wave events that "the magnitude of the wave shows little correlation with the peak thermal X-ray flux of the associated event ... the majority of EIT observations close to flare events do not show any evidence of these waves." Chen (2006) studied 14 energetic flare events that were not associated with CMEs. None of these events was associated with an EIT wave and Chen concluded that it is therefore unlikely that pressure pulses from flares are responsible for generating EIT waves. Recently, Veronig *et al.* (2008) studied a diffuse coronal wave observed by STEREO/EUVI and concluded that it is driven by the CME expanding flanks, and that the associated flare occurs too late to initiate the disturbance. Delannée *et al.* (2007) point out that CMEs will naturally lead to strong perturbations of the corona, so it is natural to expect them to result in large-amplitude fast-mode magnetoacoustic waves. In support of the CME-driven mechanism, Thompson *et al.* (2000b) consider that "the gradual formation of the dark depleted region could represent an expanding drive of the bright front, with the dimming region (CME) causing the bright front to form." Tripathi and Raouafi (2007) recently analysed a diffuse EIT wave and CME shock that propagated in the same direction. They measure the EIT wave bright front speed to be just 55 km s^{-1}, whilst finding the leading edge of the CME to move at 860 km s^{-1}. They state that this provides "strong evidence in favor of the interpretation that the EIT waves are indeed a counterpart of the CME-driven shock wave in the lower corona." Tripathi and Raouafi (2007) consider that the difference in speed may be due to the different plasma densities in the low corona and at heights of 2-3$R_{\odot}$.

Despite the strong statistical link with CMEs, and the very weak relation to flares (Nos. 4 & 5), Vršnak *et al.* (2002) conclude that the perturbation in each case for events they studied was most likely ignited by the flare. Warmuth *et al.* (2004a,b) assert that the fastest coronal waves are consistent with Uchida's weak fast-mode shocks, describable as blast-waves caused by flares. Mann *et al.* (1999) assume the coronal wave is excited by the flare and consider the disturbance to be a fast magnetosonic wave. Warmuth *et al.* (2004b) argue that (Nos. 2, 10, 11) the "signs of decay and attenuation displayed by coronal waves are features typical for freely propagating shock waves" (such as those generated by a blast-wave), "in contrast to shocks directly driven by a piston which provides a permanent energy supply". Hudson and Warmuth (2004) consider the association of TRACE observed oscillations with type II bursts (12 out of 28 events in their sample) as indicative of a "striking affinity" with flare blast-waves over CME-driven waves. They note that a flare-induced blast-wave may not necessarily steepen to a shock, therefore explaining why only 12 out of 28 events are associated with type II bursts. However, they find that the timing of some events does not support the blast-wave hypothesis and further, that 24 out of 28 oscillation events are associated with CMEs, so they conceed that the CME flow may in fact be the exciter. Vršnak and Lulić (2000b) discuss that a variety of conditions for shock wave formation are necessary and this may explain why only a small fraction of flares are associated with type II bursts.

Warmuth *et al.* (2004a,b) and Cliver *et al.* (2005) (favouring flare- and CME-driven, respectively) argue for a unified view embracing many of the different types of large-scale solar disturbances including Moreton, EIT, He I, soft X-ray waves and type II radio bursts. It is difficult to distinguish between a flare-initiated or a CME-driven shock because (as Gilbert and Holzer, 2004, highlight) in both cases a pressure pulse is at work and in both cases the end result can well be a freely propagating wave, making an unambiguous determination of the underlying physics very difficult. However, a potentially discriminating factor is identified by Gilbert and Holzer (2004) who note that CME-driven waves should have a much wider area of origin (beginning in a region with finite angular extent just beyond the boundaries of the deep dimmings observed in EIT data), whilst flare-initiated waves should essentially originate from a point-source. Indeed, Thompson *et al.* (1999) originally suggested that diffuse EIT waves may have started not from the flare site, but from the boundary of the deep coronal dimming region. In addition, Delannée *et al.* (2007) point out that EIT waves are "neither full circles, nor continuous all the way around the flare site", considering these observations an argument against the temporary pressure pulse understanding. Because many events involve both flares and CMEs, in reality, both flare- and CME-driven waves may occur together, associated with the same event. Close examination of multiple velocity wave fronts associated with a He I observation leads Gilbert and Holzer (2004) to conclude that the first two (diffuse) fronts are CME-driven, whilst the following three wave fronts (more clearly defined) are initiated by the flare. In this case, both flare-initiated and CME-driven waves are shown to exist in the same event and are not mutually exclusive.

3.5.2 Slow mode magnetoacoustic MHD wave

Given the large range of coronal wave velocities (No. 1), many coronal waves expand at speeds $< v_A$. This observation means that they may be understood in the context of slow-mode magnetoacoustic waves (Krasnoselskikh and Podladchikova, 2007). Although the slow-mode MHD wave does not propagate perpendicular to the magnetic field, initial work has pointed out that propagation of the slow-mode wave is possible if it moves at an *oblique* angle to the magnetic field.

3.5.3 Solitary waves

An alternative explanation recently suggested by Wills-Davey *et al.* (2007), is to understand EIT waves as solitary waves or "solitons". Solitary waves are so-called because they occur as a single entity which is localised (Drazin and Johnson, 1989) and which do not superpose (hence "solitary"). Solitary waves are therefore different to normal linear (plane) MHD waves. Dispersive and non-linear mediums are expected to alter the shape of any wave over time, however, the inherent non-linear steepening of the wave can, under *very exact and specific* conditions compensate for the dispersion, leading to a propagating, slowly decaying but stable wave that has an essentially constant velocity and shape (Ballai *et al.*, 2003).

A solitary wave was observed on the Edinburgh-Glasgow canal in 1834 by J. Scott Russell. After a canal boat stopped abruptly, he observed the mass of water that had been moving with the boat roll forward and "assume the form of a large solitary elevation, a rounded, smooth and well-defined heap of water, which continued its course along the channel apparently without change of form or diminution of speed." (Russell, 1844). Russell re-created laboratory experiments of solitary waves and deduced that the speed of the solitary wave, v_{sol}, is given by:

$$v_{sol}^2 = g(h + a) \tag{3.1}$$

where a is the amplitude of the wave, h is the undisturbed depth of the water and g the acceleration due to gravity. An important consequence of this equation is that solitary waves with a larger amplitude travel faster.

A strict definition of solitary waves (Drazin and Johnson, 1989) means that they must be: (i) of permanent, coherent form (so the pulse's shape doesn't change over time); (ii) localised within a region; and (iii) they can interact with other solitary waves, and emerge from the collision unchanged, except for a phase shift. Moses *et al.* (1997) describe the propagation of the wavefronts for five EIT coronal wave events as "initially propagating radially" and then they "begin to break up and travel in separate fronts." This may be interpreted as an observation against pulse coherence, however, sometimes the term soliton is used for phenomena that do not quite have these three properties. E.g. the waves may lose energy during interaction, but still be termed solitons.

In linear MHD, the wave velocity is determined solely by the properties of the ambient medium. For solitary waves the wave speed is additionally dependent on the pulse amplitude (a function of density enhancement; Wills-Davey *et al.*, 2007, also see Equation 3.1). Wills-Davey *et al.* (2007) show that (as a general trend), the most well-defined coronal waves are more density enhanced and travel faster. A soliton-like wave model therefore naturally accounts for observations of a range of velocities (No. 1), because velocity scales with pulse amplitude and the waves are not constrained to move only at speeds $\geq v_A$ (Wills-Davey *et al.*, 2007). Further work by Wills-Davey (2003) has shown that coronal waves are highly non-linear, with density perturbations of 40 - 100% above the local background level. In addition, Ballai *et al.* (2005) show for the 13th June 1998 event that there is a constant wavelet power spectrum - a signal that does not degrade, so the wave packet remains intact. These findings may be interpreted as features of solitary waves.

3.5.4 Large-scale magnetic restructuring

It has also been suggested that EIT coronal waves are not real waves at all. Rather, rearrangement of the magnetic structure during eruption of a CME may cause electric currents and pressure increases, observed as brightenings (Delannée and Aulanier, 1999; Delannée, 2000). Indeed, Hudson and Warmuth (2004) consider that the slower coronal waves are probably understandable as "motions of the medium itself during CME evolution (perpendicular flows), rather than as a simple wave propagating in a fixed corona."

3.5.4.1 EUV brightening due to compression

Propagating coronal "waves" could be a signature of gradual "opening" of the magnetic field during CMEs (Delannée and Aulanier, 1999). Wen *et al.* (2006) note that the general process of coronal restructuring takes place at a speed slower than either the Alfvén or acoustic speed in the corona. They use the term "topology waves" to describe successive topology changes (occuring at speeds 300-400 km s^{-1}) where the magnetic field changes from a closed to an "open" configuration. Delannée and Aulanier (1999) considered the large-scale, pre-CME magnetic topology and successfully showed that some stationary EIT brightenings were cospatial with the footpoints of separatrix surfaces, leading to the conjecture that the fast expansion of the magnetic field should compress the plasma at the boundaries between expanding stable flux domains, naturally leading to the enhanced emission seen in coronal

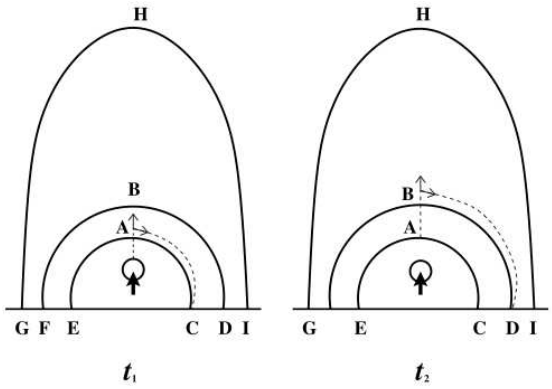

Figure 3.5: Schematic diagram illustrating how the opening-related perturbation induced by the erupting flux rope is transferred from the top to the footpoint of each field line so that EIT "wave" fronts are formed successively, from point C to point D at two different times. Figure from Chen *et al.* (2005b). Permission to reproduce this figure has been granted by the American Astronomical Society.

EUV lines. In this scenario, a front might be observed to propagate as the magnetic field "opens" up further and further from the CME launch site. This mechanism would also successfully produce closely related coronal dimming (No. 16).

In this vein, Chen *et al.* (2002) created a numerical model where the erupting filament and expanding magnetic field compress the plasma in the legs of the CME producing the bright EIT wave front (see Figure 3.5). One of the wave-like features in their model (as suggested by Delannée and Aulanier, 1999) is therefore not a wave in the physical sense and naturally produces dimming as a result of stretching the overlying magnetic field. The legs of the CME piston-driven shock create a second wave-like disturbance that they identify as a Moreton wave. The Chen *et al.* (2002) model requires a giant 2-D overlying arcade. We point out that it may be difficult to explain the semi-isotropic nature of diffuse coronal waves with this model.

Chen *et al.* (2005b) added two small active regions either side of the erupting arcade and showed that the density enhancement (identified as the EIT "wave") stopped at the boundary of the active region, so successfully reproducing the stationary bright fronts that occur at large-scale separatrices in some events (No. 17). Chen *et al.* (2005a) simulated SXT, EIT and Hα data, concluding that the SXT waves and Moreton waves can indeed be understood in terms of a fast-mode shock wave, whilst reinforcing the identification that the density feature corresponds to the EIT "wave". Wills-Davey *et al.* (2007) note that the work of Chen *et al.* (2002); Warmuth *et al.* (2001); Chen *et al.* (2005a,b) concentrate on the relationship between Moreton waves and coronal waves. However, most observations of EIT waves are "EIT wave only", with Moreton wave observations being associated with only a minority of events (Wills-Davey and Thompson, 1999). In explanation of this, Warmuth (2007) consider that in most coronal wave events the perturbation is very weak, so may be incapable of producing shocks and therefore no type II bursts or Moreton wave signatures are generated. Warmuth *et al.* (2004a) note that the simulation of Chen *et al.* (2002) shows the EIT wave to decelerate more strongly than the Moreton wave, a characteristic that Warmuth *et al.* (2004a) do not observe in the 12 events that they study.

In the work of Delannée and Aulanier (1999); Delannée (2000); Chen *et al.* (2002, 2005a,b), stationary bright fronts (a distinctly non-wave feature) are readily understood as being associated with separatrices identifiable in the large-scale pre-eruptive magnetic field configuration. Indeed, Delannée and Aulanier (1999) and Delannée (2000) show brightenings and dimmings

that appear to be confined to long loops connecting the flaring region with distant active regions. This is contrary to what is expected for the propagation of a fast-mode wave (Wang, 2000).

3.5.4.2 EUV brightening due to electric currents

More recently, Delannée *et al.* (2007) proposed a topological model for stationary parts of EIT and Moreton waves. They show that the stationary brightenings in Hα and EIT data are located at regions where there are drastic jumps of connectivity (separatrices, QSLs). They suggest that the "succession of stationary brightenings must result from the formation and dissipation of current sheets, progressively generated in large-scale QSL, as the magnetic flux expands above the flare site and pushes up the overlying trans-equatorial magnetic field lines". The "opening" magnetic field during the course of the CME initiates a perturbation which creates quasi-spontaneous current sheets in separatrices, leading to joule heating. They therefore extend previous work (Delannée and Aulanier, 1999; Delannée, 2000) to suggest that "the association of EIT waves with separatrices is still possible in the context of joule heating rather than plasma compression".

Delannée *et al.* (2007) also consider an explanation for the diffuse moving arches of EIT and Moreton waves as consequences of the restructuring of the coronal magnetic field during a CME. "The diffuse moving arch could be due to generation of electric current in the moving layers formed at the place where rapidly expanding magnetic fields encounter surrounding not yet expanded magnetic field. Magnetic field lines originating from a magnetic polarity connect all surrounding magnetic field, almost forming a circle. As the eruption takes place in a narrow portion of the arch ... it would propagate away from the flare site as the magnetic field lines are opening." This is perhaps reminiscent of Balasubramaniam *et al.* (2005)'s narrowly channelled "sequential chromospheric brightenings" that originate near the flare site, and then propagate along the path of erupting trans-equatorial (TEQ) loops. The moving bright fronts might also be produced by sheared expanding magnetic field interacting with the surrouding nearly potential magnetic field (Delannée, 2000). The interaction is envisaged to create local electric currents, heating and therefore an increased emission in EUV constituting the bright fronts.

Taking a multi-wavelength view, Delannée *et al.* (2008) describe a model for the propagation of EIT waves, Moreton waves and SXT waves. They show that "large-scale, narrow and intense current sheets form at the beginning of the dynamic phase within the initially extended and weak return currents that naturally separate the twisted flux tube from the surrounding potential fields." They find that a current shell is co-spatial with an enhanced density shell, generated by plasma compression (see Figure 3.6).

The Delannée *et al.* (2008) model requires line-of-sight integration over the altitude of the current shell to produce bright fronts, as observed in on-disk coronal wave events. However, we point out that this model fails to explain limb coronal wave events, because in such cases the requirement for line-of-sight integration over the altitude of the current shell is not met. The Delannée *et al.* (2008) current shell model initially shows an increasing velocity of the bright front, tending toward a constant velocity. This appears to be in contrast to the Warmuth *et al.* (2004a) finding from observations that coronal waves decelerate as they expand (No. 11). An additional striking difference between the Delannée *et al.* (2008) model and observations of EIT waves is that their model specifically considers that "the EIT and SXT waves are coronal structures (i.e. they evolve at quite high altitude)" and that "the dissipation of the current densities at low altitude would not be responsible for the

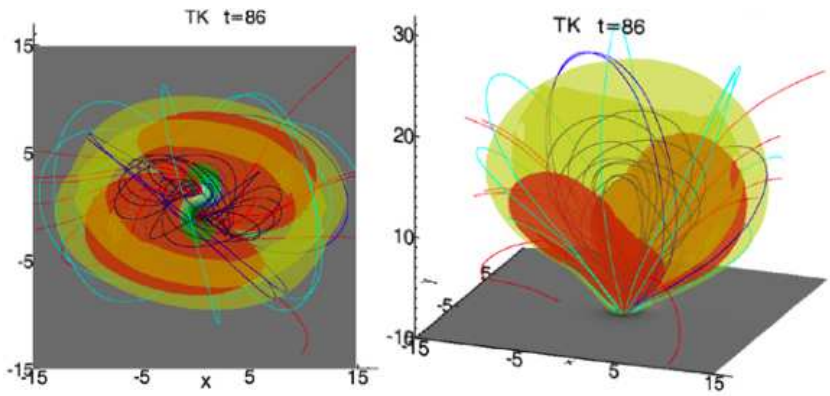

Figure 3.6: Expanding flux tube using the 3-D MHD model described in Török and Kliem (2003). Left panel shows the numerical domain as viewed from above, and in projection (right panel). Transparent isosurfaces of $\mathbf{J} \cdot \mathbf{B} / B^2$ = -1.9, 0.5 and 1.9 are drawn in red, yellow and green, respectively. These isosurfaces show the formation of the current shell surrounding the expanding flux tube. Figure from Delannée *et al.* (2008). Permission to reproduce this figure has been granted by Springer Science and Business Media.

observed structure". In their model, integration is made over all altitudes when considering the formation of the coronal wave bright fronts. Their results show that very early in the coronal wave formation (05:07 UT for the 12th May 1997 event), the top of the current and enhanced density shells have already reached heights of 2.6 $R_\odot$ (1800 Mm). They interpret this as "support for the idea that EIT waves are not low-altitude phenomena, but rather high altitude 3-D structures projected onto the solar disk". In contrast, observations show that coronal waves are generated in the low corona, and not at high altitudes (No. 21).

3.6 The controversy: So what *is* a coronal wave?

TRACE observations of the 13th June 1998 event

In this section, we endeavour to show why it is possible for so many different models to exist. We use the much-studied 13th June 1998 event, captured in TRACE data as an example. We emphasise that this event should be noted as a *non-classical* coronal wave event. Indeed, this is acknowledged by Wills-Davey (2006): "The [13th June 1998] TRACE observation ... does not fit the definition of a typical EIT wave". Despite such a statement, this event is often assumed to be representative of coronal waves in general (e.g. Ofman and Thompson, 2002). This event has been studied, with the aim of gaining information on coronal waves from high-cadence, high-resolution data. Studies include work by Wills-Davey and Thompson (1999); Delannée (2000); Harra and Sterling (2003); Wills-Davey (2006) and Ballai *et al.* (2005). These studies focus mainly on the relatively small TRACE field of view although EIT data is also analysed by Delannée (2000) and Harra and Sterling (2003). Here, we emphasise the global context of the event, as also discussed by Wills-Davey and Thompson (1999).

In classical diffuse EIT wave events (e.g. 12th May 1997, 7th April 1997) large-scale coronal loop structures do not tend to be present because the Sun is mainly free of other active regions, so there is only surrounding quiet Sun magnetic field. The 13th June 1998 event is quite different however, there are many active regions located on opposite sides of the solar equator (Figure 3.8). Base difference movies of the TRACE (*tracebd13june98.mpg*, Appendix E) and EIT (*eitbd13june98.mpg*) data (see Appendix E) show that the coronal wave bright front seems to split, moving part to the northwest and part to the northeast. Static images of this behaviour are shown in Figure 3.7. This behaviour is attributed to the presence of

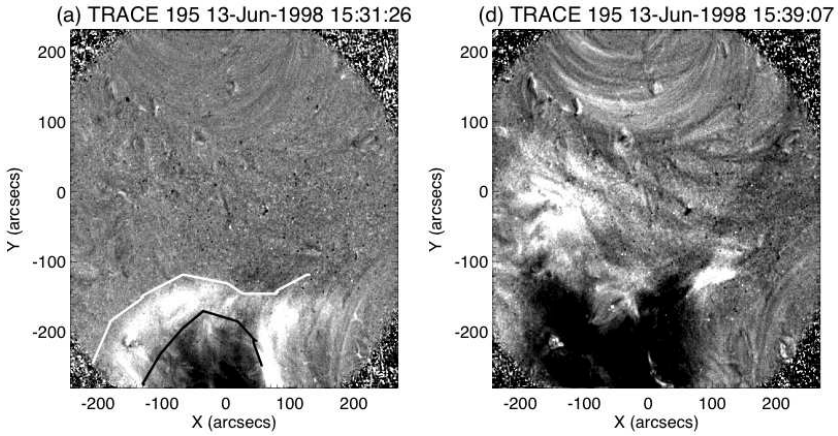

Figure 3.7: TRACE difference images showing the progression of the coronal wave front and associated dimming. The bright front initially a quite coherent wavefront-like structure, soon splits with the brightest concentrations directed along transequatorial loops (see Figure 3.8). Figures taken from Harra and Sterling (2003). Permission to reproduce this figure has been granted by the American Astronomical Society.

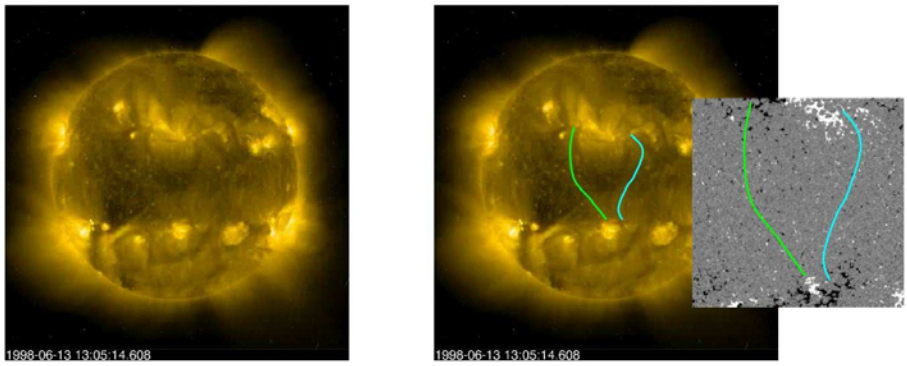

Figure 3.8: Connectivity of the EIT 284 Å TEQ loops is sketched on the MDI inset. The green line connects the positive polarity of the southern hemisphere source active region to the negative polarity of a northern hemisphere active region. The turquoise loop connects the southern negative polarity to a northern positive polarity.

two trans-equatorial (TEQ) loop structures, which act to channel (c.f. "contain" Wills-Davey and Thompson, 1999) the disturbance. Delannée (2000) observe that the dimming associated with the event is situated within the TEQ loops. These TEQ loop structures are seen as faint bright features in the EIT 195 Å movie (*eit13june98.mpg*), connecting the southern active region (NOAA 8237) to two northern ones (NOAA 8238 and 8239). Figure 3.8 shows EIT 284 Å data, in which the TEQ loops can also be identified. The connectivity of the TEQ loops is sketched on the MDI inset, zoomed-in to be slightly larger than the TRACE field of view which focuses only on the region dominated by the TEQ coronal loops. (Figure 4 in Delannée (2000) shows an EIT 195 Å image showing the TEQ loops directly overlaid with the MDI contours).

An important observation is that these TEQ loop structures are disturbed by the coronal wave event, but they are not fully destabilised (because they can be identified after the event as well). Wills-Davey and Thompson (1999) also comment on the longevity of the associated TEQ loops, noting that they display residual motion for about an hour after they are initially disturbed.

The analysis of this event by Harra and Sterling (2003) used SOHO/CDS and EIT as well as TRACE data. The CDS field of view was located in the quiet Sun region, straddling the

solar equator between the active regions seen in the TRACE field of view (see their Figure 1). Harra and Sterling (2003) observe that the coronal wave consists of two aspects - a bright wave and a weak wave. They observe that the "most well-defined portion of the coronal wave avoids the CDS field of view region" with "bright elements moving off to either side ... [but that] weaker parts of the wave do traverse that [quiet Sun] region". Harra and Sterling (2003) specify that it is the subtle, weak wave (not the bright wave) that interacts with a set of loops at the northern end of the TRACE field of view. The interaction causes these loops to oscillate.

Interpolation of points along the bright front visible in the TRACE base difference images allows the disturbance to be mapped (see Figure 3, Wills-Davey and Thompson, 1999). Wills-Davey and Thompson (1999) made a visual identification of the bright fronts. The automated mapping analysis by Wills-Davey (2006) succeeds (to first order) in describing the motion of the bright wave to the northeast (see Figure 4, Wills-Davey, 2006), but fails to track the disturbance to the northwest because the data in that region suffers from noise limitations. Due presumably to the same limitations, the weak wave of Harra and Sterling (2003) is not identified at all. The automated analysis reveals that along a given trajectory, a wave front appears to maintain (or regain) coherence. This behaviour is observed even when the wave passes across multiple loop structures. In such a case, several peaks are observed to form and often the wave will re-emerge as a single front. Wills-Davey (2006) interpret the "bright wave" and "weak wave" of Harra and Sterling (2003) as being due to the widening of the single pulse.

The analysis that the TRACE-observed part of *this* event is consistent with interpretation as waves with a well defined period (Ballai *et al.*, 2005) is cited as support for the true wave-like nature of EIT waves. The analysis by Harra and Sterling (2003) identifying two types of wave-like phenomenon is cited as support for the Chen *et al.* (2002) model. The analysis of Wills-Davey and Thompson (1999) supports arguments for the fast-mode magnetoacoustic wave theory, whereas the automatic detection method developed by Wills-Davey (2006) highlights features that may be understood by interpretation as a solitary wave (Wills-Davey *et al.*, 2007).

Given this ambiguity, great care must be taken when interpreting coronal waves and caution exercised when extending conclusions derived from analysis of such special events to global coronal waves in general. To quote Warmuth *et al.* (2005): "the fact that probably a considerable fraction of coronal transients are not really waves at all poses a problem for their use as tools for deriving ambient coronal parameters, which require the disturbances to be MHD waves." (e.g. Mann *et al.* (1999); Ballai and Erdélyi (2004); Ballai *et al.* (2005); Warmuth *et al.* (2005); Warmuth and Mann (2005)).

In summary, the high cadence and spatial resolution of TRACE allow detailed observations of how EIT waves interact with surrounding magnetic structures. However, it should be noted that this 13th June 1998 event is a *special case*, because TRACE observed dominant bright fronts formed within the domain of TEQ coronal loops, and only a very weak bright front formed in the quiet Sun (Harra and Sterling, 2003) as in "classical" coronal wave events. This cursory examination shows that the global context of a coronal wave event is crucial for a full understanding of the observations.

3.7 Summary of chapter

Despite much work, it is clear that a satisfactory understanding of EIT coronal waves continues to elude researchers. The critical problem is one of interpretation. There are many different (and specialised) observations of coronal waves, each with different instrumental limitations and selection effects. This results in an array of dramatically different suggested theoretical models (§3.5), each of which find support in observational evidence.

In this chapter, we reviewed the many different EUV observations of EIT coronal waves and their potential counterparts in radio, Hα, soft X-rays and He II wavelengths. We consider that there are two different types of coronal wave: S-waves and diffuse bright fronts. We have also discussed the various models currently proposed to explain coronal waves. We conclude that there is good evidence to identify the EIT S-waves as the coronal counterpart of a chromospheric fast-mode wave/shock. However, by far the majority of EIT waves are of the diffuse type and we have shown that there are difficulties and inconsistencies with the evidence for understanding these as true waves.

We have demonstrated that a careful analysis of the global context of an event is crucial to developing our understanding of coronal waves. It is this global context and the enigmatic diffuse EIT coronal waves that we focus on in our work presented in the following chapter.

Chapter 4

Coronal "Wave" - Magnetic Footprint of a CME?

In this chapter, we focus on the diffuse EIT coronal wavefronts and their associated dimmings. Of particular interest is the new analysis of the 12th May 1997 EIT wave by Podladchikova and Berghmans (2005a), showing that the wave displays a rotation as it propagates. Here we describe our work and show how it can place strong constraints on our current understanding of coronal waves.

4.1 Two on-disk coronal wave events

We study two events that possess the "classical", semi-isotropic diffuse bright front: the extensively studied event on 12th May 1997 (Thompson *et al.*, 1998; Podladchikova and Berghmans, 2005a) and the event on 7th April 1997 (Thompson *et al.*, 1999). Both events are associated with partial filament eruptions, flares and front-side halo CMEs.

We note that neither of these events exhibit a coronal wave counterpart detectable in *Yohkoh*/SXT data. Warmuth *et al.* (2004a) use EIT data to measure the expansion of the diffuse bright fronts of both events in three successive frames and find decelerations of -62 ms^{-2} and -242 ms^{-2} for the May and April events, respectively. Warmuth *et al.* (2004b) conclude that "consequently also the underlying physical disturbance must be decelerating."

The May event occurs in the northern hemisphere from AR 8038, which exhibits a pre-eruption reverse "S" sigmoidal structure, often cited as an indicator of left-handed twist (negative helicity) (Leamon *et al.*, 2002). The April event is associated with AR 8027, located in the southern hemisphere, where a pre-eruption forward "S" (positive helicity) sigmoidal structure is visible. Figure 4.1 shows the sigmoids for the two events visible in EIT images.

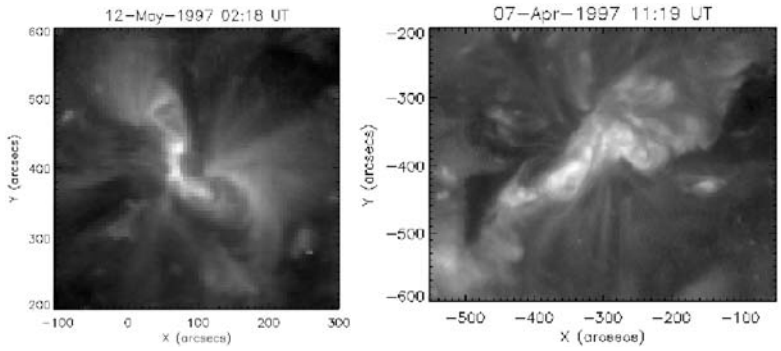

Figure 4.1: EIT 195 Å images showing the pre-eruption sigmoidal structures in the source regions of the 12th May 1997 and 7th April 1997 eruptions (left and right panels, respectively).

4.1.1 EUV Observations and Data Analysis

The coronal wave of each event is captured in two successive EIT 195 Å base difference images (Figure 4.2). We use running difference images to identify short-term transient features, but base difference images (corrected for solar rotation) to analyse intensity since running difference images can show false brightenings and dimmings (e.g. Chertok and Grechnev, 2005). The base images are at 04:50 UT for 12th May and 14:00 UT for 7th April.

4.1.1.1 Intensity analysis of the coronal wave bright fronts

After Podladchikova and Berghmans (2005a), we analyse the intensity of the coronal wavefront as a function of azimuthal angle around the wavefront. We assume an isotropic, circular expansion around an epi-centre. We account for line-of-sight (LOS) projection effects (e.g. Deforest, 2004). As a result, a circular EIT wave is observed as an ellipse in projection. The ellipse characteristics are defined by the initial location of the eruption (in particular θ, the angle at the centre of the solar sphere, between the observer's LOS and the initial epi-centre of the eruption on the solar surface; see Appendix A, Figure A.1) and by the angular radius, δ, of the EIT wave (the half-cone angle subtended at the centre of the solar sphere).

We sum the intensity, I, of the ring defined by the black ellipses shown in Figure 4.2. By changing δ and systematically shifting the centre of the ellipse about the initial epi-centre (taken as the location of the associated flare: 12th May, Thompson *et al.* (1998); 7th April, Aurass *et al.* (2002)), we objectively find the best values for the centre (so the ellipticity and the axis) and δ of the ellipse which capture most of the coronal wave intensity. The width of the ring (distance from the inner to the outer ellipse) is set at 100″. This width allows selection of a significant proportion of the bright front, whilst avoiding the deep dimmings during the earlier frames for each event (see Figure 4.2).

For the 12th May 1997 event, the location of the associated flare was N23, W07 (Thompson *et al.*, 1998). We use this location (106″, 417″) as an initial epi-centre for plotting the ellipses. Ellipses with a range of δ are plotted which will cover the spatial extent of the coronal waves shown in Figure 4.2. For the 05:07 UT bright front, an angular radius range of between 20° and 45° is explored. For the 05:24 UT bright front, the appropriate δ range is 30° - 55°. For the 7th April 1997 event, the flare location was S30, E20 (Aurass *et al.*, 2002). So (-300″, -420″) is used as an

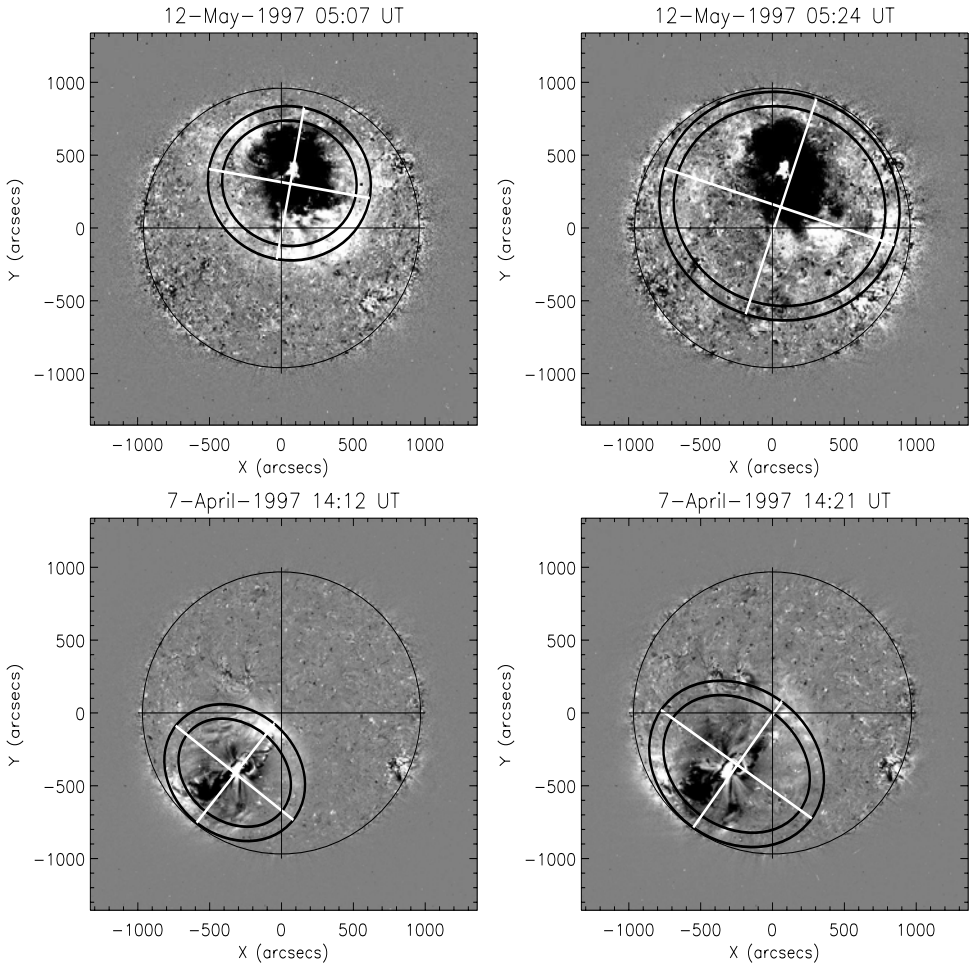

Figure 4.2: Successive base difference images for 12th May 1997 (top) and 7th April 1997 (bottom) coronal wave events. The bright fronts are overlaid with concentric *black ellipses*. Permission to reproduce this figure has been granted by the American Astronomical Society.

Table 4.1: Angular radius, δ and central co-ordinates of the ellipse that return the maximum average intensity of the coronal wave bright front.

Event and Time	Best δ	Best centre x-coordinate	Best centre y-coordinate
12th May 1997 05:07 UT	28°	56 ± 2″	307 ± 2″
12th May 1997 05:24 UT	48°	50 ± 2″	150 ± 2″
7th April 1997 14:12 UT	25°	-326 ± 2″	-410 ± 2″
7th April 1997 14:21 UT	33°	-250 ± 2″	-350 ± 2″

initial epi-centre. For the coronal wave at 14:12 UT, the δ range is 20-45°. For the bright front at 14:21 UT, the δ range is 25-50°.

We also need to determine a centre for each ellipse, since the coronal wave has expanded (and therefore the ellipse centre has shifted) since the time of the flare. For the first image of each event (05:07 UT, 12th May and 14:12 UT, 7th April) we set a range of ± 100″ in both the x and y directions in steps of 20″ that are searched as possible best centres for the ellipse. For the second image (05:24 UT, 12th May and 14:21 UT, 7th April), the range is extended to explore ± 300 ″ since the coronal wave has expanded more by this time.

For each delta, the centre of the ellipse is shifted throughout the range of locations described. For each centre, the ellipse axis are calculated, with projection effects taken into account (see Appendix B), and two ellipses are generated, separated by a width of 100″. The values of the pixels that fall within the ring defined by the two ellipses are selected and for each degree interval around the ellipse, in the radial direction (from the inner to the outer ellipse) are averaged. The averaged intensity is then summed to give an intensity for the entire ellipse. This process is repeated for each value of the angular radius δ, and for each location of the centre. The resulting data cube is then queried to find the combination of δ and centre co-ordinates that give the maximum mean intensity.

The process is then repeated, this time using the selected δ and using the determined co-ordinates as the initial epi-centre of the ellipse. For the selected δ, the ellipse centre co-ordinates are shifted over a range of ± 10″, in steps of 2″. In this way we refine the best centre of the ellipse that gives the maximum intensity for the selected δ.

The determined δ and central co-ordinates for each ellipse are given in Table 4.1.

The rings defined by the black ellipses (overlaid on the bright fronts) in Figure 4.2 are not concentric. The projection effect implies that as the EIT wave progresses (as δ increases), the centre of the projected coronal wave moves toward the disk centre. Thus a shift of the coronal wave centre is expected in the projected images, and its distance from the disk centre is given by: $R_\odot \sin\theta \cos\delta$ (see Appendix A).

Taking δ from the fitted black ellipses and measuring the distance from the disk centre to the centre of the ellipse, we compute θ for each of the ellipses. We compare this fitted θ with the θ defined by the location of the flare. The two θs correspond relatively well, with the exception of 05:24 UT on 12th May where they differ by 10°. We attribute this difference to the distorting effect of the north polar coronal hole (discussed in chapter 5 and Attrill *et al.*, 2006), altering the centre of the ellipse and the ellipticity. The 7th April event encounters no such distortion and the two θs agree to ± 2°. Thus it is a reasonable assumption that the de-projected EIT waves are concentric circles, approximately centered on the flare location. Also trying to establish an understanding

of the origin of this EIT wave, Thompson *et al.* (1999) used a linear fit to the projected speed of the bright front and found it to intercept the flare location 10 minutes before the EIT wave appeared. They concluded that either the coronal wave decelerated sharply or that the expanding bright fronts were initiated at locations outside the flaring region.

Since the projection of the wave changes as it propagates over the solar disk, using the projected azimuthal angle can give a distorted impression of the expansion. To avoid this, we plot the intensity as a function of the de-projected azimuthal angle (in the plane perpendicular to the local vertical at the epi-centre of the wave, i.e. the azimuthal angle around the real circle; see Appendix B for a full explanation of how this angle is calculated). We use the axes of the ellipse as a reference for the azimuthal angle. The tilt of the minor axis from the main solar axes is defined solely by the epi-centre of the coronal wave on the disk and therefore remains constant throughout the expansion of each event, as does the ellipticity ($= \cos\theta$).

Since the diffuse brightenings are subtle features and are highly susceptible to noise, the data is averaged in the azimuthal direction, using boxcar smoothing with a smoothing kernel of 11°.

The mean intensity of the ring is then plotted as a function of the de-projected azimuthal angle for the two sucessive images where the coronal wave is visible (Figure 4.3). The vertical lines mark the weighted mean for each peak. The lower panels show the weighted mean of the intensity of the later coronal wavefront peak(s) phase-shifted to match those of the earlier coronal wavefront peak(s). The weighted mean of the 12th May 05:24 UT intensity peak is phase-shifted by 44° anti-clockwise to match the weighted mean of the 05:07 UT peak. For the 7th April event, the weighted means of the 14:21 UT intensity peaks are phase-shifted by 22° clockwise to match the weighted means of the 14:12 UT peaks.

The IDL routine `c_correlate` was used to test for a correlation between the earlier and later datasets for each event. The test was run over three repetitions of the data (so from 0° to 1080°) for the 12th May 1997 event. The repetition constrains the programme, especially with respect to the start (0°) and end (360°) of each dataset, so that the best fit is determined. This is important because there is a significant decrease in amplitude between the main peak for the 12th May event. This is most likely due to the 17 minutes between successive images for this event. For the 7th April 1997 event, the data are only 9 minutes apart, and running `c_correlate` over just one dataset (from 0° to 359°) is sufficient. The results are presented in Figure 4.4.

Cross-correlating the mean intensity of the ring for the successive images confirms that there is a phase-shift between the earlier and later datasets for each event. For the 12th May 1997 event the maximum correlation coefficient occurs at a phase-shift of 319° clockwise. We note that this phase-shift can also be interpreted as a rotation of 41° in an anti-clockwise sense. For the 7th April 1997 event, the maximum correlation coefficient occurs where there is a phase-shift of 19° clockwise.

We present our interpretation of these phase shifts in Section 4.1.2.1.

4.1.1.2 Radial features of the coronal waves

Intensity profiles (Figure 4.5) made in a radial direction from the centre of the disturbance reveal the diffuse brightening to be consistently concentrated in two places; at the outermost edge of the

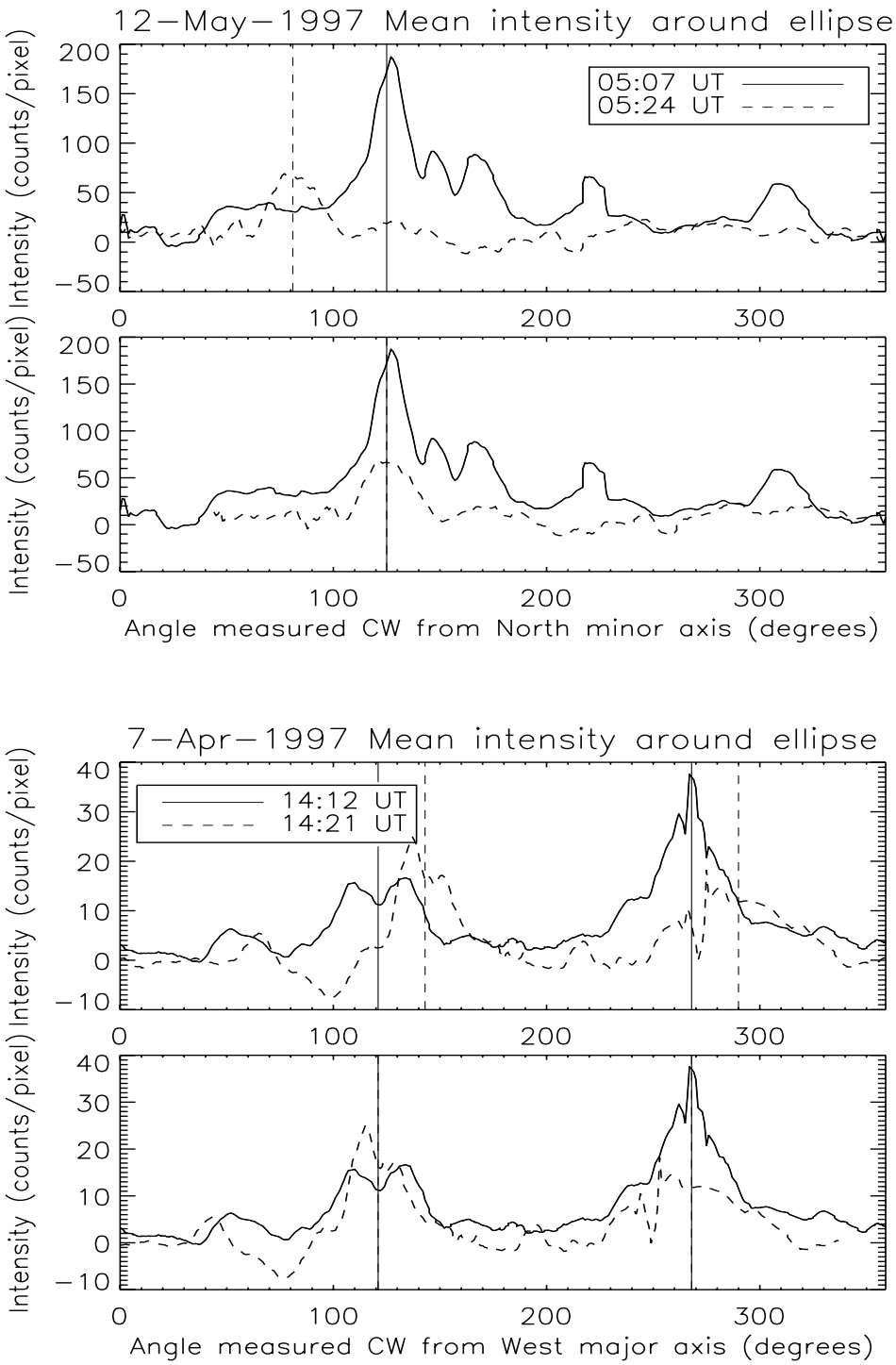

Figure 4.3: Mean intensity of the ring defined by the black ellipses shown in Figure 4.2 as a function of the de-projected azimuthal angle. Top and bottom panels show data from the 12th May 1997 and 7th April 1997 events respectively. The vertical lines mark the weighted mean for each peak. The bottom plot of each panel shows the weighted mean of the later peak(s) phase-shifted to match those of the earlier peak(s). Permission to reproduce this figure has been granted by the American Astronomical Society.

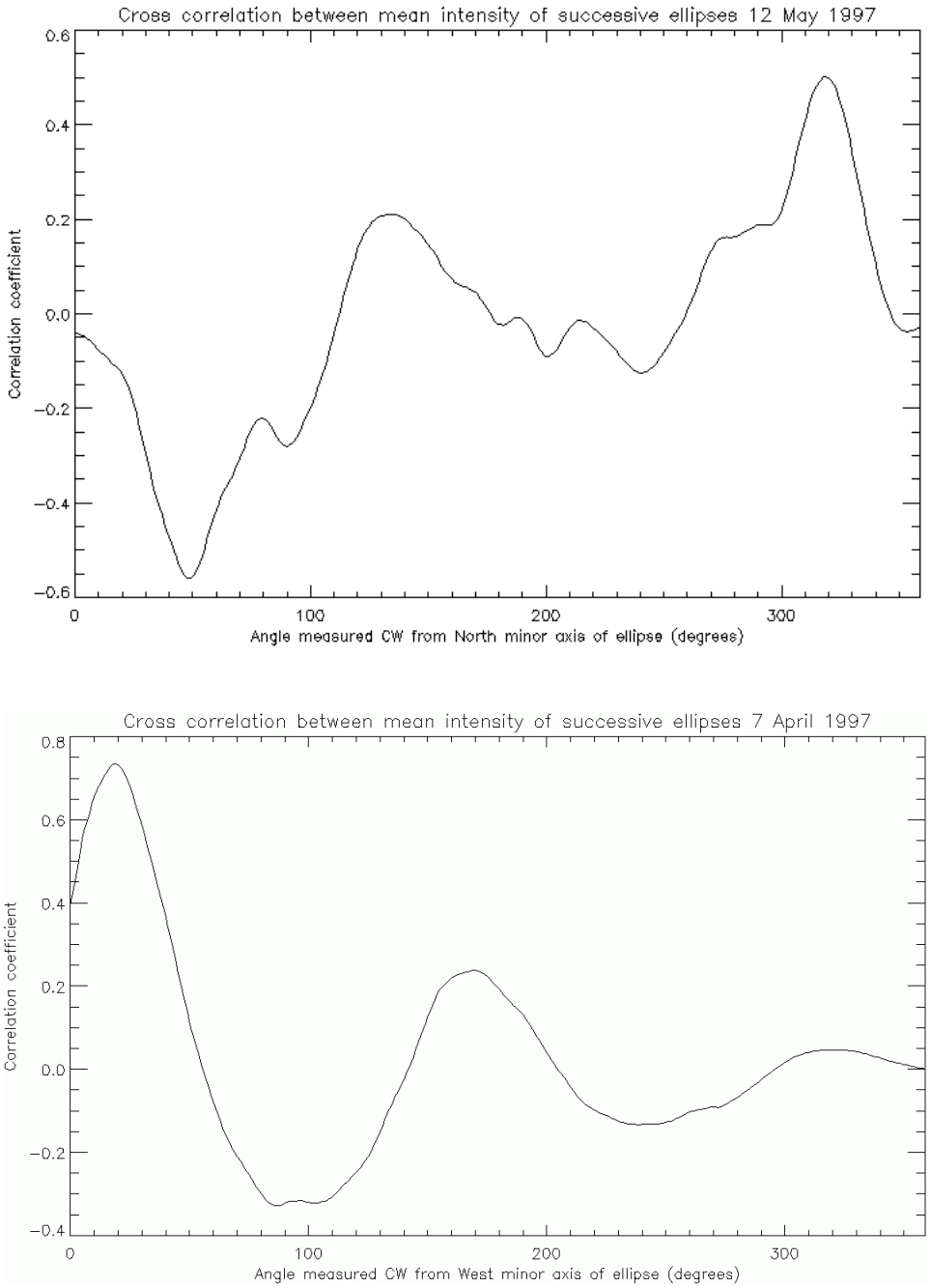

Figure 4.4: Cross-correlation of the coronal wave bright front mean intensity plotted in Figure 4.3. The correlation test is made for the mean intensity around the ring for the two successive images for each event. (Top): 05:07 UT and 05:24 UT for 12th May 1997; (Bottom): 14:12 UT and 14:21 UT for 7th April 1997.

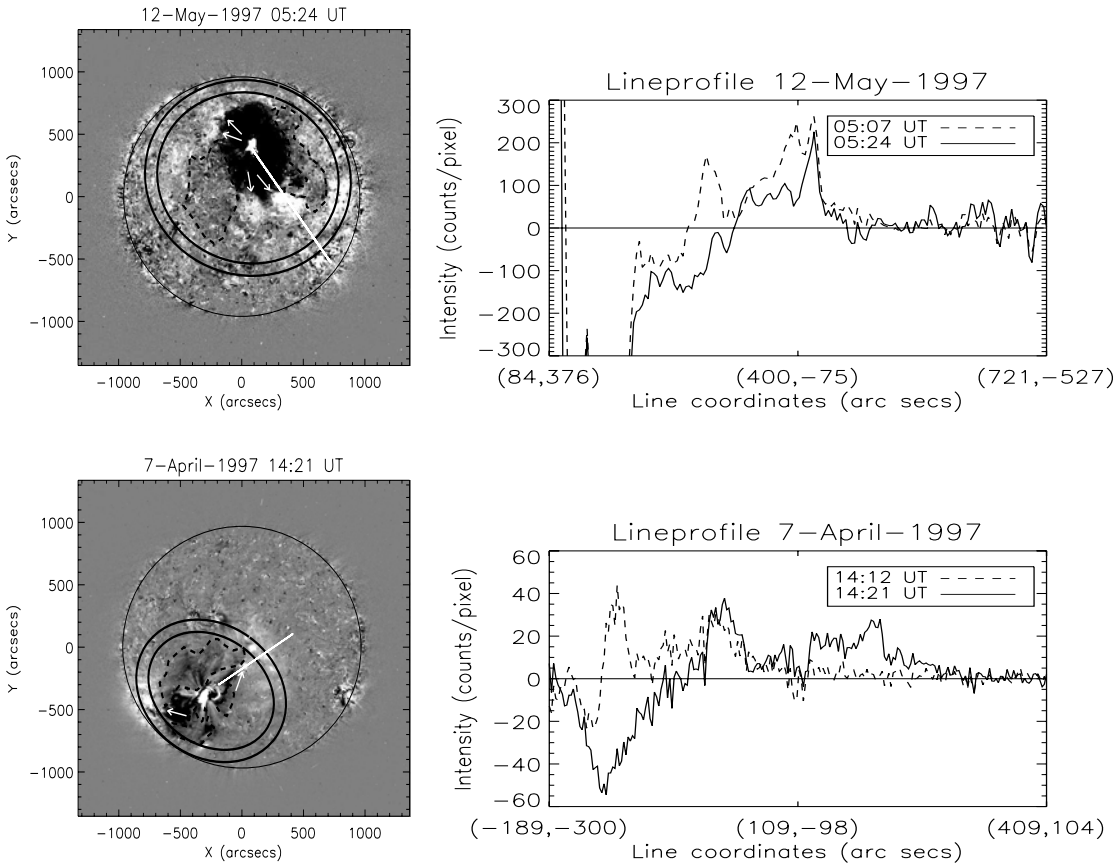

Figure 4.5: Left panels show the later base difference image for the 12th May 1997 (top) and 7th April 1997 (bottom) events, with the fitted black ellipses (Figure 4.2) marking the location of the expanded coronal wavefront. Concentrations of intensity are located at the edge of the deep core dimming regions (indicated by white arrows) and simultaneously at the leading edge of the coronal wave in both cases. The black dashed lines enclose regions of widespread diffuse dimming. The right panels show intensity profiles made along the straight white lines in the left panels. The dashed (solid) lines show the intensity profiles from the earlier (later) base difference heliograms. Permission to reproduce this figure has been granted by the American Astronomical Society.

deep dimming regions and simultaneously at the leading edge of the expanding wavefront. The brightenings show an increase in intensity by a factor eight (12th May 1997) and factor six (7th April 1997) of the respective quiet Sun intensities.

The base difference images in Figure 4.5 also show widespread diffuse shallow dimmings associated with each event (regions bounded by black dashed lines) and persistent brightenings are marked by white arrows at the edge of the deep dimmings. In contrast to the deep, core dimmings seen in the intensity profiles of Figure 4.5 that remain close to the post-eruptive arcade (also see Zarro *et al.*, 1999; Attrill *et al.*, 2006), the diffuse dimmings are weak and extend to large distances from the core dimmings. They rapidly propagate across the solar disk, behind the expanding bright front.

In the literature, we have noted (No. 16) that some authors (e.g. Zhukov and Auchère, 2004; Warmuth *et al.*, 2004a; Grechnev *et al.*, 2005) consider that there is a discrepancy in coupling the evolution of coronal waves and dimmings because in some events it appears that the bright front expands to larger distances than the dimming. The 12th May 1997 event has been cited as a case in point illustrating this.

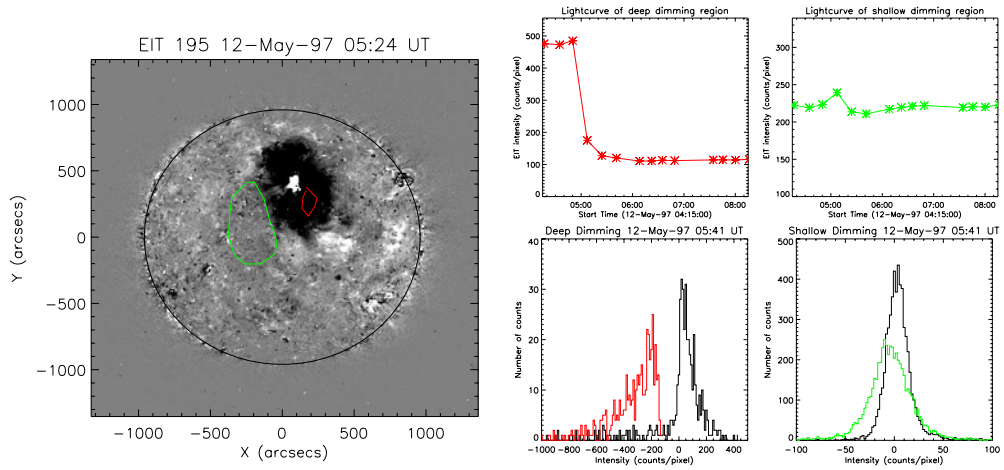

Figure 4.6: Left panel: SOHO/EIT base difference image on 12th May 1997 with deep (red) and shallow (green) dimmings identified. Upper right panels: Red (green) lightcurves showing intensity evolution of the deep (shallow) dimming regions identified in the left panel. Lower right panels: Black histograms show distribution of intensity of the selected region before the coronal wave occurs. Red (green) histograms show distribution of intensity during dimming of red (green) region identified in the left panel. Permission to reproduce these figures has been granted by the Astronomical Society of the Pacific.

An analysis of the dimmings of the 12th May 1997 (Figure 4.6) illustrates the differences between the deep, core and shallow, extended dimmings that manifest during the coronal wave event. Lightcurves of the selected regions show how the intensity changes during the event and histograms show the distribution of the intensity in the selected regions at the time of the image shown in the left panel of Figure 4.6. The core dimming (red) on the 12th May 1997 shows a large drop in intensity of 77%. Histograms showing the distribution of the pixel intensities within the selected regions are made from base difference images at 04:50 UT (black) and 05:41 UT (red, green), where the base image is at 04:35 UT. The distributions of intensity just prior to the coronal wave at 04:50 UT (black) and after the passage of the coronal wave bright front at 05:41 UT (red) show clearly separated peaks, with a shift of the dimmed (red) distribution to lower values. This is clearly consistent with the manifestation of a strong dimming, as observed. The shallow dimming (green) shows a much more subtle drop in intensity of just 5%. The distribution associated with this shallow dimming is difficult to resolve from the pre-eruption, 04:50 UT (black) distribution, since there is a significant overlap between the two distributions. However the shallow dimming (green) distribution at 05:41 UT shows that the right wing remains close to that of the pre- (black) dimming distribution, whilst the left-wing is clearly shifted to lower values, consistent with a drop in intensity. So although the shallow (green) dimming is subtle, it is a real physical feature and cannot simply be dismissed as noise because the distribution is asymmetric (non-Gaussian). We note that the 04:50 UT (black) histogram for the deep dimming shows a number of strongly negative pixels. This is due to the pre-coronal wave base difference image at 04:50 UT already showing a pre-event strong dimming inside part of the red contour. Since this analysis is focused on understanding the nature of the shallow (green) dimming, the best conditions are chosen for analysis of the green region. The cost of this is that there is some strong dimming already present in the pre-event red region, which gives the negative pixels in the black histogram.

It is well established that core deep dimming regions associated with CMEs show blueshifted velocities (e.g. Harra and Sterling, 2001; Harra *et al.*, 2007b). In several cases, it has been demonstrated that these deep core dimmings likely correspond to footpoint(s) of the erupted flux rope (Webb *et al.*, 2000; Mandrini *et al.*, 2005; Attrill *et al.*, 2006). Figures 4.6 and 4.5 show that subtle, shallow widespread dimmings also exist during coronal wave events and we expect that

these widespread dimmings observed with many coronal wave events and identified as matching the lateral extent of CMEs (e.g. Thompson *et al.*, 2000a; Attrill *et al.*, 2007b) may also be due to plasma outflows. Measurements of blue-Doppler shifted plasma outflow from such regions (e.g. with *Hinode*/EIS) would confirm or discredit this expectation.

4.1.2 Interpretation

4.1.2.1 Phase shift of intensity as a function of azimuthal angle

Figure 4.3 shows a phase shift between successive images of the mean intensity as a function of the de-projected azimuthal angle for each event. For the 12th May 1997 event, phase-shifting the weighted mean of the intensity peak at 05:24 UT to match the weighted mean of the intensity peak at 05:07 UT requires a shift of 44° anti-clockwise. We therefore independently confirm the result obtained by Podladchikova and Berghmans (2005a). The method of determining the phase-shift by matching the weighted means of the intensity peaks compares favourably with the phase-shift determined using cross-correlation, where a shift of 319° clockwise (which may also be interpreted as a phase-shift of 41° anti-clockwise) was determined (end of §4.1.1.1). For the 7th April event, the phase shift required to match the weighted means of the intensity peaks between the data at 14:12 UT and 14:21 UT is 22° clockwise. We emphasise that the same shift is required for both peaks of the 7th April 1997 event. The phase-shift derived from the cross-correlation was 19° clockwise. So the phase-shifts determined using both the weighted mean and cross-correlations are in agreement to ± 3°.

Podladchikova and Berghmans (2005a) discuss possible reasons for the rotation of the 12th May 1997 EIT wave. They consider that the transfer of a curved magnetic configuration (as evidenced by the pre-event sigmoid) to a state with minimum potential energy after reconnection will diminish the curvature of field lines (see their Figure 15). In this case, the EIT wave can be created due to an area of high density on the border of such a region because of the pressure balance, as in Delannée's model (§3.5.4.1). Thompson *et al.* (1999) reported the change in direction of the bright front in the April event, noting that "it is unlikely that the wave front was propagating eastward...and then abruptly turned northward." The change in direction of the bright fronts for the April event is also noted by Podladchikova and Berghmans (2005b) who suggest this may be due to reflection by two small active regions which subsequently microflare and dim.

Our interpretation of the rotation of the bright fronts follows. In the April event, we find (Figure 4.3) that the two bright fronts *both* rotate by 22°. We consider it unlikely that the bright fronts were reflected by two different active regions by exactly the same amount, and rather consider this as strong evidence in favour of a coherent rotation of the entire bright front. We also note that the two brightest concentrations are separated by ∼180°, which we consider to be compatible with interpretation in terms of a flux rope structure, with the brightest concentrations associated with opposite ends of the flux rope.

From the standard flare model (see Chapter 1, §1.5.2), the erupting filament/flux rope forms the core of the CME and is also the driver of the "skirt" of the CME. *We propose that the skirt of the CME in the low corona corresponds to the coronal wavefront.* If this is the case, then one expects the behaviour of the coronal wave to be linked with that of the flux rope (and therefore of the filament, since filaments are understood to be supported by the magnetic field of the flux

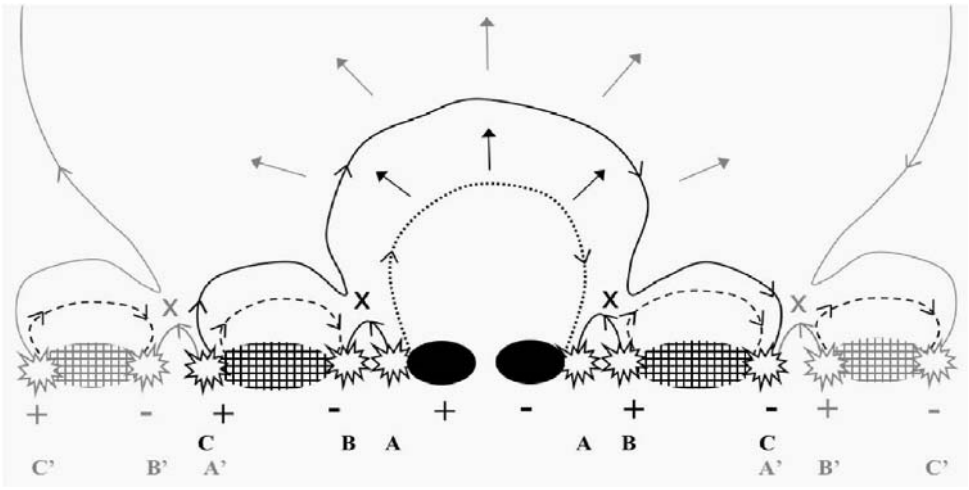

Figure 4.7: Cartoon illustrating the magnetic reconnection model proposed to generate the bright, diffuse coronal "wave" front, with the observed dual brightenings and two types of dimmings. The expanding CME (dotted line) reconnects with favourably orientated quiet Sun magnetic loops (dashed lines), displacing the footpoints of the expanding CME (solid line). The "**X**"s mark regions where magnetic reconnection occurs. The dotted/dashed lines show the pre-eruption magnetic structures, the black (grey) solid lines show the result of the first (subsequent) reconnections. Figure from Attrill *et al.* (2007a). Permission to reproduce this figure has been granted by the American Astronomical Society.

rope, see Chapter 1, §1.5.1). Webb *et al.* (2000) describe an anti-clockwise rotation of the partially erupting filament, seen in Hα data just prior to the coronal wave event on 12th May 1997. We therefore interpret the phase-shift of the EIT bright front (Figure 4.3) as an indication that the rotation of the CME magnetic structure continued following the initial rotation of the erupting core. Although a clockwise rotation is suggested for the 7th April case (Green *et al.*, 2007), it is more difficult to confidently analyse the Hα data because projection effects become important. However, Green *et al.* (2007) use different observational proxies to determine the sense of helicity of this source region, and conclude (in agreement with Leamon *et al.*, 2002) that the source region helicity is positive for the 7th April 1997 event. Since the helicity of the 12th May 1997 event source region is negative (§4.1), the two event source regions have opposite magnetic helicities. From this analysis, it appears that the helicity of the source region determines the sense of the subsequent rotation of the coronal wavefront (which we propose may be identified with the "skirt" of the CME in the low corona). This poses a challenge to the standard MHD "blast wave" interpretation: why should a flare-induced blast wave take account of the helicity of the CME source region in a manner consistent with the sense of rotation of the erupting filament? Our results suggest that the EIT coronal wave is driven by the erupting magnetic configuration.

4.2 New model for coronal "waves" as the magnetic footprint of a CME

We therefore propose a new mechanism where the bright fronts that constitute the diffuse EIT "wavefront" are due to the expanding CME magnetic field being thrust into and reconnecting with favourably orientated "open" or "closed" magnetic structures in the surrounding low corona. Since the two events we analyse occurred in a quiet-Sun (QS) environment, we focus here on interaction with QS loops and scattered "open" field lines.

With reference to Figure 4.7, the expanding CME structure (dotted line) reconnects with surrounding favourably orientated QS loops (dashed lines). These reconnections produce brightenings at points **A**, **B** and **C**, possibly as a result of chromospheric evaporation (since this is a lower energy version of the physics which happens in flares). The flux rope remains anchored in the deep dimmings but the reconnections make the outermost CME field lines step out of the vicinity of the initiation site.

In our cartoon model, it is the low part of the flux rope (near the footpoints) which is able to reconnect the most with low-lying QS loops, hence the concentrations in intensity formed $\sim 180^\circ$ apart (Figure 4.3). Brightenings **A** may be mixed with the deep dimming or be spatially unresolvable from brightenings **B**, so forming the brightening at the edge of the deep dimmings, whilst brightenings **C** are responsible for the leading edge bright front. Together these brightenings make up the diffuse dual-brightening coronal "wave" (Figure 4.5).

The brightening from each reconnected loop will progressively disappear on the time-scale defined by the thermal cooling of the plasma. However, an almost stationary brightening located at the edge of the deep dimmings (black regions) persists (Figure 4.5), because the expanding core magnetic structure remains rooted in the photosphere and may continue to drive reconnections with low-lying loops.

The reconnection can also create longer field lines (solid lines, Figure 4.7) and therefore a larger volume within the expanding CME cavity (brightenings **C** are displaced CME footpoints). Plasma previously contained by the closed QS loops (dashed lines) is suddenly released into a much larger volume. As a result, we observe diffuse dimming (hashed regions), that can develop only after the brightenings have occurred. This is commonly observed (No. 16). In our model reconnection may also occur with "open" field lines, but this would only create brightenings **A**,**B**, and would not contribute to the appearance of the diffuse dimmings. Given the large spatial distribution of the diffuse dimmings for these events (Figure 4.5), we believe that reconnection with QS loops is a more important process in the studied two cases.

After the first reconnections, the continuing expansion drives the dual-brightening signatures of the subsequent reconnections. The diffuse leading edge bright front therefore appears to propagate, being formed by successive reconnections with QS loops progressively further away, forming many brightenings **A'**, **B'**, **C'**. In this model, the "propagating" bright front is actually the response of more and more distant parts of the surrounding magnetic environment to magnetic reconnections. This implies a progression of the diffuse EIT "wave" front by steps, with a global average motion defined by the expansion of the CME core. Our model does not require a pre-existing giant bipolar arcade to span the diameter of the observed coronal wave (as in Chen *et al.*, 2002), since this is naturally created by the displacement of the expanding CME footpoints, through the successive small-scale reconnection events between the erupting magnetic configuration and QS loops.

4.2.1 Clarification of the more detailed and subtle physics of the proposed model

4.2.1.1 CME expansion in the low corona

We note that the 2-D sketch in the cartoon of Figure 4.7 is exactly that - 2-D! In 3-D, the CME is assumed to expand in all directions at about the same rate, so forming a magnetic bubble (e.g. Crooker *et al.*, 1990; Moore *et al.*, 2007). Schwenn *et al.* (2005) similarly found that the shapes of the vast majority of hundreds of CMEs they examined are consistent with a nearly perfect circular cross-section. They note that they find this observation rather surprising since CMEs result from the eruption of basically 2-D elongated filament structures. Cremades and Bothmer (2004) analysed 276 structured CMEs from LASCO/C2 observations concluding that the 3-D structure of CMEs is organized preferentially along an axial direction which "seems to correspond with the long axis of a large-scale helical magnetic flux rope that was formed in the source region", so favouring an interpretation of CMEs with a somewhat more cylindrical geometry (see their Figure 15). Work by Dere *et al.* (1997) may be able to reconcile these two viewpoints. They note that: "the images of the CME in [LASCO/]C2 do not appear to have the same loop-like or bubble-like appearance as the images in the EIT or [LASCO/]C1." It may be the case that CMEs initially expand semi-isotropically in all directions low in the corona, so that the CME starts out "with a fairly circular geometry" but becomes "more elongated with time when seen later in [LASCO/]C2" (see Figure 5, Dere *et al.*, 1997).

Regarding the morphology of EIT waves, Warmuth *et al.* (2004a) argue that "the retention of a basic circular curvature over large distances is a strong indication of the wave-like nature of the disturbances." In the light of our proposed model, where the bright front is understood to be the magnetic footprint of the bubble-like CME in the low corona, this observation can actually be interpreted as support for non-wave models!

The magnetic pressure of the CME over that of its surroundings, drives the expansion and determines the lateral extent of the CME. Moore *et al.* (2007) provide a strong, observationally supported argument for the "initiation site" (region where the flare arcade forms) as being responsible for the width of the CME. They show, for three very different events that the final angular width of the CME in the outer corona can be reasonably well estimated from the average magnetic field strength and the angular width of the source-region post-eruptive arcade. According to our proposed model, some of the field lines originally rooted in the flaring source region step out by successive reconnections, generating the diffuse bright front over as wide an area as the balance between internal and external pressure allows the departing CME to expand in a lateral direction. Through this process, magnetic structures over a large-scale area become CME *constituents*.

4.2.1.2 Energy release and issues regarding detection

In our model, the bright front does not carry energy (the bright front in our model is not a wave). Rather, it is the CME magnetic configuration that carries the energy (indeed, that drives the entire eruption). The coronal "wave" bright front is the outer shell of the CME magnetic configuration in the low corona and is bright due to the energy released during the reconnection processes. Evidence in support of our model may be found in work by Wen *et al.* (2006), who find non-thermal radio bursts at the fronts of coronal waves, in regions which later dim. Specifically, the

type IV radio bursts are found at the legs of discrete large-scale relatively strong magnetic loops which interact and subsequently become regions of deep dimming. Wen *et al.* (2006) consider the "location of the radio bursts suggest the conjunction of many sets of magnetic loops systems or magnetic separatrices" and interpret the non-thermal radio bursts as signatures of coronal reconnection, closely associated with CME initation. They also note that the general process of coronal restructuring takes place at a speed slower than either the Alfvén or acoustic speed in the corona. They define a "CME triggering speed" by dividing spatial/time scales and conclude that the process of restructuring is not a wave phenomenon but includes interactions among many individual flux loop systems, as well as the interaction between loop systems and shock fronts propagating from the CME initiation site. If such a magnetic restructuring process driven by a CME occurs in the low corona generating a coronal "wave" as we propose, then the speed of the expanding bright front is dependent only on the CME lateral expansion speed. Such a picture allows for a wide range of coronal wave velocities, even below v_A, as observed (No. 1).

Maia *et al.* (1999); Pohjolainen *et al.* (2001) and Pohjolainen *et al.* (2005) showed examples of how 2-D mapping of radio sources show signatures of CME lift-off and angular spread in the low corona. However to our knowledge, there are not many instances of radio observations unambiguously linked to diffuse coronal waves in the absence of large-scale magnetic structures. Even for the case reported by Vršnak *et al.* (2005), of broadband metric range emission (151 - 327 MHz) associated with a diffuse EIT wave, a Moreton wave was also present. In any case, Vršnak *et al.* (2005) emphasise that the radio emission is weak. It may be the case that reconnections with QS magnetic fields are just too weak to be detected. For example, Wen *et al.* (2006) report that one of their type IV bursts may contain sub-bursts unresolved in the current observations. As with diffuse EIT waves (which are very subtle features), the spatially integrated flux of the radio emission also decreases to levels where it becomes impossible to detect features distinct from the background level (Bastian *et al.*, 2001). Further, the detection of radio emission depends on the observing frequency (§1.6.2.1). For each frequency there is an altitude below which the radio wave cannot propagate (Pick, 2006). Since diffuse coronal EIT waves appear to be phenomena of the low corona (No. 21), short wavelength (high frequency) sensitive radio observations are required if a counterpart is to be detected at all.

A further issue regarding potential detection of the reconnection events in hard X-rays with current instrumentation, is dynamic range. With current indirect imaging hard X-ray telescopes (e.g. RHESSI), the dynamic range is limited to about 10:1. In our model, the bright front is made up of weak flare-like emission, however in most coronal wave events, strong flare emission is also present. Occultation of the main flare (possibly provided by the solar limb) is required if fainter coronal emission is to be observed, because weak sources are obsured at a given photon energy when one or more much brighter sources at the same photon energy are present (e.g. Emslie *et al.*, 2003). Brosius and Holman (2007) showed that chromospheric evaporation occured in a weak and noisy flare-like transient in Fe XIX emission. However, corresponding RHESSI images showed no emission at the location of the EUV transient, which Brosius and Holman (2007) attribute to limitations of the dynamic range. In addition, despite its sensitivity, it is difficult (though not impossible; Hannah *et al.*, 2007a) to study weak sources larger than $\sim 3'$ using RHESSI due to the way in which the collimators work (Hannah *et al.*, 2007b). Such difficulties may be addressed in the future as work is underway to construct a direct imaging hard X-ray telescope with the aim of measuring high-energy radiation from areas where it is not intense (Ulmer *et al.*, 2003).

4.2.1.3 Waves as well

We emphasise that a diffuse coronal EIT "wave" created by successive reconnection events does not exclude, and in fact can co-exist with, an MHD (shock) wave formed by a fast expanding CME front or indeed a flare-induced blast wave (chapter 3 §3.5.1.4). Thus our model is compatible with observations where both a sharp S-wave *and* a more diffuse bright front are present (e.g. chapter 3, Figure 3.2). However, in our model we emphasise that the two phenomena are physically distinct, with the S-wave being a true MHD wave, but the diffuse bright front being generated by reconnection events. (This differs from the interpretation of Thompson *et al.* (2000b) and Warmuth and co-workers, where it is suggested that both the S-wave and diffuse bright front may be generated by the same mechanism, e.g. a strongly driven and later freely propagating counterpart of one common driver). Zhukov and Auchère (2004) consider that EIT waves are bi-modal, comprising both a wave mode (a wave-like propagating disturbance, which probably represents a fast-mode magnetosonic wave) and an eruptive mode (propagation of a dimming as a result of the successive "opening" of magnetic field lines during CME lift-off). They consider that probably both modes are present in any event, but that observations are limited with current instrumentation.

4.2.1.4 Dynamic behaviour

In our model, reconnection is expected to occur at the interface between the main erupting structure and favourably orientated surrounding magnetic structures. These interfaces will correspond to separatrices and quasi-separatrices (QSLs; Démoulin *et al.*, 1996). They are not identifiable in pre-event extrapolations since they are created by a globally unstable and expanding magnetic structure (CME) which is not present in any static extrapolation of the photospheric field. Moreover, the connectivities of the erupting configuration are transformed by the successive reconnections with the surrounding fields, creating a new topology which was not present in the pre-eruption magnetic configuration.

Démoulin (2006) related brightenings in many emission lines, including in EUV and Hα, to reconnection in the corona at QSLs. Delannée *et al.* (2007) note that "in this context, EUV emission may either be directly caused by early joule heating, or by late chromospheric evaporation, while Hα brightenings probably result from the local heating of the chromosphere by non-thermal electrons accelerated high above in the corona from the reconnection regions." Delannée *et al.* (2007) cite this work as explanation for the stationary brightenings observed in EIT and Moreton waves. Whilst not disagreeing with the work of Delannée and Aulanier (1999); Delannée (2000); Delannée *et al.* (2007), we cite this work as explanation for the *moving* bright fronts of EIT waves. We expect that on occasion, when the reconnection rate is high enough and acceleration of the electrons is strong, a moving diffuse bright front corresponding to the chromospheric counterpart of the *diffuse* EIT "wave" may be detected in Hα data. A possible example of such an event is shown in Figure 1.26, §1.6.2.2 (the Hα "tsunami" event of 6th December 2006). To our knowledge, no EUV data exist of this event so it is not possible to determine whether an EIT wave also occured, although a halo CME is recorded in LASCO/C2 data at 20:12 UT. We do not expect every diffuse coronal "wave" event to produce such tsunami events observed in Hα data. As Švestka (2001) states in the context of active region flares: "the only difference between flare-associated and non-flare-associated CMEs is the strength of the magnetic field in the region of the field line opening". We argue that the same physical reasoning should apply to our coronal "wave" bright

front, consisting of multiple small-scale flare-like events. The coronal response (i.e. brightening) should remain the same, regardless of whether a chromospheric counterpart is observed or not.

4.2.1.5 Triggering loop oscillations

If there is a particular structure that is orientated such that magnetic reconnection with the expanding CME structure is not favorable, then the CME expansion will act to compress the magnetic field that is encountered. This compression will induce a directional pressure pulse in the encountered magnetic field. Such a pressure pulse would be capable of triggering a loop oscillation of the encountered magnetic field (No. 3).

4.2.1.6 Formation altitude of coronal "waves"

From the measured projection effect described in §4.1.1, we understand that diffuse coronal waves should form in the low corona. Work by Feldman *et al.* (1999) used 195 Å TRACE images to show that at temperatures $\sim 1.4\times10^6$K, the quiet Sun is populated by loops at heights of 1.03-1.5 $R_\odot$ (716 - 1044 Mm). Since our model requires reconnection with quiet Sun loops, the height of the bright front formation in our model is not expected to exceed this approximate radial distance. However, the bright front in our model is formed by flare-like events and the loop generated by the reconnection will be shorter than the quiet Sun loop with which the expanding CME shell interacts, so the altitude of formation of the bright front will depend on the height and length of the quiet Sun loop encountered by the expanding CME.

Recent data taken by STEREO/EUVI in all four passbands show the diffuse bright front of a coronal wave to have similar kinematics in all four EUVI bandpasses (Long *et al.*, 2008, No. 19). As noted in §3.5.1.3, this is a puzzling result if it is interpreted in the context of wave theory, however in our model, this observation is actually *expected* since the bright front is formed by weak flare-like events, thus affecting many layers of the solar atmosphere simultaneously.

In summary, our model proposes that diffuse coronal "waves" are the **magnetic footprint of a CME** in the low corona, where the expanding magnetic skirt of a CME reconnects with surrounding small-scale magnetic loops distributed all over the quiet Sun. The successive reconnections with randomly oriented loops of different lengths and heights (Feldman *et al.*, 1999) are driven by the expansion of the CME core. Events with a high core pressure are expected to have an EUV coronal wave that reaches further away (e.g. 28th October 2003 event, see Mandrini *et al.*, 2007) than weaker events which will be less extended. The reconnections lead to small-scale flare-like events and a gradual stepping-out of magnetic field lines originally rooted in a small source region. Such a process naturally generates a diffuse expanding bright front (identified as a coronal or EIT "wave"). The displacement of the brightenings will naturally stop when the internal pressure is no longer large enough to drive the stepping reconnections. Wide-spread coronal dimming manifests behind the expanding diffuse bright front, since field lines rooted in the quiet Sun successively become part of the expanding CME. Our model naturally and intrinsically implies that the extent of the diffuse coronal dimming matches the angular extent of the CME, and that surrounding magnetic structures become constituents of the CME. Such a mechanism appears to explain the dual bright fronts and the widespread diffuse dimming (§4.1.1.2), while the deep core dimmings correspond to the footpoints of the expanding flux rope, where most of the field lines remain rooted.

4.2.2 Predictions of our model

(i) All large-scale coronal "waves" (such as the events described in detail in this chapter: 12th May 1997, 7th April 1997, 25th January 2007, 29th April 2006), should mark the magnetic footprint in the low corona of their corresponding large-scale CMEs. For the limb events (25th January 2007 and 29th April 2006), we will show (§4.3) that the spatial extent of the large-scale coronal "wave" and widespread dimmings do indeed map the angular extent of the CME in the low corona. For the halo CME events (12th May and 7th April, 1997), using Sun-Earth line-of-sight instruments like SOHO/EIT and SOHO/LASCO, we cannot prove that these halo CMEs were also large-scale in the low corona (since a halo CME can be created simply due to it being observed at a large radial distance from the Sun). However, for the 12th May 1997 event, Plunkett *et al.* (1998) find the CME to move at approximately constant velocity and estimate a frontal CME speed (toward Earth) of 600 km s^{-1}, assuming a typical cone angle of 50°. An alternative, similar estimate for the CME frontal speed of 550 km s^{-1} may be made due to the detection of a related magnetic cloud at $\sim$ 10:00 UT on 15th May 1997 at 1 AU (see chapter 4). The flare occurs at 04:42 UT and the halo CME is first detected in LASCO/C2 data at 06:30 UT. Assuming the flare to temporally correspond to initiation of the CME, at 06:30 UT the CME must be at a height of $\sim 5.1R_{\odot}$ from the solar surface. So already at $5.1R_{\odot}$, the CME must have a large lateral extent for it to be viewed on opposite sides of the coronagraph occulting disk. This estimate therefore supports our expectation that the 12th May 1997 CME was large-scale even in the low corona. In the coming years, we have the possibility to combine STEREO coronagraph (COR) and SOHO/EIT (or STEREO/EUVI and SOHO/LASCO) observations in order to observe on-disk coronal "wave" events, and at the same time image the lateral extent of the CME in the low corona. Large-scale halo CMEs have the greatest probability of interaction with the Earth's magnetic environment, so coronal "waves" may serve as an early warning space weather diagnostic, not just of the lateral extent of the CME, but also (as we will demonstrate in the next section), analysis of the locations and behaviour of the bright front can be used to deduce the magnetic connectivity and magnetic orientation of the ICME.

(ii) Since magnetic reconnection between the CME and surrounding magnetic structures conserves magnetic flux, the external constituents of the CME (from surrounding magnetic systems) are not expected to increase the magnetic flux of the CME (except in the case where there are overlying loops, which would be forced to expand, e.g. as in Delannée and Aulanier (1999); Harra *et al.* (2007a)). The wide-spread coronal dimming, however, suggests that the the surrounding magnetic systems that become constituents do supply mass to the CME.

(iii) The magnetic pressure of the CME is defined by the physical conditions of the CME source region, such as free energy in the CME core. Sheared loops, although not a necessary condition for a strong eruption, do indicate a significant build-up of magnetic energy and may therefore be considered an observational indicator of the potential for a strong eruption. Therefore we consider that CME source regions with compact, strong magnetic fields are likely candidates for producing CMEs that have a large lateral extent in the low corona. Moore *et al.* (2007) have already shown this observationally for 3 cases, and the first detailed simulation of CME evolution in the low corona ($< 5R_{\odot}$) by Liu *et al.* (2008) shows that the magnetic pressure is dominantly responsible for the acceleration of the CME at $< 3R_{\odot}$. This expectation can be further observationally tested by using SOHO/MDI or SDO/HMI to measure the magnetic field strength of the source region at the same time as the lateral extent of the CME in the low corona with STEREO/COR1 data.

(iv) Finally, we expect that diffuse EIT bright fronts do not "stop" at or "avoid" active regions or coronal holes (Nos. 8 & 17). Rather, they slow down substantially, and they undergo many magnetic reconnections if the skirt of the CME encounters a concentrated region of favourably orientated magnetic field. Or conversely, if the skirt encounters a region of unfavourably orientated magnetic field, then the conditions required for magnetic reconnection will not exist, and the bright front will vanish.

What happens to the energy when the bright front disappears? If the magnetic field is orientated unfavourably for reconnection, then the CME configuration will no longer be able to expand laterally through reconnection at this location. The stored magnetic energy that is being released during the CME expansion will not be dissipated through reconnection at this particular location. The magnetic pressure of the expanding CME will act to compress the surrounding magnetic field. If the surrounding magnetic field is strong enough to resist the compression of the expanding CME magnetic configuration, then the CME will no longer be able to expand horizontally at the location of the strong magnetic field. However the CME configuration will still expand upward, so the expansion will occur, but no longer in a horizontal, lateral direction at this particular location. If the surrounding field is not strong enough to resist the compression, then the CME magnetic structure should continue to expand over this region, but the coronal bright front will vanish because there will be a negligible amount of reconnected magnetic flux. If the expanding CME magnetic structure again later comes into contact with favorably orientated magnetic field, then if there is still sufficient lateral force from the expanding CME configuration to drive reconnections, then theoretically, the bright front can reappear.

It is clear that coronal holes do not consist purely of "open" magnetic field, but contain low closed loops as well (Chapter 1, §1.2.3.1). Why should the coronal "wave" bright front stop or vanish at the edge of the coronal holes and not continue to expand, stepping through the coronal hole by reconnections with these closed loops within the coronal hole? As the CME expands, even if it initially has a strong lateral component to the expansion, it nevertheless also expands in a radial direction. It is therefore expected, in the proposed model, that the skirt of the expanding CME will reconnect with low closed loops most efficiently during the strongest/earliest stage of the lateral expansion. As the expansion progresses, the radial component becomes dominant, so that further from the initiation site, reconnections occur with progressively higher and larger magnetic structures. Upon interaction with the "infinitely long", "open" magnetic field of a coronal hole the expanding CME is deflected, and the CME configuration will preferentially expand upward at the location of interaction. If the polarities are favourable for reconnection, then the magnetic field preferentially available for reconnection will be the "open" extended magnetic field, not the small closed loops that exist within coronal holes. However, whether reconnection will occur with closed loops within the coronal hole depends heavily on the size of the loops and on the extent to which they are isolated by surrounding "open" field.

4.3 Two limb coronal wave events that interact with neighbouring coronal holes

We analyse two limb coronal wave events that both expand into the vicinity of disk (low-latitude) coronal holes. The aim is to test prediction (iv) made in the previous section that the behaviour of the coronal "wave" bright front (if it is indeed a magnetic feature), should depend on the magnetic

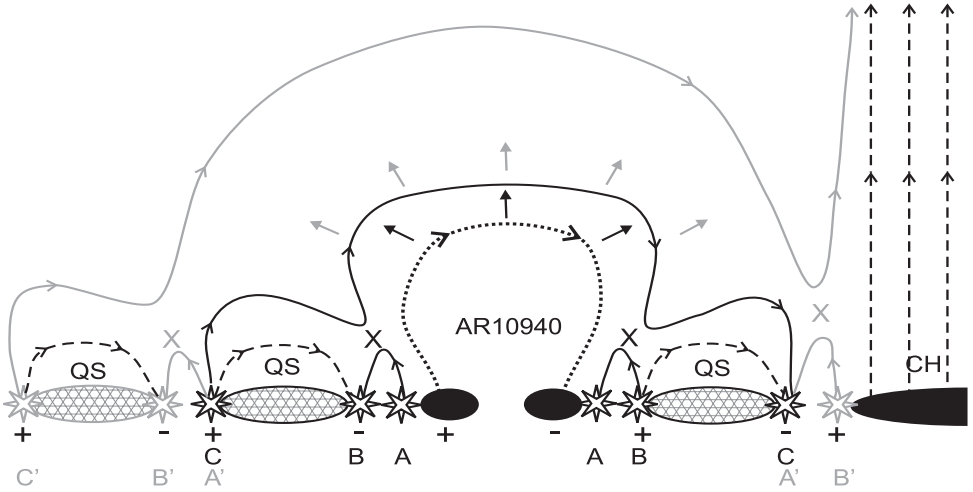

Figure 4.8: Cartoon (left side) illustrating the magnetic reconnection model proposed to generate the bright, diffuse coronal "wave" front and associated dimmings. The expanding CME (dotted line) reconnects with quiet Sun (QS) magnetic loops (dashed lines), displacing the footpoints of the expanding CME (solid line). Right side illustrates the process of interchange reconnection, between the expanding CME and "open" field in a coronal hole (CH). The "**X**"s mark regions where magnetic reconnection occurs (null point in 2-D, thinnest part of QSLs in 3-D). The dotted/dashed lines show the pre-eruption magnetic structures, the black (grey) solid lines show the result of the first (subsequent) reconnections. The loops formed by reconnection between the expanding CME and the coronal hole boundary (B' → A') will be relatively long loops. Figure from Attrill *et al.* (2007b). Permission to reproduce this figure has been granted by Wiley-VCH Verlag GmbH & Co. KGaA.

orientation between the expanding CME outer shell and surrounding magnetic structures. This is a prediction that can be tested and is a powerful discriminant between the many models for coronal waves. As Balasubramaniam *et al.* (2005) note, waves/shocks do not have such preferences for the magnetic polarity. For the same reason, we can also therefore determine if the bright front is due to the compression of plasma (as e.g. in the Delannée and Aulanier (1999); Delannée (2000); Delannée *et al.* (2008) and Chen *et al.* (2002, 2005a,b) models), or due to magnetic reconnection, as proposed in our model.

We analyse the first coronal wave to be observed by STEREO/EUVI(B), occurring on 25th January 2007 and associated with a source region just behind the limb, NOAA 10940. The second event was observed by SOHO/EIT, occurring on 29th April 2006 and associated with a source region just on the limb, NOAA 10878. As Veronig *et al.* (2006) note, observational studies of the interaction of coronal waves with active regions and coronal holes are rare and are usually hampered by the low cadence of the EIT instrument ($\sim$ 12-15 min), which restricts studies to slow waves. In both cases, we apply our coronal "wave" model to explain the evolution of the observed diffuse bright fronts, thereby arguing that the bright fronts and dimmings are due to magnetic reconnections between the expanding CME core and surrounding magnetic structures.

For the STEREO/EUVI 25th January 2007 event, we use 195 Å full disk images from EUVI (B) on board STEREO at approximately 10 minute intervals with a pixel size of $1.59''$. The heliograms used were made between 06:00 and 08:00 UT on 25th January 2007. The EUV heliograms are differentially de-rotated (using `drot_map`) to the same pre-event time (06:36 UT). To visualise the dimmings clearly, we produce base difference images where the same pre-event image is subtracted from all subsequent images. For the SOHO/EIT 29th April 2006 event, we use 195 Å full disk images at approximately 12 minute intervals with a pixel size of $2.63''$. The base image used is at 15:59 UT. In both cases, we supplement the EUV data with white light coronagraph data from the SOHO LASCO/C2 coronagraph.

4.3.1 EUV base difference images

Figures 4.9 and 4.10 show sequences of EUV 195 Å base difference images of the 25th January 2007 and 29th April 2006 limb coronal wave events, respectively. The sequences show expansion of the diffuse bright front (white areas), constituting the coronal "wave" feature, and the deep and diffuse dimming (black regions). In each event, the white arrows indicate the location of the bright front in each frame. Note the wide angular spatial extent of the diffuse dimming behind the bright front in each image.

For the **25th January 2007 EUVI event**, in the first frame (06:52 UT), the bright front is a coherent feature, as indicated by five white arrows. By 07:06 UT, the bright front has expanded northward. This frame (07:06 UT) and the following three frames (07:16, 07:26 and 07:36 UT) show persistent brightenings in the southern hemisphere, located at approximately the same location in each frame. In the northern hemisphere, the bright front, having moved northward from AR 10940, continues to expand onto the solar disk throughout the remaining frames. Taking into account projection effects, the estimated speed of this part of the bright front between 07:06 and 07:16 UT is 288 $\pm$ 50 km s^{-1}. The uncertainty is due to the broad nature of the bright front as a result of the range of quiet Sun loops and the erratic process of reconnection with favourably orientated loops. After 07:06 UT, the front in the northern hemisphere becomes more patchy and diffuse. In the last two frames (07:26 and 07:36 UT), the approximate location of this very diffuse brightening is marked by a white "X". The reader is encouraged to view the base difference movie provided for this event (*cwsubdiskbasediff.mpg*, Appendix E), in order to observe these subtle features more clearly. As well as the dimming (black regions) located just above the east limb, on the disk a weak, diffuse dimming can also clearly be identified, appearing behind the expanding bright front. The last frame of Figure 4.9 shows a composite of an EUVI base difference image at 07:36 UT and a LASCO C2 white light coronagraph image at 07:32 UT. Note how the spatial extent of the dimming matches the angular extent of the associated CME.

For the **29th April 2006 EIT event**, the second frame at 16:11 UT shows a clear coronal wave bright front, the subsequent frames at 16:25 and 16:47 UT show the progressive expansion of the bright front. It rapidly becomes more diffuse and fragmented. The bright front is identified by white arrows to the north and south of the source region on the disk, but there is no discernable feature directly to the west. The reader is encouraged to view the base difference movie provided for this event (*cwsubdiskbasediff_290406.mpg*, Appendix E), in order to observe the subtle bright fronts and dimming more clearly than the images can show. As well as the deep dimming that manifests above the limb, a more diffuse dimming is also observed to expand onto the disk, following the bright front. Again, the spatial extent of the coronal wave and dimming matches the angular extent of the CME.

4.3.2 Magnetic environments and source regions

To understand the magnetic environment associated with these events, we use SOHO/Michelson Doppler Imager (MDI; Scherrer *et al.*, 1995) level 1.8 full disk magnetogram data on January 25th 2007 at 06:23 UT, and on 29th April 2006 at 09:35 UT, with a pixel size of 1.98″. For both events, the MDI data was corrected for radial projection effects using the standard *SolarSoft* `zradialize` routine. For the 25th January 2007 case, when comparing MDI data taken by SOHO with EUVI images taken by STEREO, data from both spacecraft are first aligned to the same view using the

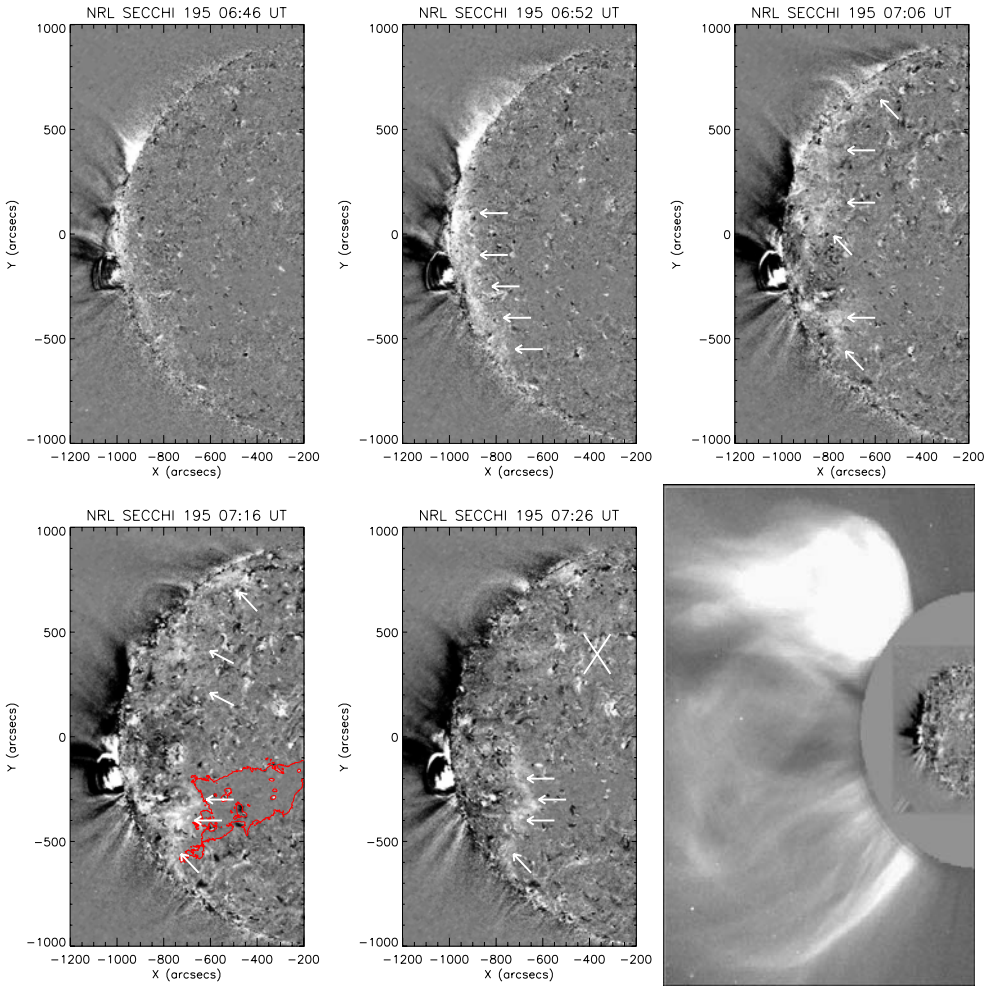

Figure 4.9: Successive EUVI 195 Å base difference images of the 25th January 2007 limb CME event. The location of the bright front in each image is indicated by white arrows. Very diffuse brightenings are marked by a white "X". Note the wide angular spatial extent of the dimming. The base difference image at 07:16 UT is overlaid with a red contour identifying the location of a disk coronal hole. Final panel shows a composite of an EUVI base difference image at 07:36 UT and a white light C2 coronagraph image at 07:32 UT. Note how the wide angular spatial extent of the dimming matches the wide angular extent of the CME. Permission to reproduce this figure has been granted by Wiley-VCH Verlag GmbH & Co. KGaA.

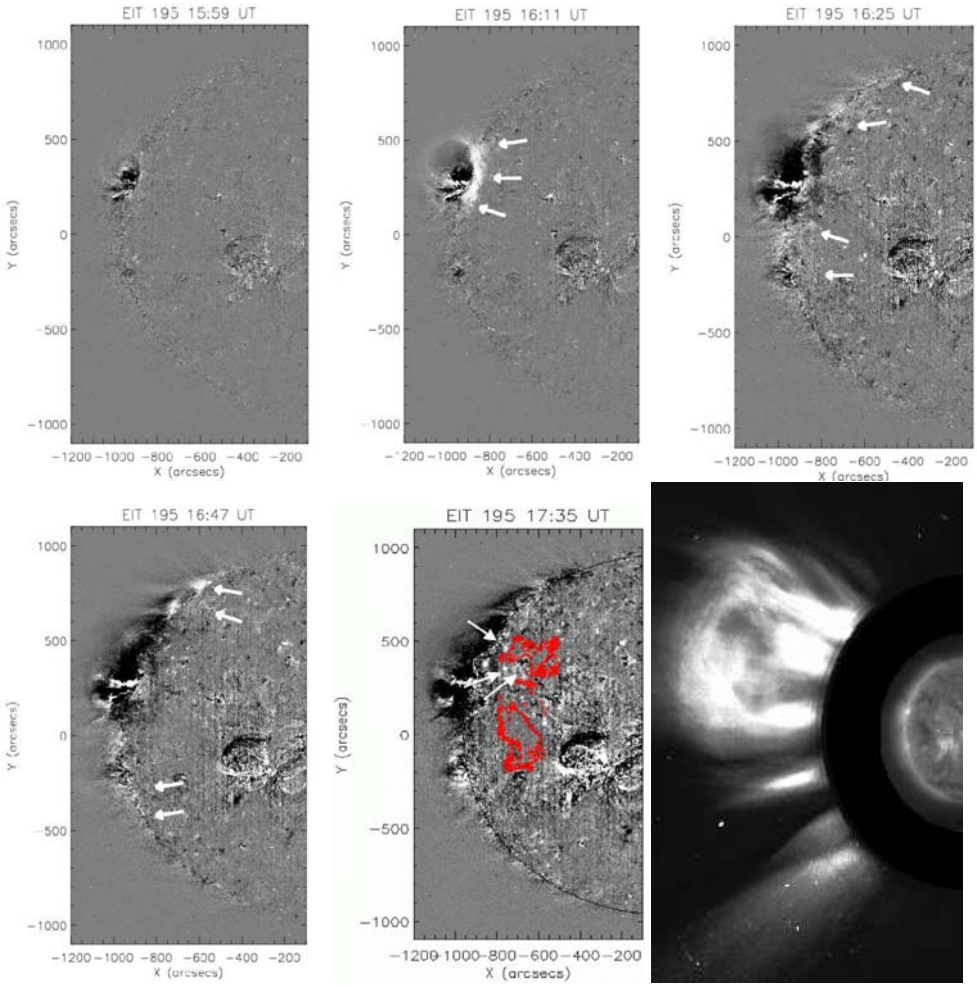

Figure 4.10: Successive EIT 195 Å base difference images of the 29th April 2006 limb CME event. The location of the bright front in each image is indicated by white arrows. The base difference image at 17:35 UT is overlaid with red contours showing the location of two disk coronal holes. White arrows in the frame at 17:35 UT indicate persistent brightenings that lie at the eastern boundary of the north disk coronal hole. Final panel shows a composite of an EIT image at 17:48 UT and a white light C2 coronagraph image at 17:54 UT. Note how the wide angular spatial extent of the dimming matches the wide angular extent of the CME.

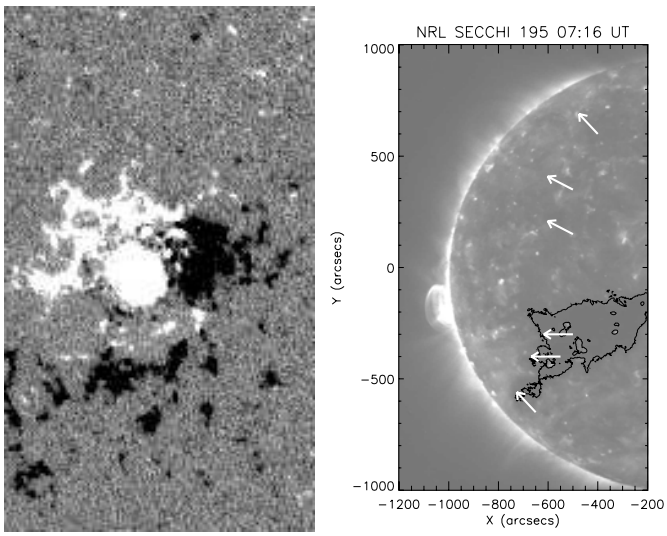

Figure 4.11: Left panel shows NOAA 10940, the most likely source region for the 25th January 2007 CME. Right panel shows an EUVI 195 Å image at 07:16 UT. Overlaid are black contours set at 650 counts, identifying the location of a coronal hole. The white arrows are the same as the ones overlaid on the base difference image at 07:16 UT in Figure 4.9. Permission to reproduce this figure has been granted by Wiley-VCH Verlag GmbH & Co. KGaA.

SolarSoft routine `map2earth`.

On 25th January 2007, NOAA active region (AR) 10940 was located on the eastern limb, and AR 10939 was approaching the western limb. Mixed polarity quiet Sun magnetic field dominated the rest of the solar disk, with the exception of a disk coronal hole (see Figure 4.11, right panel). Figure 4.11, left panel shows a SOHO/MDI magnetogram on 2nd February 2007, showing AR 10940 (the most likely source region of the 25th January 2007 CME). Examination of the magnetic configuration of AR 10940 shows it to have a strong concentrated negative leading polarity, newly emerged since the previous rotation, which is embedded in a decaying active region.

On 29th April 2006, NOAA AR 10878 was located on the eastern limb, and there were two large, low-latitude dispersed active regions near solar disk center. Mixed polarity quiet Sun magnetic field dominated much of the solar disk and there were two disk coronal holes located near to the east limb (see Figure 4.12, right panel). Figure 4.12, left panel shows a SOHO/MDI magnetogram on 3rd May 2006, showing AR 10878 and an AR in the southern hemisphere (SH). AR 10878 in the northern hemisphere is the most likely candidate for the source region of the 29th April 2006 CME. Examination of the magnetic configuration of AR 10878 shows it to be a dispersed quadrupolar active region, with a positive leading polarity.

4.3.3 Interaction with surrounding magnetic structures

As explained in §4.2.2, prediction (iv) of our model is that diffuse EUV coronal "wave" bright fronts do not "stop" at or "avoid" active regions or coronal holes as sometimes reported in the literature (Nos. 8 & 17). Rather, we understand that they slow down substantially, and undergo many magnetic reconnections if the skirt of the CME encounters a concentrated region of favourably orientated magnetic field. Conversely, if the skirt encounters a region of unfavourably orientated magnetic field, then the conditions required for magnetic reconnection will not exist. As a result, the bright front generated by the reconnections will vanish because there will be a negligible amount

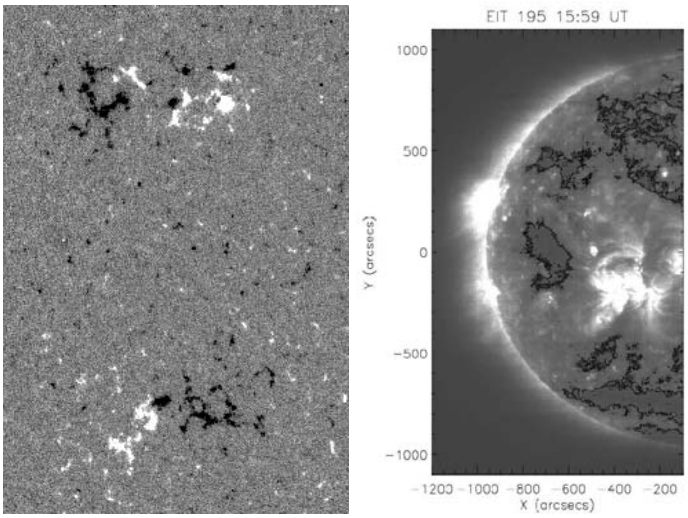

Figure 4.12: Left panel shows NOAA 10878 (northern hemisphere), the most likely source region for the 29th April 2006 CME. An active region in the southern hemisphere is also shown. Right panel shows an EIT 195 Å image at 15:59 UT. Overlaid are black contours set at 40 counts, identifying the location of disk coronal holes.

of reconnected magnetic flux.

For the **25th January 2007 EUVI event**, Figure 4.11 (right panel) shows the persistent brightenings identified in the southern hemisphere to be located at the eastern edge of a coronal hole. Measurement of the magnetic flux of this coronal hole shows it to be dominantly positive: positive flux = 4.1×10^{21} ($\pm$ 1.6×10^{19}) Mx, negative flux = -2.9×10^{21} ($\pm$ 1.4×10^{19}) Mx (see §5.2.5 for details regarding MDI data and calculation of errors). Figure 4.11 (left panel) shows the most likely source region of the CME. After the eruption, a post-eruptive arcade develops, with loops orientated East-West (e.g. EIT 195 Å frame at 09:24 UT). This orientation of loops is expected after an eruption from NOAA 10940, supporting the identification of this active region as the source region for this event. As the western (negative) edge of the expanding CME pushes against the oppositely orientated "open" field lines of the disk coronal hole, a current sheet is expected to form at their interface. These represent favourable conditions for successive magnetic interchange reconnection to take place. The term "interchange reconnection" is used to describe reconnection between small-scale closed loops and magnetic field that is so grossly expanded, that relative to the small loops it is only connected to the Sun at one end (Crooker *et al.*, 2002). So the southern hemisphere brightenings in this event can be described in the context of our model.

Expected products of interchange reconnection are (i) the production of a new loop between the reconnected "open" coronal hole field and the expanding CME and (ii) a retreat of the coronal hole boundary as the "open" field is displaced to the far side of the expanding CME. Both of these features can be identified in the EIT (not differenced) movie (*euvi_b_dmap_subfov.mpg*; Appendix E). Also see Figure 4.13.

The northern hemisphere brightenings do not persist at one location, but rather exhibit motion to the north and across the disk to the west. The northern bright fronts move across mixed polarity QS magnetic field: positive flux = 2.1×10^{22} ($\pm$ 3.4×10^{19}) Mx, negative flux = -2.3×10^{22} ($\pm$ 3.5×10^{19}) Mx. The gradual movement of the bright fronts across this mixed polarity region is an observation that is readily interpreted and understood using our model. With reference to the left side of Figure 4.8, the expanding CME structure (dotted line) reconnects with surrounding

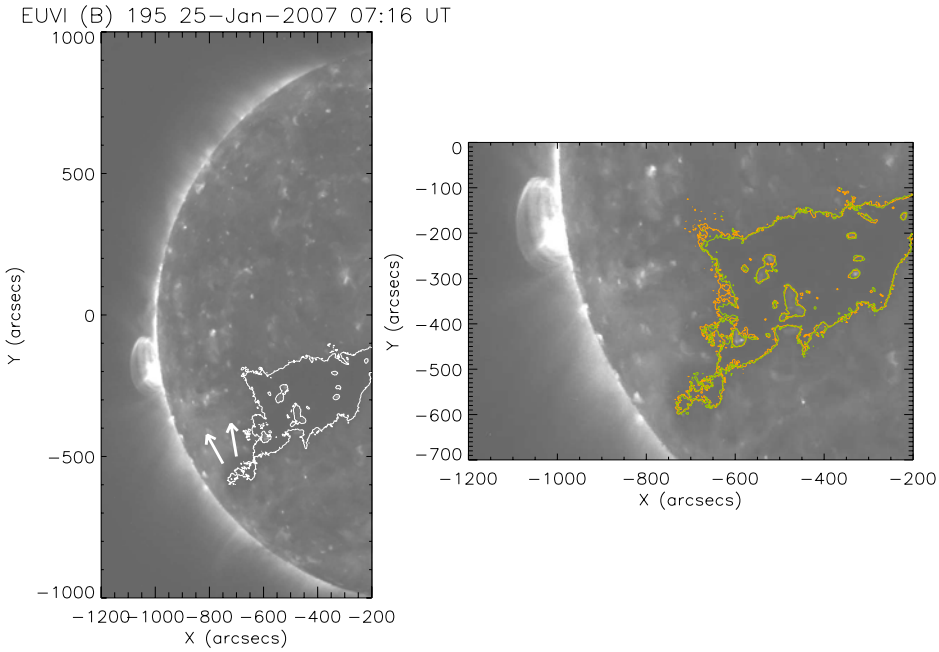

Figure 4.13: Left panel shows the EUVI image at 07:16 UT, during the coronal wave event. A long loop can be identified, indicated by the white arrows, stretching from the limb to the coronal hole boundary (white contour). (The loop can also be identified in the base difference image at 07:16 UT in Figure 4.9 and in the movie). Right panel shows the evolution of the coronal hole boundary. Orange (green) contour shows the coronal hole boundary at 06:36 UT (07:36 UT), before (after) the event. The retreat of the eastern boundary can be seen.

favourably orientated QS loops (dashed lines). These reconnections produce brightenings at points **A**, **B** and **C**. The reconnection also creates longer field lines (solid lines, Figure 4.8) and therefore a larger volume within the expanding CME cavity (brightenings **C** are displaced CME footpoints and are responsible for the expanding EUV bright front). As a result, we observe diffuse dimming (hashed regions), that can develop only after the brightenings have occurred. This is consistent with the sequence of base difference images shown in Figure 4.9. After the first reconnections, the continuing expansion drives the subsequent reconnections. The diffuse bright front therefore appears to propagate, being formed by successive reconnections with QS loops progressively further away, forming many brightenings **A'**, **B'**, **C'**. This implies a progression of the diffuse coronal "wave" front by steps, with a global average motion driven and defined by the expansion of the CME core.

For the **29th April 2006 EIT event**, Figure 4.10 shows the expansion of the coronal "wave" bright front from $\sim$ -900″ to -600″ in the x-direction. The original intensity EIT 195 Å images show that there are two disk coronal holes near the east limb, one in the northern hemisphere, and one straddling the equator (see right panel, Figure 4.12). Measurement of the magnetic fluxes shows the north coronal hole to have a slight dominant negative polarity: negative flux = -3.2 $\times 10^{21}$ ($\pm$ 1.0 $\times 10^{19}$) Mx, positive flux = 3.0 $\times 10^{21}$ ($\pm$ 9.6 $\times 10^{18}$) Mx, and the trans-equatorial coronal hole to be dominantly positive: positive flux = 4.1$\times 10^{21}$ ($\pm$ 1.2 $\times 10^{19}$) Mx, negative flux = -3.3 $\times 10^{21}$ ($\pm$ 1.1 $\times 10^{19}$) Mx. Figure 4.12 (left panel) shows an MDI magnetogram showing the magnetic configuration of the two limb active regions on 3rd May. The most likely source region of the CME is the northern active region. As the western (positive) edge of the CME expands westward, in the north it reaches the dominantly negative disk coronal hole. The base difference image at 17:35 UT in Figure 4.10 is overlaid with red contours showing the location of the disk coronal holes.

White arrows indicate persistent brightenings that lie at the eastern boundary of the north coronal hole. (These persistent brightenings can also be viewed in the base difference movie of this event). Because the flux measurements show a slight dominance of the negative polarity, we might expect interchange reconnection to occur as the opposite polarity flux domains come into contact, driven by the expanding CME. To the south-west of the source region, the positive leading edge of the expanding CME pushes against the dominantly positive "open" field lines of the trans-equatorial disk coronal hole. No current sheet is expected to form at this interface because the interacting flux systems are of the same orientation. Therefore, these do not represent favourable conditions for successive magnetic interchange reconnection to take place. So in this case, the bright front of the coronal "wave" is expected to vanish, as observed.

4.4 Coronal "waves" are semi-isotropic

There is currently an impression in the literature and solar scientific research community that only a handful of coronal waves are semi-isotropic in nature. Here we show that this is a false impression. We use the Thompson and Myers (2009) EIT wave catalogue, spanning March 1997 - June 1998, since EIT waves are independently identified in this work. After viewing a series of un-differenced 195 Å images side-by-side with the running difference images, Thompson and Myers (2009) derived the location of the wavefront by visually identifying the leading edges of the transients. The authors caution that there is great ambiguity in the final frame due to the very diffuse nature of the EIT disturbances. The catalogue is comprised of sketches where a solid black line is used to denote the location of the leading edge of a wavefront if it is relatively clear. When the location is difficult to resolve, or when it is not clear whether the change in emission is a continuation of a previous wave location, the uncertainty is indicated with a dashed line. Thompson and Myers (2009) also assign a quality rating ("Q1" indicating poor quality to "Q5" indicating high quality) for each event. This is a subjective parameter indicating the confidence of Thompson and Myers (2009) that the transient event observed is really an EIT wave. A "Q5" rating refers to a confidence level of nearly 100% and these events can definitely be identified as EIT waves.

Restricting ourselves to just the five Q5 events that are classed as EIT waves with near 100% certainty, the catalogue records the following transients:

7th April 1997, 12th May 1997, 24th September 1997 (02:32 UT), 21st October 1997 and 29th April 1998. The sketches for these events are shown in Figure 4.14. The 7th April and 12th May 1997 events are identified as semi-isotropic events already in both the catalogue and the literature (Podladchikova and Berghmans, 2005a; Attrill *et al.*, 2007a). The 24th September 1997 (02:32 UT) event is identified as an S-wave event, but running difference images capture the later diffuse bright fronts showing a semi-isotropic nature (also see Figure 3.2). The 21st October 1997 event is identified as semi-isotropic in the catalogue. Finally the 29th April 1998 event is identified as being almost semi-isotropic in the catalogue, but with no expansion to the south. We believe that this is due to the presence of the south polar coronal hole preventing the expansion of the bright front in a southerly direction. We therefore conclude that *all* Q5 events can be described as semi-isotropic diffuse events.

The catalogue also records sixteen "Q4" events which are identified as EIT waves with $> 75\%$ confidence. Figure 4.15 shows examples of two Q4 events; one disk event (1st April 1997) and one

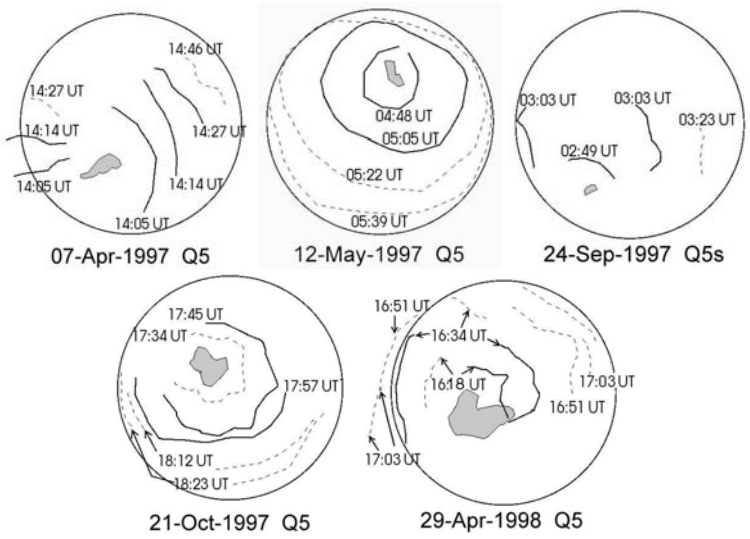

Figure 4.14: Q5 events identified in the Thompson and Myers (2009) EIT wave catalogue. Permission to reproduce these figures has been granted by B. Thompson.

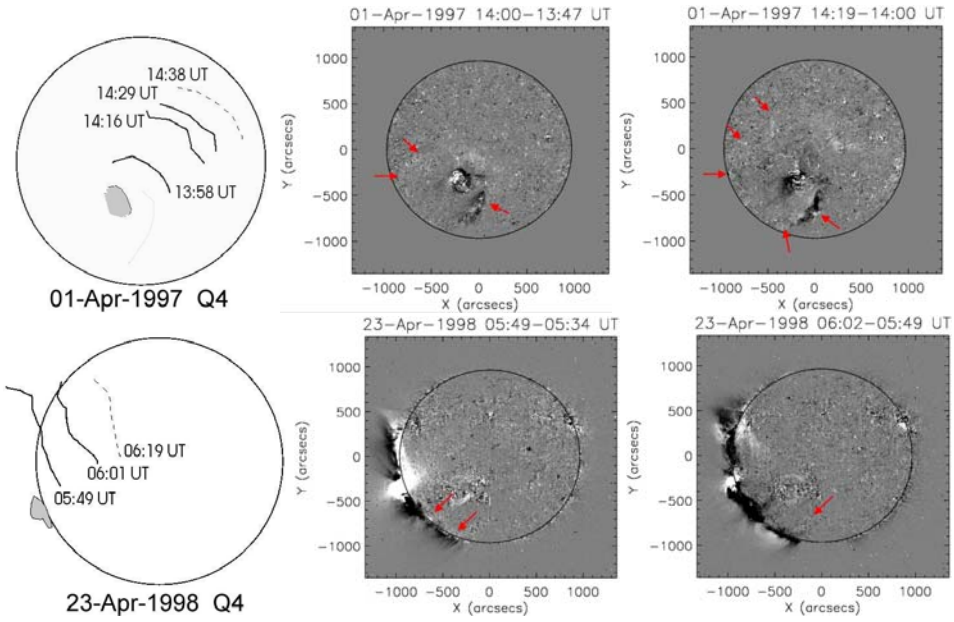

Figure 4.15: Examples of disk (top) and limb (bottom) Q4 events identified in the Thompson and Myers (2009) EIT wave catalogue. Left panels show sketches from the catalogue, identifying the strongest bright fronts. Center and right panels show running difference images of the events. Red arrows indicate more subtle bright fronts, not included in the catalogue. Permission to reproduce the figures in the left column has been granted by the B. Thompson.

limb event (23rd April 1998). The remaining fourteen Q4 events are detailed in Appendix C.

- 1st April 1997. The catalogue identifies this event as expanding only to the north-west. However, running difference images clearly show the disturbance also expands to the south of the active region. To the south the disturbance seems to "stop" at the same place from 14:00 to 14:31 UT (at least). This persistent feature is located right along the boundary of the south polar coronal hole. Also to the solar east, expanding features are discernable in the running difference movie.
- 23rd April 1998 is an event on the east limb. The catalogue only shows expansion to the north

(on the disk and above the limb), but running difference images also show disturbance on the disk and above the limb to the south. We consider that the identification of expansion to the north and south as well as to the west, on disk, are consistent with interpretation as a semi-isotropic expansion, should it have been observed on-disk, rather than on the limb.

A similar description and analysis is made for the other fourteen Q4 events in Appendix C.

Thompson and Myers (2009) emphasise that the identification of the bright fronts is subjective and done by eye. We stress that this section is not meant to criticise their valuable work, simply to address the misconception currently widely prevalent in the solar research community that EIT waves are only seldom identified as being semi-isotropic. We have shown here (and in Appendix C) that *all* EIT waves independently identified as such with more than 75% confidence, are in fact, semi-isotropic. We are able to highlight subtle bright fronts previously not identified in the Thompson and Myers (2009) work because we are working with the *expectation* from our model, that EIT waves *should* be semi-isotropic, corresponding to the footprint of the CME bubble, which at solar minimum is not disrupted significantly by surrounding magnetic structures. This section shows that close scrutiny of the difference images reveals features consistent with a diffuse bright front that expands semi-isotropically.

4.5 Coronal waves are not necessarily associated with active regions

Another prevalent perception is that the source region of a coronal wave is commonly understood to be an active region transient (flare or CME; Warmuth, 2007). Although this holds true for the majority of events, it is not necessarily the case. Coronal waves associated with quiescent filament eruptions, as well as their active region counterparts, were identified by Attrill *et al.* (2004). The following example (Figure 4.16) shows EIT 195 Å base difference images of a quiescent filament eruption that occured on 19th May 1998. The coronal wave associated with this event is categorised in the catalogue of Thompson and Myers (2009) as a "Q3" event. According to their definition, the transient event is independently classed as really being an EIT wave with a confidence level of $>$ 50%. A large quiescent prominence erupts, driving the diffuse coronal wave bright front ahead of it. Association with an active region source is therefore *not* a necessary requirement for classification as an EIT wave, rather we consider that an erupting flux rope is required to generate a diffuse bright front. Tripathi and Raouafi (2007) also recently reported a diffuse EIT wave associated with a quiescent filament eruption.

4.6 Large-scale CMEs and global coronal "waves" as a subset of CMEs

From our model, *all* CMEs with any lateral expansion are expected to interact with the surrounding low coronal magnetic environment, generating a coronal "wave". However, it is plausible that the cadence of current instrumentation is too low to detect much less than really global-scale events. An additional observational problem with CMEs that do not have a strong horizontal expansion could be that in such cases, the EIT "wave" would stay close to the eruption site, so it

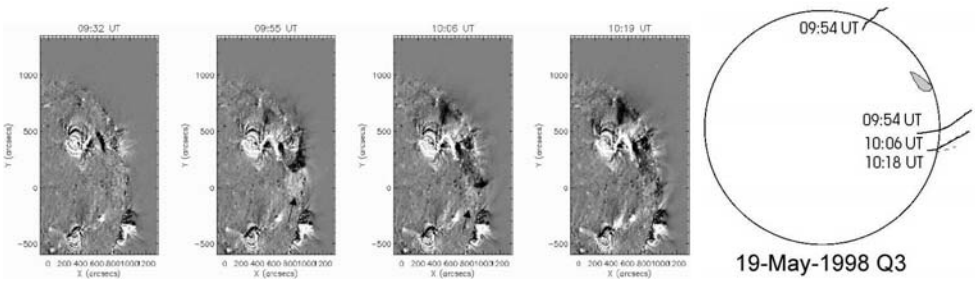

Figure 4.16: Base difference images showing a quiescent filament eruption and associated diffuse EIT wave event on 19th May 1998. The bright coronal wave front is indicated by black arrows. The base image used for subtraction is at 07:34 UT. The right panel shows a sketch for the same event from the Thompson and Myers (2009) catalogue, where the coronal wave is identified as a "Q3" event (with a confidence level > 50%). Permission to reproduce the figure in the right panel has been granted by B. Thompson.

may be masked by the flare brightness. In order to examine the relationship between large-scale CMEs in the low corona and their expected one-to-one correlation with global-scale coronal "wave" events, a study of all large-scale limb CMEs was made between January 1997 and June 1998. We aim to test prediction (i) of our model (§4.2.2), that all large-scale CMEs have a coronal "wave" footprint. The criteria for event selection are explained below:

- The limb CMEs viewed in LASCO/C2 data had to reach a lateral extent of $\geq 2R_{\odot}$ (cone angle of $\geq 40°$) when at a distance $< 3R_{\odot}$ from the solar surface. This apparently arbitrary condition ensures that the CME must be truly global-scale whilst still in the low corona.
- Both LASCO/C2 and good cadence ($\sim$ 12 minute) EIT 195 Å data had to be available.
- No halo or partial halo CME events are included, unless the source can be unambiguously identified and is clearly within 60° of the limb (e.g. 6th November 1997, 25th January 1998, 20th, 23rd and 27th April 1998, 6th, 9th, 19th and 27th May 1998, 11th June 1998).
- In the absence of a low-coronal signature of a CME (coronal wave, dimming, flare, filament eruption or post-eruptive arcade), the CME is classed as probably being a far-side event.

Data on whether a flare occurred at the time of the CME is taken from GOES using `pr_gev` in *Solarsoft*.

Table D.1 is displayed in Appendix D and details all the large-scale limb CMEs meeting our criteria between January 1997 and June 1998. Table D.1 shows the time at which the limb CME is first detected in LASCO/C2 data and the time at which the CME is classed as being large-scale ($\geq 2R_{\odot}$) in LASCO/C2 data. Table D.1 indicates events where there is a low-coronal signature associated with the CME. CME events that have a coronal wave counterpart (identified in EIT running difference data) are also highlighted.

Table 4.2 places the large-scale CMEs identified in Table D.1 in context with all limb CMEs observed for the given dates. (The number of limb CMEs is taken to be all CMEs in the LASCO-CME catalogue (Yashiro *et al.*, 2004), minus any marked halo or partial halo. Since we do not determine the source regions of each limb CME, some will be far-side and some will have origins further than 60° from the limb. Therefore, this number constitutes only an estimate of the total number of limb CMEs detected by LASCO. We consider that this is still useful for giving our study some context, so that we can estimate what percentage of CMEs are classified as large-scale

Table 4.2: Wide CMEs constitute only a subset (< 20%) of CMEs. A "wide" CME is defined for our study as reaching a lateral extent of $\geq 2R_\odot$ (cone angle of $\geq 40°$) when at a distance $< 3R_\odot$ from the solar surface. (See main text).

Month	No. Limb CMEs	No. wide CMEs	% wide CMEs
January 1997	19	1	6%
February 1997	20	0	0%
March 1997	16	0	0%
April 1997	21	2	10%
May 1997	37	4	12%
June 1997	32	2	6%
July 1997	30	1	3%
August 1997	25	2	8%
September 1997	41	6	15%
October 1997	34	6	18%
November 1997	42	4	10%
December 1997	32	1	3%
January 1998	58	11	19%
February 1998	81	6	7%
March 1998	74	6	8%
April 1998	81	4	5%
May 1998	92	15	16%
June 1998	105	10	10%

according to the criteria explained above).

From this study, we conclude that < 20% of the limb CMEs in the survey reach a lateral extent of $\geq 2R_\odot$ (cone angle of $\geq 40°$) when they are at a distance $< 3R_\odot$ from the solar surface. Therefore, CMEs with such a wide lateral extent in the low corona constitute only a subset of CMEs. St. Cyr *et al.* (2000) plot the apparent angular size of CMEs from January 1996 to June 1998, observed in LASCO/C2 data at typically 2.0 - 2.5 $R_\odot$. They find significant "tails" to the distributions, showing CMEs with an apparent size larger than $\sim 115°$. They find that these large events comprise $\sim 13\%$ of the total number of CMEs detected by LASCO. Our results are consistent with those of their study.

Our study deliberately focuses on CMEs which exceed the average angular size of CMEs (e.g. $\sim 45°$, $\sim 40°$ and $\sim 47°$; Howard *et al.*, 1985; Hundhausen, 1993; St. Cyr *et al.*, 2000, respectively). In our sample, where there is an unambiguous solar front-side coronal counterpart to the CME (e.g. flare or filament eruption) *all* CMEs with this large lateral extent have associated diffuse coronal EIT "wave" counterparts.

Summary of statistical study results presented in Table D.1 (Appendix D):
- 81 large-scale limb CME events identified between January 1997 - June 1998.
- 20/81 events have no coronal wave or associated flare or filament eruption. These are likely to be far-side events.
- 6/81 events could plausibly be temporally associated with flares, but either the location of the flare could not be identified unambiguously, or there was no plausible spatial association between the flare and CME (i.e. flare occurred on the opposite limb of the Sun to the CME).
- So 61 CMEs are likely to be front-side events, 55 of these have clear front-side signatures (either flare or filament eruption).
- All 55 large-scale CMEs with a front-side source region have associated diffuse coronal "waves".

The survey results show that *every* front-side CME that has a large lateral extent in the low

corona has an associated EIT wave. We consider that this work may suggest an answer to the question of why not every CME has an associated coronal EIT wave, even though every coronal wave is associated with a CME (Biesecker *et al.*, 2002). Not every CME has an associated EIT wave because not every CME is large-scale enough to drive reconnections with the surrounding magnetic field to such a lateral extent that the bright front will be detected by EIT at its imaging cadence of 12-17 minutes. These results are in agreement with the finding of Cliver *et al.* (2005) that the median width of 25 fast (> 700 km s^{-1}) CMEs that were associated with EIT waves was 165°. However, there seems to be a disagreement with their result that the median width of 31 such CMEs that lacked EIT waves was 60°. (Our results suggest that for any front-side CME with a cone angle $\geq 40°$, there should be a coronal "wave" counterpart footprint. Cliver *et al.* (2005) do not provide the dates of these events, so we do not explore this apparent discrepancy further at this time). Biesecker *et al.* (2002) conclude that "there does not appear to be a need for impulsive, fast CMEs for there to also be an EIT wave." Indeed, our results also suggest that the requirement for a diffuse coronal "wave" is that the CME is large-scale enough in the low corona for detection at a given cadence.

We reach this conclusion because it is the lateral expansion of the CME in the low corona that, via reconnections with surrounding quiet Sun magnetic loops generates the EIT "wave". The majority of CMEs do not expand significantly in the lateral direction (Robbrecht, 2007). Therefore, most CMEs are, in principle, bad candidates for EIT waves. What makes the difference between a large-scale and narrow CME? It will depend to a large extent on the magnetic over-pressure. (We note that here "narrow" refers to narrow bubble-like CME events with a core magnetic structure, we do not include narrow jet-like CME events in this discussion). Events with a high core pressure compared to that of the surrounding magnetic environment are expected to expand more strongly in the lateral (as opposed to purely radial) direction. (Gopalswamy and Thompson (2000) also discuss the non-radial propagation of CMEs during their early phase). These CMEs are thus more likely to drive interactions with the low-coronal magnetic environment and are expected to generate lower-coronal disturbances including EIT coronal "waves" and dimming signatures that reach further away than events with a lower ratio of core-to-surrounding field pressure which will have a smaller cone-angle and will be less extended. The coronal "wave" will naturally stop when the internal pressure is no longer large enough to drive the reconnections.

Another reason for disparity in the CME-coronal "wave" relationship may be understood as follows. The erupting CME field and thus the leading-edge reconnections will occur with the structures that interact with the expanding CME magnetic field first. If there are large-scale field lines linking to distant active regions and the interfacing reconnecting flux densities are sufficient, then the CME outer shell will be stepped out to the opposite end of the large-scale linking field line. Thus the outer shell of the expanding field is not able to interact with the small quiet Sun loops underneath the linking field line (the QS loops are "protected" from reconnection) and the CME simply steps over them. An example of such an event is the eruption on 28th October 2003, where the reconnection "stepping" happens primarily with the large-scale magnetic structures (with strong magnetic flux densities, so the surrounding active regions), rather than with quiet Sun loops (details in Mandrini *et al.*, 2007, and chapter 5). No coronal "wave" is observed until the CME footprint has stepped out through all the ARs, finally reaching isolated patches of QS magnetic field. Therefore, it is expected that there are CME events where no discernable coronal "wave" will be observed, only coronal dimming resulting from the CME expansion. However, when a diffuse coronal "wave" is observed, according to our model, it must *a priori* be accompanied by coronal dimming.

4.7 Implications of our model: *How* CMEs become large-scale *in the low corona*

Despite much work on the CME phenomenon, some fundamental questions remain unanswered. For example, Dere *et al.* (1997): "Initiation begins in a small volume. The initiation of a large-scale CME in a small-scale eruption is a key fact that must be included in our understanding of the creation of CMEs". Similarly, Klimchuk (2001): "coronagraph observations suggest that the horizontal scale of the opened field can be many times greater than that of the reconnection arcade, and this may be difficult to reconcile with the geometry of the [existing] model[s]". van Driel-Gesztelyi *et al.* (2008) note that the observed extent of coronal disturbances well matching the angular width of CMEs is not strongly featured in any current understanding of the low-coronal development of CMEs. Recent work by Zhukov and Veselovsky (2007) on global-scale coronal dimmmings highlights the current lack of understanding concerning local and global eruption phenomena: "In most ... CME events, ... there is at most one post-eruption arcade ... although multiple magnetic flux systems may erupt. The interplay between global (e.g. dimmings) and local (e.g. post-eruption arcade) phenomena in the process of energy release during CMEs is not clear."

Zhang *et al.* (2004) suggest that the disparity between the flare region size and the CME size is caused by the super-expansion of the CME in the low corona during its acceleration phase, and that the expansion can be non-radial (i.e. lateral). In light of our work and the discussion presented here, we consider that our proposed model explains specifically *how* the horizontal scale of the erupting field in the low corona *naturally* becomes many times greater than the initial erupting configuration by successive reconnections, driven by significant expansion in the low corona. We note that this is a process which is forced to occur independently of the type of mechanism driving the eruption, and hence we are not concerned here with the initial trigger mechanism of the CME, rather the early stages of its development in the low corona.

Many previous works have considered that CMEs start small-scale, from a local source region and *evolve* to become large-scale due to interaction with surrounding large-scale magnetic structures (e.g. Manoharan *et al.*, 1996; Webb *et al.*, 1997; Pick *et al.*, 1998; Maia *et al.*, 1999; Delannée and Aulanier, 1999; Pohjolainen *et al.*, 2001, 2005; Mandrini *et al.*, 2007; Moore *et al.*, 2007). Indeed, signatures of these interactions are detected by radio bursts of nonthermal origin, in the dm-m wavelength domain (Pick *et al.*, 1998; Maia *et al.*, 1999; Pohjolainen *et al.*, 2001, 2005; Pick, 2006). The importance of the large-scale surrounding magnetic topology is also highlighted in studies by Delannée and Aulanier (1999); Delannée (2000); Delannée *et al.* (2007), linking dimmings and distant stationary brightenings to the locations of separatrices and QSLs in the large-scale topology.

But what about at solar minimum, when the solar disk is devoid of large-scale coronal structures? CMEs and coronal "waves" also clearly occur (indeed, preferentially so) in quiet Sun prevalent at solar minimum. In such cases, the large-scale magnetic topology required for the CME to become large-scale (as in the works mentioned above) simply does not exist! The contribution that our model makes is to consider not just the large-scale magnetic environment, with its pre-existing associated separatrices and QSLs, but to consider the *entire* surrounding magnetic environment, and how it is affected by, and reacts to, the dynamic expansion of another magnetic flux system in the form of a CME.

4.8 How does our model fit with the observations?

We consider that any successful understanding of EIT waves must be capable of robustly explaining the observations identified and numerically listed in chapter 3. We summarise below how our model fits these observational constraints.

1. **Huge range of coronal wave velocities** - The coronal "wave" in our model progresses at whatever speed the CME expands in a lateral direction, even below v_A.

2. **The bright front becomes broader, more diffuse and less intense as it expands further from the source region** - Podladchikova and Berghmans (2005a) find with expanding distance, r, the diffuse bright front broadens as a function $1/r^2$. This is expected from a stocastic process such as random reconnections with quiet Sun magnetic loops of a range of lengths. In addition, since the CME bubble expands $\propto 1/\mathrm{r}^2$, so the flux density of the CME magnetic field decreases as $1/\mathrm{r}^2$, and the intensity drops as the brightening from the reconnections becomes less concentrated. As the CME progresses, it is expected to reconnect with progressively larger quiet Sun loops, also contributing to the broadening, diffusion and decrease in intensity of the bright front.

3. **Coronal waves are observed to deflect magnetic features** - When the magnetic polarity is unfavourable for reconnection, the magnetic pressure from the CME expansion will instead compress the magnetic field, inducing a directional pressure pulse which could trigger loop oscillations. Our model does not exclude the presence of MHD waves as well, which may also instigate oscillations.

4. **Diffuse coronal waves can rotate** - In our model the bright front is driven by the expanding flux rope. If the flux rope rotates upon eruption, plausibly as a result of the kink instability (e.g. Török *et al.*, 2004; Török and Kliem, 2005) then the bright fronts will also be observed to rotate.

5. **There is no close association between coronal waves and the magnitude of flares** - Our model is independent of flares and so requires no such association. Although large flares (e.g. X-class) are generally associated with large-scale CMEs and therefore coronal waves, even relatively small flares can be associated with large-scale CMEs and top-quality (Q5) coronal waves (e.g. 12th May 1997 event discussed in this work only had a C1.3 class flare). Indeed, we have shown that even a quiescent filament eruption (ranked as a Q3 event by Thompson and Myers (2009)) associated with a B7.9 flare, can drive a diffuse coronal wave. Our model requires an expanding magnetic flux rope to drive successive reconnections with the surrounding magnetic environment to generate a diffuse coronal "wave" bright front. There is no requirement for a flare.

6. **Every coronal wave is associated with a CME**, but the converse does not apply - Our model requires a CME to drive the coronal "wave" footprint. Discussion on why the converse may not apply is discussed in the context of our model in §4.6.

7. **Coronal waves are observed primarily in the ambient quiet Sun corona** - Our model specifies that the diffuse bright front is formed by reconnections with quiet Sun loops.

8. **Coronal waves do not traverse active regions or propagate into coronal holes** - The CME outer shell will either slow down substantially, or vanish upon meeting such structures. The CME may "step" *over* an active region if the magnetic orientation is favourable for

reconnection to occur. Expansion of the bright front *into* coronal holes will be dependent on the size and accessibility of the closed loops within the coronal hole.

9. **Coronal waves have a 3-D nature**, such that the transients can be observed extending beyond the limb of the Sun - The coronal "wave" bright front in our model is only the low-coronal footprint of the CME. The outer shell of the CME indeed extends in 3-D.

10. **The brightening is a transitory phenomenon** - Our model suggests the brightening is due to series of weak flare-like events. This brightening is a transitory process and once the heated plasma cools, the brightening will disappear.

11. **Coronal waves decelerate as they expand** - The lateral expansion of a CME decelerates, thus the coronal "wave" in our model must also do so, since it is directly driven by the CME's lateral expansion.

12. **Velocity of coronal wave and velocity of CME in same directions are proportional** - Naturally expected from our model, since the coronal "wave" is identified as the low coronal footprint of the CME.

13. **There is a weak (statistically insignificant) trend for EIT wave quality (high rating = clearly defined bright front) to increase with CME speed** - Our model requires a large-scale CME to produce an observable EIT wave. We do not expect a strong dependence of EIT wave quality on the speed of the CME, since even a slowly expanding CME may interact and reconnect effectively with the surrounding magnetic field, producing a well-defined bright front.

14. **There is a definite trend for CME-EIT wave association to increase with increasing CME speed** - Fast CMEs may be driven by a high core pressure, and are therefore likely candidates for becoming large-scale in the low corona. It is this large-scale condition that is required for the CME to interact strongly with the surrounding magnetic field over a large spatial area facilitating detection in observations.

15. **CME width is an important factor for EIT wave formation/detection** - We have shown that for truly large-scale CMEs ($\geq 2\mathrm{R}_{\odot}$) in the low corona ($< 3R_{\odot}$), there is *always* a corresponding EIT wave. In our model, the lateral expansion (width) of the CME in the low corona directly determines the extent of the EIT "wave".

16. **Coronal dimmings manifest following the expanding bright front** - This is a natural consequence of our model. The reconnections make the surrounding magnetic field part of the CME, leading to plasma evacuation within the expanding CME volume.

17. **Stationary/persistent bright fronts** are sometimes found at coronal hole boundaries - When the magnetic polarities are favourable for reconnection to occur, an apparently stationary bright front is expected to form. We have shown that in cases unfavourable for reconnection, the bright front instead vanishes.

18. **Coronal waves are observed in many different EUV bandpasses** - Our model suggests small flare-like events may be responsible for generating the bright fronts so observation of the bright front in many different EUV bandpasses is expected.

19. **A diffuse coronal wave has similar kinematics in four different EUV bandpasses** - This observation is expected from our model, since the bright front is formed by weak flare-like events, thus effecting many layers of the solar atmosphere simultaneously.

20. **Bright front: due to density or temperature enhancement?** - The reconnections in our model will generate both.

21. **Formation altitude of coronal waves** - Coronal "waves" must be generated in the low corona in our model, in order to produce the observed projection effect of the shift of the coronal "wave" centre toward disk centre as the bright front expands (see §4.1.1.1 and Appendix A). Feldman *et al.* (1999) showed that at temperatures $\sim 1.4\times10^6$K, the quiet Sun is populated by loops at heights of 1.03-1.5 $R_\odot$ (716 - 1044 Mm). Since our model requires reconnection with quiet Sun loops, the coronal "wave" bright front formation in our model is not expected to exceed this approximate height range. Because the bright front in our model is formed by flare-like events and the loop generated by the reconnection will be shorter than the quiet Sun loop with which the expanding CME shell interacts, so the altitude of formation of the bright front will depend on the height and length of the quiet Sun loop encountered by the expanding CME.

A summary table is shown below, outlining the various models described in chapter 3 (including our contribution, described in §4.2), along with the non-viable points for each model.

Notes for Table 4.3:
Note 1: A blast wave shouldn't show any rotation, let alone a coherent rotation, which appears to depend on the helicity of the CME.
Note 2: The existence of a piston-driven fast-mode MHD wave should not depend on the polarity of the magnetic field that it encounters.
Note 3: A fast-mode MHD shock should travel at speeds exceeding the Alfvén velocity of the corona.
Note 4: The velocity of MHD soliton-waves should increase with larger amplitude waves. It is expected that this be detected as a function of the intensity of the bright front.
Note 5: The electric current shell model (Delannée *et al.*, 2008), depends on the integration of the current shell along the line-of-sight, projected onto the solar disk, to create the perception of an EIT wave bright front. This line-of-sight integration does not occur when we view limb EIT wave events.
Note 6: The Delannée and Aulanier (1999); Delannée (2000); Chen *et al.* (2002, 2005a,b) models, in which the bright front is created by the compression of plasma (due to magnetic field lines being stretched during eruption of a flux rope) implies that the existence of the bright front should be independent of the magnetic polarity of the surrounding magnetic field.
Note 7: The driven magnetic reconnections between the CME and the surrounding magnetic field in the Attrill *et al.* (2007a) model described in this chapter, mean that the bright front will slow dramatically (appear almost stationary) when the surrounding magnetic field is of a polarity favorable for reconnections to occur. If the polarity is unfavorable, the bright coronal EIT "wave" front should vanish.

4.9 First steps toward numerical simulation of our model

This section describes work in collaboration with Duncan Mackay (St. Andrews University).

The sample initial condition is a fully 3-D field. Cuts in the x-y and x-z plane are shown here (Figure 4.17) for ease of interpretation. The initial condition was produced by defining

Model	Pressure-pulse fast-mode MHD waves	Piston-driven fast-mode MHD waves	Freely propagating fast-mode MHD shock	MHD soliton-like waves	LOS integration of CME electric current shell	Pressure increases due to expanding magnetic field	Driven magnetic reconnections
Velocity	Must be $\geq$ v_A	Must be $\geq$ v_A	Must be $\geq v_A$ (Note 3)	Should vary $\propto$ Intensity (Note 4)			Should = lateral expansion velocity of CME
Intensity	Increase	Increase	Increase	Increase	Increase	Increase	Increase
CME Helicity Dependence	None expected (Note 1)	Possible			Possible	Possible	Yes, directly
Density	Increase	Increase	Increase	Increase	Increase	Increase	Increase
Temperature	Increase	Increase	Increase	Increase	Increase	Increase	Increase
Velocity Flows	None expected	None expected	None expected	None expected	None expected	None expected	Upflows
Relationship with B	Does not propagate $\|\|$ B	Does not propagate $\|\|$ B	Does not propagate $\|\|$ B	Must have some $\|\|$ B propagation	Bright front confined to LOS projection of CME I shell	Expansion extent $\propto$ |B| surroundings	Expansion $\propto$ |B| surroundings
Surrounding Polarity of B		Irrelevant (Note 2)				Irrelevant (Note 6)	Bright front stationary / vanishes (Note 7)
CME width vs bright front ext.	No correlation	No correlation	No correlation		Correlation expected	Strong correlation	Strong correlation
Additional Comments					Model fails to explain limb events (Note 5)		

Table 4.3: Summary of how observed physical properties can constrain the various models for EIT waves. NON-VIABLE POINTS OF EACH MODEL ARE HIGHLIGHTED (see notes).

a bipolar flux distribution about the origin and then constructing a potential magnetic field from it. Initially the four other flux regions to either side are not present. The four independent bipoles are then inserted, two on either side of the main bipolar flux distribution. In the side view picture (x-z plane, bottom panel Figure 4.17) you can see the 2-D representation of the X-points. The initial set-up thus looks promising for our model, since the X-points between the main flux distribution (representing the CME core field), and the surrounding quiet Sun loops indicate locations where magnetic reconnection is expected to occur.

Inserting this initial condition into an MHD code will test the dynamic evolution. This is currently difficult to do numerically, and so this remains an open project, presenting a challenge to solar researchers working with numerical simulations. Does a dynamic simulation behave in the manner of our model? Does the CME become large-scale in the low corona through reconnection with surrounding small-scale magnetic loops as suggested?

4.10 Summary of chapter

The work presented in this chapter has introduced several new observational constraints (in addition to those numerically listed in chapter 3) that must also be considered when striving to develop a comprehensive understanding of coronal waves:

• **Diffuse coronal waves rotate in the sense determined by the magnetic helicity of the CME source region** (Attrill *et al.*, 2007a). This is an extension to the work of Podladchikova and Berghmans (2005a), and our model directly attributes the behaviour of the bright front to that of the expanding flux rope.

• **Diffuse coronal waves are generated in the low corona** (Attrill *et al.*, 2007a). We have shown that there is a projection effect (described in §4.1.1 and Appendix A) which shifts the projected centre of the coronal "wave" toward disk centre as the bright front expands. This implies that the surface curvature is important. So this work adds to the evidence regarding the low corona formation altitude of coronal waves, which is the specified region for formation of the bright front in our model (No. 21).

• **Diffuse coronal waves have a magnetic *restructuring* nature**, since it appears that the interacting polarities determine whether the bright fronts become apparently stationary or if they vanish upon interaction with concentrated regions of magnetic field (Attrill *et al.*, 2007b). This constraint suggests that the diffuse bright fronts are not simply due to compression of the plasma, or to MHD waves as suggested in other models, rather magnetic reconnection must play a pivotal role.

• **Coronal wave bright fronts and dimmings are strongly coupled** (Attrill *et al.*, 2007a,b; Mandrini *et al.*, 2007). In each of the case studies presented in this chapter, the bright front is observed to preceed widespread, diffuse dimming. Core, deep dimmings are also identified remaining close to the post-eruptive arcade for each event. We are not the first to notice this coupling, or to comment on it (e.g. Thompson *et al.*, 2000b; Gopalswamy and Kaiser, 2002; Zhukov and Auchère, 2004; Delannée *et al.*, 2007), but the model that we have developed explains the *two types* of dimming (plasma evacuation) as a direct consequence of the bright front (reconnection), intrinsically coupling these two phenomena.

• **Coronal waves are not exclusively initiated in active regions**. This is a common misconception (e.g. Klassen *et al.*, 2000; Warmuth, 2007; Delannée *et al.*, 2008) and is not necessarily the case, as we have demonstrated in §4.5. Tripathi and Raouafi (2007) also recently report an EIT wave (diffuse type) from a quiescent filament eruption. Rather than

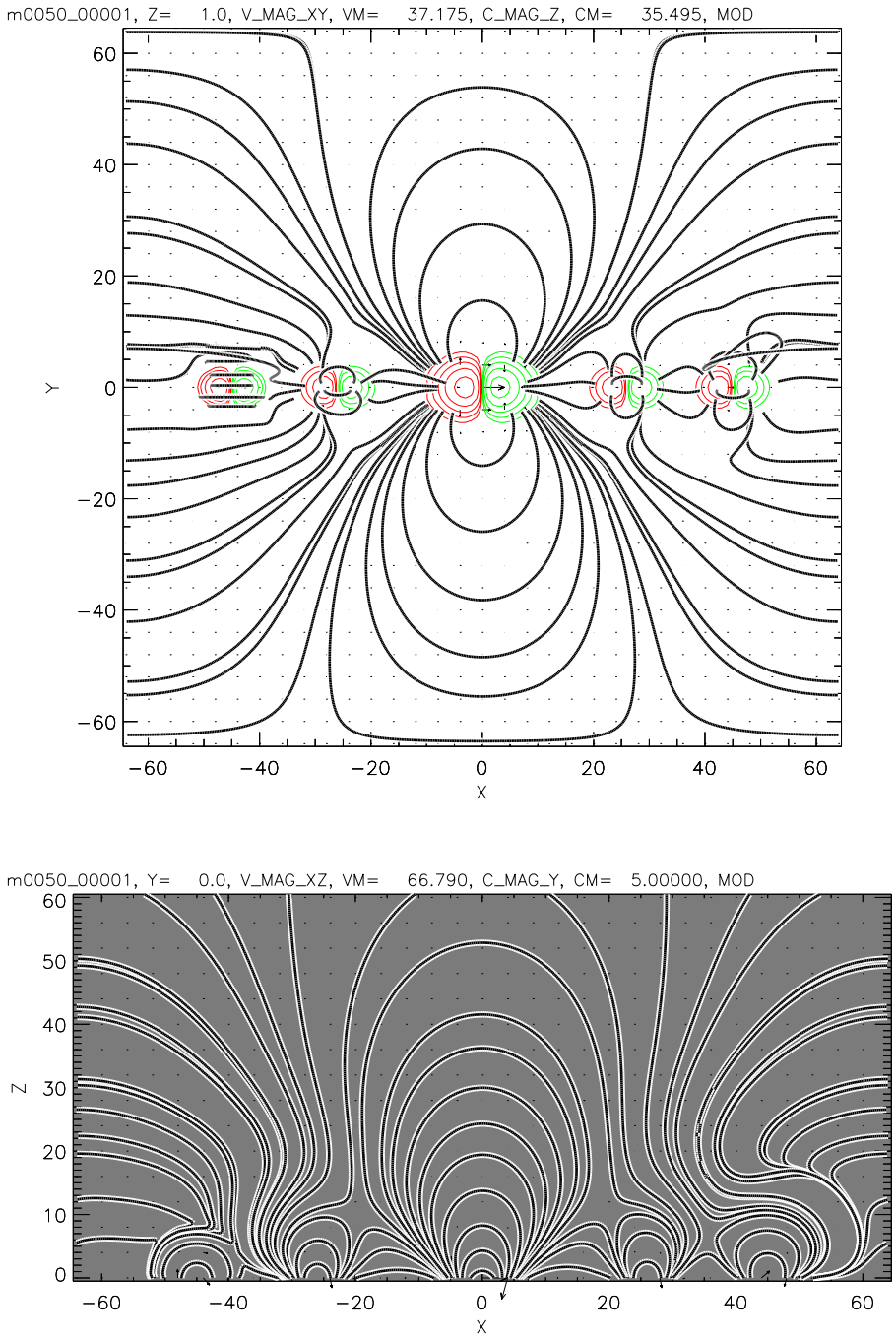

Figure 4.17: 2-D "slices" of 3-D numerical simulations produced by Duncan Mackay. Top panel shows a cut in the x-y plane, showing a bird's eye view of the initial condition. Bottom panel shows a cut in the x-z plane, showing a side-on view. This work is the first step toward taking our cartoon sketch (Figure 4.7) into the domain of numerical simulations. The next step is to dynamically drive this initial condition.

an active region, our model identifies that an expanding magnetic structure (i.e. a flux rope) is the necessary component required to generate the coronal "wave" bright front.

• **All confidently identified coronal waves are semi-isotropic.** It is commonly perceived that coronal waves are only rarely semi-isotropic. E.g. Delannée *et al.* (2008) report that "very few events display a clearly propagating EIT wave with an almost circular shape". Indeed only 4 have been reported in the literature so far. However, we have shown that *all* coronal waves independently identified with $> 75\%$ confidence level in the Thompson and Myers (2009) catalogue have a semi-isotropic nature. This morphology is an expected feature of our model, which considers the diffuse coronal "wave" bright front to be the magnetic footprint of the CME's semi-isotopic, bubble-like expansion in the low corona.

Several of the new observations of diffuse EIT coronal wave bright fronts presented in this chapter struggle to find a natural or comprehensive explanation when interpreted within a wave context, as plasma compression or as CME-associated current shells which form high in the corona. The primary reason for our inability to reconcile observations with these interpretations is because we have shown that diffuse coronal "waves" have a magnetic restructuring nature.

We propose a new model, where the diffuse coronal "wave" is understood to be the magnetic footprint of a CME. In this model, diffuse coronal "waves" form in the low corona, and the mechanism of formation is understood to be expansion of the core CME magnetic field into the surrounding quiet Sun environment, *dynamically* generating QSLs where reconnection is expected to occur generating weak flare-like events which constitute the diffuse bright front. We have discussed that our model has implications for developing our understanding of *how* CMEs become large-scale in the low corona, even though they may start from a very localised source region.

Chapter 5

Early-Stage Evolution of Coronal Dimmings

The work presented in this chapter focuses on the extensively studied eruption on 12th May 1997. This event is revisited, as it is an excellent case with which to present the specially-developed method of analysis. In the following sub-section, a synthesis of already published results is presented.

5.1 The event of 12th May 1997

The event occurred just after solar minimum, hence the magnetic structure of the Sun was relatively simple. The eruption originated in active region (AR) 8038 (N21W09) and was associated with a long duration GOES class C1.3 flare, starting at 04:42 UT and reaching its peak around 04:55 UT (Thompson *et al.*, 1998). AR 8038 was an isolated AR and the result of new flux emergence during Carrington rotation 1922.

A diffuse, semi-isotropic coronal wave signature with a velocity of 245 ± 40 kms^{-1} was associated with the eruption, and it has been noted that the appearance of the coronal wave coincided with the appearance of the coronal dimming regions (Thompson *et al.*, 1998). The coronal wave propagated fairly isotropically, emanating from or near AR 8038, exhibiting deceleration as it approached the north polar coronal hole (Thompson *et al.*, 1998).

A long emitting chain, visible as a conspicuous brightening, gradually encompassed the entire coronal hole boundary remaining visible for several hours (Chertok and Grechnev, 2003). Such a feature has also been observed in other events (e.g. 13th November 1994) and referred to as "Aurora Solaris" (Hudson *et al.*, 1996). Sterling and Moore (2001) reported a similar phenomenon which they termed "EIT crinkles".

There was also a filament eruption associated with this event. Webb *et al.* (2000) provided Hα data (see their Figure 2) showing the eruption to commence sometime between 04:43 UT and 04:47 UT. The LASCO/CME catalogue records a full halo CME associated with this eruption.

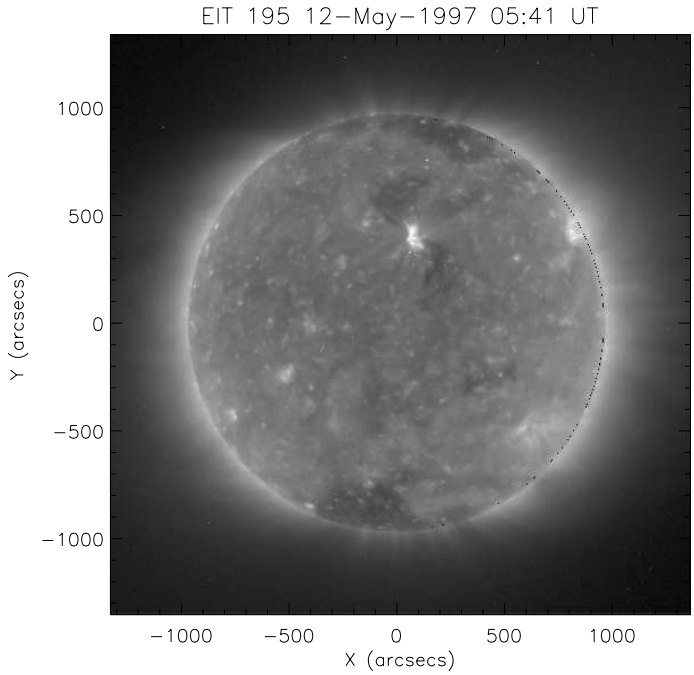

Figure 5.1: EIT 195 Å image showing the existing polar coronal holes and the two main dimming regions at 05:41 UT on 12th May 1997. The main dimmings appear to be adjacent to the bright flare loops. Permission to reproduce this figure has been granted by Springer Science and Business Media.

Figure 5.1 shows an EIT 195 Å image. The two main dimming regions can easily be identified, located slightly to the north of the centre of the solar equator. This image shows that the dimming regions have an intensity similar to the north and south polar coronal holes, hence the term "transient coronal holes".

Webb *et al.* (2000) provided a detailed analysis of this event. They measured the magnetic flux in the dimming regions, finding the north-east dimming to have a dominant negative polarity and the south-west dimming to have a dominant positive polarity. They suggested that the dual dimming regions that are joined to the flare loops may be the foot-points of a magnetic flux rope structure that erupts forming the core of the CME.

In the same paper, Webb *et al.* (2000) analysed the interplanetary events linked to the solar eruption. An interplanetary shock was observed arriving at the *Wind* spacecraft on 15th May at 01:15 UT, and a MC followed the shock at $\approx$ 10:00 UT on the same day. The authors modelled the interplanetary flux rope and computed its physical parameters which they compared to the corresponding coronal ones. The southward magnetic field associated with these structures lasted long enough to trigger a geomagnetic storm at Earth.

In this analysis, SOHO/EIT (Delaboudinière *et al.*, 1995) 195 Å data and Michelson Doppler Imager (SOHO/MDI, Scherrer *et al.*, 1995) magnetic maps are combined to build up a picture of the evolution of the dimming regions. *Yohkoh*/SXT (Tsuneta *et al.*, 1991) observations are also

used to study the global aspects of the event. The MC is modelled using *in situ* data from the Magnetic Field Investigation (MFI; Lepping *et al.*, 1995) aboard *Wind*, and compare its magnetic flux with that measured within the dimming regions. From the analysis of the asymmetric evolution of the unidentical twin dimming regions, a new scenario is derived that explains both the global observations of this event and the magnetic flux measurements in the associated MC.

5.2 Solar Data Analysis and Results

5.2.1 Processing EIT data

SOHO/EIT 195 Å full disk images, at approximately 17 minute intervals with a pixel size of $5.26''$, are used in this study. All EIT heliograms are differentially de-rotated to the same pre-event time (00:12 UT). To visualise the dimmings clearly, base difference images are produced where the same pre-event image is subtracted from all subsequent images. Base difference images (as opposed to running difference images) are used because false dimmings (due to a change in intensity of a bright structure or displacement of a feature between successive frames) can be created when using the running difference method (Chertok *et al.*, 2004; Chertok and Grechnev, 2005).

The dataset runs from 00:00 UT on 12th May 1997 until $\approx$ 00:00 UT on 14th May 1997 before limb brightening/darkening effects, due to the de-rotation, encroach on disk centre where the main dimming regions are located.

5.2.2 Defining the boundary of the dimmings

In order to carefully analyse the dimming regions, a quantifiable boundary must be imposed. Since a TCH is defined as a region where there is an intensity decrease from a "normal" intensity to that of a coronal hole (Rust, 1983), the contours are set to lie halfway between the intensity of an area of the quiet Sun and that of an existing coronal hole.

Figure 5.2 shows the main dimming regions and the application of the criterion described above to define the boundaries. It is encouraging to note that at the maximum spatial extent of the dimmings, the contour method highlights a region which is very similar to that corresponding to the "full size of the dimmings", automatically defined by the region-growing method of Podladchikova and Berghmans (2005a) (see their Figure 3d). Having defined the boundaries of the dimmings, it is possible to select separate regions for analysis. Figure 5.2 (right panel) shows the selected regions.

5.2.3 Temporal intensity evolution of the dimmings

Light-curves (see Figure 5.3) are generated from the EIT data in the selected regions to measure quantitatively the variation of emission in time. The light-curves are made for each region independently by averaging the EUV emission over the corresponding area (see Figure 5.2). In addition, the south polar coronal hole is examined, as well as a (relatively undisturbed) quiet Sun region of

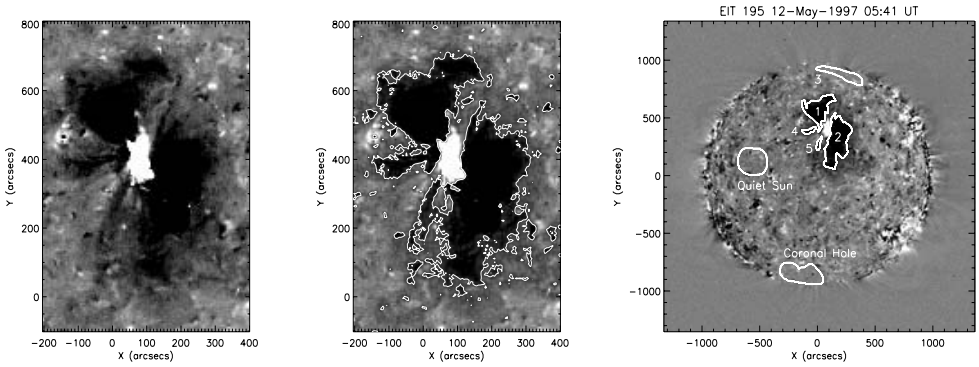

Figure 5.2: Left panel: Base difference image (05:41 UT - 00:12 UT) at the maximum spatial extent of the dimmings, showing the main dimming area. Centre panel shows the dimming regions defined by the contour boundary method. Right panel shows the regions selected for analysis. Regions 1 and 2 are the main dimming regions. Regions 4 and 5 are smaller dimming regions identified by the contour method. Region 3 is situated in the north polar coronal hole. Also shown are the (relatively undisturbed) quiet Sun and south polar coronal hole regions, used for comparison purposes in this study. Permission to reproduce this figure has been granted by Springer Science and Business Media

Table 5.1: Time of onset and of maximum dimming for each region.

Region	Dimming onset (UT)	Dimming maximum (UT)
1 (Main N dimming)	04:50	05:41
2 (Main S dimming)	04:34	09:10
4 (Small N dimming)	04:50	07:45
5 (Small S dimming)	04:50	09:10

the solar disk. The corresponding light-curves are shown for comparison at the base of each plot in Figure 5.3 with thin solid and thin dashed lines, respectively.

The intensity in the two main dimmings (regions 1 and 2) drops significantly at 04:50 UT and 04:34 UT, respectively. Region 3 (the north polar coronal hole) shows a significant gradual brightening to approximately the quiet Sun intensity level. Table 5.1 shows the time of the dimming onset and the time of the maximum dimming for each region, as inferred from the light-curves.

The light-curves can be used as a tool to visualise the physical restructuring of the magnetic field connectivity. The sharp drop in intensity seen in the light-curves is consistent with the process of plasma evacuation, caused by the rapid expansion or "opening" of the magnetic field during the initial phase of the eruption. The point where the intensity starts to recover is interpreted as the magnetic field experiencing a change in its physical condition, from an "open" towards a "closed" state that allows the re-accumulation of plasma, producing the observed recovery in intensity.

The results show that the time of the maximum dimming occurs in region 1 at 05:41 UT and in region 2 at 09:10 UT (see Table 5.1). Prior to this study, the dimming regions have been considered only as one unit, "twin" dimmings, rather than as separate entities (e.g. Thompson *et al.*, 1998, state that the strongest decrease in emission measure occurs near 06:22 UT).

The recovering intensity of the dimmed regions appears to be a relatively steady, gradual process, although the light-curves do show some variation. The sharp gradient visible in the light-curve of region 1, immediately after the point of maximum dimming is most probably due to the

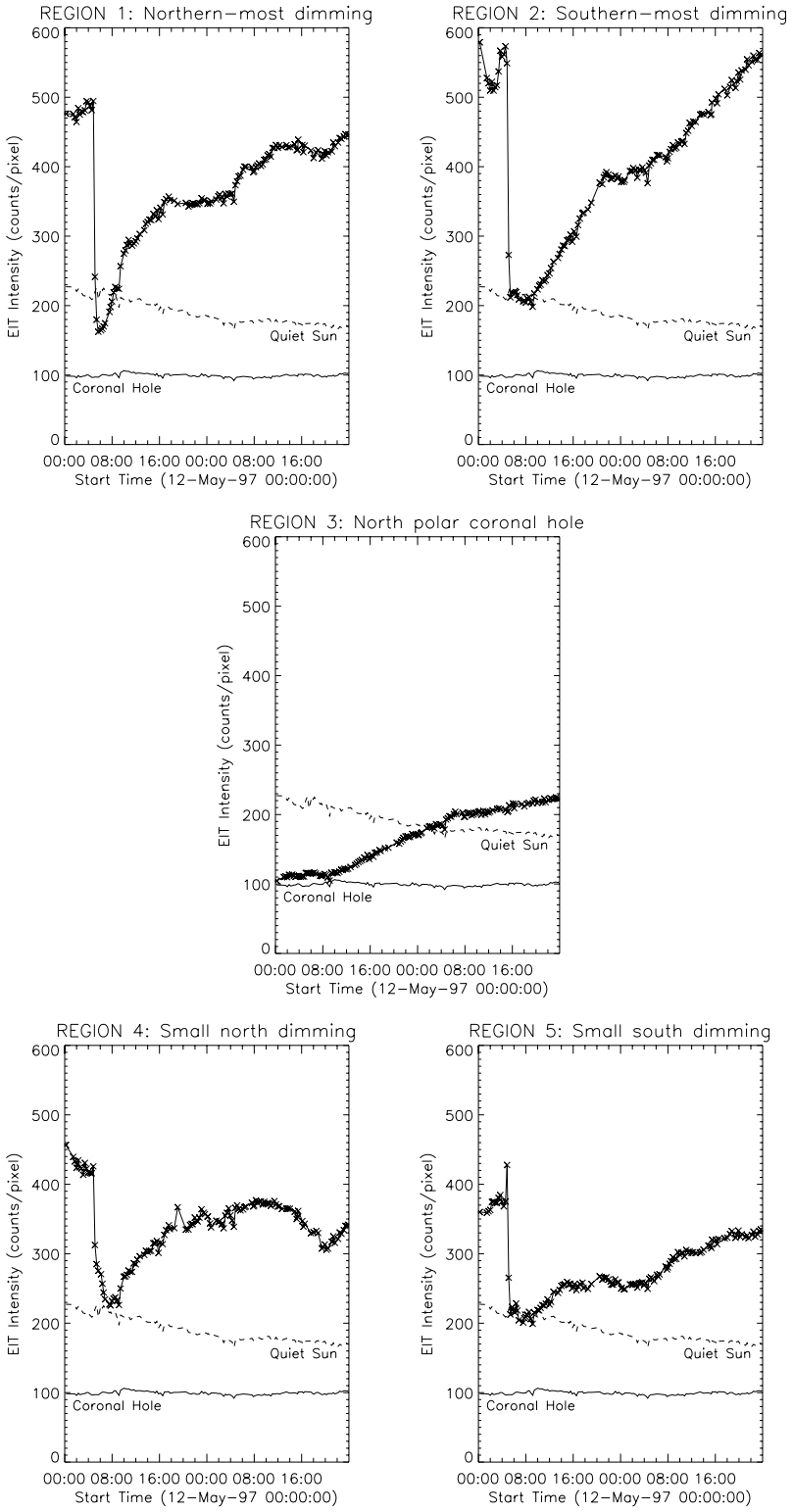

Figure 5.3: Light-curves showing the temporal variation in EUV intensity averaged over the selected region (counts/pixel). The light-curves are made from the static regions of interest shown in Figure 5.2. The thin solid and thin dashed light-curves at the base of each plot show the intensity variation in the (relatively undisturbed) south polar coronal hole and quiet Sun, respectively. Permission to reproduce this figure has been granted by Springer Science and Business Media

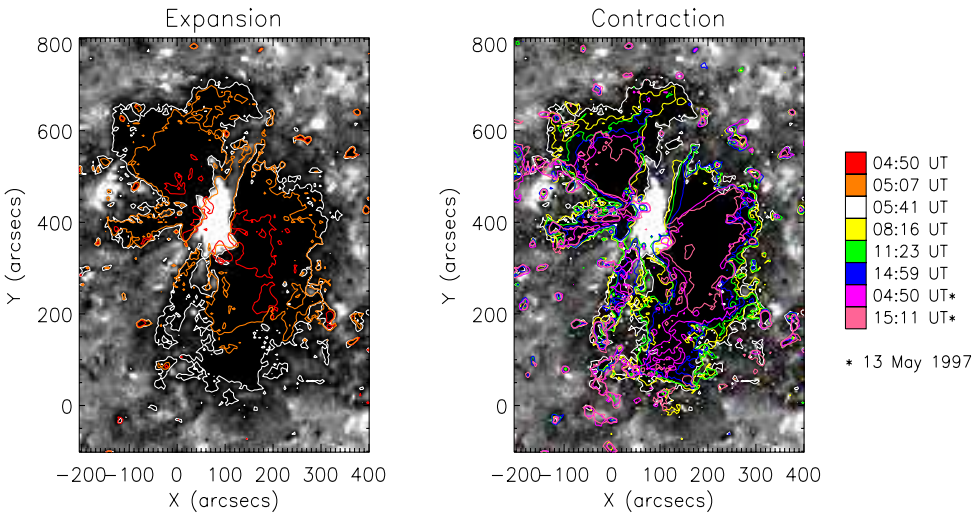

Figure 5.4: Asymmetric temporal and spatial evolution of the unidentical twin dimmings. The image on the left shows the expansion of the dimming regions. The image on the right shows the contraction of the dimming region boundaries. The colour-bar on the right shows the times of the coloured contours. The contours are overlaid on a background showing the base difference image at 05:41 UT. Permission to reproduce this figure has been granted by Springer Science and Business Media

expansion and brightening of the flare loops that appear to link the two main dimming regions. The bright flare loops seem to affect region 1 more than region 2, probably because of line-of-sight projection effects. Although the contour method does not include the high intensity region dominated by the flare loops, brightening due to scattered light can still influence the average intensity evolution of the regions selected by the contours.

The time at which the dimmings appear suggests that the magnetic field rooted in region 2 has expanded first (either driven by the erupting filament or creating the conditions for the eruption to occur). In either case, the disturbance starts in the south, proceeding northward. The onset of the dimming of region 1 occurs at $\approx$ 04:50 UT. The disturbance also appears to reach the location of dimming region 1 at this time.

5.2.4 Evolving dimmings

As noted by Kahler and Hudson (2001), the boundaries of TCHs are constantly evolving. To study the evolution of the dimming boundaries, contours are examined from images at successive intervals throughout the dataset. Figure 5.4 shows the expansion and subsequent contraction of the dimming regions.

The expansion of the dimming regions happens very fast, too quickly for the cadence of EIT to capture in much detail. In contrast, the contraction or recovery is more gradual, allowing us to examine the evolution. The shrinking of the dimming regions can actually be seen in the EIT 195 Å movie (*970512_195.mpg*, Appendix E). Figure 5.5 shows the change in area of the two main dimming regions, as a function of time. It is clear from Figures 5.4 and 5.5 that the twin dimming regions are unidentical. They exhibit an asymmetric temporal and spatial evolution, particularly evident in the recovery phase. Region 1 (the northern-most dimming region) starts to contract

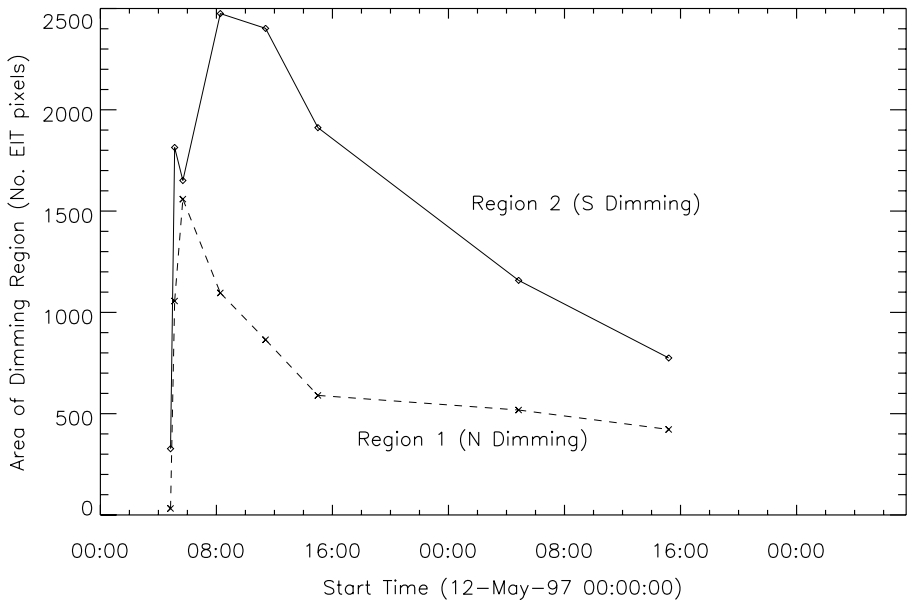

Figure 5.5: Evolution of the area of the two main dimming regions. The dashed line shows the change in area of region 1 and the solid line shows the change in area of region 2. The graph clearly shows the rapid expansion of the dimming regions and the relatively gradual contraction. Permission to reproduce this figure has been granted by Springer Science and Business Media

before region 2 (the southern-most dimming region).

5.2.5 Processing MDI data

SOHO/MDI level 1.8 full disk magnetograms with a 96 minute cadence and a pixel size of 1.98″ were used in this study. The level 1.8 magnetograms are data which have been corrected for plate scale, zero offset, sensitivity and cosmic rays. The data were corrected for radial projection effects using the standard `zradialize` routine, giving an estimation of the normal field component (B_n). Since previous studies (e.g. Berger and Lites, 2003; Wang *et al.*, 2003) have shown that MDI significantly underestimates the magnetic flux, both the linear and non-linear response of MDI is corrected for, using the expression: $\phi_{\text{corrected}} = 1.45(\phi + 0.3_{\phi>1200\text{G}})$, as indicated in Green *et al.* (2003).

After correcting for underestimation, the magnetic flux within the dimming regions, which extend from the AR main polarities to the quiet Sun, is measured. Therefore, the magnetic flux associated with the dimmings has two components: an AR and a quiet Sun part. To accurately calculate the magnetic flux in each dimming region, the following method (described in Section 3.2 of Mandrini *et al.*, 2005) is used. Part of the flux in the dimmings in the quiet Sun regions is due to noise and part forms small-scale connectivities. Such flux does not contribute to the overall net flux of the dimmings. To avoid incorporating this flux into the calculations, the AR flux from each dimming region is first removed. The remaining quiet Sun magnetic flux is then filtered for noise and small-scale connectivities which may otherwise contribute to the quiet Sun flux measurement. Finally, the AR flux is then added to the filtered quiet Sun flux to obtain the total magnetic flux

in each dimming region. So the magnetic flux measurement is the sum of both the active region *and* the filtered quiet Sun magnetic flux components.

The noise level in MDI measurements is found to range between 9 G (Green *et al.*, 2003), and 14 G (Hagenaar *et al.*, 2003). We consider an error of ± 10 G in each pixel measurement. A threshold of 20 G is used for the filtering (described above) when considering the magnetic flux through dimming regions, since we wish to filter low closed loops and noise from the measurements.

To calculate the error on the total flux measured through a given region (σ_{total}), the errors of ± 10 G on each pixel measurement (σ_i) combine as follows:

$$\sigma_{total} = \pm\sqrt{\Sigma {\sigma_i}^2} \tag{5.1}$$

E.g. For a region consisting of 5000 MDI pixels, the error in the measurement of the total magnetic flux would be calculated as: $\sigma_{total} = \pm\sqrt{5000 \times 10^2} = \pm$ 707 G. For a magnetogram with a pixel size of 1.98″, this corresponds to a magnetic flux of $\pm$ 707×$1.98^2 \times (725 \times 10^5)^2 = \pm$ 1.5×10^{19} Mx (since 1″ corresponds to 725×10^5 cm, also see §1.2).

5.2.6 Magnetic flux at the maximum extent of the dimmings

The MDI image shown in Figure 5.6 is used to measure the magnetic flux within the EIT dimming region boundaries shown (the same as in Figure 5.2). The only concentrated AR on the visible disk is AR 8038, consisting of a somewhat dispersed negative polarity and a compact positive polarity. The north pole is dominantly positive whilst the south pole is dominantly negative, consistent with the global configuration for 1997 during the first part of solar cycle 23.

Table 5.2 shows the measurements of the magnetic flux through each dimming region. The magnetic flux within regions 1, 2, 4 and 5 is measured. The magnetic flux within region 3 is not measured because it is located in the north polar coronal hole, where the magnetogram suffers from serious projection effects (Hagenaar *et al.*, 2003). The total positive and total negative magnetic flux in each dimming region is first measured; then the absolute flux is calculated as the sum of the magnitude of both the positive and negative fluxes. Finally, the net flux is computed by subtracting them. Since the majority of small-scale mixed polarities close in their direct vicinity, the net flux provides an estimate of how much flux is potentially free for connection with magnetic flux outside the selected region. At the maximum extent of the dimming, the net flux in region 1 is found to be -9×10^{20} Mx and the net flux in region 2 is found to be 21×10^{20} Mx (see Table 5.2). The total absolute flux through regions 1, 2, 4 and 5 is 41×10^{20} Mx.

The measurement of the net flux through region 1 is in agreement with that of Webb *et al.* (2000), but the measurement through region 2 is almost double their result. They found the flux for region 1 to be -9×10^{20} Mx and for region 2 to be 12×10^{20} Mx. The authors note that their measurement for region 2 is less precise due to the presence of the positive polarity sunspot. The same uncertainty remains in the measurement in this work, since the magnitude of the measured magnetic flux depends strongly on the extent of involvement of this concentrated magnetic field. Since the dimming boundaries can be determined with a precision of ± 2 EIT pixels in MDI data (after Mandrini *et al.*, 2005), the change in the magnetic flux is measured when the dimming region

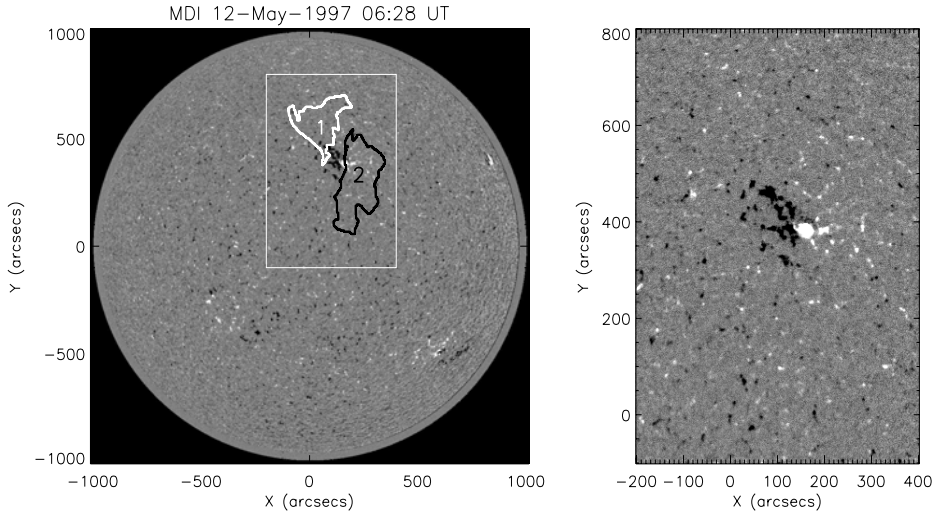

Figure 5.6: The left panel shows the MDI full-disk image at 06:28 UT on 12th May 1997. Overlaid are the locations of the two main dimming regions seen in Figure 5.2. The right panel shows a close-up of the rectangular region defined in the left panel. White (black) indicates regions of positive (negative) polarity. Permission to reproduce this figure has been granted by Springer Science and Business Media

Table 5.2: Magnetic flux measurements in the dimming regions at their maximum spatial extent (see Figures 5.2 and 5.6). The total positive (negative) magnetic flux is the sum of all of the positive (negative) flux that lies within the dimming region boundary. The absolute flux is the sum of the magnitude of both positive and negative fluxes, and the net flux is the difference between them.

Region	Positive flux (Mx)	Negative flux (Mx)	Absolute flux (Mx)	Net flux (Mx)
1	2×10^{20}	-11×10^{20}	13×10^{20}	$-9(\pm\ 0.2)\times10^{20}$
2	24×10^{20}	-3×10^{20}	27×10^{20}	$21(\pm\ 0.3)\times10^{20}$
4	0.1×10^{20}	-1×10^{20}	1.1×10^{20}	$-0.9(\pm\ 0.1)\times10^{20}$
5	0.2×10^{20}	-0.1×10^{20}	0.3×10^{20}	$0.1(\pm\ 0.1)\times10^{20}$

boundary is purposely shifted by 2 EIT pixels in all four cardinal directions. A maximum difference of $\pm 7 \times 10^{20}$ Mx is measured, obtained when moving the boundary east-west, due to the extent to which the sunspot is included in the measurement. We take $\pm 7 \times 10^{20}$ Mx as the uncertainty in all the measured solar flux measurements. (We note that this error is the dominant source of uncertainty, exceeding the errors in the net flux measurements in regions 1 and 2 of $\pm$ 0.2×10^{20} Mx and $\pm$ 0.3×10^{20} Mx, respectively). If the interpretation of Webb *et al.* (2000), is correct, so that the main dimming regions (1 and 2) do indeed mark the foot-points of the magnetic flux rope that erupts as the core of the CME, then the calculation of the total absolute flux should be halved to account for the fact that the flux is measured through both foot-points. This yields a total "linked" flux of $(20 \pm 7) \times 10^{20}$ Mx and is substantially larger than the total "linked" flux result $(10 \pm 2) \times 10^{20}$ Mx of Webb *et al.* (2000). There are probably three main reasons for this. Firstly, the regions through which the magnetic flux is calculated are substantially larger in this study than in Webb's (compare their Figure 3 and Figure 5.6 of this chapter), although the larger extent of the regions selected in this study just increases the quiet Sun magnetic flux content, so this probably only accounts for a small proportion of the larger value. Secondly, as described above, the measured flux through dimming region 2 depends substantially on the extent of involvement of the sunspot. Thirdly, this analysis has corrected MDI measurements for the recently found underestimation and projection effects, which yields substantially larger magnitudes for the estimated flux contained in the dimming regions. The latter two factors most likely explain the larger values measured in this work.

5.2.7 Global nature of the event

In order to build a complete picture of the evolving global magnetic topology of the eruption, more far-flung effects, such as the brightening at the boundary of the north polar coronal hole (described in Section 5.1) are also examined. The brightening at the north polar coronal hole boundary is visible in both EIT 195 Å and SXT data, Figures 5.7 and 5.8, respectively. Figure 5.7 shows a 2-D intensity profile made across the boundary of the north polar coronal hole. The centre and right panels show the retreating boundary and the brightening. The brightening takes place in two bursts. Co-temporal with the coronal wave associated with this event and with the dimming of region 1, a brief gentle brightening along the north polar coronal hole boundary (from 245 to 275 counts/pixel) occurs between 04:50 and 05:07 UT. A return to pre-disruption conditions takes place by 05:41 UT. Later, between 06:49 and 07:34 UT, a significant brightening is observed at the same location, increasing in intensity steadily, from 245 to a maximum of about 500 counts/pixel between 12:16 and 13:26 UT, before gradually fading to reach a fairly constant condition around 19:00 UT. By this time, the intensity of the pixels has reached a level similar to that of pre-eruption conditions, but the polar coronal hole has shrunk, shifting the boundary considerably farther North.

In addition to the brightening along the north polar coronal hole boundary, the SXT image at 08:54 UT (Figure 5.8) also shows an extended brightening along the eastern edge of dimming region 2. This brightening may be due to the arcade that presumably formed beneath the main body of the erupted filament (see Section 5.2.3). This arcade is formed in a weak-field region, which may be why it appears less bright than the flare loop arcade at the heart of AR 8038.

We discuss the implications of these global features in §5.4.

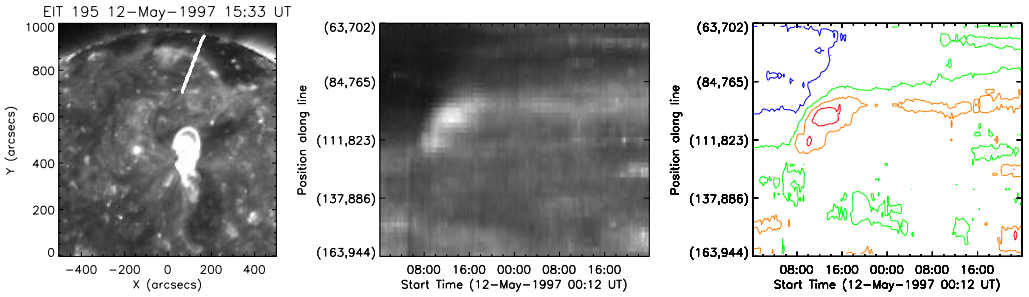

Figure 5.7: 2-D intensity profile made along the thick white line shown in the left panel of this figure. The centre panel shows the intensity change along the selected line profile with time. The right panel is a contour plot of the intensity profile. Red, orange, green and blue contours at 400, 300, 200 and 100 counts/pixel respectively. The brightening (commencing between 06:49 and 07:35 UT) along the shrinking boundary of the north polar coronal hole is clearly visible. Permission to reproduce this figure has been granted by Springer Science and Business Media.

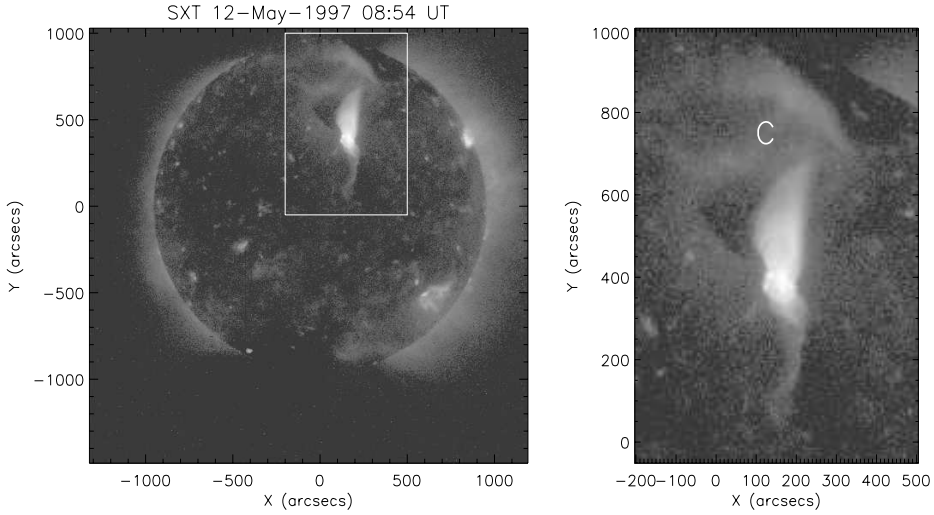

Figure 5.8: *Yohkoh* SXT image at 08:54 UT on 12th May 1997 made using the thin aluminium filter. The two main dimming regions can be seen, as well as the cusp-shape over the flare loops. A zoom of the rectangular area defined in the left panel is shown in the right panel. "**C**" marks the location of hot loops connecting the northern edge of dimming region 1 to the boundary of the north polar coronal hole. Permission to reproduce this figure has been granted by Springer Science and Business Media.

5.3 Interplanetary Data Analysis and Results

The work presented in this section was carried out by Prof. Cristina Mandrini, Dr. Sergio Dasso and Ms. Maria Soledad, of the Instituto de Astronomía y Física del Espacio, University of Buenos Aires, Argentina.

5.3.1 *In situ* measurements at 1 AU

The flux rope ejected from the Sun on 12th May 1997 was observed by the spacecraft *Wind* at 1 AU as a left-handed helical structure lying in the ecliptic plane (Webb *et al.*, 2000). In this work, *in situ* magnetic observations (3 seconds temporal cadence) obtained by the MFI are analysed. The data were downloaded from the public database `http://cdaweb.gsfc.nasa.gov/cdaweb/istp_public/`. In particular, the magnetic field vector components measured in the Geocentric Solar Ecliptic (GSE) system are used, between 10:00 UT on 15th May and 01:00 UT on 16th May, which is the same time period taken by Webb *et al.* (2000). The interplanetary magnetic data in GSE components and other interplanetary observations (such as the bulk wind velocity, electron temperature, etc.) are illustrated in Webb *et al.* (2000), mainly in their Figure 4.

A local direction, called $\hat{z}_{\rm cloud}$, is defined to be the direction that agrees with the direction of the main cloud axis. A Minimum Variance (MV) method (e.g. Sonnerup and Scheible, 1998) is applied. During the passage of a MC, the magnetic field vector $\mathbf{B}$ is measured many times. The mean value of the magnetic field vector, $\langle \mathbf{B} \rangle$ is calculated, and then the mean quadratic deviation of the individual measurements of $\mathbf{B}$ from $\langle \mathbf{B} \rangle$ are determined. The smallest deviation gives the MV (see Bothmer and Schwenn, 1998). MV gives a good determination of $\hat{z}_{\rm cloud}$ when the distance between the spacecraft trajectory and the cloud axis (i.e. the impact parameter, p) is small. Webb *et al.* (2000) found that p is 20% of the cloud radius, which justifies the use of the MV method. At the same time, and using the orientation given by MV, the observed magnetic field vector shows a large and coherent rotation (more than 180^0, not shown here) in the largest and intermediate variance planes. This is also an indication of a very low impact parameter. The observed magnetic field components are rotated to the cloud local components (as done by Bothmer and Schwenn, 1998; Dasso *et al.*, 2003, 2005). The angle between the cloud axis, which is chosen such that the magnetic field is positive at the cloud centre, and the ecliptic plane (ecliptic latitude) is found to be $-2°$. Thus, the MC axis is almost on the ecliptic plane and points slightly to heliospheric south. The angle between the projection of the cloud axis on the ecliptic plane and the Earth-Sun direction is found to be 114° (this projection points to solar east). Thus, the orientation angles determined by us are in good agreement with the ones found by Webb *et al.* (2000). From the obtained MC orientation, the duration of the cloud observations and its velocity, the cloud radius, $R_{\rm MC} = 0.08$ AU.

5.3.2 Magnetic flux in the magnetic cloud

Webb *et al.* (2000) computed the axial magnetic flux of the interplanetary rope using a single model for its magnetic structure. They compared the computed axial flux to the magnetic flux they determined for the observed dimming regions. In this section, the interplanetary data analysis

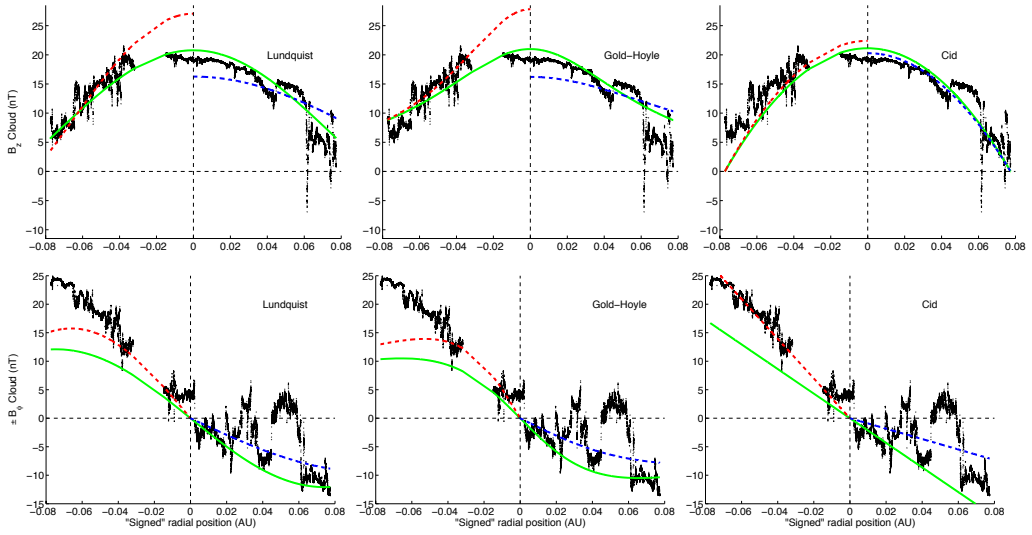

Figure 5.9: Axial ($B_{z,\mathrm{cloud}}$) and azimuthal ($\pm B_{\varphi,\mathrm{cloud}}$) components of the magnetic field in the cloud (data and fitted curves, see Section 3.2, main text). The three upper panels correspond to $B_{z,\mathrm{cloud}}$: models **L** (left), **G** (middle), and **C** (right). Likewise for $\pm B_{\varphi,\mathrm{cloud}}$ in the lower panel. Green solid lines correspond to the symmetric fitting, dashed red and blue lines to the in-bound and out-bound branches of the asymmetric fitting, respectively. Permission to reproduce this figure has been granted by Springer Science and Business Media.

is extended a step farther to determine more stringent values for the MC physical parameters. The magnetic flux for both components of the cloud field (axial and azimuthal) is computed and different models for the magnetic field structure of the cloud are explored.

The local magnetic configuration of the cloud is modelled with three different cylindrical and static models: (i) Lundquist's model (model **L**, a linear force-free field; Lundquist (1950)), (ii) Gold and Hoyle's model (model **G**, a uniformly twisted and non-linear force-free field; Gold and Hoyle (1960)) and (iii) Cid's model (model **C**, a non force-free model with a constant axial current density and a linear dependence on the radius for the azimuthal component of the current density; Cid *et al.* (2002)). These three models have significantly different helical magnetic configurations with very different distributions of magnetic twist.

The three unit vectors of the cylindrical coordinate system are defined, following convention, such that $\hat{r}$, $\hat{\varphi}$, and $\hat{z}$ correspond to the radial, azimuthal, and axial directions. Thus, $B_{r,\mathrm{cloud}}$, $B_{\varphi,\mathrm{cloud}}$, and $B_{z,\mathrm{cloud}}$ are the local cloud components of the magnetic field.

The spacecraft distance relative to the magnetic cloud axis is determined, assuming a constant speed for the MC during *Wind* observations. This distance is null when the spacecraft crosses the cloud axis, so that its radial position is $-R_{\mathrm{MC}}$ when *Wind* enters the MC and $+R_{\mathrm{MC}}$ when it leaves the cloud.

First the free parameters of the three models (magnetic field amplitude and torsion at the cloud axis) are fitted to the full cloud data series (as done in Dasso *et al.*, 2003, 2005). This first step is labelled the symmetric fitting. Then, the time series is split into two parts: (1) the in-bound part (before the spacecraft reaches the magnetic cloud axis) and (2) the out-bound part (after it crosses the axis). In this way, six different fittings are performed, that correspond to three different models in each of these two branches. This allows analysis of the effect of the in- and out-bound asymmetry, present in the cloud data, on the computed fluxes (see Figure 5.9).

Figure 5.9 shows the curves for the different fittings (symmetric **L, G**, and **C**, in-bound **L, G**, and **C**, and out-bound **L, G**, and **C**) and the observations for the two main components of the cloud magnetic field. The figure is drawn as a function of the radial spacecraft position, as defined above. The three upper panels correspond to the $B_{z,\mathrm{cloud}}$ component and the three lower panels to the $\pm B_{\varphi,\mathrm{cloud}}$ component. The negative sign before $B_{\varphi,\mathrm{cloud}}$ (vertical axis in Figure 5.9) corresponds to $r < 0$ (i.e., the in-bound branch) and the positive to $r > 0$ (i.e., the out-bound branch). The first column in Figure 5.9 corresponds to model **L**, the second to model **G**, and the third one to model **C**. In each figure, the green continuous line shows the symmetric fitting, the red dashed line the in-bound and the blue dashed line the out-bound fitting for the asymmetric case, respectively. Two of the models **L** and **G** behave in a very similar way, but they do not fit the data as well as model **C** does. The data gap that appears near the axis of the cloud is probably responsible for this drawback, this effect can be clearly seen on the asymmetric fittings for $B_{z,\mathrm{cloud}}$ using models **L** and **G**.

The values of χ^2 (defined as the square root of the mean difference between the observed and corresponding modelled components of the magnetic field to the second power for each model), which give a quantitative estimation of the fitting quality, are also affected by the presence of the data gap. For model **C** the lowest χ^2 is obtained. The ratio between the maximum (model **G**, symmetric case) and minimum (model **C**, asymmetric in-bound case) χ^2 values is 1.7. If this ratio is equal to 1, it would mean that both fittings have a similar quality but, in this particular case, model **C** is by far the one that best represents the magnetic structure of the cloud.

From the fitted parameters the axial (Φ_z) and azimuthal (Φ_φ) magnetic fluxes are computed, which are given by:

$$\Phi_z = 2\pi \int_0^{R_{\mathrm{MC}}} B_z(r) r \mathrm{d}r, \qquad \Phi_\varphi / L = \int_0^{R_{\mathrm{MC}}} B_\varphi(r) \mathrm{d}r \tag{5.2}$$

where L is the cloud length. Different models (**L**, **G**, and **C**) have different expressions for these integrals. (Dasso *et al.*, 2006, explains further details.)

Table 5.3 shows the obtained values for the axial and azimuthal (per unit length) fluxes. The upper block corresponds to the symmetric fittings and the lower one to the asymmetric ones. The last two rows of each block correspond to the means and the standard deviations of the flux values for symmetric and asymmetric cases, these results (except for the standard deviation in the azimuthal flux) prove to be similar.

On comparison, models **L** and **G** give similar values in all cases, differing from those obtained using model **C**. The range of flux values found for the symmetric fitting is included within the range of fluxes for the asymmetric case. As the cloud observations are asymmetric, but the full data fitting is forced to be symmetric (for the three models), the dispersion in the fitting of the split temporal data are larger. Each flux value is taken to be its mean $\pm$ the dispersion obtained in the asymmetric case. Thus, the MC fluxes are estimated as: $\Phi_z \approx (4.8 \pm 0.8) \times 10^{20}$ Mx, and $\Phi_\varphi / L \approx (13 \pm 6) \times 10^{20}$ Mx AU^{-1}.

Table 5.3: Magnetic fluxes computed for the MC observed on 15th May 1997, at 1 AU. The first column indicates the models, second and third columns show the values of the axial and azimuthal (per unit length) magnetic fluxes. First (upper) block corresponds to the symmetric fitting, and second one (lower) to the asymmetric case. Last two rows of each block show the means and the standard deviations of the fluxes in each case.

Model	Φ_z (Mx)	$\Phi_\varphi L^{-1}$ (Mx AU^{-1})
Symmetric model		
Lundquist	5.0×10^{20}	12×10^{20}
Gold-Hoyle	5.1×10^{20}	12×10^{20}
Cid	3.9×10^{20}	13×10^{20}
Mean	4.7×10^{20}	12×10^{20}
Std	0.7×10^{20}	0.2×10^{20}
Asymmetric model		
Lundquist (in-bound)	5.7×10^{20}	17×10^{20}
Gold-Hoyle (in-bound)	5.8×10^{20}	17×10^{20}
Cid (in-bound)	4.1×10^{20}	21×10^{20}
Lundquist (out-bound)	4.8×10^{20}	8×10^{20}
Gold-Hoyle (out-bound)	4.9×10^{20}	8×10^{20}
Cid (out-bound)	3.7×10^{20}	5×10^{20}
Mean	4.8×10^{20}	13×10^{20}
Std	0.8×10^{20}	6×10^{20}

5.4 Discussion

5.4.1 Magnetic connectivity scenario and its link with the interplanetary observations

From the analysis of the magnetic character and evolution of the dimming regions, a scenario is proposed which links the formation of the CME with the formation of the coronal dimming regions. The interpretation of Webb *et al.* (2000) is followed, so that the two main dimming regions are understood to mark the foot-points of the flux rope that erupts to form the CME.

Kahler and Hudson (2001) state that the contraction of TCHs must be at least partially due to magnetic reconnection. Interestingly, they suggest that larger-scale newly "opened" magnetic field does not re-close in the arcade or even in the vicinity of the neutral line, but with an independent source of "open" magnetic field of opposite polarity. They propose that such a magnetic field could be found in previously existing coronal holes. Combining these ideas with the data analysis presented suggests the following scenario (see Figure 5.10): (**A**) and (**B**) reconnect to form closed loops (**C**) and "open" magnetic field lines (**D**).

The magnetic loops of the CME (**A**) expand and eventually push against the "open" magnetic field lines of the north polar coronal hole (**B**). The polarity of the northern edge of the expanding magnetic loops is negative and the north polar coronal hole field is positive. As the expanding loops push against the oppositely orientated "open" field lines, a current sheet is expected to form at their interface. These represent favourable conditions for successive magnetic reconnection to take place.

After reconnection, magnetic loops (**C**) are created, connecting the positive north polar coronal hole field (**OCH**) with the outer boundary of the negative dimming region 1 (**O1**). These hot loops are actually visible in the SXT image shown in Figure 5.8, marked by the letter "**C**".

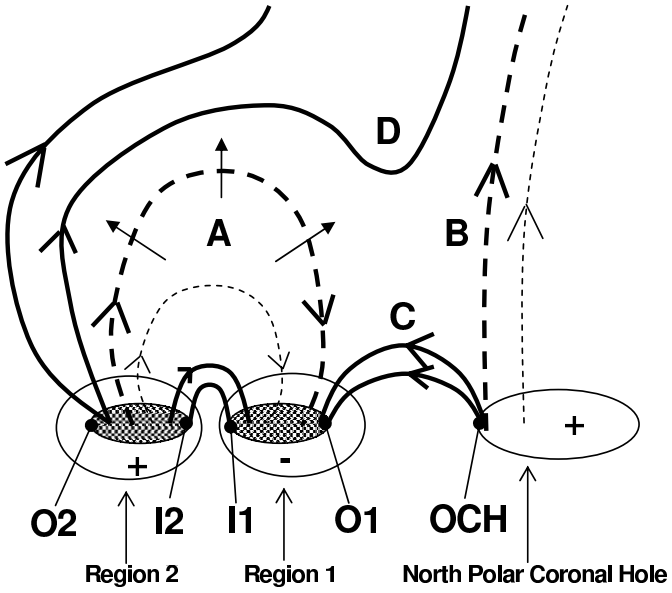

Figure 5.10: Sketch of the evolution of the global magnetic field connectivity of the 12th May 1997 CME eruption. Dashed (solid) lines represent the pre (post) -reconnection magnetic structure. The hashed regions represent the main dimming regions. **A** and **B** reconnect to form **C** and **D**. **A** marks the expanding magnetic loops connecting the opposite polarity regions in AR8038. **B** marks the positive polarity "open" magnetic field in the north polar coronal hole. **C** marks the reconnected field lines that form between the north polar coronal hole boundary (**OCH**) and the outer boundary of region 1 (**O1**). **D** marks the newly "opened" magnetic field. **O1 (I1)** and **O2 (I2)** denote the outer (inner) boundaries of coronal dimming regions 1 and 2, respectively. Permission to reproduce this figure has been granted by Springer Science and Business Media.

This connection acts to close down the outer boundary of the negative dimming region 1, with reconnection of successive field lines closing down the boundary from "outside in". The noticeable shrinking of region 1 at the **O1** boundary (as shown by the contracting contours in Figure 5.4) starts between 06:49 and 07:34 UT. Likewise, the successive closing down at **OCH** creates a shrinking of the north polar coronal hole boundary (also starting between 06:49 and 07:34 UT), as observed (see Figure 5.7).

The apparent motion of the polar coronal hole boundary could alternatively be attributed to the influence of loop brightening and 3-D projection effects. However, such an interpretation is invalid in this case because the polar coronal boundary remains shrunken, even after the brightening has disappeared (see Figure 5.7).

As well as creating closed loops between **O1** and **OCH** as discussed above, the magnetic reconnection also creates "open" magnetic field lines (**D**). Upon reconnection with the north polar coronal hole, the magnetic field rooted at **O2** is changed from an expanded loop connectivity to an "open" magnetic field configuration. Successive reconnections, due to the expansion of **A** effectively enforce the effect of an "open" magnetic field at **O2**, maintaining the magnetic field conditions under which plasma evacuation is likely to occur. The data analysis reflects this: **O2** shows only a reluctant contraction, with successive boundaries rather remaining close to the maximum spatial extent boundary until 09:10 UT (see Figures 5.4 and 5.5).

If the flare loops are interpreted as a post-eruptive arcade structure (Carmichael, 1964; Sturrock, 1966; Kopp and Pneuman, 1976), then the inner boundaries (**I1**, **I2**) are probably also closed down due to magnetic reconnection, with the inner boundaries of the dimming regions partially obscured

by the bright flare loops.

Based on high-energy electron observations, Webb *et al.* (2000) concluded that uni-directional electron flows were present in the MC on 15th May (see their Section 3 and Figure 4, fourth and fifth panels from the bottom). If the cloud orientation and the sense of the axial magnetic field in the MC (Sections 5.3.1 and 5.3.2) are compared to the pitch angle distribution of high-energy electrons (mainly Figure 4 in Webb *et al.*, 2000), one can conclude that the end of the MC that could still be connected to the Sun during *Wind* observations was anchored in a positive polarity region. In view of our interpretation, the location of this anchorage is specified to be dimming region 2. Recently, Crooker and Webb (2006) independently suggested a similar scenario.

In summary, expansion of the magnetic field containing the flux rope leads to interaction with the north polar coronal hole magnetic field, which through forced, global-scale interchange reconnection (Crooker *et al.*, 2002) effectively closes part of both dimming region 1 and the north polar coronal hole "open" magnetic field. Thus, dimming region 2, where the magnetic field remains "open", becomes the region where the developing magnetic cloud stays connected to the Sun.

5.4.2 Quantitative comparison of the dimmings and MC magnetic fluxes

In order to test the validity of the suggested scenario, the magnetic flux in the southern-most dimming region (which as argued above best represents the flux involved in the ejection), is compared with the magnetic flux in the MC. Webb *et al.* (2000) used Lepping *et al.*'s (1990) method to fit the cloud magnetic data to Lundquist's (1950) model. From the derived model parameters, the authors estimated an axial cloud flux of $\approx 7.35 \times 10^{20}$ Mx. This value is three times smaller than the net flux in region 2 (see Table 5.2). When comparing interplanetary to coronal global quantities, it is a common practise to include only the axial cloud flux in the comparison. This is probably because the "standard" view for an ejection is that of an expanding coronal flux tube extending into the interplanetary medium in a self-similar manner. However, in recent works (Mandrini *et al.*, 2005) that quantitatively link interplanetary events to their coronal sources, it was shown that the azimuthal cloud flux should also be included in the comparison. Indeed, when the cloud length can be estimated and the azimuthal flux calculated, it proves to be almost an order of magnitude higher than the axial flux and its value is closer to the solar flux measured in the dimming regions.

As seen in Equation 5.2, the value of Φ_φ depends on the MC length (L). This parameter is one of the unknowns when modelling a MC magnetic configuration, since *in situ* observations provide data along a single cloud direction. How then, is it possible to estimate a value for L? Because of the presence of uni-directional electron flows, the flux rope was probably attached to the Sun only at one end when observed by *Wind*. Following the proposed scenario, the disconnection of the ejected rope is related to the reconnection process that shifts the northern coronal hole boundary farther north (see Section 5.2.7). This process starts at $\approx$ 07:00 UT, reaches a maximum at $\approx$ 13:00 UT and finishes by $\approx$ 19:00 UT on 12th May 1997. Given the proposed association of the brightening as a signature of reconnection, it is assumed that disconnection occurs throughout these 12 hours that the brightening is observed. If the central interval time (13:00 UT) is considered to represent the disconnection time, and taking into account that the MC is observed at Earth 77 hours (15th May at $\approx$ 10:00 UT) after ejection (on 12th May at $\approx$ 05:00 UT), a cloud length of $\approx$ 1.1 AU can be estimated, neglecting any probable curvature and assuming a constant travel velocity from Sun to Earth. However if, when the flux rope disconnects from the solar surface it

is able to reconnect with the ambient solar wind large-scale field lines, then the magnetic twist contained in the ejected flux tube propagates along the new connections as a torsional Alfvén wave. Taking a typical Alfvén velocity of 100 kms^{-1}, from 13:00 UT, the twist can propagate from the disconnected end of the flux tube over a length of 0.2 AU in the remaining 69 hours before the MC arrives at Earth (10:00 UT). Therefore, the probable length of the MC is $L \sim 1.3$ AU, which is a lower limit since, as stated above, any flux rope curvature is neglected. Finally, the MC fluxes are: $\Phi_z \approx (4.8 \pm 0.8) \times 10^{20}$ Mx, and $\Phi_\varphi \approx (17 \pm 8) \times 10^{20}$ Mx, with a cloud length of 1.3 AU. This gives the total flux in the MC as: $\Phi_{\mathrm{MC}} \approx (22 \pm 9) \times 10^{20}$ Mx. The error bar in the estimated MC flux arises from the fact that the cloud observations are asymmetric. This yields a larger error bar than found when considering a symmetric model (see Table 5.3).

The value of $\Phi_{\mathrm{MC}} \approx (22 \pm 9) \times 10^{20}$ Mx is in very good agreement with the net flux in the southern-most dimming region, $(21 \pm 7) \times 10^{20}$ Mx, that is considered to best represent the MC flux (see Section 5.4.1). The measurement of the magnetic flux from dimming region 2 is probably a minimum estimate for the magnetic flux contained within the MC because it is not possible to determine the extent to which the dimming regions may extend into the region obscured by the bright flare loops. The flare loops sit at the heart of AR 8038 and, therefore, some contribution of the strong active region solar flux within the dimming regions is not measured.

Recently, Odstrcil *et al.* (2005), using a numerical coronal outflow model for this event, found that the excursion of the southern TCH toward the helio-equator was the source of a moderate fast solar wind stream that interacted with the interplanetary CME. In view of the scenario derived from this work, it is proposed that the southern TCH was, in fact, where the MC was connected to the Sun. Further, Ivanov *et al.* (2003) concluded that the low-latitude TCH was one of the sources of the near-Earth disturbance, which supports the suggested scenario.

5.5 Implications for CME models

In the previous analysis, describing the 12th May 1997 solar event and associated MC, the fact that the azimuthal cloud flux (≈ 4 times larger than the flux in the axial component) is the closest to the solar flux participating in the ejection should have implications for CME models.

The comparison of coronal and interplanetary data, associated with the same event, allows constraints to be placed on the CME mechanism. In particular (as discussed in Mandrini *et al.*, 2007), is the flux rope found in the IP already present in the corona, subsequently becoming unstable and then erupting, or is it formed dominantly during the eruption of an initially sheared arcade by magnetic reconnection? It is expected that the flux in the dimming regions should be comparable to either the axial flux of the MC or the total flux, respectively, depending on which mechanism is at work.

The dominance of azimuthal flux in the 12th May 1997 case suggests that during the ejection, twist might be created by reconnection in a sheared arcade overlying the expanding flux tube, significantly increasing the twist in the ejected flux rope in a similar way as that proposed by Mandrini *et al.* (2005). In such a case, the photospheric "open" flux will mainly contribute to the azimuthal cloud component. In such a case, the arcade above the flux rope expands significantly before reconnecting. As a result, the dimmings will be formed at the footpoints of the flux rope, and also all along the footpoints of the sheared magnetic arcade as this expansion occurs. Later, the

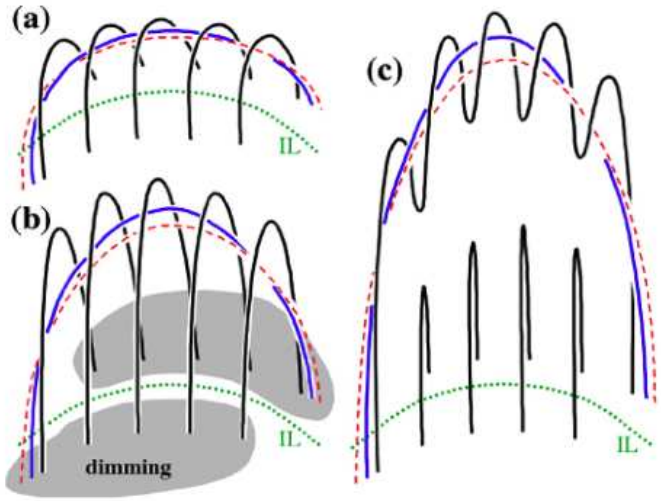

Figure 5.11: Figure from Mandrini *et al.* (2007). A scenario for flux rope eruption: (a) A flux tube (blue and red lines) is embedded in a sheared arcade (black lines). (b) The arcade above the flux rope expands significantly before reconnecting. Dimmings (light gray areas) are formed at the footpoints of the flux rope and also all along the footpoints of the sheared arcade. (c) The reconnection of the sheared arcade progressively incorporates more flux to the erupting flux tube. In this scenario the magnetic flux in the dimmings should correspond to the sum of the axial and azimuthal flux in the associated MC. The dotted green line is the magnetic photospheric inversion line (IL). Permission to reproduce this figure has been granted by Springer Science and Business Media.

reconnection of the sheared arcade field lines progressively incorporates more flux to the erupting flux tube. In this case, the flux in the dimming regions is expected to be comparable to the sum of the axial and azimuthal MC flux.

On the other hand, in a model case, the flux rope may already be formed pre-eruption and during the eruption, remains rooted in the dimming regions, at the same time expanding upward in the corona and out into the solar wind. Recently, Qiu *et al.* (2007) compared the flux in coronal dimmings with the flux in the MCs associated with the eruptive solar events, considering both the flux in the axial and azimuthal MC field components. These authors found that the flux in the dimmings was comparable in an order-of-magnitude sense to the axial MC flux. In this case, dimmings will be formed only at the footpoints of the flux tube as it expands and erupts. Therefore, the flux measured in the dimmings will be comparable mainly to the MC axial flux. The result of Qiu *et al.* (2007) is therefore expected in the model case described.

5.6 Conclusion

This study uses a specially developed contour method to quantitatively define coronal dimming region boundaries and to follow their manifestation and evolution. SOHO/EIT, MDI and *Yohkoh*/SXT data were used to analyse the changing intensity and the magnetic character of the coronal dimming regions, as well as the global features that appear in conjunction with the CME eruption from AR 8038 on 12th May 1997.

From analysis of the evolution of the coronal dimming regions and a synthesis of already published results, a new interpretation of this event is derived. Multi-wavelength observational evidence shows that the magnetic field of the expanding CME forced global-scale magnetic inter-

change reconnection with "open" field lines of the north polar coronal hole, closing down expanding magnetic field lines of the northern side of the CME, while transferring "open" coronal hole field lines to the southern side. This scenario explains both the asymmetric temporal and spatial evolution of the two main dimming regions, as well as the gradual brightening and shrinking of the north polar coronal hole boundary. Combining this scenario with interplanetary observations, it is found that the southern-most of the two unidentical twin dimming regions was the principal foot-point of the associated magnetic cloud observed at Earth. This is supported by a thorough analysis of *Wind* data, using three different magnetic cloud models and two computation methods. The magnetic flux from the southern-most dimming region and that of the MC are found to be in close agreement, within the same order of magnitude: 10^{21} Mx. This study highlights the crucial contribution of the azimuthal flux in such calculations, and has potential implications for CME models. This is the first work to show that study of the evolution and magnetic nature of coronal dimming regions can be used to probe the *post-eruptive* evolution of the CME.

5.7 Complex Case Study - 28th October 2003

Our work on the 12th May 1997 event strongly supports the model suggested by Webb *et al.* (2000) that coronal dimmings (TCHs) do indeed correspond to the footpoints of the magnetic flux rope that erupts and expands into interplanetary space as the core of the ICME. However, are CME-related dimmings *always* a simple signature of interplanetary magnetic cloud footpoints? We take the 28th October 2003, notoriously complex event as a case study. The CME from NOAA 10486 on 28th October 2003 was associated with large-scale dimmings, located on either side of the main flaring region. The flare was classified as a GOES X.17 event, starting at 11:01 UT with a peak at around 11:10 UT. A filament eruption also occurred in association with this event. A fast, diffuse coronal wave signature associated with the eruption was visible in EIT 195 Å data and a Moreton wave was captured in Meudon Observatory Hα data. Both phenomena appeared to propagate across the entire solar disk. The spatial distribution of EUV dimmings and coronal waves during the strong activity period of October - November 2003 has been also studied by Grechnev *et al.* (2005), combining observations of SOHO/EIT and CORONAS-F/Spectrographic X-Ray Imaging Telescope (SPIRIT, Zhitnik *et al.*, 2002).

In a similar analysis to the 12th May 1997 event, described previously, SOHO/EIT and SOHO/MDI magnetic maps are combined for this case study event to identify and measure the magnetic flux in the dimming regions. The associated magnetic cloud is modelled and computations of its magnetic flux are performed by Prof. Cristina Mandrini, Dr. Sergio Dasso and Maria Soledad, of the Instituto de Astronomía y Física del Espacio, University of Buenos Aires, Argentina. In contrast with the 12th May 1997 analysis, it is found that the magnetic fluxes of the dimmings and magnetic cloud are incompatible for this 28th October 2003 event. The conclusion of this case study is that, in certain cases, especially in large-scale events and eruptions that occur in regions that are not isolated from other flux concentrations, the interpretation of the early-stage evolution of dimmings requires a deeper analysis of the surrounding global magnetic field configuration, since at least a fraction of the dimmed regions appear to be formed by reconnection between the erupting field and the surrounding magnetic structures.

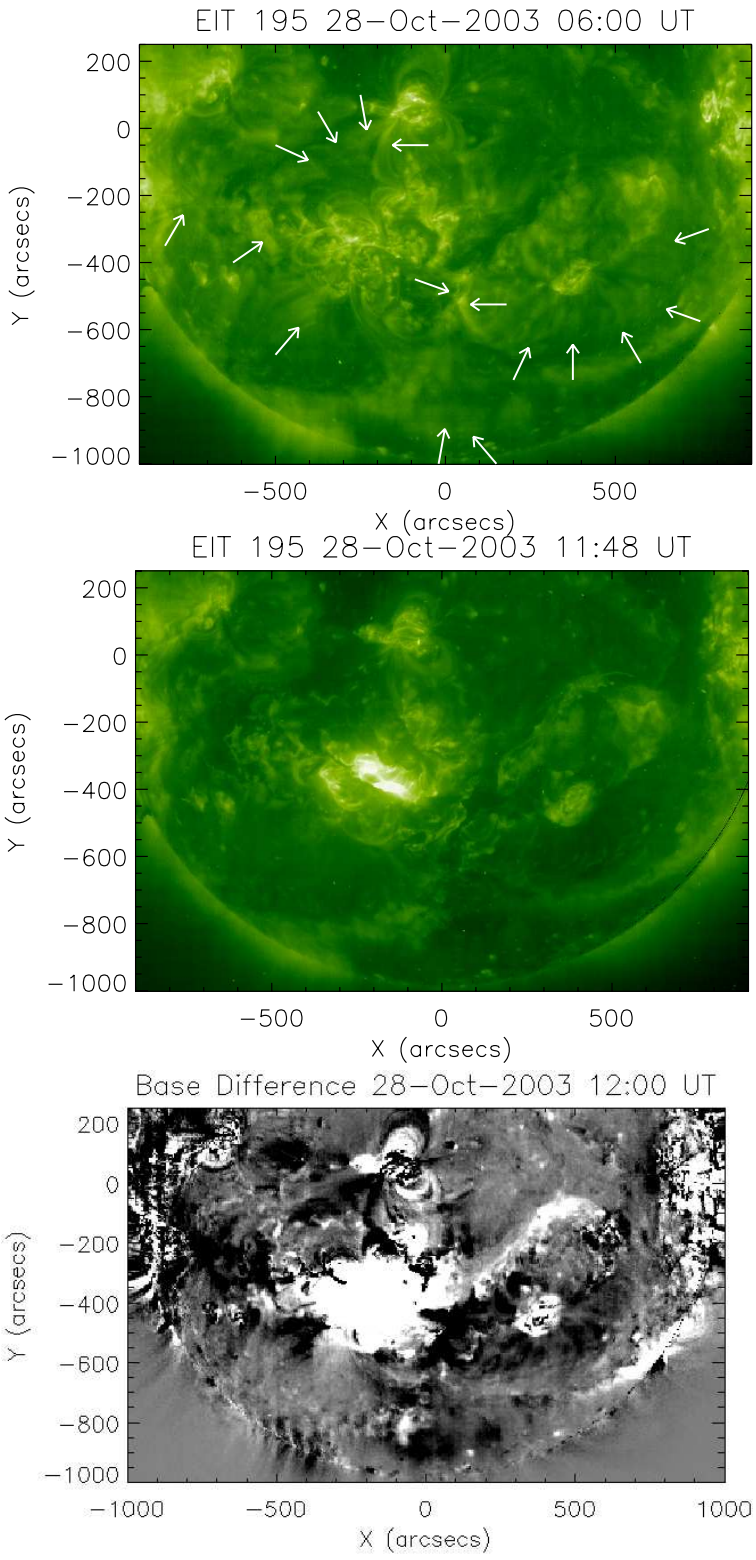

Figure 5.12: SOHO/EIT 195Å images before (top panel) and after (center and bottom panels) the X.17 flare. The images show the formation of dimmings around the flare site. The white arrows in the top panel highlight regions that later show a reduction in intensity when compared to the middle and bottom panel images. The bottom panel shows a base difference image (12:00 UT - 05:00 UT). The dimmings (black regions) are clearly identified. Figure from Mandrini *et al.* (2007). Permission to reproduce this figure has been granted by Springer Science and Business Media.

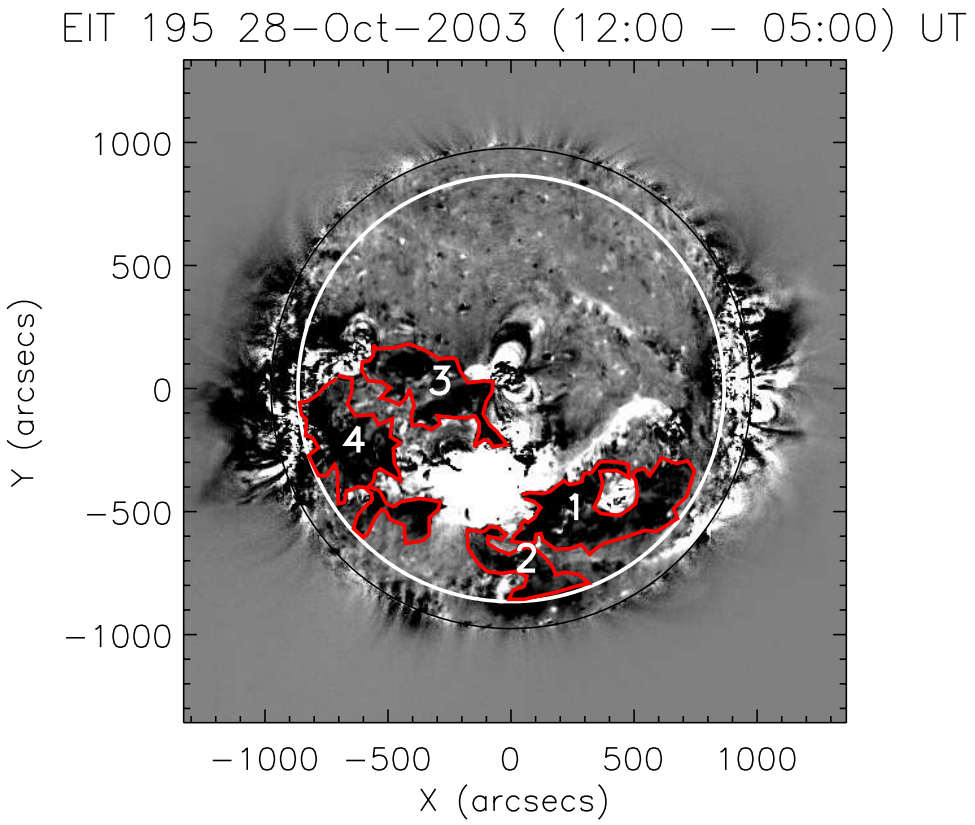

Figure 5.13: SOHO/EIT 195 Å base difference image (12:00 05:00 UT) showing the dimming regions about 1 hour after the start of the X.17 flare and associated CME. The dimming regions selected for analysis are numbered and surrounded by red polygons. The white circle is drawn at an angular distance of 60° from the disk center, MDI flux measurements are made within this limit (see Figure 5.14). Figure from Mandrini *et al.* (2007). Permission to reproduce this figure has been granted by Springer Science and Business Media.

5.7.1 Solar Data Analysis and Results

SOHO/EIT 195 Å full-disk images, at approximately 12-minute intervals with a pixel size of 5.26″, are used in this case study. Figure 5.12 shows the EIT data before and after the eruption. To visualize the dimmings clearly, we produce base difference images (e.g. bottom panel, Figure 5.12) where the same pre-event image (05:00 UT) is subtracted from all subsequent images. All EIT heliograms are differentially de-rotated to this pre-event time. The dimming regions, located on either side of the flaring region, can be easily identified in the base difference images. In Figure 5.13, red polygons surround the regions selected for study; this gives us a global view of the dimming spatial distribution. A closer inspection shows that many dimmings are present and are, in fact, spread all around AR 10486.

SOHO/MDI level 1.8 full-disk magnetograms with a 96-minute cadence and a pixel size of 1.98″ were used in this case study. The data were then also corrected for radial projection effects by using the standard `zradialize` routine. Finally, the MDI data were corrected for underestimation as described previously in §5.2.5.

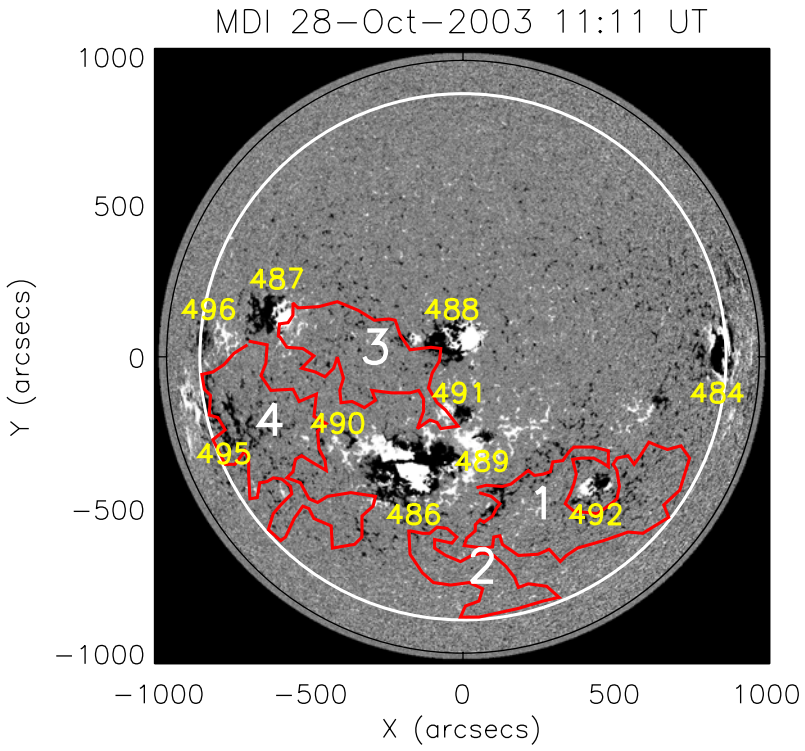

Figure 5.14: Selected dimming regions overplotted on a deprojected (with radial hypothesis) MDI magnetogram. Black (white) represents the negative (positive) radial magnetic field component. The white circle marks the 60° angular limit up to which MDI measurements are considered reliable. The NOAA numbers of the ARs present on the solar disk at that time are added in yellow (format: e.g. 10490). Figure from Mandrini *et al.* (2007). Permission to reproduce this figure has been granted by Springer Science and Business Media.

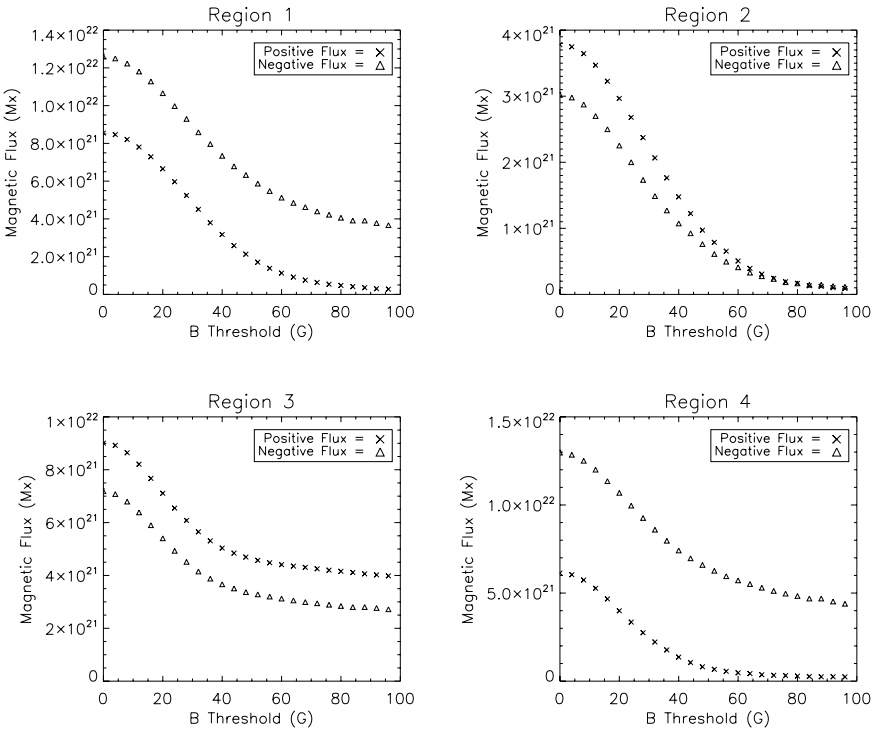

Figure 5.15: Positive and negative magnetic flux measured through each dimming region (Figure 5.14) as a function of the magnetic threshold (the flux of a pixel is counted only if its absolute value is larger than the threshold). Permission to reproduce this figure has been granted by Springer Science and Business Media.

Table 5.4: Magnetic flux measured through each of the dimming regions defined in Figure 5.14, with a threshold field value of 20 G (see Figure 5.15).

Region	Positive Flux (10^{21} Mx)	Negative Flux (10^{21} Mx)	Absolute Flux (10^{21} Mx)	Net Flux (10^{21} Mx)
1	6.7	-11.1	17.0	-4.0 ($\pm$ 0.04)
2	3.0	- 2.3	5.2	0.7 ($\pm$ 0.03)
3	7.1	- 5.4	13.0	1.7 ($\pm$ 0.04)
4	4.0	-11.0	15.0	-6.7 ($\pm$ 0.04)

Part of the magnetic flux in the dimmings is due to noise and part forms small-scale connectivities. Such flux does not contribute to the overall net flux of the dimmings. To avoid incorporating this flux into our calculations, we filtered $|B_n|$ in the dimmings using various lower value thresholds (as in Mandrini *et al.*, 2005; Attrill *et al.*, 2006). Table 5.4 lists the magnetic flux measured in the selected regions shown in Figures 5.13 and 5.14. Notice that, in contrast to what is found when double or core dimmings are present after an eruption (net flux in each dimming having the opposite sign, as for 12th May 1997 event, see Table 5.2), the net flux in each of the largest regions (1 and 4) have the same negative sign. Furthermore, the total net flux is strongly negative. The same is true for different threshold field values in Figure 5.15. Taking different threshold values for the filter value of the magnetic flux does affect the magnitude of the absolute flux through each region (see Figure 5.15). However, the net flux is largely independent of the filter threshold chosen. Since our study requires determination of the net magnetic flux through the dimmings, our conclusions are not strongly dependent on the filter threshold chosen, although the filtering remains an important step as we do not wish to take noise or small-scale connectivities into account.

5.7.2 Interplanetary Data Analysis and Results

Mandrini *et al.* (2007) summarise the extensive previous work done on modelling and study of the 28th October 2003 interplanetary event. MAG/ACE observed a magnetic cloud associated with this event from before midday on 29th October until the early morning of 30th October 2003. For this case study, a start time of 11:25 UT on 29th October and an end time at 02:00 UT on 30th October 2003 are chosen. These times correspond to a transition from a fluctuating field to a homogeneous and strong field inbound, and the reverse outbound (see Figure 5.16).

In situ magnetic observations are analysed, obtained by MAG with 64-second temporal cadence. The magnetic cloud axis direction, z_{cloud}, is defined using the minimum variance (MV) method. The MC is found to be in expansion at the time it is observed by MAG. Mandrini *et al.* (2007) discuss details of this effect and the correction applied.

After applying the MV method to the normalized field data, we rotate the observed magnetic field components to the cloud frame, (x_{cloud}, y_{cloud}, z_{cloud}), (see Dasso *et al.*, 2006, 2007). In this frame, when one considers a small impact parameter, $p \sim 0$ (the minimum distance between the cloud axis and the spacecraft trajectory) and a cylindrical structure for the cloud, the vectors are such that x_{cloud}, y_{cloud}, and z_{cloud} are parallel to the radial, azimuthal, and axial directions, respectively.

The magnetic flux in the cloud is quantified by fitting three models to the observations: the classical static Lundquists model (Lundquist, 1950) and two self-similar expansion cases (the expansion Lundquists model and the modified expansion Lundquists model, see Dasso *et al.* (2007)). Even though the cloud orientation can be found quite precisely using the MV method, assuming a low impact parameter, p, implies an underestimation of the magnetic flux values (because the magnetic field measured is lower than for a central crossing and the MC radius is underestimated).

Figure 5.16 shows the curves for the different fittings: static, expansion, and modified expansion Lundquists models (red, blue, and green dash-dotted lines, respectively). As seen in the top panel, none of the models can fit the structure observed between 11:31 UT and 11:43 UT on 29th October. However, the modified expansion Lundquists model (green line, Figure 5.16) is the one that best reproduces the asymmetric beginning and end of the cloud for $B_{y,cloud}$. For $B_{z,cloud}$, both expansion models closely follow the data; the static model is the one that gives the worst fitting.

From the fitted parameters we compute the axial (ϕ_z) and azimuthal (ϕ_ϕ) magnetic fluxes, as done in Dasso *et al.* (2007). The results are listed in Table 5.5. The MC fluxes are then estimated, taking the range given by the three models, as: $2.8{\times}10^{21}$ Mx $\leq \phi_z \leq 3.1{\times}10^{21}$ Mx and $5.7{\times}10^{21}$ Mx $\leq \phi_{y/L} \leq 8.0{\times}10^{21}$ Mx/AU.

Analyzing ACE/Solar wind electron proton alpha monitor observations of suprathermal electrons, Skoug *et al.* (2004) found the presence of counterstreaming electron flows for a period of time within the MC, though there were periods when electron measurements were unreliable. This would imply (see chapter 1, §1.7.6.1) that the cloud is anchored to the Sun at both ends when observed at 1 AU; so the MC length should be at least 2 AU. Considering this minimum length and summing F_z and F_y gives a total cloud flux in the range $14{\times}10^{21}$ Mx $\leq \phi_{MC} \leq 19{\times}10^{21}$ Mx. It is noteworthy that this value is a lower bound estimate for the MC flux.

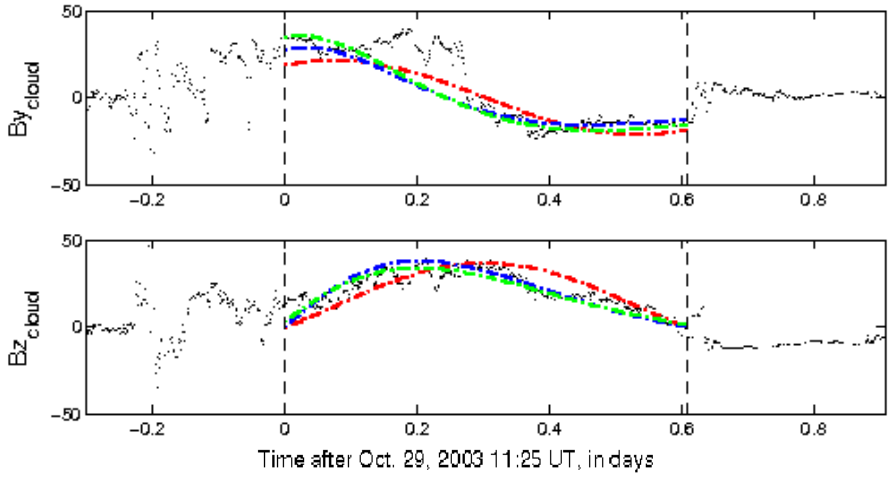

Figure 5.16: Top and bottom panels show the $B_{y,cloud}$ and $B_{z,cloud}$ components of the magnetic field (measured in nT) in the cloud frame (data from MAG as small dots and fitted curves). The red dash-dotted line corresponds to the static Lundquist's model. The blue and green dash-dotted lines correspond to the expansion Lundquist's and the modified expansion Lundquist's models, respectively. The two vertical lines mark the "in" and "out" boundaries. The x-axis shows the days elapsed after 29th October 2003, 11:25 UT, the initial start time of the magnetic cloud. Figure adapted from Mandrini *et al.* (2007). Permission to reproduce this figure has been granted by Springer Science and Business Media.

Table 5.5: Magnetic fluxes computed for the MC observed on 29th-30th October, 2003, at 1 AU. The *first* column indicates the fitting model, and the *second* and *third* columns show the values of the axial and azimuthal (per unit length) magnetic fluxes.

Model	ϕ_z (10^{21} Mx)	$\phi_y\ L^{-1}$ (10^{21} Mx AU^{-1})
static	3.1	5.7
expansion	2.9	6.6
modified	2.8	8.0

5.7.3 Case Study Discussion

Even though the two most extended dimmings (dimmings 1 and 4; see Figures 5.13 and 5.14) appear on either side of AR 10486, they do not present the typical characteristics of double or core dimmings. Core dimmings are present on both sides of the eruptive magnetic configuration and have magnetic net fluxes of opposite signs with approximately the same absolute values. For the event on 28th October 2003, we find that dimmings 1 and 4 have net negative fluxes, whereas the net fluxes in the others (dimmings 2 and 3) are positive. Furthermore, if we add the net fluxes in dimmings 1 and 4 and those of 2 and 3, the latter value is one order of magnitude lower (i.e. the total net flux is not balanced). Indeed both dimmings 2 and 3 are located above quiet Sun regions where the positive flux only dominates slightly (see Figure 5.15, showing positive and negative flux curves that are close together). The net result is that all the flux covered by the dimming regions has a strong negative imbalance. Dimming 1 extends above the negative polarity of the decaying AR by which AR 10486 is bounded to the west. It also encompasses the negative field surrounding AR 10492. These negative fields are not balanced by the positive fields within this dimming (Figure 5.14). Dimming 4 extends mainly above the negative field in AR 10495. There is also an important dimming close to dimming 4, lying above the eastern limb (Figure 5.13). This dimming is located over the positive flux part of AR 10495. Its location near the limb does not allow us to estimate its flux, but in view of its location the flux is expected to be dominantly positive and to have a comparable magnitude to the flux found in dimming 4. Since the following polarity of AR 10486 is positive, and the erupting flux rope is rooted there (see Mandrini et al., 2006), at least at the beginning of the eruption, positive dimmings both there and at some location to the east are expected. The dimming above the eastern limb is the only one that plausibly has enough positive flux to coincide with the positive footpoint of the erupting magnetic configuration. The net flux in dimming 1 is $\sim$ -4.0$\times10^{21}$ Mx, this value is close to the axial MC flux range (2.8 - 3.1)$\times10^{21}$ Mx. This suggests that dimming 1 might correspond to the original negative MC footpoint in the classical scenario in which an already existing flux tube expands and erupts. However, we argue that this cannot be the case since the eruption occurred inside AR 10486 and dimming 1 is located far to the west of the region; furthermore, we do not find the corresponding associated positive dimming. However, if the flux rope is dominantly formed by reconnection *during* the eruption, we have to compare the dimming flux to the total MC flux observed in the interplanetary space. The total negative net flux in dimmings 1 and 4 ($\sim 11\times10^{21}$ Mx) is close to the lower limit of the total MC flux for the estimated cloud length, 14×10^{21} Mx $\leq \phi_{MC} \leq 19\times10^{21}$ Mx. However, considering that this estimation is a lower bound, we conclude that the flux in the dimmings identified on the disk does not match the total flux in the cloud and, in view of their spatial distribution and net flux, the observed dimmings (1 to 4) do not represent the initial footpoints of the ejected magnetic configuration (initial flux and surrounding arcade).

5.7.4 Origin of the 28th October 2003 Dimmings

In chapter 4 we highlighted that besides core dimmings, there is another type of dimming, more widespread, that corresponds to the spatial extent of CMEs detected in coronagraph data (Thompson *et al.*, 2000a). Here we call these secondary dimmings. Our results in the previous sections are an indication that, in this particular event, we do not observe the core dimmings, but rather the secondary dimmings, the origin of which we discuss in the following. Recently, Attrill *et al.* (2007a) proposed a new mechanism (described in chapter 4) where driven magnetic reconnection between the outer edge of an expanding CME magnetic field and quiet-Sun magnetic loops can generate

the observed diffuse bright fronts that constitute the leading edge of EIT coronal "waves". It is noteworthy that the magnetic configuration of surrounding ARs can replace some of the quiet-Sun loops of the events they studied (which occurred close to solar minimum). In this scenario, the presence of widespread secondary dimmings behind the diffuse bright front is a natural consequence of the driven reconnections. Could this mechanism be responsible for the dimmings observed in this 28th October 2003 event? Figure 5.17 illustrates the way in which dimmings 1 and 4 could have been formed. As the main filament in AR 10486 erupts, the magnetic field of the AR expands and to the west encounters a nearby filament channel between the positive and negative polarities (where dimming 1 lies; Figure 5.17a) of the decaying AR preceding AR 10486. To the east, quiet-Sun fields are encountered (where dimming 4 lies; Figure 5.17a). The expanding CME magnetic loops reconnect with the favorably oriented loops that are encountered both to the west and the east. Magnetic reconnection creates two new sets of connections. One set is formed by small loops (red field lines in Figure 5.17b). These loops will be bright owing to the reconnections (these loops constitute the bright front surrounding the core dimmings of the AR, as shown by Attrill *et al.*, 2007a). The second result of the magnetic reconnections is to form long loops (blue field line in Figure 5.17b), still belonging to the erupting magnetic configuration but with new, displaced footpoints (which form the diffuse leading bright front of the coronal "wave"). Dimmings are associated with these large loops as the plasma, initially contained in the surrounding loops, becomes free to expand into the larger volume created by the long (blue) loop. This process is repeated many times as the continuing lateral expansion of the CME core drives progressively new reconnections (see Figure 5.17c). To the west, the expanding structure encounters and reconnects with the favorably orientated magnetic loops in AR 10492 (represented by the three black field lines on the right side of Figures 5.17a and 5.17b). To the east, reconnection with favorably oriented quiet-Sun loops continues until the still expanding CME encounters loops belonging to AR 10495 (represented by the three black field lines on the left side of Figures 5.17a and 5.17b). The removal by reconnection of the outer set of loops in AR 10495 produces dimmings of both polarities; this is the main reason why dimming 4 has a net negative flux. This continuous step-like reconnection process results in the spread of the secondary dimming 4 and the appearance of dimming over the east limb. The secondary dimmings 2 and 3 are understood to form by the same mechanism. Reconnection occurs in these regions with loops of the quiet Sun in a more mixed field environment, with some new features as follows. Dimming 2 extends south to the positive polar coronal hole. There the negative expanding edge of the CME configuration reconnects with open positive field lines, creating small reconnected loops (see Benevolenskaya, 2004). The reconnection region progressively shifts its location along the inversion line so that a zipper-like, moving brightening is observed (similar to that discussed for the 12th May 1997 event in §5.2.7, see also Attrill *et al.*, 2006). These interchange reconnections (Crooker *et al.*, 2002) also imply a partial, but true, disconnection of this southern part of the negative leg of the CME from the Sun. The disconnection of the negative leg of this part of the CME field implies that the other (positive) end of the field is "open", leading to dimming in the positive leg. This process may well contribute to the formation of dimming region 3. For dimming 3, besides the latter mechanism, two other mechanisms contribute to dimming formation: quiet-Sun reconnections, as proposed by Attrill *et al.* (2007a), and the "disappearance" of bright loops connecting AR 10496 to the northern AR 10487, and AR 10491 to AR 10488, as described in other events by Delannée (2000).

5.7.5 Case Study Conclusion

In summary, the basic skeleton of a CME consists of the upward extension of the erupting configuration and the formation of a pair of core dimmings. However, none of the observed dimmings on the 28th October 2003 event can be associated with such core dimmings. Instead, we have identified the observed dimmings as secondary dimmings, forming in the manner proposed by Attrill *et al.* (2007a). The strong energy release during the X.17 flare in AR 10486 led to reconnections with a concentrated magnetic flux density, leading to the formation of dense and bright coronal loops. The strong emission of these loops, combined with the spreading of the saturated signal, covers most of AR 10486. Any core dimming, strong as it could be, is masked by the intense emission of the flaring region so that none of the expected core dimmings can be observed. We expect that this is a general property of very strong events.

The magnetic reconnection process that creates the secondary dimmings should conserve magnetic flux. When we are able to observe both core and secondary dimming regions (in the case of less energetic flares), we would expect that the total flux of the dimmings divided by 2 should equate to the total flux in the associated MC. However, the formation of secondary dimmings is a time-dependent complex process. As the flux connectivity is transferred from the core dimmings to the surrounding regions, the disappearance of the dimmings in the core takes time and a delay can be also expected in the formation of the secondary dimmings (the time needed for the plasma to be evacuated). Moreover, brightenings are expected to form very close to the dimmings and only the deeper part of the dimming is expected to be detectable. Observations only give only the total intensity integrated along the line of sight, in particular, brightenings and dimmings can be mixed up. This bias is expected to be important since the physics of the CME eruption involves the *coupled* formation of brightenings and dimmings (as discussed in chapter 4 and in Attrill *et al.*, 2007a). Indeed, Thompson *et al.* (1999) note that in the coronal wave patchy bright front, some pixels increase in intensity, mixed with others that show a depletion in intensity. This mixing effect increases as one observes farther away from the disk center. In large events, where signatures extend to a large fraction of the solar disk, this effect cannot be avoided, even by analyzing events that start close to the disk center. The dynamic process discussed here leads to uncertainties in defining the boundary of such secondary dimmings at a given time; so, there are uncertainties when adding the magnetic flux of the core and secondary dimmings at any given time. Moreover, these uncertainties grow with the number of reconnecting steps needed to create the secondary dimmings.

In addition, strong magnetic field in the AR means that the erupting field has a significant magnetic pressure. This implies a strong expansion of the erupting field, not only vertically but also *laterally* over neighboring quiet-Sun regions and ARs. As a result, magnetic reconnection is expected in most cases (cases with almost parallel fields are rare). These reconnections imply the formation of new brightenings (contributing to the diffuse EIT "wave" phenomena), as well as a reorganization of the magnetic connectivities, which enables the spread of the dimmings over a region much larger than that of the original eruption (Attrill *et al.*, 2007a). These reconnections imply that *CMEs become large scale even in the low corona*, as evidenced by radio observations at metric wavelengths (Pick *et al.*, 2005) and by the large spatial extent of CME-associated limb dimmings observed in EUV 195 Å (Thompson *et al.*, 2000a; Attrill *et al.*, 2007b).

Finally, a large event can also induce strong effects in neighboring active regions, for example, the destabilization of interconnecting loops (between the initial eruption site and surrounding re-

gions) and/or inside nearby ARs (Delannée *et al.*, 2007). Destabilization of surrounding structures can be recognized by the loop shape of the dimmings and by comparing the locations of the dimmings (using difference images) with EUV and X-ray direct images where coronal loop structures can be identified before the CME.

Therefore, direct comparisons between the magnetic flux in the dimmings and the total flux of the associated MC are difficult in large-scale events (with a large flare and/or a large lateral expansion and reconnection with many surrounding bipoles).

5.8 Summary of chapter

Previous work has suggested that coronal dimming regions located either side of the flare loops mark the position of the erupting flux rope footpoints (Webb *et al.*, 2000). This was later confirmed by Mandrini *et al.* (2005) and Attrill *et al.* (2006) (as described in §5.1 - §5.6 of this chapter), in a scenario in which the flux rope found in the interplanetary medium was mostly formed by reconnection *during* the eruption process. During the ejection of the magnetic configuration (which makes up the associated CME), magnetic loops drastically expand. The plasma can expand upward into this larger volume, forming dimming regions at these locations. However, in large-scale (powerful) events such a simple interpretation encounters difficulties because of the presence of brightenings (owing to the flare and often a global-scale EIT coronal wave and associated persistent brightenings) and because of reconnection of the erupting field with the surrounding environment.

We conclude that a careful analysis of the origin of the various dimmings is required before their magnetic flux can be compared to that of the associated interplanetary MC since dimmings that form either side of flare loops do not necessarily correspond to flux-rope footpoints, as is the case for some events. This is especially true in large events because of the failure to observe core dimmings and the biases induced by mixing brightenings and dark regions. This is also present in medium and small events because of the interaction of the expanding field with neighbouring fields (both for quiet Sun and nearby ARs).

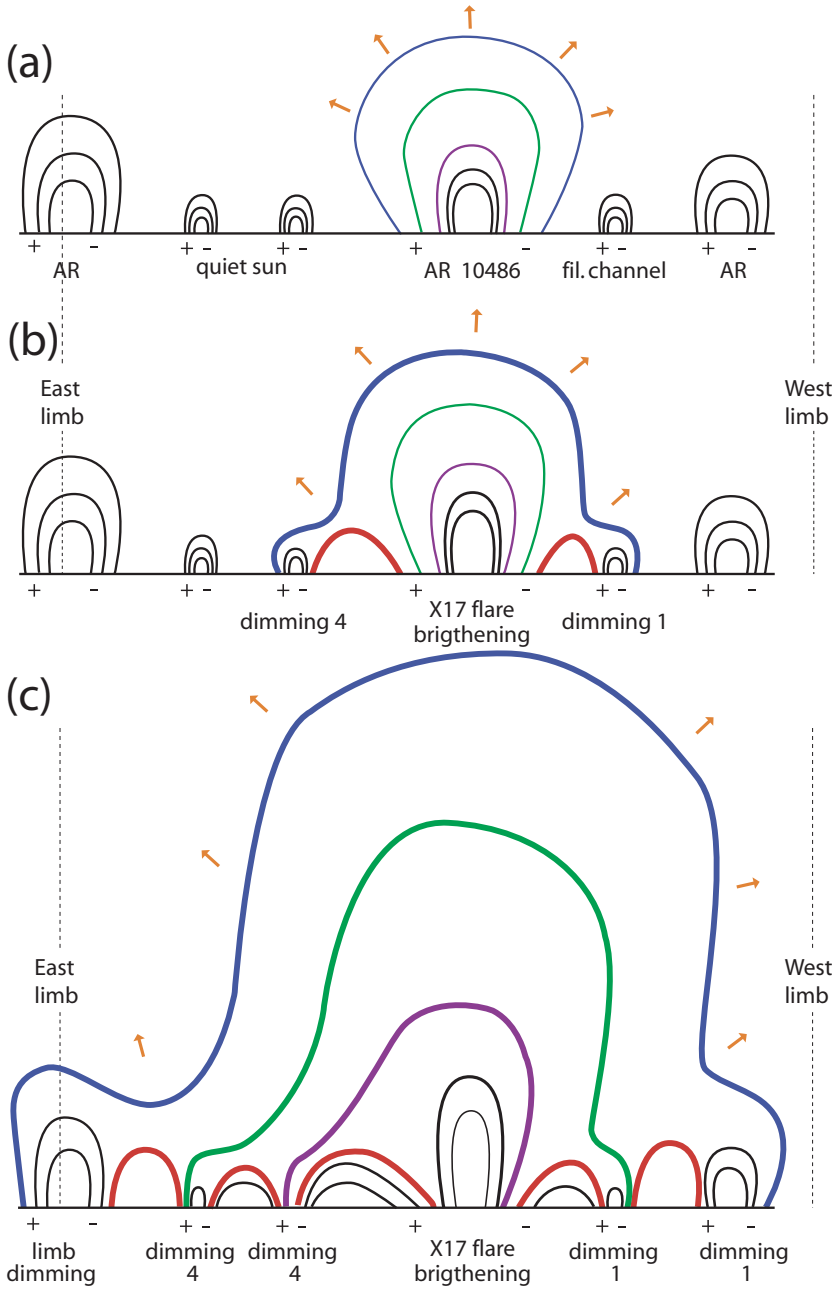

Figure 5.17: Reconnection of the expanding CME field configuration with the surrounding bipoles: dimming spreading (mechanism proposed by Attrill *et al.*, 2007a, applied to the 28th October 2003 event). (a) The CME lift-off. AR 10486 is represented by five black field lines, while nearby bipoles are represented with three black field lines. (b,c) By successive reconnections the outer shell of the CME expanding magnetic field is progressively rooted in more distant regions. This mechanism explains the spreading of the dimmings to progressively larger spatial scales. In these figures the just reconnected field lines are thicker (and set to red for the short loops). Figure from Mandrini *et al.* (2007). Permission to reproduce this figure has been granted by Springer Science and Business Media.

Chapter 6

Late-Stage Recovery of Coronal Dimmings

In chapter 5 we discussed the early-stage closing-down of a coronal dimming due to a large-scale, somewhat remote, interchange reconnection between the CME and the "open" magnetic field of the north polar coronal hole. In this chapter we focus on the small-scale, long-term localised recovery of coronal dimmings. In particular we discuss the recovery of CME-related dimmings and the ICME's enduring magnetic connection to the Sun.

It is generally accepted that transient coronal holes (TCHs, dimmings) correspond to the magnetic footpoints of CMEs which remain rooted in the Sun as the CME expands out into the interplanetary space. However, the observation that the average intensity of the 12th May 1997 dimmings recover to their pre-eruption intensity in SOHO/EIT data within 48 hours, whilst suprathermal uni-directional electron heat fluxes are observed at 1 AU in the related ICME more than 70 hours after the eruption, leads us to question why and how the dimmings disappear whilst the magnetic connectivity is maintained. In this chapter we also examine two other CME-related dimming events: 13th May 2005 and 6th July 2006. We study the morphology of the dimmings and how they recover. We find that, far from exhibiting a uniform intensity, dimmings observed in SOHO/EIT data have a deep central core and a more shallow extended dimming area. The dimmings recover not only by shrinking of their outer boundaries but also by internal brightenings. We quantitatively demonstrate that the model developed in Fisk and Schwadron (2001) of interchange reconnections between "open" magnetic field and small coronal loops, is a strong candidate for the mechanism facilitating the recovery of the dimmings. This process disperses the concentration of "open" magnetic field (forming the dimming) out into the surrounding quiet Sun, thus recovering the intensity of the dimmings whilst still maintaining the magnetic connectivity to the Sun.

6.1 Questions concerning the relationship between dimmings and ICMEs

Despite the often assumed association between dimmings and ICMEs/MCs, Kahler and Hudson (2001) have questioned why coronal dimmings are often observed to disappear well before the

associated MCs reach 1 AU. If the identification of coronal dimmings as the footpoints of the expanded erupted magnetic flux rope is correct (as indeed seems plausible given the works of Webb *et al.* (2000); Mandrini *et al.* (2005); Attrill *et al.* (2006)), then we need to understand why and how dimmings disappear despite the magnetic connectivity to the Sun being maintained as indicated by electron heat flux measurements at 1 AU.

In search of answers, in this chapter we examine the recovery in intensity of dimmings using SOHO/EIT data and examine the results in the context of interplanetary detection of the associated ICME/MC. We study the morphology of the dimmings and how they evolve. We discuss the interplanetary *in situ* data for the three events in § 6.2, present our analysis and results of the solar data in § 6.3, critically discuss the results and suggest a possible physical mechanism for the recovery of the dimmings in § 6.4.

6.2 The interplanetary signatures of the CME-related dimming events

6.2.1 12th May 1997 event

This is a much-studied "classical" dimming event, originating from NOAA AR 8038, and associated with a long-duration C1.3 class flare, a diffuse coronal wave and a halo CME. The study of the evolution and magnetic nature of these unidentical twin dimmings was described in chapter 5 (see also Attrill *et al.*, 2006). The interpretation of this event by Webb *et al.* (2000) that the dimmings marked the footpoints of the associated erupted flux rope is strongly supported by both studies.

Figure 6.1 (a) shows data from the Magnetic Field Investigation (MFI; Lepping *et al.*, 1995), aboard the *Wind* spacecraft. *In situ* magnetic observations (3 s temporal cadence) were obtained by the MFI instrument. The data were downloaded from the public database `http://cdaweb.gsfc.nasa.gov/cdaweb/istp public/`. Figure 6.1 shows the magnetic field vector components measured in the Geocentric Solar Ecliptic (GSE) system. The *Wind* 3-D Plasma and Energetic Particle experiment (3DP; Lin *et al.*, 1995) electron spectrogram data (displayed in the bottom panels of Figure 6.1) were downloaded from `http://sprg.ssl.berkeley.edu/wind3dp/esahome.html`. In the interval identified as the MC (10:00 UT 15th May to 01:00 UT 16th May (Webb *et al.*, 2000; Attrill *et al.*, 2006) - between vertical dashed lines in Figure 6.1), there is a weak uni-directional electron heat flux (green, indicated by the black arrow), starting at 10:00 UT on 15th May. This uni-directional electron stream is directed parallel to the magnetic field (pitch angle 0°) and so is understood to originate from a positive polarity source on the Sun. As discussed in chapter 5, the uni-direction electron heat flux in this event is expected as a result of the global interchange reconnection between the northern negative leg of the CME and the "open" positive field of the north polar coronal hole (see Figure 5.10). An explanation of the interpretation of electron heat fluxes with regard to the magnetic field connectivity can be found at the end of §1.7.2.

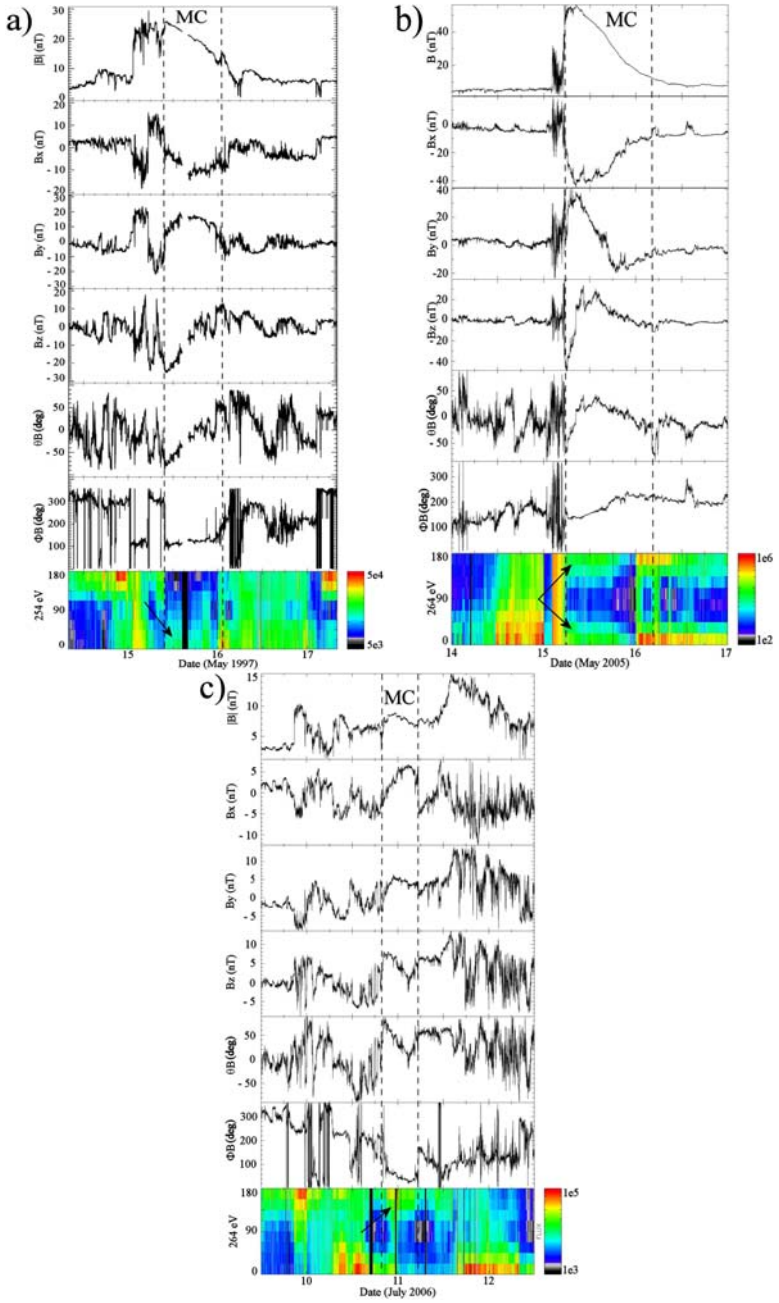

Figure 6.1: Interplanetary data from the *Wind* and ACE spacecraft showing the relationship between the MC and electron heat fluxes for the three events (a) 12th May 1997, (b) 13th May 2005 and (c) 6th July 2006, respectively. Vertical dashed lines indicate the duration of the magnetic cloud for each event. The first 4 panels of each plot (reading from top to bottom) show the interplanetary magnetic field (IMF) and its components. The 5th panel shows the θ angle of the IMF vector, with time, where θ is the angle between the ecliptic plane (defined by X_{GSE}, Y_{GSE}) and the IMF in GSE coordinates. The 6th panel shows the ϕ angle of the IMF with time, where ϕ is the angle between X_{GSE} and the projection of the IMF in GSE onto the ecliptic plane. The bottom panels show the pitch-angle distribution of the energetic electron heat fluxes. Black arrows indicate the electron streams within the magnetic clouds. Permission to reproduce this figure has been granted by Springer Science and Business Media.

6.2.2 13th May 2005 event

This full-halo CME event originating from NOAA AR 10759 was associated with a long duration M8.0 class flare and a diffuse coronal wave. The event has been studied by Yurchyshyn *et al.* (2006) and Qiu *et al.* (2007), who both examine the solar data and interplanetary counterpart. Liu *et al.* (2007) concentrate their study on the detailed process of the sigmoid eruption. The event is also under study by the SHINE community. In some ways it is perceived to be a similar event to 12th May 1997. However, despite the apparently similar "double dimming" signature, there are key differences. Namely, this event takes place during the declining phase of the last solar cycle, not at the rise phase of a new cycle. As such, the background magnetic field is considerably more complex than that of 12th May 1997. We believe that this is a key reason why the dimming signatures of 13th May 2005 are considerably more complex. We discuss this further in § 6.3.1 and § 6.3.3. Figure 6.1b (panels 1-6) shows data from the Magnetometer instrument (MAG; Smith *et al.*, 1998), aboard the ACE spacecraft. *In situ* magnetic observations were obtained at a temporal cadence of 16 s. The bottom panel of Figure 6.1b shows the *Wind* 3DP electron spectrogram data. Yurchyshyn *et al.* (2006) identify bi-directional heat flux (green, indicated by black arrows) between 05:30 UT 15th May - 08:00 UT 18th May 2005 and place the boundaries of the MC from 06:00 UT - 19:12 UT on 15th May. Qiu *et al.* (2007) identify the start of the MC at 05:40 UT on 15th May, stating its duration as being 23 hours, taking the "end" of the MC to 04:40 UT on 16th May.

6.2.3 6th July 2006 event

This event also exhibits the classical "double dimmings" signature. The halo CME originated from NOAA AR 10898 and was associated with an M2.5 class flare and a diffuse coronal wave. The onset of the event was studied in detail by Jiang *et al.* (2007) and the recovery phase has been examined by McIntosh *et al.* (2007). Figure 6.1c shows data from the ACE/MAG instrument at a temporal cadence of 16 s. The bottom panel shows electron spectrogram data from *Wind* 3DP. A MC is identified between approximately 21:30 UT on 10th July and 06:00 UT 11th July. There are three intervals that show evidence for uni-directional suprathermal electron signatures. The interval closest in time with the MC is between 21:30 UT on 10th July to 04:15 UT on 11th July. In this interval, there are uni-directional electrons (green, indicated by a black arrow) at 180° to the magnetic field, which are understood to originate from a negative polarity source.

6.3 Solar Data Analysis and Results

We use SOHO/EIT (Delaboudinière *et al.*, 1995) 195 Å full disk images, at approximately 17, 17 and 12 minute intervals with pixel sizes of 5.26″, 5.26″ and 2.63″ for the 12th May 1997, 13th May 2005 and 6th July 2006 events, respectively. All EIT heliograms are differentially de-rotated to the same pre-event time at the start of each dataset, using the *SolarSoft* `drot_map` routine. This routinue corrects for the latitudinal dependence of the solar differential rotation function, however we note that projection effects in the derotated 3-D corona still remain in the data. The 12th May 1997 dataset runs from 00:12 UT on 12th May 1997 until 23:55 UT on 13th May 1997 before limb brightening/darkening effects, due to the de-rotation, make a significant contribution to the region where the main dimmings are located. Similarly, the 13th May 2005 dataset runs from 14:05 UT

on 13th May until 13:46 UT on 15th May 2005 and the 6th July 2006 dataset runs from 03:54 UT on 6th July until 19:48 UT on 7th July 2006.

To visualise the dimmings clearly, we produce base difference images where the same pre-event image is subtracted from all subsequent images. In order to carefully analyse the evolution of the dimmings, we need to impose reproducible and quantifiable boundaries. We use the contour method described in chapter 5, §5.2.2 (§2.2 of Attrill *et al.*, 2006), where iso-contour brightness levels are set to lie halfway between the intensity of an area of the quiet Sun and that of an existing coronal hole. We choose reference coronal hole and quiet Sun regions that are far from the source region of the CME and are as large in area as is feasible. For the 12th May 1997 event, a region in the south polar coronal hole centred at (-80″, -860″) extending 100″ in each direction is used and the quiet Sun reference level is from a region centred at (-560″, 170″), extending 100″ in each direction. For the 13th May 2005 event, a region in the north polar coronal hole centred at (-135″, 890″) extending 75″ in each direction is used and the quiet Sun reference level is from a region centred at (-400″, -265″), extending 100″ in each direction. For the 6th July 2006 event, a region in the north polar coronal hole centred at (30″, 880″) extending 75″ in each direction is used and the quiet Sun reference level is from a region centred at (-390″, -70″), extending 100″ in each direction.

6.3.1 Contraction of the dimmings

Figures 6.2, 6.3 and 6.4 show EIT 195 Å heliograms with the dimmings near their maximum spatial extent for the 12th May 1997, 13th May 2005 and 6th July 2006 events, respectively. The top right panels of each figure show a corresponding base difference image, overlaid on which are contours calculated at the times shown during the recovery phase of the dimmings. The shrinking of the contours reflects the shrinking of the spatial extent of the dimmings which occurs in a fragmentary, inhomogeneous, gradual manner; a recovery from the outer boundary inward. Table 6.1 quantifies the change in area of the dimmings. The evolution of the contour plots (Figures 6.2, 6.3 and 6.4) can also be viewed as movies (see Appendix E).

In the 12th May 1997 event (Figure 6.2) shrinking of the spatial extent of both the dimmings is clearly visible. The northernmost part of dimming 1 shows a larger contraction than the periphery of dimming 2. This is discussed in chapter 5 and in Attrill *et al.* (2006) and Crooker and Webb (2006) where this more substantial spatial recovery is attributed to a large-scale interchange reconnection between the magnetic field of the expanding CME rooted in dimming 1 and the "open" magnetic field of the north polar coronal hole.

Identified as a "twin dimmings" event in the literature, the evolution of the 13th May 2005 dimmings (Figure 6.3) is clearly asymmetric and more complex than that of the 12th May 1997 event. The only region which shows a clear contraction in the time-scale covered by our dataset is the southern part of dimming 2. Liu *et al.* (2007) note that an extension to the south of dimming 2 went on to develop "into an elongated transequatorial coronal hole".

The 6th July 2006 event exhibits clear contraction of only dimming 2 (Figure 6.4) in all directions. Although dimming 1 shows a contraction from the north-east, the extent of the rest of this region remains constant throughout our dataset - a noteable feature that also applies to the scattered dimmings surrounding dimming 1.

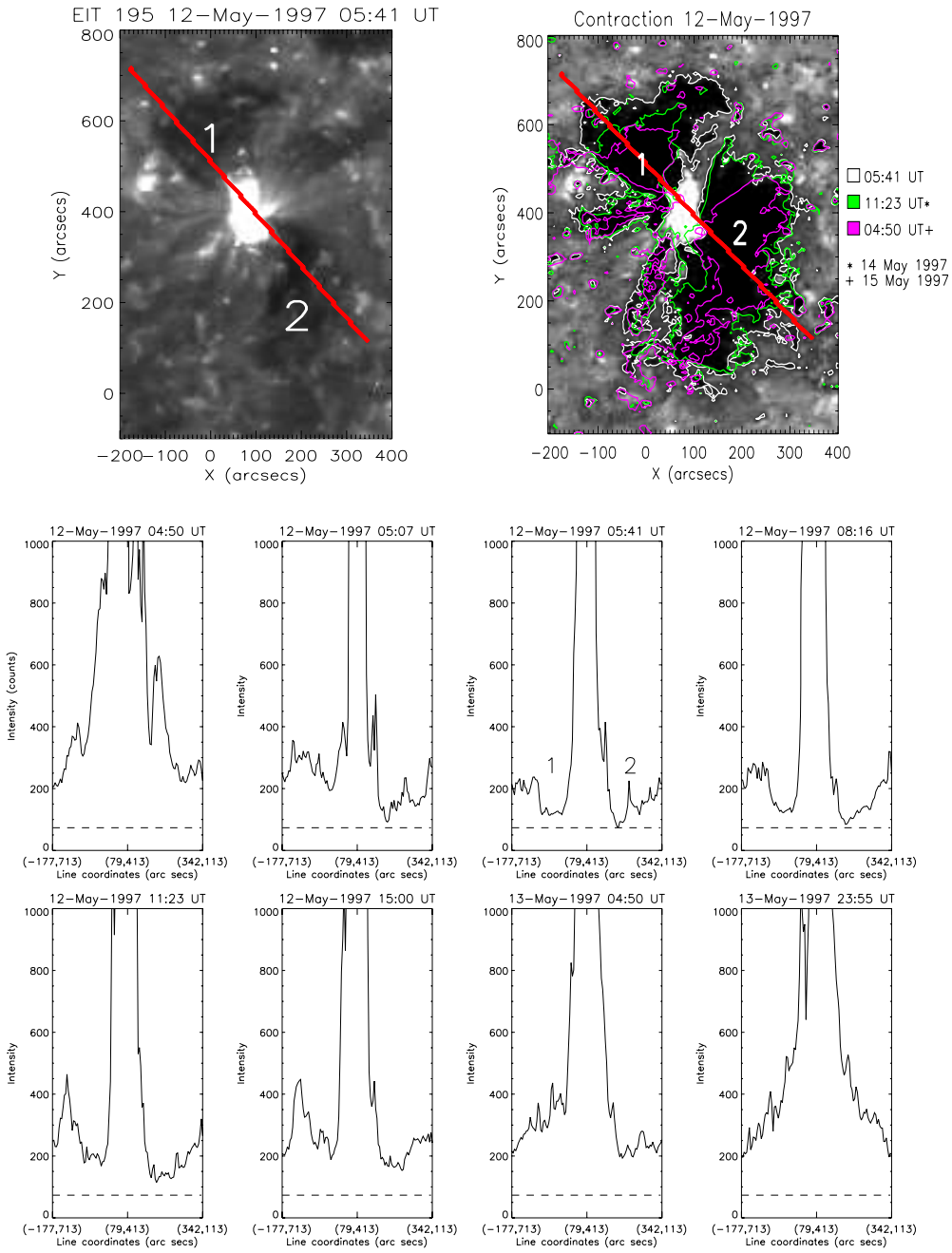

Figure 6.2: The top left panel is an EIT intensity heliogram showing the 12th May 1997 dimmings. The top right is a base difference image showing the dimmings, with contours overlaid at the times shown in the colourbar. *This plot is best viewed as a movie showing the evolution of these dimmings:* **contraction_120597.mpg, Appendix E**. The red line overlaid on both figures shows the location of the original EIT intensity data used to produce the following intensity profile plots. Bottom: Intensity profile plots made along the red line across the cores of the dimmings, at various times during the dimming recovery. The dimmings are identified by the numbers 1 and 2. The dashed line shows the deepest dimming level reached inside the dimmings in this time series. Permission to reproduce this figure has been granted by Springer Science and Business Media.

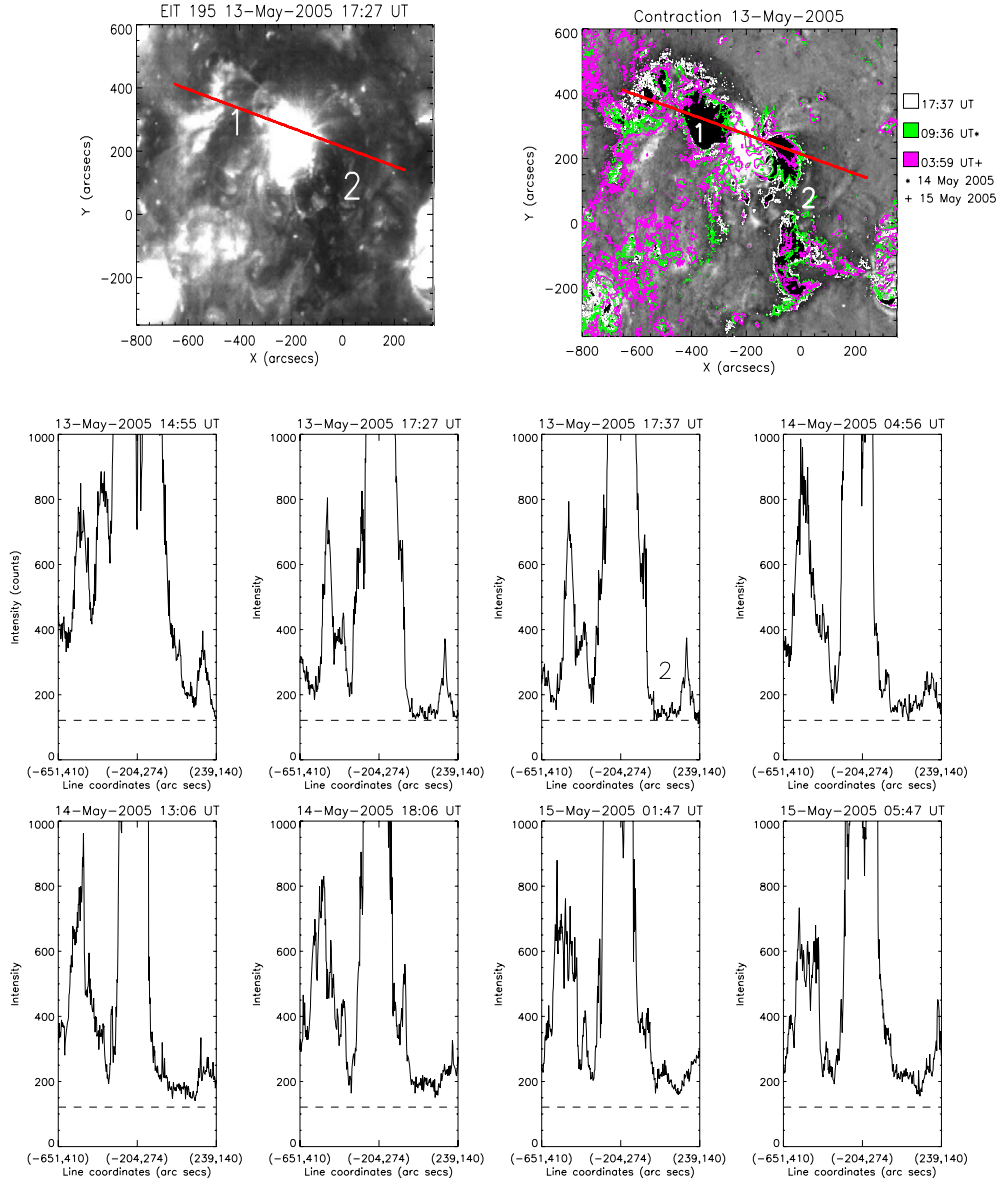

Figure 6.3: The same quantities are plotted in this figure as for Figure 6.2, but for the 13th May 2005 event. *The contour plot is best viewed as a movie showing the evolution of these dimmings:* **contraction_130505.mpg, Appendix E**. Permission to reproduce this figure has been granted by Springer Science and Business Media.

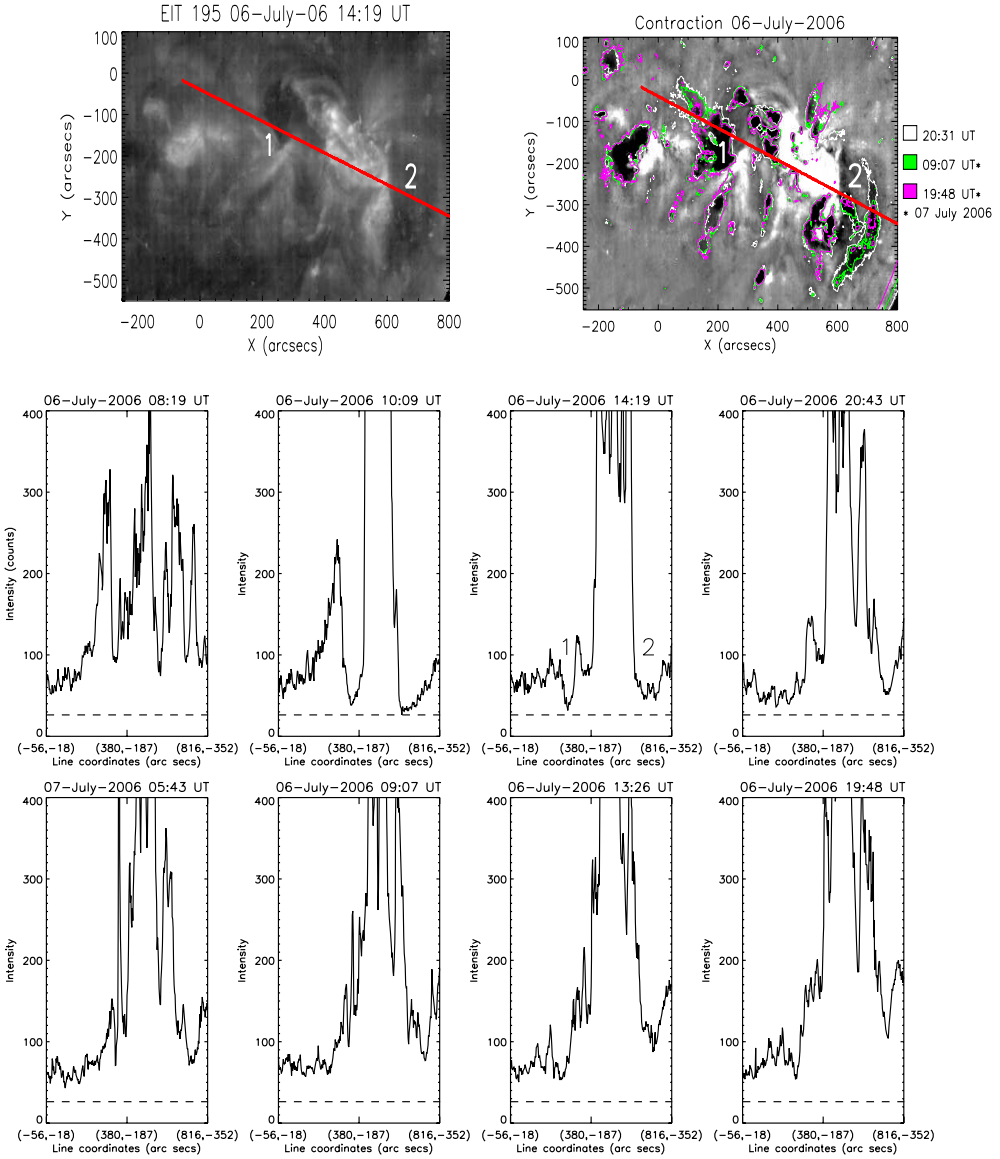

Figure 6.4: The same quantities are plotted in this figure as for Figure 6.2, but for the 6th July 2006 event. *The contour plot is best viewed as a movie showing the evolution of these dimmings:* **contraction_060706.mpg, Appendix E**. Permission to reproduce this figure has been granted by Springer Science and Business Media.

Table 6.1: Area and difference (dArea) in units of 10^{10} km^2 of the dimmings defined by the white, yellow, green and blue contours in the movies accompanying Figures 6.2, 6.3 and 6.4 for each of the three events. dTime is the time difference between contours (in hrs). dArea/dTime is the rate of change of the dimming areas (in units of 10^5 km^{2}s^{-1}).

Contour & Time	Area	dArea	dTime	$\frac{\text{dArea}}{\text{dTime}}$	Area	dArea	dTime	$\frac{\text{dArea}}{\text{dTime}}$
12/05/97		dimming 1				dimming 2		
White 05:41 UT	3.50				5.15			
		0.95	2.58	-10.2		0.54	2.58	-5.81
Yellow 08:16 UT	2.55				4.61			
		0.70	3.12	-6.24		0.44	3.12	-3.92
Green 11:23 UT	1.85				4.17			
		0.55	3.60	-4.24		0.87	3.60	-6.71
Blue 14:59 UT	1.30				3.30			
13/05/05		dimming 1				dimming 2		
White 17:37 UT	1.62				1.05			
		0.14	5.33	-0.73		0.13	5.33	0.67
Yellow 22:57 UT	1.48				1.18			
		0.03	10.65	-0.08		0.16	10.65	-0.42
Green 09:36 UT*	1.45				1.02			
		0.08	3.88	-0.57		0.30	3.88	-2.15
Blue 13:26 UT*	1.53				0.72			
06/07/06		dimming 1				dimming 2		
White 20:31 UT	1.19				0.67			
		0.24	9.20	-0.72		0.29	9.20	-0.87
Yellow 05:43 UT*	0.95				0.38			
		0.98	3.40	-0.08		0.12	3.40	-0.11
Green 09:07 UT*	0.85				0.26			
		0.69	4.31	-0.44		0.15	4.31	-0.97
Blue 13:26 UT*	0.78				0.11			

* denotes the event date plus one day.

Table 6.2: Extrapolated recovery times and lifetimes for the core and the periphery of the dimmings (assuming that the recovery gradient remains the same as that displayed in Figures 6.5, 6.6, and 6.7 - see § 6.3.3). The start of the recovery time is defined by the minima of the lightcurves. The time difference between the recovery and the start times define the lifetime of the dimmings.

Event & Dimming	Time core recovery (UT)	Time peripheral recovery (UT)	Lifetime core	Lifetime periphery
12/05/97 1	16/05/97 00:00	13/05/97 04:00	92 hrs	22 hrs
..... 2	15/05/97 02:00	13/05/97 16:00	68 hrs	34 hrs
13/05/05 1	No recovery	-	-	-
..... 2	17/05/05 16:00	15/05/05 07:00	89 hrs	32 hrs
06/07/06 1	No recovery	-	-	-
..... 2	08/07/06 06:00	07/07/06 14:00	44 hrs	27 hrs

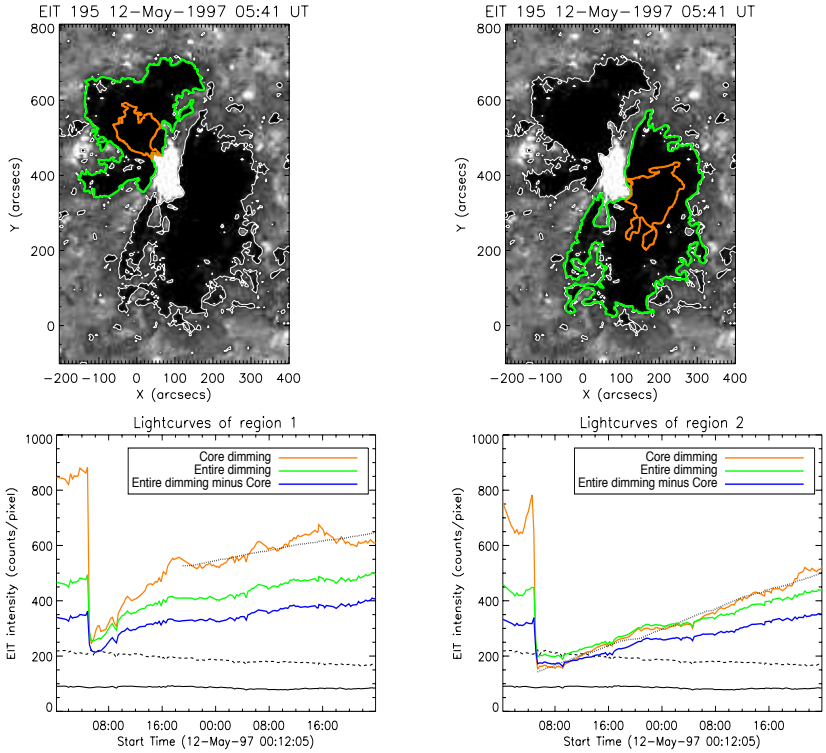

Figure 6.5: Top: Base difference images showing 12th May 1997 dimmings with contours (white) overlaid at 05:41 UT. Green regions mark out the full extent of the dimming analysed in the bottom panels. Orange regions mark out the cores of these regions, corresponding to dimmings still existing at 23:55 UT on 13th May 1997. Lightcurves: Green lightcurves show the average intensity of the entire dimming region (marked in green in the images above). Orange lightcurves show the average intensity of just the core (orange) dimming region. Overlaid is the black dotted line of best fit calculated during the recovery phase. Blue lightcurves show the average intensity of the peripheral dimming region (the full dimming, minus the core of the dimming). In all plots, the dashed line shows the intensity level in a region of quiet Sun, and the solid line indicates the intensity level in a pre-existing coronal hole for comparison. Permission to reproduce this figure has been granted by Springer Science and Business Media.

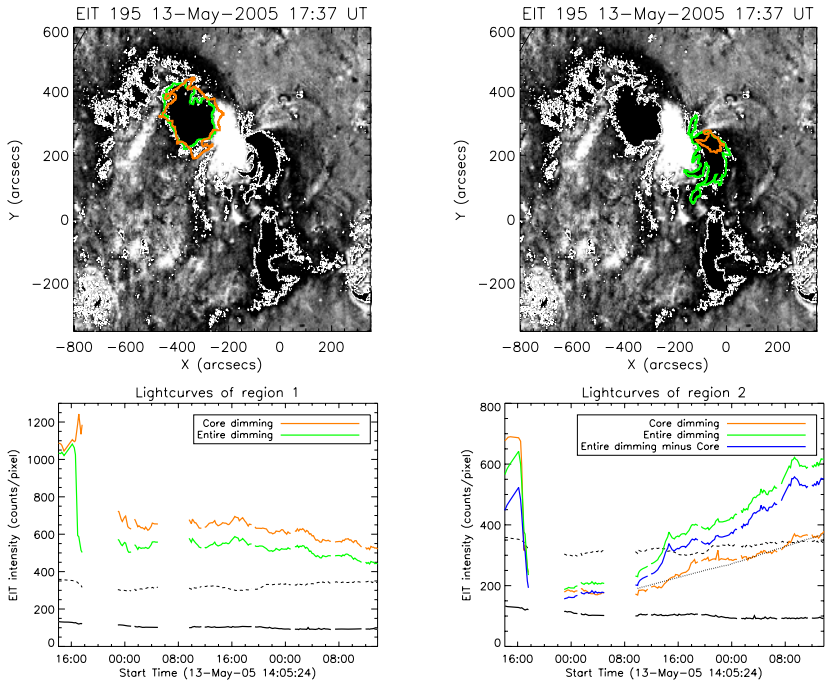

Figure 6.6: Top: Base difference images showing 13th May 2005 dimmings with contours (white) overlaid at 17:37 UT. The coloured regions and lightcurves have the same meanings as described in Figure 6.5. The orange cores of these regions correspond to dimmings still existing at 13:47 UT on 15th May 2005. Bottom: Region 1 does not show a substantial difference between the full and core dimmings during our dataset, so the resulting peripheral lightcurve does not contribute substantially different data to that already displayed and is omitted. Permission to reproduce this figure has been granted by Springer Science and Business Media.

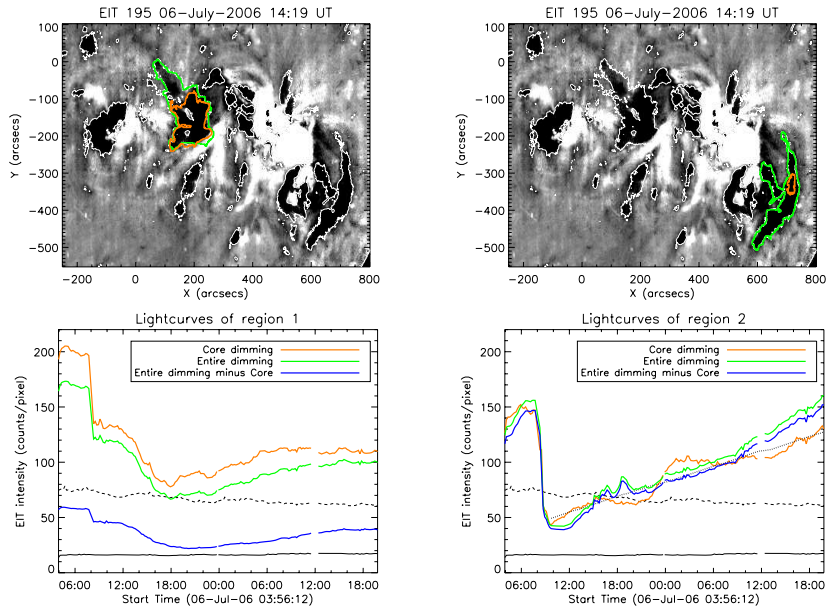

Figure 6.7: Top: Base difference images showing 6th July 2006 dimmings with contours (white) overlaid at 20:31 UT. The coloured regions and lightcurves have the same meanings as described in Figure 6.5. The orange cores of these regions correspond to dimmings still existing at 19:48 UT on 7th July 2006. Permission to reproduce this figure has been granted by Springer Science and Business Media.

6.3.2 Internal brightening of the dimmings

Overlaid on both the EIT intensity heliogram and base difference image in Figures 6.2, 6.3 and 6.4 is a red line which passes through the longest-lived part of each dimming. From here on, we refer to the longest-lived part of the dimming as the "core". Below the heliograms are a time series of intensity profiles (from the EIT intensity heliogram data) made along each red line. The top left intensity profile shows the intensity along the red line before the event and the other profiles show snapshots during the recovery process, following the eruption. The intensity profiles clearly show an increase in intensity *within* the dimmings for each event.
For the 12th May 1997 event (Figure 6.2), both dimming regions 1 and 2 can be identified in the intensity profiles. Dimming 2 reaches a lower intensity level than dimming 1. During the time series, both dimmings show a gradual increase in brightness. The 13th May 2005 event (Figure 6.3) clearly shows dimming region 2, exhibiting a gradual increase in brightness as the time series progresses. Dimming region 1 is not so easily identified, but there is a sharp drop in intensity immediately to the west of the post-eruptive arcade (PEA) - the intensity level of this region remains approximately constant throughout the time series. We discuss possible reasons for this in §6.3.3. The 6th July 2006 event (Figure 6.4) originates from an older, more dispersed active region than the other events - the intensity profile before the event (top left) reflects this, showing the more dispersed brightenings that correspond to the strong magnetic field concentrations of this active region. Both dimmings can be identified in the intensity profiles - especially the migratory nature of dimming 1 (discussed further in §6.3.3), initially near to the PEA, moving east during the event. Dimming 1 settles to a relatively constant intensity level. Dimming 2 on the other hand, reaches its minimum intensity early on in the recovery phase, thereafter showing a progressive increase in intensity throughout the time series.

6.3.3 Intensity evolution and structure of the dimmings

At the top of Figures 6.5, 6.6 and 6.7 are base difference images near the maximum spatial extent of the dimmings. The *green* regions correspond to the full spatial extent of the dimmings as identified by the contour method. The *orange* core regions correspond to the longest-lived dimmings that still exist at the end of each dataset (see figure captions for details of times). Lightcurves of the average intensity within each region are plotted as a function of time. The onset of dimming in each event is clearly identifiable by a dramatic drop in intensity, followed by a gentle positive gradient, which we identify as the recovery phase of each event.

In each event (except dimming 1 of 13th May 2005 and 6th July 2006), the *blue* lightcurve (taken from the periphery of the dimmings) shows a full recovery to (or exceeding) pre-dimming intensity levels. In contrast, the *orange* lightcurves, showing the average intensity evolution of the cores of the dimmings, although generally exhibiting a constant, gradual recovery (exceptions: dimming 1 of 13th May 2005 and 6th July 2006) do not show a return to pre-event conditions by the end of these datasets. If we assume that the recovery gradient remains the same as that already displayed on the core lightcurve plots, then we can perform a least-square linear fit to the recovery part of the existing lightcurves and extrapolate the resulting fit to estimate the time at which the dimmings might reasonably be expected to recover to pre-event intensity levels. Table 6.2 shows the extrapolated recovery times for both the cores and the periphery of the dimmings for each event. Recent statistical analysis of 96 CME-associated EUV coronal dimmings by Reinard and Biesecker (2008) showed that the majority of dimmings show a gradual recovery that can be

fit by a single recovery slope.

Although the *minimum* average intensity for both the core (orange) and the entire dimming (green) regions (periphery + core) reach similar intensity levels (Figures 6.5, 6.6 and 6.7), for the May 1997 event, the average intensity of the core region tends to exceed that of the periphery throughout the datasets - both before and during the manifestation of the dimmings. The original EIT data (not the base difference images), shows that a sigmoid structure reforms on 13th May 1997 (especially visible at 14:50 UT). So together with the sigmoid on 12th May before the eruption, the intensity of the core region is high before the event, dims during the eruption, and then recovers to a level significantly higher than the periphery again, due to the reformation of the sigmoid in the vicinity of the core regions.

We note that the lightcurve of dimming 1, 13th May 2005 does not show any tendency toward recovery during our dataset (Figure 6.6). Before the eruption, the source region is highly sheared, showing a sigmoidal structure. The sigmoid has oppositely curved "elbows" at each end, where the elbows appear to be illuminated strands of the sigmoidal core field (see Moore *et al.*, 2001). The eruption of the core field blows away these elbow loop structures, exposing the quiet Sun underneath. Due to the large PEA that forms following the eruption, and the considerable projection of the PEA onto the location of dimming 1, we consider that possibly we do not actually observe the core dimming of the north end of the flux rope in this event. It may well be obscured by the PEA. This interpretation is supported by the lightcurves in Figure 6.6 which remain significantly above the intensity of an undisturbed area of quiet Sun during the whole event, consistent with the exposure of background quiet Sun after the overlying sigmoidal structure relaxed following the eruption. We note that the disappearance of a large-scale coronal feature seen by *Yohkoh*/SXT, similarily leading to a coronal dimming was documented by Hudson *et al.* (1996).

Dimming 1 of 6th July 2006 also shows a comparatively unusual evolution - instead of a straightforward dramatic drop in intensity at the onset of the dimming as in the other lightcurves, the progression toward minimum intensity is more gradual, taking place over $\sim$ 10 hours. The recovery of the lightcurves for the 6th July 2006 event levels to an approximately zero gradient near the end of our dataset. In the SOHO/EIT 284 Å heliogram at 07:01 UT (not shown) there are large-scale loops extending from the positive dimming 1 to a remote negative polarity located north-west of AR 10898. During the course of the eruption, it is clear that these large-scale loops are successively "opened" up (visible in the SOHO/EIT 284 Å movie from 07:01 UT - 19:01 UT), which we suggest may lead to the somewhat migratory movement of dimming region 1. Initially dimming region 1 is close to the PEA at 09:19 UT, apparently at the same location as the footpoint of an erupting filament (visible in emission in the SOHO/EIT 195 Å movie), then the dimming progressively migrates to the north-west, reaching its furthest extent from the PEA by about 16:30 UT. The disruption of large-scale loops leading to coronal dimming at their footpoints is a well-documented feature of solar eruptions (Manoharan *et al.*, 1996; Khan and Hudson, 2000; Delannée, 2000; Harra *et al.*, 2007a) and may facilitate the continued "openness" and prolonged lifetime of dimming 1 in this event.

Even though they are located far from the outer boundaries of the dimmings, the cores of the dimmings start to show an increase in intensity very soon after the dimming has taken place. This is consistent with the results displayed by the intensity profiles in Figures 6.2, 6.3 and 6.4, where the dimmings show an internal increase in intensity. Although the contour plots in Figures 6.2, 6.3 and 6.4 show that the dimmings do shrink from their outer

boundaries inward, the intensity profiles in Figures 6.2, 6.3, 6.4 and the lightcurves of Figures 6.5, 6.6, 6.7 demonstrate that there is also an *internal* contribution to the recovering intensity level.

To more directly understand the structure of the dimmings, we make 3-D surface plots of the intensity (Figure 6.9, from original EIT intensity data) and intensity change (Figure 6.8, from base difference images) within the dimmings when they are near their maximum spatial extent. The intensity change is with respect to pre-event data.

The non-uniformity of the intensity change within the dimmings is striking. A clear and consistent structure is evident in all events. The deepest dimming change occurs adjacent to the bright PEA, with the extended dimming becoming gradually less intense with increasing distance from the PEA. This consistent change in intensity between pre-event and dimmed data may be due to the pre-event data being most bright near to the core of the active regions in all events. Particularly the 12th May 1997 and 13th May 2005 events have well-defined sigmoids associated with the active regions before the eruptions occur. Therefore, the most dramatic drop in intensity occurs where the bright pre-eruption sigmoidal loops disappear.

Figure 6.9 shows 3-D surface plots of the original EIT data showing the dimmings near their maximum spatial extent. Figures 6.8 and 6.9 show different things, since the base difference data highlight changes and the original EIT data shows the intensity at a given time. Figure 6.9 shows that the intensity within the dimmings is not uniform. The concentrations of the deepest dimming are patchy and tend to occur in the innermost part of the dimming region, gradually progressing outward to surrounding quiet Sun intensity level.

6.4 Physical constraints implied by the observed dimming recovery

Our examination of the evolution of the dimming regions during the recovery phase has revealed several new results that must be taken into account when considering our understanding of the physical process(es) responsible for the recovery. We find that in all three studied cases, the dimmings shrink in their spatial extent, so recovering the intensity of the dimmed region from the outer boundary (see Figures 6.2, 6.3, and 6.4). We note that this shrinkage occurs in a fragmentary and inhomogeneous manner. This observation is consistent with the results of Kahler and Hudson (2001) who studied 19 dimmings with *Yohkoh*/SXT data (including the 12th May 1997 event studied here) and found that the dimmings tend to disappear "by a net contraction of the boundaries".

Interestingly, Kahler and Hudson (2001) specify that the net contraction of the boundaries is the *only* way in which the dimmings are observed to recover in *Yohkoh*/SXT data. They state that in *none* of the 19 cases they studied did they see the interior dimming brightness increase systematically with time. In contrast, in this work we have analysed EUV SOHO/EIT 195 Å data, and we have shown that there is clearly a progressive increase of the intensity *within* the dimmings (see Figures 6.2, 6.3, 6.4 and 6.5, 6.6, 6.7). Such an internal recovery in intensity is not observed in *Yohkoh*/SXT data. We independently confirm this finding of Kahler and Hudson (2001) using *Yohkoh*/SXT data from the AlMg filter between 06:52 UT and 20:22 UT for the 12th May 1997

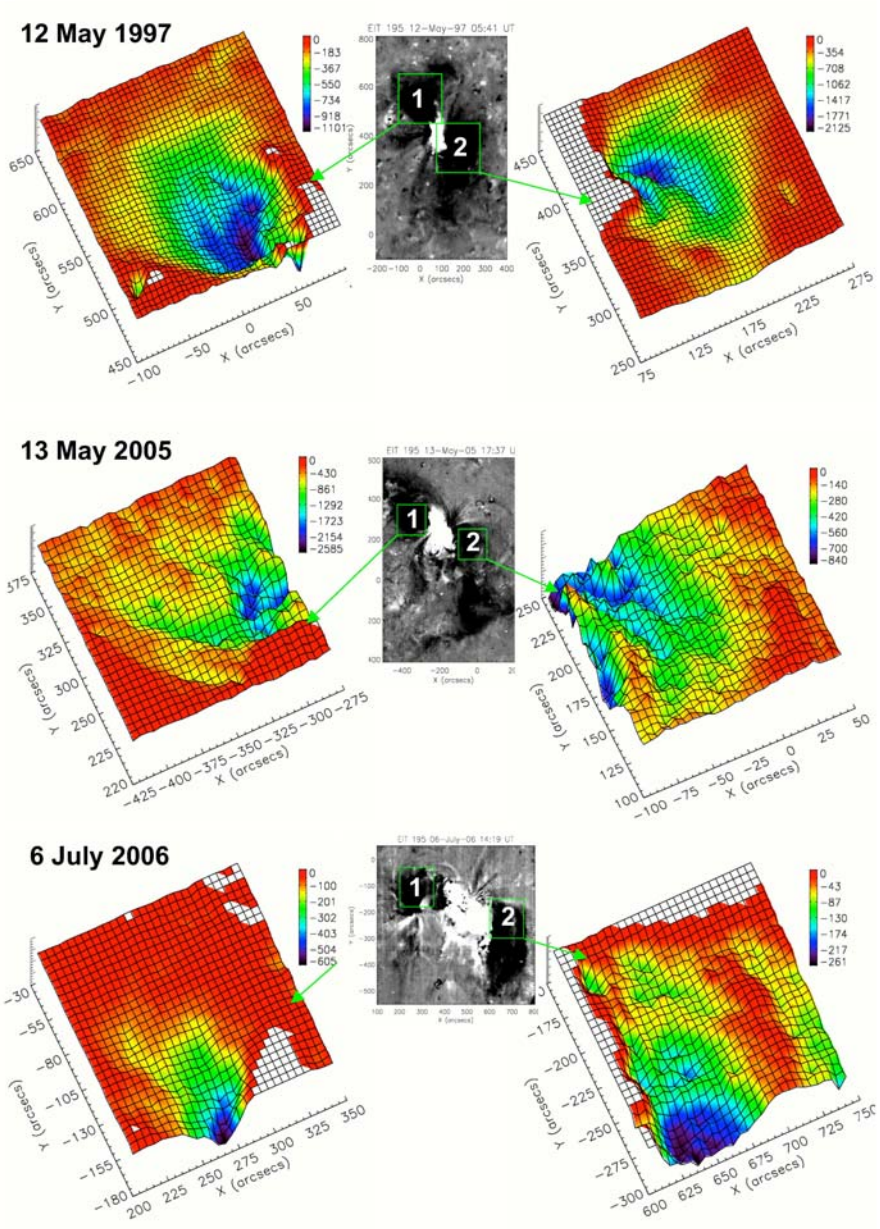

Figure 6.8: For each row, the central insert shows a base difference image. Green boxes indicate data used to make 3-D surface plots of intensity shown on the sides. The surface plots show the intensity change compared to the pre-event level (in counts/pixel). The regions of increased intensity are cut (where the surface is flat and white). The intensity change of the regions from pre-event to during dimming is clearly structured, with the most dramatic drop in intensity located close to the post-eruptive arcade. Permission to reproduce this figure has been granted by Springer Science and Business Media.

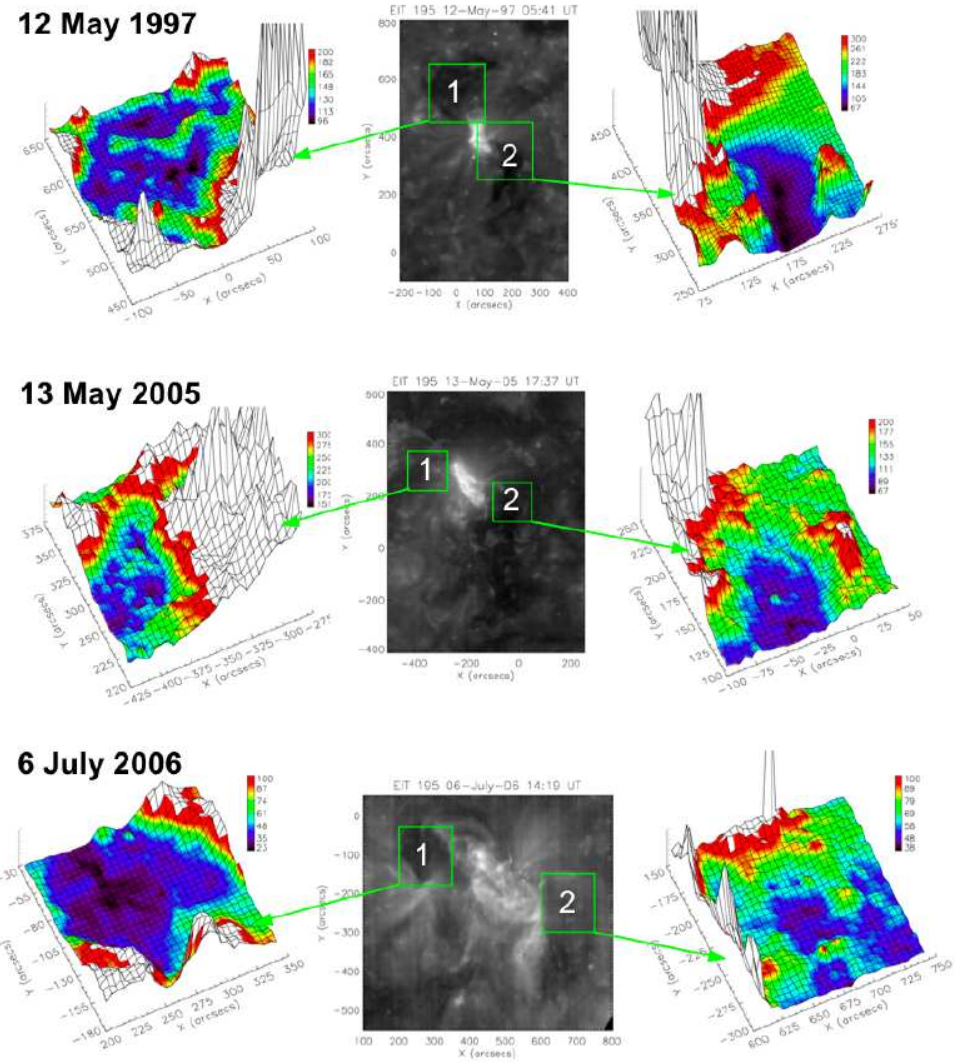

Figure 6.9: 3-D surface plots of the original (not differenced) data showing the intensity within the dimmings (in counts/pixel). For each row, the central insert shows an original EIT image. Green boxes indicate data used to make 3-D surface plots of intensity shown on the sides. The intensity of the dimmings is clearly non-uniform, with the deepest dimming occurring towards to the centre of the regions.

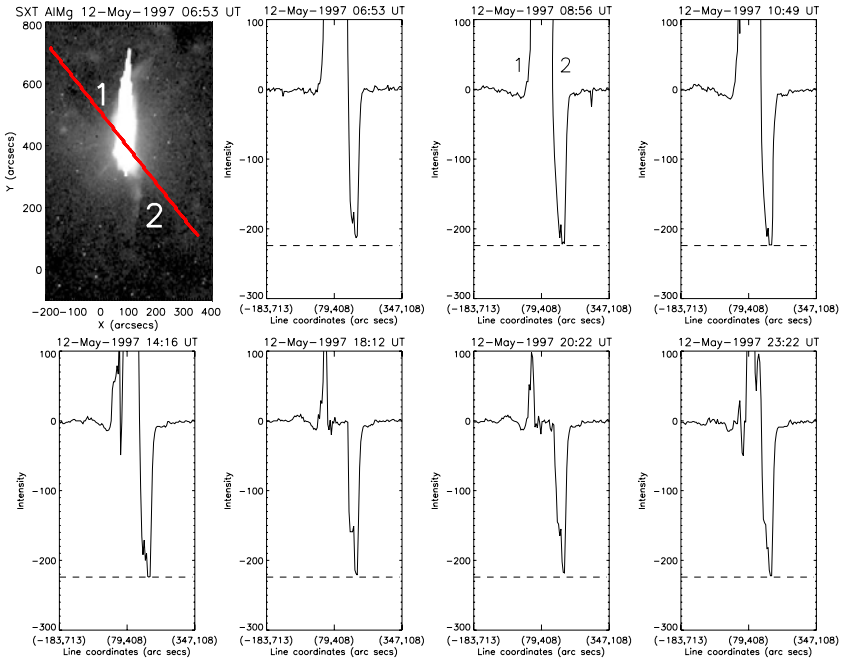

Figure 6.10: The top left panel is a *Yohkoh*/SXT AlMg filter intensity heliogram showing the 12th May 1997 dimmings. The red line overlaid shows the location of the data used to produce the following intensity profile plots. Intensity profile plots made along the red line (shown in the top left panel), at various times during the dimming recovery. The dimmings are identified by the numbers 1 and 2. The dashed line shows the deepest dimming level reached inside dimming 2 in this time series. The bright post-eruptive arcade coupled with the geometric projection effect largely obscures dimming region 1. Permission to reproduce this figure has been granted by Springer Science and Business Media.

event (see Figure 6.10). The observation of internal brightening is observed in the SOHO/EIT 195 Å bandpass, which corresponds to a characteristic formation temperature of $\approx 1.5 \times 10^6$ K at typical coronal densities. In contrast, *Yohkoh*/SXT detected plasma at temperatures $> 3 \times 10^6$ K. Thus *Yokhoh*/SXT and SOHO/EIT probe plasmas of different temperature. It would appear that during the recovery process there is not enough power to heat the plasma to a high enough temperature for detection in *Yohkoh*/SXT data.

The 3-D surface plots showing the distribution of the intensity within the dimmings (Figures 6.8 and 6.9) are also in contrast with the data obtained by *Yohkoh*/SXT, with Kahler and Hudson (2001) noting the "uniformly dark interiors" of the dimmings they studied. The nature of coronal dimmings revealed here with SOHO/EIT data (Figure 6.9, showing that the intensity within the dimmings is non-uniform) has implications for the study of coronal dimmings, particularly regarding the intensity change in these regions during the recovery phase. The structure of the dimming must be analysed carefully since the interpretation of the resulting variation in emission will heavily depend on the location selected for analysis; e.g. Table 6.2 shows how the "lifetime" of the dimming differs substantially between its core and periphery.

6.4.1 Recovery does not necessarily mean disconnection

Our analysis shows that for the 12th May 1997 event, the average intensity of both the dimmings has recovered by the end of our dataset. Assuming the cores of the dimmings continue to recover

at the rate displayed within our dataset, we have calculated that the core of dimming 1 is expected to recover by 00:00 UT on 16th May, and the core of dimming 2 by 02:00 UT 15th May (see § 6.3.3 and Table 6.2). However, from 10:00 UT to ∼ 22:00 UT on 15th May, uni-directional electrons from a positive source are detected at 1 AU (see § 6.2.1). The travel time to 1 AU for the slowest electrons is 6 hours (Larson *et al.*, 1997). Taking this electron travel time into account, uni-directional electrons must leave the Sun between 04:00 UT and ∼ 16:00 UT 15th May. Dimming 2 is the positive polarity dimming (Attrill *et al.*, 2006), so we observe a uni-directional electron stream from the positive polarity dimming even though that core dimming is expected to have recovered in intensity and disappeared by 02:00 UT on 15th May.

For the 13th May 2005 event, Qiu *et al.* (2007) identify the MC duration from 05:40 UT on 15th May to 04:40 UT on 16th May (see § 6.2). During this interval the cores of both dimmings remain un-recovered, so the presence of bi-directional electron heat fluxes is expected.

For the 6th July 2006 event, the average intensity of the core of dimming 2 is expected to have recovered by 06:00 UT on 8th July. The lightcurves for dimming 1 (Figure 6.7) tend toward a zero gradient, so we cannot infer any information about the recovery rate from this data. The candidate for the interplanetary MC counter-part of this eruption in Figure 6.1c shows a uni-directional electron stream originating from a negative solar source, after ∼ 21:30 UT on 10th July. So we observe a uni-directional electron stream, presumably from the negative polarity dimming (region 2), even though dimming 2 is estimated to have recovered in intensity by 06:00 UT on 8th July.

Either, as Kahler and Hudson (2001) query, dimmings are not the source regions of the subsequent magnetic cloud (and associated electron heat fluxes), or, if they are the source regions (as considered by Webb *et al.*, 2000; Mandrini *et al.*, 2005; Attrill *et al.*, 2006), then we need to reconcile how the dimmings recover, yet the magnetic connection of the ICME/MC to the Sun is maintained.

6.4.2 Constraints that our analysis places on possible theories

In view of our results and the discussion above, we consider that any potential recovery mechanism must be capable of explaining shrinkage of the dimmings, internal brightenings, the relatively low temperature/low power produced in the dimmings during the recovery, all whilst still maintaining the magnetic connectivity of the ejecta to the Sun. For the intensity in the dimmings to recover, plasma must be present to generate the emission. Thus we expect that to constrain the plasma, the magnetic field must form closed flux tubes. In particular then, we consider the question of what is the physical process by which dimmings recover in intensity and how do they change from being regions of "open" to re-establish closed magnetic field?

McIntosh *et al.* (2007) discuss the post-eruptive evolution of the dimmings on 6th July 2006. They report the reintroduction of moss spreading outward from the active region and interpret this as the post-CME closure of the global coronal field above the active region following "disconnection" of the CME. In cases where the core dimmings are located adjacent to the PEA, the core dimmings are expected to shrink as the PEA expands, thus the recovery can indeed be at least partially due to closing-down of "opened" field lines, in accordance with the results of McIntosh *et al.* (2007). However, dimmings extend considerably far out into the quiet Sun magnetic field (Webb *et al.*,

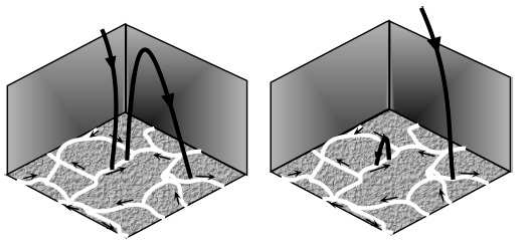

Figure 6.11: Illustration of the interaction between "open" magnetic field lines and small coronal loops. Left shows the pre-reconnection configuration comprising an "open" magnetic field line and a closed magnetic loop. Right shows the post-reconnection configuration and the displacement of the "open" magnetic field line. Figure from Fisk and Zurbuchen (2006). Permission to reproduce this figure has been granted by the American Geophysical Union.

2000; Mandrini *et al.*, 2005; Attrill *et al.*, 2006), away from the active region and the domain where moss is observed (Berger *et al.*, 1999).

Rather than purely a *closure* of the global coronal magnetic field, we consider that interchange reconnections between the "open" magnetic field of the dimming, small coronal loops and emerging flux bipoles may act to *disperse* the concentration of "open" magnetic field forming the dimming out into the surrounding quiet Sun. Reconnections with closed loops will "step" the "open" magnetic field out of the dimming (dispersing the "open" flux), whilst reconnection with "open" magnetic field will physically disconnect the magnetic field line from the Sun. Given the detection of electron heat fluxes at 1 AU after the dimmings are expected to recover, we consider that the most dominant process should be reconnection with closed magnetic field, which acts to disperse the "open" magnetic field out into regions of quiet Sun, thus recovering the intensity of the dimming whilst *maintaining* the magnetic connectivity to the Sun.

In the following, we analyze the processes which are expected to participate in the recovery of the dimmings. Reconnections should occur dominantly at the outer boundaries of dimmings (as suggested by Kahler and Hudson, 2001), where the "open" magnetic flux can interact most with surrounding quiet Sun magnetic field. The interchange reconnections at the outermost boundary of dimmings should occur in a similar manner to the flux emergence/expansion near coronal holes as shown by Baker *et al.* (2007). They find that interchange reconnections produce bright closed loops between the "open" field of the coronal hole and the bipolar region, whilst "stepping" the "open" field out of the coronal hole region. In our case, the bright loops at the boundary of the dimming would act to shrink the outer boundary at the point of interaction (as observed), while at the same time dispersing the "open" magnetic field of the dimming.

Within the dimming, there is also the possibility of reconnection between the "open" field and the existing field as well as emerging bipoles. Fisk and Zurbuchen (2006) note that within coronal holes (in our case dimmings), small loops are indeed observed to be present. These loops are interpreted as the result of localized reconnection (they are equivalent, at smaller scales, to flare loops). This idea finds support in the work of Larson *et al.* (1997) who interpreted the localized patches of brightening within a dimming as energy release at the footpoint of an interplanetary magnetic cloud, resulting from 3-D field line reconnection.

Emerging flux, most probably in the form of ephemeral regions, also contributes to the recovery process within the dimming. In quiet Sun regions, the timescale for flux replenishment by emergence was found to be between 1.5 and 3 days (Schrijver *et al.*, 1997). On comparision with the

lifetimes of the dimmings shown in Table 6.2, it is apparent that such a timescale is sufficient for the recovery of the peripheral regions of the dimmings, but in some cases the cores remain dimmed for longer.

6.4.3 Implications of reconnections within the dimmings

The emergence of new ephemeral regions brings closed loops into the "open" magnetic field environment of the dimmings, likely driving interchange reconnections which would have the effect of "opening" the emerged loops and evacuating the plasma they contain. (This would actually *sustain* dimming so effectively decreasing the rate of recovery of the dimmings, compared to the case with emergence but without reconnection.) Within the dimmings, the "open" flux is not so subjected to the "stepping out" by interchange reconnections with surrounding quiet Sun loops. So the internal recovery is expected to be a slower process than the one at the periphery. A test of this would be to see how long outflows are measured in the cores of the dimmings. If outflows are measured at the beginning, as expected during the initial creation of the dimmings, then they stop, it would indicate recovery just by emergence of new closed loops without any interaction with pre-existing magnetic field. But if outflows are maintained well into the recovery phase, then it shows that interchange reconnections are continually occurring between the previously "opened" field and the newly emerged flux, allowing plasma to escape out into the solar wind. *Hinode*/EIS would be the ideal instrument with which to test this expected observational signature.

The above is also plausibly a key process responsible for forming the fast solar wind in coronal holes. Just like in dimmings, the new emerging flux in coronal holes is able to provide both the plasma and the magnetic energy to accelerate it, while the reconnected "open" field permits the escape of the plasma. However in coronal holes the emergence rate is significantly smaller (Zhang *et al.*, 2006; Abramenko *et al.*, 2006), than for the quiet Sun (Schrijver *et al.*, 1997), so the mean expected Doppler signal is expected to be much weaker in coronal holes than in dimmings. For a consistent, but different result see Hagenaar *et al.* (2008).

The interchange reconnections between emerging flux and "open" field are expected to occur in very episodic (as opposed to continuous) events. Such a mechanism provides a natural origin of the very patchy nature of electron heat fluxes observed frequently in MCs and ICMEs.

6.4.4 Mechanisms for dispersal of "open" magnetic field

The main area of the dimming extends out into, and is surrounded by, regions of quiet Sun magnetic field. The quiet Sun magnetic field is subject to transport by convective motions, leading to its "diffusion" (e.g. Hagenaar *et al.*, 1999).

If the location of a magnetic field line footpoint is displaced a distance r in a time t, then the "diffusion coefficient" (rate of dispersal of flux) is given by:

$$D \equiv \frac{\langle r^2 \rangle}{4t} \tag{6.1}$$

Hagenaar *et al.* (1999) find that the diffusion coefficient of small-scale flux by granular buffetting

is dominated by large-scale drifts which on timescales > 24 hrs, randomises into a second diffusive motion where both small- and large-scale dispersal processes combine to give a diffusion coefficient of 284 km^2s^{-1}. Comparison of the Hagenaar *et al.* (1999) diffusion coefficent with the rate of change in area of the dimmings for the three events of this study (see Table 6.1) shows that the dispersal of the "open" magnetic field of the dimmings due to granular buffetting alone is inadequate to explain the observed recovery rates of the dimmings.

Fisk and Schwadron (2001), Fisk (2005) and Fisk and Zurbuchen (2006) developed a quantitative model of interchange reconnection (Crooker *et al.*, 2002) between "open" and closed magnetic field. They primarily discuss their model in a global context, but we suggest that it also appears to apply to the recovery phase of dimmings. In this approach, reconnection between the "open" magnetic field of the dimmings and the surrounding quiet Sun magnetic field would act to accelerate the convective dispersal process described above by extending the distance, r, by which a magnetic field line footpoint is displaced (see Figure 6.11). Fisk and Schwadron (2001) consider that if there are numerous, randomly orientated loops in the low corona, then the reconnection mechanism illustated by Figure 6.11 can be described as a diffusive process. The interaction between "open" flux and closed loops is captured by the "diffusion coefficient", κ:

$$\kappa = \frac{(\delta h)^2}{2\delta t} \tag{6.2}$$

where δh is the displacement (related to the loop size) and where δt is the characteristic time for reconnection with the loops.

Fisk and Schwadron (2001) estimate κ in the quiet Sun, outside a coronal hole at low latitudes. They use $\delta h \sim 2 \times 10^{10}$cm, an average value for the loop height, since although the displacement distance should be on the order of twice the loop height, reconnection may occur anywhere along the loop. They use $\delta t \sim 1.5 \times 10^5$ s (38 hours), derived from the characteristic time for reconnection with loops at low latitudes. Using these values, the diffusion coefficient is calculated to be $\kappa \sim 1.6 \times 10^5$ km^2s^{-1}. Comparison of this estimated rate of dispersal of "open" flux with the measured rate of recovery of the dimmings examined in this study (Table 6.1) shows a very good agreement. Therefore the Fisk and Schwadron (2001) model supports our proposal that interchange reconnections facilitating a dispersal of "open" magnetic flux is a likely mechanism via which the recovery in intensity of dimmings is primarily achieved.

Since the recovery process is essentially a relaxation process (lacking the strong coherent driver of the CME expansion), the interchange reconnections would not be expected to form strong current sheets (as e.g. in a flare). We conclude that the lack of power generated by the interchange reconnection recovery process is therefore expected and supports the identification of many small-scale interchange reconnections with low coronal quiet Sun loops as the primary candidate for the mechanism facilitating recovery of the dimmings. We expect that the speed of recovery is closely related to the magnetic environment in which the dimmings form, proceeding faster in a quiet-sun environment, while a much slower recovery is expected for dimmings formed in a strong monopolar magnetic environment, where there is little opposite polarity flux present. This expectation can be tested and is a candidate for future work on this subject.

6.5 Summary of chapter

We consider why and how CME-related dimmings (identified as the footpoints of magnetic flux ropes in the interplanetary space), recover, despite the "open" magnetic connectivity to the Sun being maintained as indicated by electron heat flux measurements at 1 AU. Study of the intensity evolution of dimmings using SOHO/EIT data shows that they recover by shrinking of their outer boundaries as well as by internal brightenings that we consider are constrained to the *low* corona. We show that the SOHO/EIT dimmings have a clear spatial structure, with a deeply dimmed core gradually progressing to a lesser-dimmed periphery.

We propose that (i) the recovery of the dimmings by shrinking from their outer edges occurs mainly by interchange reconnection with existing closed quiet Sun loops and emerging bipoles and (ii) that the internal recovery of the dimmings can be due to emergence of new closed loops (ephemeral regions) that bring new plasma into the dimmings.

We quantitatively demonstrate that the model developed in Fisk and Schwadron (2001) of interchange reconnections between "open" magnetic field and small coronal loops, is a strong candidate for the primary mechanism facilitating the recovery of the dimmings. The interchange reconnections disperse the concentration of "open" magnetic field forming the dimming out into the surrounding quiet Sun. This process acts to generate the apparent recovery in intensity of the dimming, whilst still maintaining the magnetic connectivity to the Sun.

Chapter 7

Conclusions and Suggestions for Future Work

This thesis has discussed work on the closely associated low-coronal phenomena of coronal waves and dimmings, particularly with emphasis on their relationship to coronal mass ejections (CMEs). This thesis has detailed how close examination of these phenomena can be used to derive an understanding of the global magnetic development of CMEs. In particular, the magnetic environment surrounding coronal dimming and coronal wave events has been studied.

7.1 Conclusions

7.1.1 Coronal waves

We have reviewed the many different EUV observations of EIT coronal waves and their potential counterparts in radio, Hα, soft X-ray and He II wavelengths. We have compiled a comprehensive list of all observed signatures of EUV coronal waves reported in the literature to date. We consider that there are two different types of coronal wave: S-waves and diffuse bright fronts. We have also discussed the various models currently proposed to explain coronal waves. We conclude that there is good evidence to identify the EIT S-waves as the coronal counterpart of a chromospheric fast-mode wave/shock. However, by far the majority of EIT waves are of the diffuse type and these have been the focus of our work. We have shown that there are difficulties in understanding some key observations of diffuse coronal waves within the context of the various existing models. We have demonstrated that a careful analysis of the global context of an event is crucial to developing our understanding of coronal waves.

Our studies have resulted in new observational analysis of diffuse EIT coronal wave bright fronts which fail to be reconciled with existing models, i.e. as interpretation within a wave context, as plasma compression or as CME-associated current shells which form high in the corona. The primary reason for our inability to reconcile observations with these interpretations is because we have shown that diffuse coronal "waves" have a strongly magnetic nature.

We therefore propose a new model, where the diffuse coronal "wave" is understood to be the magnetic footprint of a CME. In this model, diffuse coronal "waves" form in the low corona, and the mechanism of formation is understood to be expansion of the core CME magnetic field into the surrounding quiet Sun environment, *dynamically* generating QSLs where reconnection is expected to occur generating weak flare-like events which constitute the diffuse bright front. We have discussed that our model has implications for developing our understanding of *how* CMEs become large-scale in the low corona, even though they may start from a very localised source region.

7.1.2 Coronal dimmings

We developed an iso-contour method to quantitatively define coronal dimming region boundaries, allowing us to study their manifestation and evolution. From analysis of the evolution of the coronal dimming regions and a synthesis of already published results, a new interpretation of the much-studied 12th May 1997 event is derived. Using multi-wavelength data, we showed that the magnetic field of the expanding CME forced global-scale magnetic interchange reconnection with "open" field lines of the north polar coronal hole, closing down expanding magnetic field lines of the northern side of the CME, while transferring "open" coronal hole field lines to the southern side. This scenario explains both the asymmetric temporal and spatial evolution of the two main dimming regions, as well as the gradual brightening and shrinking of the north polar coronal hole boundary. Combining this scenario with interplanetary observations, it is found that the southern-most of the two unidentical twin dimming regions was the principal foot-point of the associated magnetic cloud observed at Earth. This is supported by a thorough analysis of *Wind* data, using three different magnetic cloud models and two computation methods. The magnetic flux from the southern-most dimming region and that of the MC are found to be in close agreement, within the same order of magnitude: 10^{21} Mx. This study highlights the crucial contribution of the azimuthal flux in such calculations, and has potential implications for CME models. This is the first work to show that study of the evolution and magnetic nature of coronal dimming regions can be used to probe the *post-eruptive* evolution of the CME.

Study of the dimmings of the complex large-scale 28th October 2003 event show that coronal dimmings cannot always be interpreted simply as corresponding to flux rope footpoints of the expanded erupted magnetic flux rope, despite some common characteristics upon first apraisal. The model developed to understand the observational characteristics of diffuse coronal "waves" was applied to this complex event, since the model allows us to understand the nascent stages of CME development in the low corona. Application of our model allows an interpretation of this complex event, where the formation of each dimming region can be understood, through reconnection between the expanding core CME magnetic field and the surrounding magnetic environment. Thus our model is useful in its own right as a tool with which to progress our understanding of how CMEs become large-scale in the low corona, along with their associated signatures: a diffuse coronal "wave" and the coupled formation of widespread secondary dimmings.

Finally, we studied the late-stage recovery phase of coronal dimmings. We considered why and how CME-related dimmings (identified as the footpoints of magnetic flux ropes in the interplanetary space), recover, despite the "open" magnetic connectivity of the ejecta to the Sun being maintained as indicated by electron heat flux measurements at 1 AU. Study of the intensity evolution of dimmings using SOHO/EIT data shows that they recover by shrinking of their outer

boundaries as well as by internal brightenings that we consider are constrained to the *low* corona. We show that the SOHO/EIT dimmings have a clear spatial structure, with a deeply dimmed core gradually progressing to a lesser-dimmed periphery.
We propose that (i) the recovery of the dimmings by shrinking from their outer edges occurs mainly by interchange reconnection with existing closed quiet Sun loops and emerging bipoles and (ii) that the internal recovery of the dimmings can be due to emergence of new closed loops (ephemeral regions) that bring new plasma into the dimmings.
We quantitatively demonstrate that a model of interchange reconnections between "open" magnetic field and small coronal loops, is a strong candidate for the primary mechanism facilitating the recovery of the dimmings. The interchange reconnections disperse the concentration of "open" magnetic field forming the dimming out into the surrounding quiet Sun. This process acts to generate the apparent recovery in intensity of the dimming, whilst still maintaining the magnetic connectivity of the ejecta to the Sun.

7.2 Future work

7.2.1 Coronal waves

The immediate next steps for the work on coronal waves are (i) to scrutinise and test our model further by exploiting the spectroscopic diagnostic capabilities of *Hinode*/EIS, the unique viewpoint provided by STEREO and the high spatial-temporal resolution data anticipated from SDO/AIA; and (ii) to test the development of the initial numerical set-up of our cartoon model in a fully dynamic MHD code.

Further, the higher time-cadence of data from *Hinode*, STEREO and SDO should allow a greater statistical analysis of the relationship between the helicity of the event source region, the sense of rotation of the erupting filament/flux rope and the behaviour displayed by the expanding coronal "wave" bright front. Coupled observations between STEREO and SOHO and/or SDO will allow study of the magnetic environment of a coronal "wave" event, as well as simultaneous determination of the lateral extent of the associated CME.

7.2.2 Coronal dimmings

With regard to coronal dimmings, we expect that the speed of recovery of the dimmings is closely related to the magnetic environment in which the dimmings form, proceeding faster in a quiet Sun environment, while a much slower recovery is expected for dimmings formed in a strong monopolar magnetic environment, where there is little opposite polarity flux present. This expectation can be tested and is a candidate for future work on this subject.

In conclusion, this thesis contributes new scientific research on coronal waves and coronal dimmings. The magnetic nature of both phenomena is demonstrated and it is shown how the innate coupling between the two may be naturally understood within the context of the new model developed as a result of these studies. The work contained in this thesis has implications for developing our understanding of how CMEs can become large-scale in the low corona.

Appendix A

Shift of the coronal "wave" centre

As the EIT bright front expands across the solar disk, the angular radius of the bright front, δ, increases (Figure A.1). The bright front expanding over the 3-D sphere of the Sun undergoes a projection effect when viewed in 2-D images, as in EIT data (see Figure A.2). The projection effect can be calculated and implies that as the EIT wave progresses (as δ increases), the centre of the projected coronal wave (in the EIT images) appears to move toward the disk centre (see Figure A.2). Thus a shift of the projected coronal wave centre is expected in the EIT images, and its distance from the disk centre is given by: $R_{\odot} \sin\theta \cos\delta$.

Calculation of the distance to disk center, L_{DC}:
L_{DC} refers to the distance between the letters D and C marked in Figure A.2.

$$L_{DC} = \frac{(L_{DA} - L_{DB})}{2} + L_{DB} \tag{A.1}$$

$$L_{DA} = R_{\odot} sin(\theta + \delta) \tag{A.2}$$

$$L_{DB} = R_{\odot} sin(\theta - \delta) \tag{A.3}$$

Substituting Equations A.2 and A.3 in Equation A.1, combined with use of the vector calculus identity:

$$sin(a \pm b) = sin(a)cos(b) \pm cos(a)sin(b) \tag{A.4}$$

gives:

$$L_{DC} = R_{\odot} sin\theta cos\delta \tag{A.5}$$

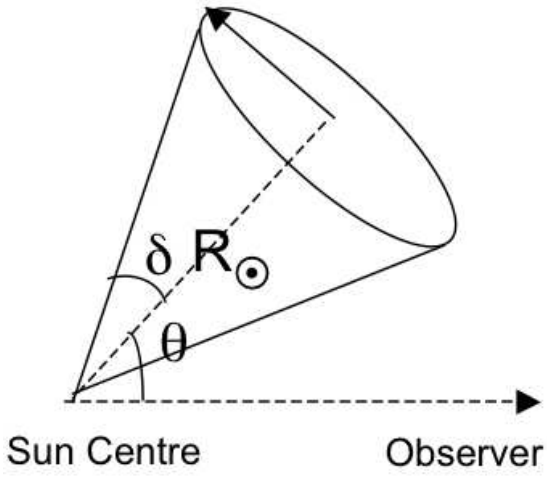

Figure A.1: The bright front of the EIT coronal wave is represented by the circle. The angular radius of the bright front is δ. θ is the angle subtended between the observer's line of sight, the centre of the 3-D solar sphere and the epicenter of the EIT wave.

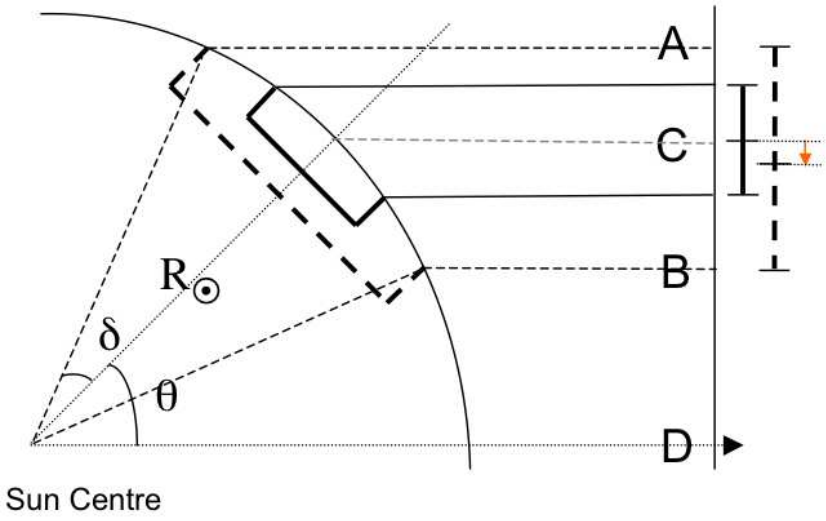

Figure A.2: Figure shows the expansion of the EIT coronal wave bright front across the spherical solar surface. The heavy solid and dashed lines trace the radii of the bright front as it expands. The horizontal lines trace the radii of the bright front, showing how the expansion is viewed when projected onto a 2-D surface. The distortion of the expansion due to the projection effect is evident, with the center of the projected image being shifted toward solar disk center (indicated by the orange arrow). Note that the *real* epicenter of the expanding bright front on the Sun does not change.

Appendix B

Calculating the projection effect

Instead of plotting the intensity of the coronal wave bright front as a function of the azimuthal (ring) angle of the projected 2-D image, it is better to use the de-projected azimuthal (ring) angle in the plane of the real Sun. This real plane lies perpendicular to the local vertical of the epicenter of the event. In order to plot this real azimuthal (ring) angle, the relationship between the features that we observe in the 2-D projected images and the real Sun must be determined. Figure B.1 illustrates the relationship between the real and projected planes. β is the angle between the real plane, tangent to the event epicenter, and the observer's line of sight.

If a line lies perpendicular to the observer's line-of-sight, there is no projection effect. Figure B.2 illustrates this concept. The left panel shows a 2-D sketch of a point (solid black dot), at the limb of a circle, radius R. The right panel shows the projected 2-D image, as would be seen by the observer on the projected plane in Figure B.1. If the figure in the left (real plane) panel of Figure B.2 is tilted back and forth about the horizontal axis, there is no projection effect on the line labelled L, only on the distance labelled X.

The real and projected planes of Figure B.2 may be set in their 3-D context, with their relation to the observer specified as shown in Figure B.3.

The projection effect on the distance labelled X, means that there is also a projection effect on R and α as well. Using simple trigonometry on the real right-angled triangle shown in the left

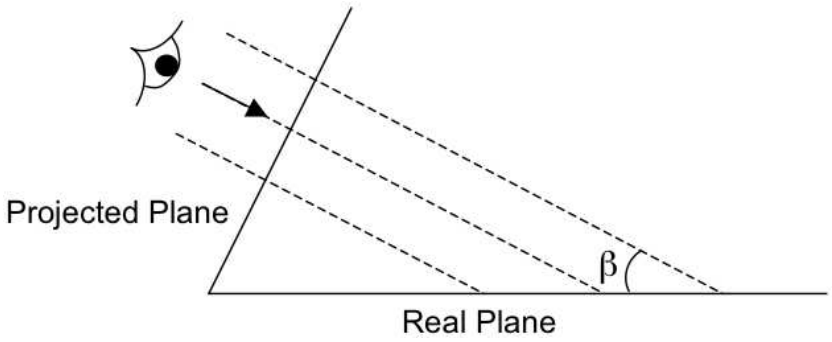

Figure B.1: Figure illustrating the relationship between the real and projected planes, where β is the angle between the real plane and the observer's line of sight.

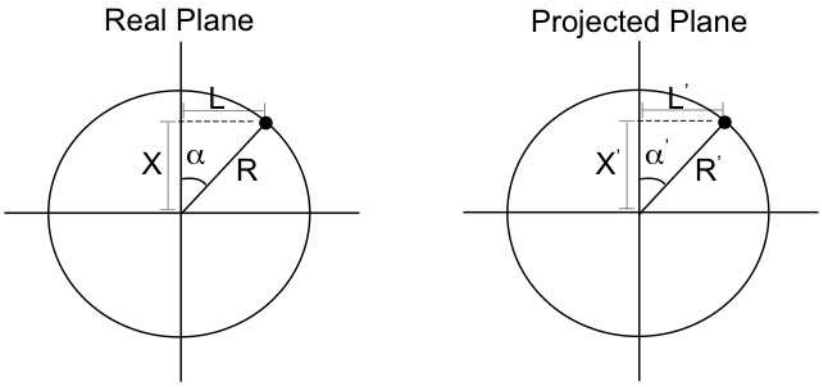

Figure B.2: The left panel shows a 2-D sketch of a point (solid black dot), at the limb of a circle, radius R. The dot is positioned at an azimuthal (ring) angle, α. The right panel shows the projected 2-D image, as would be seen by the observer on the projected plane in Figure B.1.

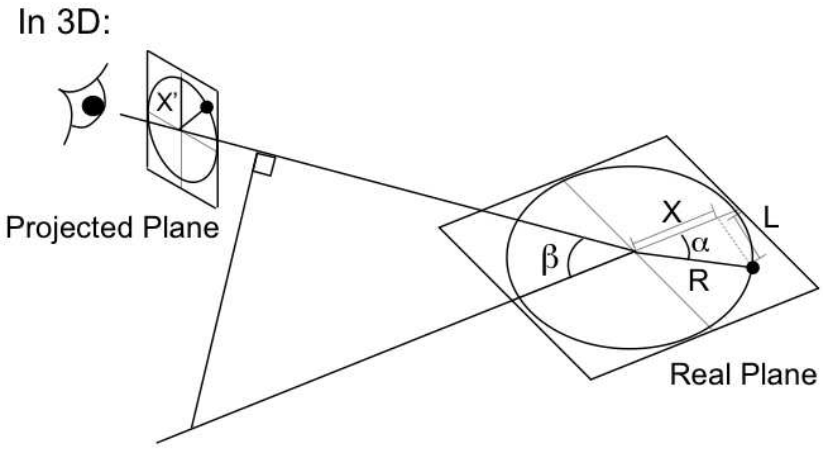

Figure B.3: Figure showing the relation between the real plane and the projected plane that the observer sees, where the real plane is at an angle β to the observer's line of sight.

panel of Figure B.2 gives the following relations:

$$sin\alpha = \frac{L}{R}cos\alpha = \frac{X}{R}tan\alpha = \frac{L}{X} \tag{B.1}$$

In the same way, for the projected right-angled triangle shown in the right panel of Figure B.2:

$$sin\alpha' = \frac{L'}{R'}cos\alpha' = \frac{X'}{R'}tan\alpha' = \frac{L'}{X'} \tag{B.2}$$

The relationship between the features that are observed in the 2-D projected images and the real Sun must be determined. In order to do this, first relationships for L' → L, X' → X, and R' → R must be found. Then the relationship for $\alpha' \rightarrow \alpha$ can be found from Equations B.1 and B.2.

As discussed, L is directed perpendicular to the line of sight, so there is no projection effect in the direction along the line of sight. Therefore;

$$L' = L \tag{B.3}$$

From Figure B.3;

$$X' = Xsin\beta \tag{B.4}$$

From Figure B.2, using Pythagorus and Equations B.3 and B.4:

$$R' = \sqrt{X'^2 + L'^2} = \sqrt{X^2 sin^2\beta + L^2} \tag{B.5}$$

Substituting the above expressions for L', X' and R' (Equations B.3, B.4 and B.5 into Equations B.2 gives:

$$sin\alpha' = \frac{L}{Xsin^2\beta L^2} = \frac{Rsin\alpha}{\sqrt{R^2cos^2\alpha sin^2\beta + R^2sin^2\alpha}} = \frac{sin\alpha}{\sqrt{cos^2\alpha sin^2\beta + sin^2\alpha}} \tag{B.6}$$

$$cos\alpha' = \frac{Xsin\beta}{Xsin^2\beta L^2} = \frac{Rcos\alpha sin\beta}{\sqrt{R^2cos^2\alpha sin^2\beta + R^2sin^2\alpha}} = \frac{cos\alpha sin\beta}{\sqrt{cos^2\alpha sin^2\beta + sin^2\alpha}} \tag{B.7}$$

$$tan\alpha' = \frac{L}{Xsin\beta} = \frac{Rsin\alpha}{Rcos\alpha sin\beta} = \frac{sin\alpha}{cos\alpha sin\beta} \tag{B.8}$$

So that the projected azimuthal (ring) angle, α' is expressed as a function of the real azimuthal (ring) angle, α and the angle between the plane tangent to the event epicenter and the observer's line of sight, β. Figure B.4 illustrates the geometric relationship between the plane tangent to the

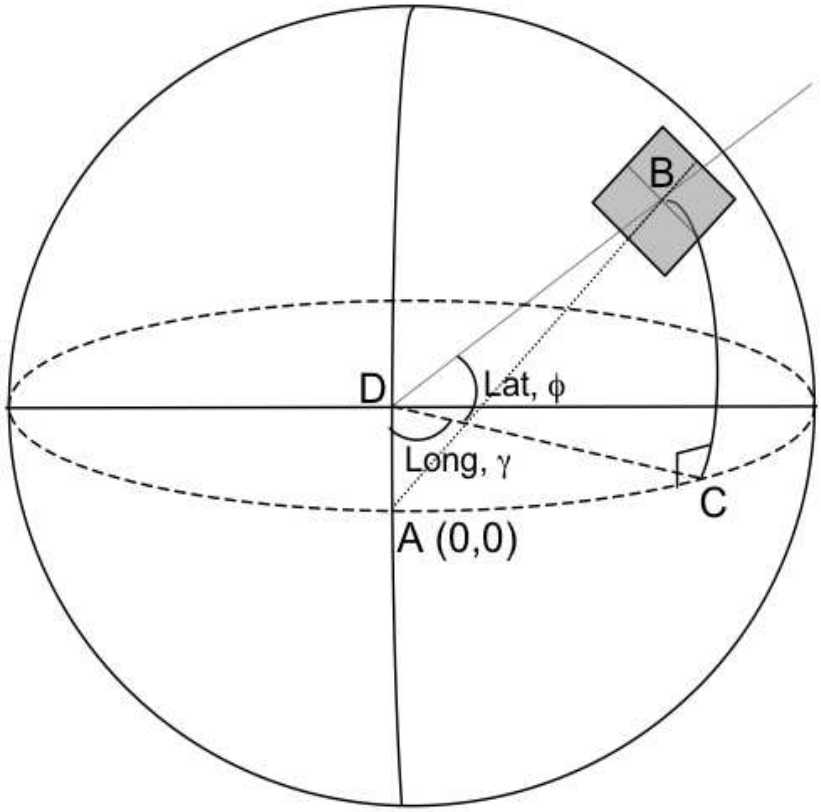

Figure B.4: A (0,0) indicates the center of the 2-D projected image of the solar disk. The epicenter of the event under study is indicated by "B". The shaded square about B shows the plane tangent to the epicenter of the event. C indicates the longitude of the event epicenter at the solar equator. D indicates the center of the 3-D solar sphere.

event epicenter (shaded square), and the 3-D Sun.

Since the plane tangent to the epicenter (B) of the event (shaded square in Figure B.4) is itself related to the 3-D solar sphere, spherical Pythagorus must be used (see left panel, Figure B.5) to obtain the following relation between the event epicenter known latitude, ϕ, known longitude, γ, and the angle, θ, subtended between the centre of the projected 2-D image of the solar disk (A), the center of the Sun (D) and the epi-centre of the event (B):

$$cos\theta = cos\phi cos\gamma \tag{B.9}$$

Finally, taking a bird's eye view from above the north solar pole, Figure B.5 (right panel) shows how β may be determined once θ is known:

$$\beta = 90 - \theta \tag{B.10}$$

Once β is known for any event epicenter, Equations B.6, B.7, B.8 can be used to calculate the real azimuthal (ring) angle, α from the azimuthal (ring) angle, α', measured from the projected 2-D images.

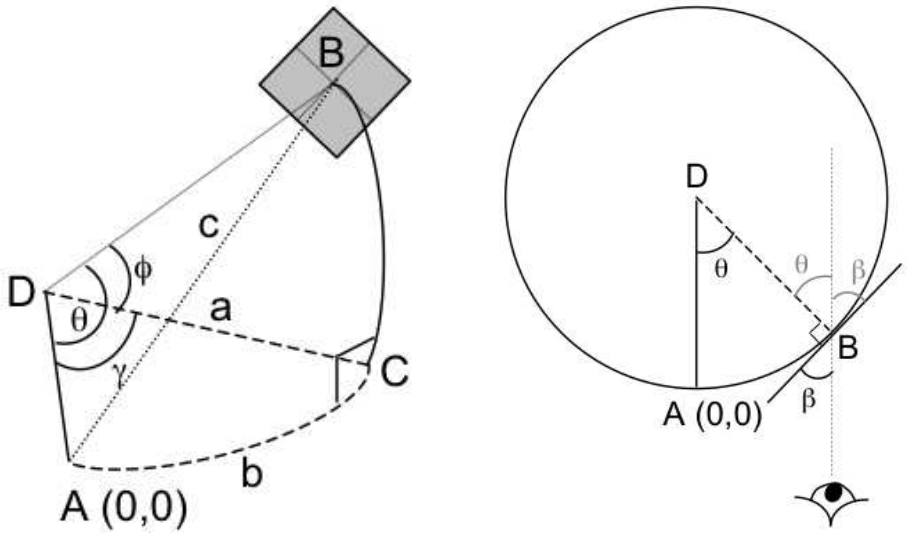

Figure B.5: Left: A spherical right-angled triangle, extracted from Figure B.4. The plane ADB exists perpendicular to the plane indicated by the shaded square, that lies tangent to the epicenter of the event under study. ϕ = angle BDC, γ = angle ADC and θ = angle ADB. Right: Viewing the geometry from above the Sun's north pole, a bird's eye view shows how β may be determined once θ is known.

Appendix C

Semi-isotropic nature of diffuse Q4 coronal "waves"

The remaining fourteen coronal waves identified as "Q4" events in the Thompson and Myers (2009) catalogue. (See main text, §4.4, for full details). Figure C.1 shows sketches from the catalogue for each event, identifying the strongest bright fronts. Running difference images of the events are also shown. Red arrows indicate more subtle bright fronts, not included in the catalogue. Where no running difference images are shown, the bright fronts are already identified as being semi-isotropic in the catalogue.

- 15th April 1997, already identified in the catalogue as semi-isotropic.
- 25th May 1997, already identified in the catalogue as semi-isotropic.
- 20th September 1997 is an event on the east limb. Identified as having bright fronts to both north and south off-limb in catalogue. There are also disturbances on-disk, near the south polar coronal hole at 10:32 UT and on-disk in the northern hemisphere at 10:49 UT (times where disturbances visible in running difference images). The identification of expansion to the north and south as well as to the west, on disk, are consistent with interpretation as a semi-isotropic expansion, so a circle, should it have been observed on-disk, rather than on the limb.
- 24th September 1997 (two S-wave events, 11:06 and 18:47 UT) running difference images capture the later diffuse bright fronts showing a semi-isotropic nature, with disturbance to the south of the source region as well as to the east and west as shown in the catalogue.
- 28th September 1997 is an event on the east limb. Identified as having bright fronts to both north and south off-limb in catalogue. There are also disturbances on-disk, e.g. clearly at 14:42 UT (time where disturbances visible in running difference images). The identification of expansion to the north and south as well as to the east, on disk, are consistent with interpretation as a semi-isotropic expansion, so a circle, should it have been observed on-disk, rather than on the limb.
- 11th October 1997, catalogue only records expansion to south of active region. But there is also an expansion to the north, e.g. from 08:48 - 09:38 UT (time where disturbances visible in running difference images).
- 12th October 1997, an event on the west limb. Identified as having bright fronts to both north and south off-limb in catalogue. However, there are also clearly disturbances on-disk until 07:22 UT (time where disturbances visible in running difference images). The identification of expansion to the north and south as well as to the west, on disk, are consistent with interpretation as a

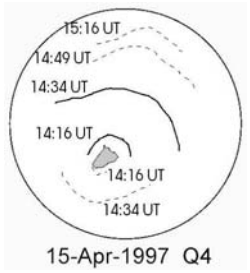
15:16 UT
14:49 UT
14:34 UT
14:16 UT
14:16 UT
14:34 UT
15-Apr-1997 Q4

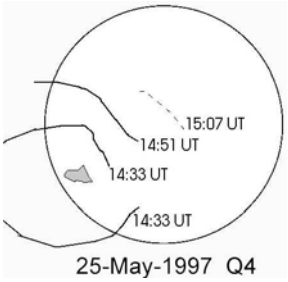
15:07 UT
14:51 UT
14:33 UT
14:33 UT
25-May-1997 Q4

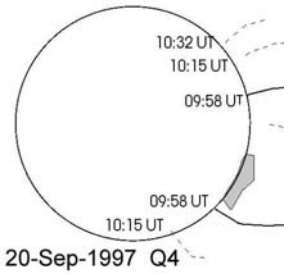
10:32 UT
10:15 UT
09:58 UT
09:58 UT
10:15 UT
20-Sep-1997 Q4

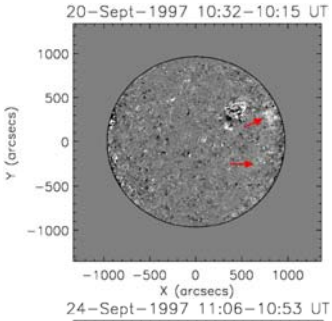
20-Sept-1997 10:32-10:15 UT
Y (arcsecs)
X (arcsecs)

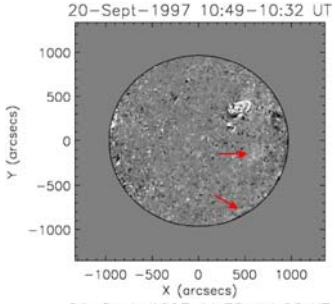
20-Sept-1997 10:49-10:32 UT
Y (arcsecs)
X (arcsecs)

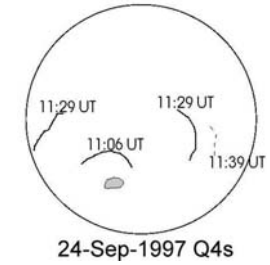
11:29 UT
11:29 UT
11:06 UT
11:39 UT
24-Sep-1997 Q4s

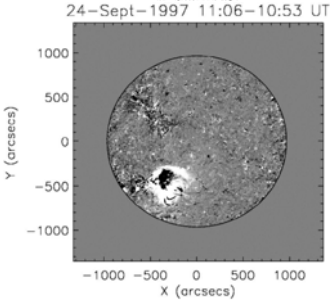
24-Sept-1997 11:06-10:53 UT
Y (arcsecs)
X (arcsecs)

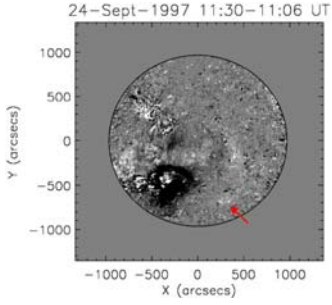
24-Sept-1997 11:30-11:06 UT
Y (arcsecs)
X (arcsecs)

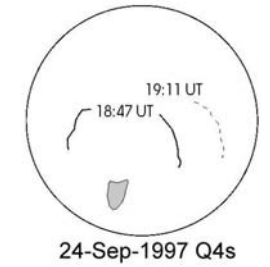
19:11 UT
18:47 UT
24-Sep-1997 Q4s

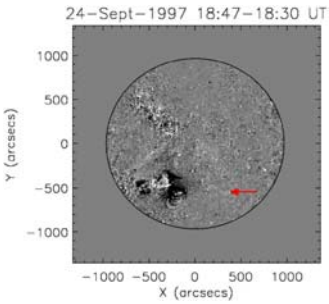
24-Sept-1997 18:47-18:30 UT
Y (arcsecs)
X (arcsecs)

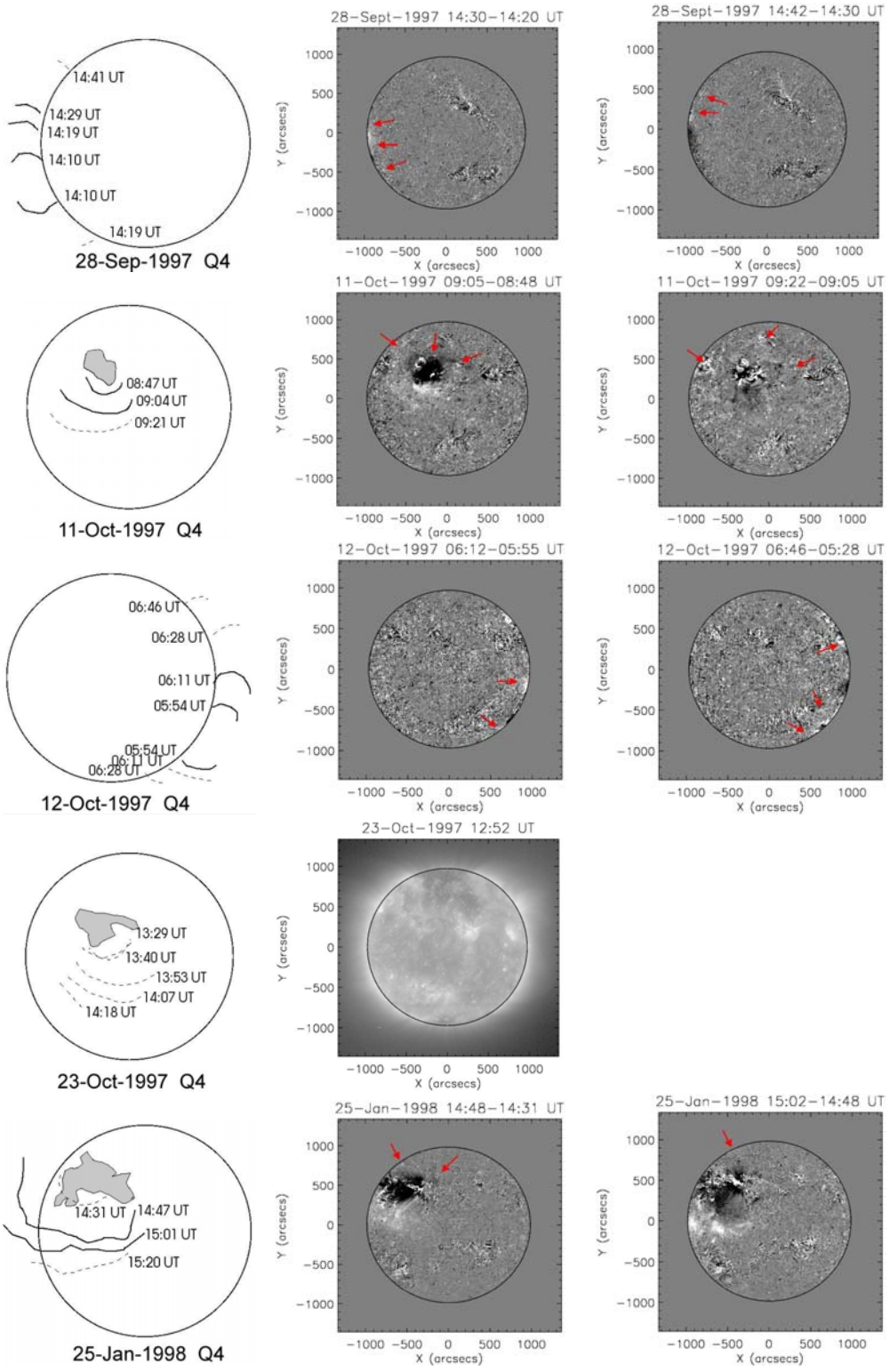
14:41 UT
14:29 UT
14:19 UT
14:10 UT
14:10 UT
14:19 UT
28-Sep-1997 Q4
28-Sept-1997 14:30-14:20 UT
28-Sept-1997 14:42-14:30 UT
08:47 UT
09:04 UT
09:21 UT
11-Oct-1997 Q4
11-Oct-1997 09:05-08:48 UT
11-Oct-1997 09:22-09:05 UT
06:46 UT
06:28 UT
06:11 UT
05:54 UT
05:54 UT
06:11 UT
06:28 UT
12-Oct-1997 Q4
12-Oct-1997 06:12-05:55 UT
12-Oct-1997 06:46-05:28 UT
13:29 UT
13:40 UT
13:53 UT
14:07 UT
14:18 UT
23-Oct-1997 Q4
23-Oct-1997 12:52 UT
14:31 UT
14:47 UT
15:01 UT
15:20 UT
25-Jan-1998 Q4
25-Jan-1998 14:48-14:31 UT
25-Jan-1998 15:02-14:48 UT
Y (arcsecs)
X (arcsecs)
1000
500
0
-500
-1000

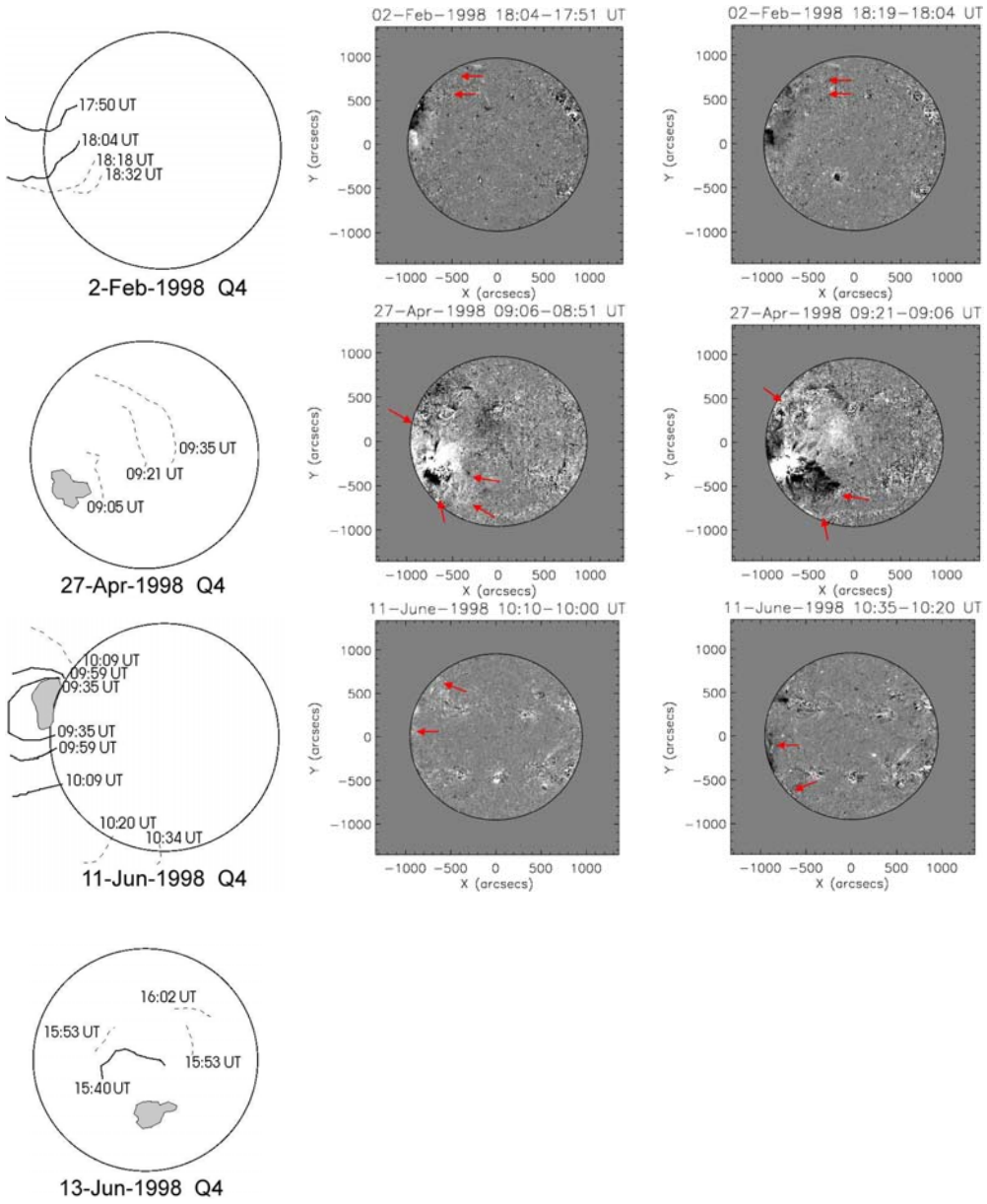

Figure C.1: Q4 events identified in the Thompson and Myers (2009) EIT wave catalogue. Left panels show sketches from the catalogue, identifying the strongest bright fronts. Center and right panels show running difference images of the events. Red arrows indicate more subtle bright fronts, not included in the catalogue. Where no running difference images are shown, the bright fronts are already identified as being semi-isotropic in the catalogue. Permission to reproduce the figures shown in the left panel has been granted by B. Thompson.

semi-isotropic expansion, so a circle, should it have been observed on-disk, rather than on the limb.

- 23rd October 1997, catalogue identifies expansion to the south of the source region. However, the eruption source region is a dispersed filament-like corridor, right at the edge of the large north polar coronal hole (NPCH). The northern edge of the source region is positive polarity. The NPCH is also positive, so no interaction (via interchange reconnection and therefore brightening) at the boundary is expected and none is observed. The expansion of the bright front to the north is prohibited by the presence of the large NPCH. So this event is likely to have exhibited a semi-isotropic expansion, if the polar coronal hole had not distorted the expansion.
- 25th January 1998. Catalogue only shows expansion to the south, but there is also disturbance on disk to the north.
- 2nd February 1998 event on the east limb. Catalogue shows expansion on the disk and above limb to the south, but running difference images also expansion of the diffuse bright front to the north. So the identification of expansion to the north and south as well as to the west, on disk, are consistent with interpretation as a semi-isotropic expansion, so a circle, should it have been observed on-disk, rather than on the limb.
- 27th April 1998. Catalogue only shows expansion to the north-west, across the disk. Running difference images show expansion semi-isotropically.
- 11th June 1998. Catalogue shows expansion to north and south, above limb. Running difference images also show expansion onto the disk. So the identification of expansion to the north and south as well as to the west, on disk, are consistent with interpretation as a semi-isotropic expansion, so a circle, should it have been observed on-disk, rather than on the limb.
- 13th June 1998. The TRACE-observed event, previously discussed in §3.6, and identified as a coronal wave event that must be considered as a special case, due to the presence of trans-equatorial loop structures.

Appendix D

Large-scale CMEs and coronal "waves"

Examining the correlation between large-scale CMEs in the low corona and their correlation with coronal "wave" events.

Table D.1 details all the limb CMEs between January 1997 - June 1998 meeting our selection criteria (§4.6). Table D.1 shows the time at which the limb CME is first detected in LASCO/C2 data and the time at which the CME is recorded as being large-scale ($\geq 2R_{\odot}$) in LASCO/C2 data. The table also indicates events (marked by "!") where there is a low-coronal signature (i.e. flare or filament eruption) associated with the CME. CME events that have a coronal wave counterpart (identified in EIT running difference data) are also highlighted, marked by "(*)".

Summary of statistical study results presented in Table D.1:
- 81 large-scale limb CME events identified between January 1997 - June 1998.
- 20/81 events have no coronal wave or associated flare or filament eruption. These are likely to be far-side events.
- 6/81 events could plausibly be temporally associated with flares, but either the location of the flare could not be identified unambiguously, or there was no plausible spatial association between the flare and CME (i.e. flare occurred on the opposite limb of the Sun to the CME).
- So 61 CMEs are likely to be front-side events, 55 of these have clear front-side signatures (either flare or filament eruption).
- All 55 large-scale CMEs with a front-side source region have associated diffuse coronal "waves".

Table D.1: Examining the correlation between large-scale limb CMEs in the low corona and their relationship with coronal "wave" events. "!" indicates events where there is a low-coronal signature (i.e. flare or filament eruption) associated with the CME. "(*)" indicates CME events that have a coronal wave counterpart.

Date	First appearance in C2 (UT)	CME Time (UT)	CME extent low corona	Coronal wave?	Matches extent of CME?	First appearance coronal wave (UT)	Flare?	Comment
18/01/97	03:30	05:30	$>2R_\odot$	No	-	-	No GOES	Probably far-side event.
! (*) 04/04/97	05:09 UT	09:38	$\sim 2R_\odot$	Yes	Yes	02:03	No	Faint & slow on NW limb, 02:00 - 06:30 UT.
! (*) 30/04/97	04:50	05:27	$\sim 2R_\odot$	Yes	Yes	04:55	No GOES	Faint event on NE limb.
! (*) 05/05/97	from 23:30 on 04/05/97	08:35	$\sim 2R_\odot$	Yes	Yes	00:43	Yes B4.3 max 01:00	Very gradual inflation of streamer.
! (*) 16/05/97	13:35	13:35	$\sim 2R_\odot$	Yes	Yes	12:41	Yes B2.1 max 13:01	Dimmings more prominent than bright front.
! (*) 25/05/97	15:25	15:25	$>2R_\odot$	Yes	Yes	14:35	Yes B6.5 max 15:00	Sigmoidal, dispersed bipolar source region.
31/05/97	18:38	00:31 on 01/06/97	$\sim 2R_\odot$	No	-	-	No	Very gradual & probably far-side event.
16/06/97	21:31	23:31	$\sim 2R_\odot$	No	-	-	No GOES	Probably far-side event.
! (*) 30/06/97	00:30	01:30	$\sim 2R_\odot$	Yes	Yes	23:58 on 29/06/97 max 23:52	Yes C1.1	Event on NW limb.
! (*) 30/07/97	19:32	19:32	$\sim 2R_\odot$	Yes	Yes	17:45	No GOES	Clear post-eruptive arcade.
08/08/97	17:23	17:23	$\sim 2R_\odot$	No	-	-	No	Probably far-side event.
22/08/97	06:45	07:30	$\sim 2R_\odot$	No	-	-	No GOES	Probably far-side event.
09/09/97	13:59	14:57	$\sim 2R_\odot$	No	-	-	Yes B6.4 max 13:52	Slow, gradual event. Flare on opposite side of disk.
! (*) 09/09/97	20:06	20:33	$> 2R_\odot$	Yes	Yes	19:26	Yes 2 possibilities C2.5 or B7.1 max 18:44 & 20:11	Source region just behind north-west limb.

Date	First appearance in C2 (UT)	CME Time (UT)	CME extent low corona	Coronal wave?	Matches extent of CME?	First appearance coronal wave (UT)	Flare?	Comment
! (*) 20/09/97	10:20	10:53	$> 2R_\odot$	Yes	Yes	10:15	Yes C2.3 max 10:44	Source region on south-west limb.
! (*) 22/09/97	12:26	12:55	$\sim 2R_\odot$	Yes	Yes	11:30	Yes C1.0 max 11:26	TEQ loops involved.
! (*) 28/09/97	14:50	15:09	$> 2R_\odot$	Yes	Yes	14:10	Yes B3.7 or C1.0 max 14:00 or 14:42	South-east limb event.
! (*) 29/09/97	18:30	18:52	$> 2R_\odot$	Yes	Yes	14:25	Yes B1.7 max 14:59	Coronal wave just on, and source region behind, north-east limb.
! (*) 06/10/97	11:12	11:12	$> 2R_\odot$	Yes	Yes	10:07	No GOES	Disturbance on west limb, source region behind limb.
! (*) 12/10/97	06:26	07:29	$> 2R_\odot$	Yes	Yes	06:11	Yes B2.3 max 06:54	West limb event.
! (*) 13/10/97	11:51	12:50	$> 2R_\odot$	Yes	Yes	10:16	Yes B6.8 start 09:10 max 12:40	Source is slow quiescent filament eruption. Very long duration flare.
! (*) 16/10/97	23:27	23:27	$> 2R_\odot$	Yes	Partially	22:26	Yes B1.5 max 21:47	Event just comes over E limb. Source region just behind/on limb.
19/10/97	10:27	12:07	$\sim 2R_\odot$	No	-	-	No	Very gradual event, probably far-side event.
! (*) 21/10/97	01:41	02:05	$\sim 2R_\odot$	Yes	Yes	00:43	Yes B3.4 max 02:36	Filament eruption from dispersed quadrupole.
! (*) 06/11/97	12:10	12:10	$> 2R_\odot$	Yes	Yes	11:59	Yes C4.7 or X9.4 max 11:36 or 11:55	Global event, starts near east limb, becomes halo.

Date	First appearance in C2 (UT)	CME Time (UT)	CME extent low corona	Coronal wave?	Matches extent of CME?	First appearance coronal wave (UT)	Flare?	Comment
! (*) 14/11/97	10:14	10:14	$> 2R_\odot$	Yes	Yes	09:50	Yes C4.6 max 10:38	West limb event.
15/11/97	20:23	20:23	$\sim 2R_\odot$	No	-	-	No	Probably far-side event.
! (*) 27/11/97	13:56	13:56	$> 2R_\odot$	Yes	Yes	13:37	X2.6 max 13:17	Event on east limb.
05/12/97	09:27	09:27	$\sim 2R_\odot$	No	-	-	No GOES	Gradual event, probably far-side event.
! (*) 03/01/98	09:42	10:11	$\sim 2R_\odot$	Yes	Yes	09:20	No	High latitude quiescent filament eruption.
! (*) 08/01/98	08:36	09:04	$\sim 2R_\odot$	Yes	Yes	07:19	No GOES	Clear post-eruptive arcade.
10/01/98	20:55	22:29	$\sim 2R_\odot$	No	-	-	Yes B3.3 or B2.7 max 20:13 or 22:26 Not associated with CME	Probably far-side event.
19/01/98	06:37	12:28	$\sim 2R_\odot$	No	-	-	Maybe B2.4 max 05:05	Extremely slow, very gradual event. Large time-span so can't associate clearly with flare.
! (*) 19/01/98	07:33	08:03	$\sim 2R_\odot$	Yes	Yes	07:19	Yes B3.0 or B2.5 max 07:11 or 08:54	Quiescent prominence eruption.
! (*) 25/01/98	15:26	15:51	$> 2R_\odot$	Yes	Yes	14:31	Yes C1.1 max 15:12	Quiescent prominence eruption, develops to halo.
! (*) 25/01/98	22:19	22:19	$> 2R_\odot$	Yes	Yes	21:54	Yes M1.3 max 21:36	
26/01/98	17:27	18:27	$\sim 2R_\odot$	No	-	-	Yes B7.8 max 17:55 Not associated with CME	Slow, faint CME, probably far-side event.
! (*) 26/01/98	23:27	23:27	$\sim 2R_\odot$	Yes	Yes	22:33	Yes C5.4 max 22:35	
28/01/98	15:27	17:29	$\sim 2R_\odot$	No	-	-	No	
31/01/98	12:41	13:38	$\sim 2R_\odot$	No	-	-	No	
! (*) 02/02/98	18:27	18:27	$\sim 2R_\odot$	Yes	Yes	17:50	Yes B7.7 max 17:55	

Date	First appearance in C2 (UT)	CME Time (UT)	CME extent low corona	Coronal wave?	Matches extent of CME?	First appearance coronal wave (UT)	Flare?	Comment
! 10/02/98	02:27	04:46	$\sim 2R_\odot$	No	-	-	Maybe B1.1 max 01:41. Location unclear.	Very gradual expansion & faint, possibly far-side event.
! (*) 23/02/98	03:08	05:08	$> 2R_\odot$	Yes	Yes	00:18	Maybe B2.7 on 22/02/98 max 23:23	CME starts slow expansion from 00:55.
23/02/98	23:27	23:27	$> 2R_\odot$	No	-	-	No	EIT only hour cadence prior to event.
! (*) 24/02/98	07:55	08:27	$\sim 2R_\odot$	Yes	Yes	06:50	No	Faint coronal wave on east limb.
! 25/02/98	23:27	23:27	$\sim 2R_\odot$	No	-	-	Yes B1.5 max 22:42 Location unclear.	Faint event, maybe far-side.
! 07/03/98	04:39	06:13	$\sim 2R_\odot$	No	-	-	Maybe B3.4 max 06:30 Location unclear.	Possibly far-side event.
! (*) 13/03/98	21:30	22:06	$\sim 2R_\odot$	Yes	Yes	21:01	C5.8 or B8.8 max 21:11 or 21:56	
! 17/03/98	13:34	14:32	$\sim 2R_\odot$	No	-	-	Maybe C3.6 max 13:35 possible association	Faint, fine CME.
! (*) 25/03/98	13:14	13:14	$> 2R_\odot$	Yes	Yes	12:30	Yes C5.3 max 13:25	
! (*) 27/03/98	01:23	01:23	$\sim 2R_\odot$	Yes	Yes	00:44	Yes C1.0 max 00:46	
! (*) 27/03/98	20:07	22:06	$> 2R_\odot$	Yes	Yes	19:13	Yes M2.4 max 22:27	
! (*) 14/04/98	05:26	05:48	$> 2R_\odot$	Yes	Yes	05:37	No	EIT first frame at 05:48 UT, coronal wave already underway. Source on North-East limb.
! (*) 20/04/98	10:07	10:07	$> 2R_\odot$	Yes	Yes	09:35	Yes M1.4 max 10:21	Source region on west limb, develops to partial halo.

Date	First appearance in C2 (UT)	CME Time (UT)	CME extent low corona	Coronal wave?	Matches extent of CME?	First appearance coronal wave (UT)	Flare?	Comment
! (*) 23/04/98	05:27	05:55	$> 2R_\odot$	Yes	Yes	05:49	Yes X1.2 max 05:35	Source region on east limb, develops to full halo.
! (*) 27/04/98	08:56	09:26	$> 2R_\odot$	Yes	Yes	08:21	Yes X1.0 max 09:20	Source region within 60° east limb, develops to full halo.
! (*) 06/05/98	00:02	00:28	$\sim 2R_\odot$	Yes	Yes	23:36	Yes M2.5 max 23:46 on 05/05/98	
(*) 06/05/98	02:28	03:27	$\sim 2R_\odot$	Yes	Partially	01:18	No	Coronal wave disturbance faintly visible above east limb. Source behind limb.
! (*) 06/05/98	08:29	08:29	$> 2R_\odot$	Yes	Yes	08:10	Yes M2.9 or X2.7 max 07:25 or 08:09	Source close to west limb, develops to partial halo.
! 07/05/98	00:58	04:26	$\sim 2R_\odot$	No	-	-	Maybe C3.5 max 01:10 possible association	Gradual, slow CME.
! (*) 08/05/98	13:01	13:36	$\sim 2R_\odot$	Yes	Yes	12:24	Yes C5.4 max 13:06	Source just on/behind west limb.
! (*) 09/05/98	03:35	04:09	$> 2R_\odot$	Yes	Yes	03:28	Yes M7.7 max 03:40	Source on west limb, develops to partial halo.
! (*) 09/05/98	20:29	20:29	$> 2R_\odot$	Yes	Yes	20:11	Yes C3.9 max 20:35	Source just behind west limb, develops to partial halo. Coiled core.
12/05/98	03:55	04:26	$\sim 2R_\odot$	No	-	-	Maybe C1.2 max 05:27	Probably far-side event. Flare at center disk.
(*) 12/05/98	08:55	08:55	$> 2R_\odot$	Yes	Yes	08:20	No	Source region behind west limb.
(*) 19/05/98	02:01	02:01	$\sim 2R_\odot$	Yes	Yes	01:12	No	Source region behind east limb.
! (*) 19/05/98	10:27	10:27	$> 2R_\odot$	Yes	Yes	09:55	Yes B7.9 max 10:15	Quiescent filament eruption.
! (*) 27/05/98	13:45	13:45	$> 2R_\odot$	Yes	Yes	13:32	Yes C7.5	Source region near west limb, develops to partial halo.

Date	First appearance in C2 (UT)	CME Time (UT)	CME extent low corona	Coronal wave?	Matches extent of CME?	First appearance coronal wave (UT)	Flare?	Comment
! 27/05/98	09:40	19:40	$\sim 2R_\odot$	No	-	-	Multiple possibilities. Uncertain.	Very gradual event.
! (*) 28/05/98	05:33	05:33	$> 2R_\odot$	Yes	Yes	04:59	C2.9 or C3.1 max 04:13 or 04:39	
30/05/98	15:54	17:06	$> 2R_\odot$	No	-	-	No	Very gradual event.
02/06/98	02:59	03:27	$\sim 2R_\odot$	No	-	-	No	Gradual event, faint, possibly far-side.
(*) 02/06/98	09:37	10:29	$\sim 2R_\odot$	Yes	No	10:10	No	Helical CME, persistent low coronal brightening.
03/06/98	12:02	12:02	$> 2R_\odot$	No	-	-	Maybe B5.3 max 13:10	CME long departed by time of flare.
! (*) 04/06/98	21:27	22:00	$\sim 2R_\odot$	Yes	Yes	20:36	Yes C1.0 max 20:39	Coronal wave disturbance over east limb.
09/06/98	06:56	07:55	$> 2R_\odot$	No	-	-	Maybe B6.1 max 08:39	Faint and gradual CME, probably far-side event.
							Location unclear	CME long departed.
! (*) 11/06/98	00:28	00:55	$\sim 2R_\odot$	Yes	Yes	23:36 on 10/06/98	Yes C1.1 max 00:14	Source region behind E limb.
! (*) 11/06/98	10:28	10:28	$> 2R_\odot$	Yes	Yes	10:00	Yes M1.4 max 10:27	Source region on E limb, develops to partial halo.
! (*) 13/06/98	03:27	03:55	$> 2R_\odot$	Yes	Yes	02:19	Yes C2.6 or M1.9 max 03:57 or 04:20	Source region on west limb.
(*) 16/06/98	06:27	07:27	$> 2R_\odot$	Yes	Partially	05:02	No	Source region behind W limb, probably far-side event.
! (*) 16/06/98	18:27	18:27	$> 2R_\odot$	Yes	Yes	18:18	Yes M1.0 max 18:42	Source region on E limb, develops to partial halo.

Appendix E

Accompanying CD-ROM

A CD-ROM accompanies this thesis. It can be found inside the back cover. The movies on this CD-ROM are relevant to the following chapters:

Chapter 3:

- tracebd13june98.mpg
- eitbd13june98.mpg
- eit13june98.mpg

Chapter 4:

- cwsubdiskbasediff.mpg
- euvi_b_dmap_subfov.mpg
- eit_195_290406.mpg
- cwsubdiskbasediff_290406.mpg

Chapter 5:

- 970512_195.mpg

Chapter 6:

- contraction_120597.mpg
- contraction_130505.mpg
- contraction_060706.mpg

References

Abramenko, V. I., Fisk, L. A., and Yurchyshyn, V. B.: The Rate of Emergence of Magnetic Dipoles in Coronal Holes and Adjacent Quiet-Sun Regions, *Astrophys. J. Lett.*, **641**, L65–L68, doi:10.1086/503870, 2006.

Alfvén, H.: Existence of electromagnetic-hydrodynamic waves, *Nature*, **150**, 405, 1942.

Asai, A., Hara, H., Watanabe, T., Imada, S., Sakao, T., Narukage, N., Culhane, J. L., and Doschek, G. A.: Strongly Blueshifted Phenomena Observed with *Hinode*/EIS in the 2006 December 13 Solar Flare, *ArXiv e-prints*, **805**, 2008.

Aschwanden, M. J., Poland, A. I., and Rabin, D. M.: The New Solar Corona, *Ann. Rev. Astron.*, **39**, 175–210, doi:10.1146/annurev.astro.39.1.175, 2001.

Attrill, G., Nakwacki, M. S., Harra, L. K., van Driel-Gesztelyi, L., Mandrini, C. H., Dasso, S., and Wang, J.: Using the Evolution of Coronal Dimming Regions to Probe the Global Magnetic Field Topology, *Solar Phys.*, **238**, 117–139, doi:10.1007/s11207-006-0167-5, 2006.

Attrill, G. D. R., Harra, L. K., Matthews, S. A., Foley, C. R., and Sterling, A. C.: The Relationship between Prominence Eruptions and Global Coronal Waves, in The Solar-B Mission and the Forefront of Solar Physics, edited by T. Sakurai and T. Sekii, vol. 325 of *Astronomical Society of the Pacific Conference Series*, pp. 409–414, 2004.

Attrill, G. D. R., Harra, L. K., van Driel-Gesztelyi, L., and Démoulin, P.: Coronal "Wave": Magnetic Footprint of a Coronal Mass Ejection?, *Astrophys. J. Lett.*, **656**, L101–L104, doi:10.1086/512854, 2007a.

Attrill, G. D. R., Harra, L. K., van Driel-Gesztelyi, L., Démoulin, P., and Wülser, J.-P.: Coronal "wave": A signature of the mechanism making CMEs large-scale in the low corona?, *Astronomische Nachrichten*, 2007b.

Aulanier, G. and Demoulin, P.: 3-D magnetic configurations supporting prominences. I. The natural presence of lateral feet, *Astron. Astrophys.*, **329**, 1125–1137, 1998.

Aulanier, G., Pariat, E., and Démoulin, P.: Current sheet formation in quasi-separatrix layers and hyperbolic flux tubes, *Astron. Astrophys.*, **444**, 961–976, doi:10.1051/0004-6361:20053600, 2005.

Aurass, H., Vourlidas, A., Andrews, M. D., Thompson, B. J., Howard, R. H., and Mann, G.: Nonthermal Radio Signatures of Coronal Disturbances with and without Coronal Mass Ejections, *Astrophys. J.*, **511**, 451–465, doi:10.1086/306653, 1999.

Aurass, H., Shibasaki, K., Reiner, M., and Karlický, M.: Microwave Detection of Shock and Associated Electron Beam Formation, *Astrophys. J.*, **567**, 610–621, doi:10.1086/338417, 2002.

Babcock, H. W.: The Topology of the Sun's Magnetic Field and the 22-YEAR Cycle., *Astrophys. J.*, **133**, 572, 1961.

Baker, D., van Driel-Gesztelyi, L., and Attrill, G. D. R.: Evidence for interchange reconnection between a coronal hole and an adjacent emerging flux region, *Astronomische Nachrichten*, **328**, 773–776, doi:10.1002/asna.200710787, 2007.

Balasubramaniam, K. S., Pevtsov, A. A., Neidig, D. F., Cliver, E. W., Thompson, B. J., Young, C. A., Martin, S. F., and Kiplinger, A.: Sequential Chromospheric Brightenings beneath a Transequatorial Halo Coronal Mass Ejection, *Astrophys. J.*, **630**, 1160–1167, doi:10.1086/432030, 2005.

Balasubramaniam, K. S., Pevtsov, A. A., and Neidig, D. F.: Are Moreton Waves Coronal Phenomena?, *Astrophys. J.*, **658**, 1372–1379, doi:10.1086/512001, 2007.

Ballai, I. and Erdélyi, R.: Damping of Coronal EIT Waves as a Tool for Plasma Diagnostics, in SOHO 13 Waves, Oscillations and Small-Scale Transients Events in the Solar Atmosphere: Joint View from SOHO and TRACE, edited by H. Lacoste, vol. 547 of *ESA Special Publication*, p. 433, 2004.

Ballai, I., Thelen, J. C., and Roberts, B.: Solitary waves in a Hall solar wind plasma, *Astron. Astrophys.*, **404**, 701–707, doi:10.1051/0004-6361:20030580, 2003.

Ballai, I., Erdélyi, R., and Pintér, B.: On the Nature of Coronal EIT Waves, *Astrophys. J. Lett.*, **633**, L145–L148, doi:10.1086/498447, 2005.

Bastian, T. S., Pick, M., Kerdraon, A., Maia, D., and Vourlidas, A.: The Coronal Mass Ejection of 1998 April 20: Direct Imaging at Radio Wavelengths, *Astrophys. J. Lett.*, **558**, L65–L69, doi:10.1086/323421, 2001.

Baumjohann, W. and Treumann, R. A.: Basic space plasma physics, London: Imperial College Press, 1997.

Benz, A. O. and Krucker, S.: Heating the Quiet Corona by Nanoflares: Evidence and Problems, in Recent Insights into the Physics of the Sun and Heliosphere: Highlights from SOHO and Other Space Missions, edited by P. Brekke, B. Fleck, and J. B. Gurman, vol. 203 of *IAU Symposium*, pp. 471–474, 2001.

Berger, T. E. and Lites, B. W.: Weak-Field Magnetogram Calibration using Advanced Stokes Polarimeter Flux Density Maps - II. SOHO/MDI Full-Disk Mode Calibration, *Solar Phys.*, **213**, 213–229, 2003.

Berger, T. E., de Pontieu, B., Fletcher, L., Schrijver, C. J., Tarbell, T. D., and Title, A. M.: What is Moss?, *Solar Phys.*, **190**, 409–418, doi:10.1023/A:1005286503963, 1999.

Bewsher, D., Harrison, R. A., and Brown, D. S.: The relationship between EUV dimming and coronal mass ejections. I. Statistical study and probability model, *Astron. Astrophys.*, **478**, 897–906, doi:10.1051/0004-6361:20078615, 2008.

Biesecker, D. A., Myers, D. C., Thompson, B. J., Hammer, D. M., and Vourlidas, A.: Solar Phenomena Associated with "EIT Waves", *Astrophys. J.*, **569**, 1009–1015, doi:10.1086/339402, 2002.

Bothmer, V. and Schwenn, R.: The structure and origin of magnetic clouds in the solar wind, *Ann. Geophys.*, **16**, 1–24, 1998.

Brosius, J. W. and Holman, G. D.: Chromospheric Evaporation in a Remote Solar Flare-like Transient Observed at High Time Resolution with SOHO's CDS and RHESSI, *Astrophys. J. Lett.*, **659**, L73–L76, doi:10.1086/516629, 2007.

Brown, J. C.: The Deduction of Energy Spectra of Non-Thermal Electrons in Flares from the Observed Dynamic Spectra of Hard X-Ray Bursts, *Solar Phys.*, **18**, 489–502, doi:10.1007/BF00149070, 1971.

Brueckner, G. E., Howard, R. A., Koomen, M. J., Korendyke, C. M., Michels, D. J., Moses, J. D., Socker, D. G., Dere, K. P., Lamy, P. L., Llebaria, A., Bout, M. V., Schwenn, R., Simnett, G. M., Bedford, D. K., and Eyles, C. J.: The Large Angle Spectroscopic Coronagraph (LASCO), *Solar Phys.*, **162**, 357–402, doi:10.1007/BF00733434, 1995.

Burlaga, L., Sittler, E., Mariani, F., and Schwenn, R.: Magnetic loop behind an interplanetary shock - Voyager, Helios, and IMP 8 observations, *J. Geophys. Res.*, **86**, 6673–6684, 1981.

Carmichael, H.: A Process for Flares, in The Physics of Solar Flares, p. 451, 1964.

Carrington, R. C.: Description of a Singular Appearance seen in the Sun on September 1, 1859, *Mon. Not. Roy. Astron. Soc.*, **20**, 13–15, 1859.

Chen, P. F.: The Relation between EIT Waves and Solar Flares, *Astrophys. J. Lett.*, **641**, L153–L156, doi:10.1086/503868, 2006.

Chen, P. F., Wu, S. T., Shibata, K., and Fang, C.: Evidence of EIT and Moreton Waves in Numerical Simulations, *Astrophys. J. Lett.*, **572**, L99–L102, doi:10.1086/341486, 2002.

Chen, P. F., Ding, M. D., and Fang, C.: Synthesis of CME-Associated Moreton and EIT Wave Features from MHD Simulations, *Space Science Reviews*, **121**, 201–211, doi:10.1007/s11214-006-3911-0, 2005a.

Chen, P. F., Fang, C., and Shibata, K.: A Full View of EIT Waves, *Astrophys. J.*, **622**, 1202–1210, doi:10.1086/428084, 2005b.

Chertok, I. M. and Grechnev, V. V.: Large-scale Dimmings Produced by Solar Coronal Mass Ejections According to SOHO/EIT Data in Four EUV Lines, *Astronomy Reports*, **47**, 934–945, doi:10.1134/1.1626196, 2003.

Chertok, I. M. and Grechnev, V. V.: Large-Scale Activity in the Bastille Day 2000 Solar Event, *Solar Phys.*, **229**, 95–114, doi:10.1007/s11207-005-3654-1, 2005.

Chertok, I. M., Grechnev, V. V., Hudson, H. S., and Nitta, N. V.: Homologous large-scale activity in solar eruptive events of 24-26 November 2000, *Journal of Geophysical Research (Space Physics)*, **109**, 2112, doi:10.1029/2003JA010182, 2004.

Cid, C., Hidalgo, M. A., Nieves-Chinchilla, T., Sequeiros, J., and Viñas, A. F.: Plasma and Magnetic Field Inside Magnetic Clouds: a Global Study, *Solar Phys.*, **207**, 187–198, 2002.

Cliver, E. W., Webb, D. F., and Howard, R. A.: On the origin of solar metric type II bursts, *Solar Phys.*, **187**, 89–114, 1999.

Cliver, E. W., Nitta, N. V., Thompson, B. J., and Zhang, J.: Coronal Shocks of November 1997 Revisited: The Cme Type II Timing Problem, *Solar Phys.*, **225**, 105–139, doi:10.1007/s11207-004-3258-1, 2004.

Cliver, E. W., Laurenza, M., Storini, M., and Thompson, B. J.: On the Origins of Solar EIT Waves, *Astrophys. J.*, **631**, 604–611, doi:10.1086/432250, 2005.

Cremades, H. and Bothmer, V.: On the three-dimensional configuration of coronal mass ejections, *Astron. Astrophys.*, **422**, 307–322, doi:10.1051/0004-6361:20035776, 2004.

Crooker, N. U. and Webb, D. F.: Remote sensing of the solar site of interchange reconnection associated with the May 1997 magnetic cloud, *Journal of Geophysical Research (Space Physics)*, **111**, 8108–8114, doi:10.1029/2006JA011649, 2006.

Crooker, N. U., Gosling, J. T., Smith, E. J., and Russell, C. T.: A bubblelike coronal mass ejection flux rope in the solar wind, *Washington DC American Geophysical Union Geophysical Monograph Series*, **58**, 365–371, 1990.

Crooker, N. U., Gosling, J. T., and Kahler, S. W.: Reducing heliospheric magnetic flux from coronal mass ejections without disconnection, *Journal of Geophysical Research (Space Physics)*, **107**, 1028–1032, doi:10.1029/2001JA000236, 2002.

Culhane, J. L.: Instrumentation for Photon Detection in Space, p. 365, Space Science, 2004.

Culhane, J. L., Harra, L. K., James, A. M., Al-Janabi, K., Bradley, L. J., Chaudry, R. A., Rees, K., Tandy, J. A., Thomas, P., Whillock, M. C. R., Winter, B., Doschek, G. A., Korendyke, C. M., Brown, C. M., Myers, S., Mariska, J., Seely, J., Lang, J., Kent, B. J., Shaughnessy, B. M., Young, P. R., Simnett, G. M., Castelli, C. M., Mahmoud, S., Mapson-Menard, H., Probyn, B. J., Thomas, R. J., Davila, J., Dere, K., Windt, D., Shea, J., Hagood, R., Moye, R., Hara, H., Watanabe, T., Matsuzaki, K., Kosugi, T., Hansteen, V., and Wikstol, Ø.: The EUV Imaging Spectrometer for Hinode, *Solar Phys.*, **243**, 19–61, doi:10.1007/s01007-007-0293-1, 2007.

Dasso, S., Mandrini, C. H., Démoulin, P., and Farrugia, C. J.: Magnetic helicity analysis of an interplanetary twisted flux tube, *Journal of Geophysical Research (Space Physics)*, **108**, 3, doi:10.1029/2003JA009942, 2003.

Dasso, S., Mandrini, C. H., Démoulin, P., Luoni, M. L., and Gulisano, A. M.: Large scale MHD properties of interplanetary magnetic clouds, *Advances in Space Research*, **35**, 711–724, doi:10.1016/j.asr.2005.02.096, 2005.

Dasso, S., Mandrini, C. H., Démoulin, P., and Luoni, M. L.: A new model-independent method to compute magnetic helicity in magnetic clouds, *Astron. Astrophys.*, **455**, 349–359, doi:10.1051/0004-6361:20064806, 2006.

Dasso, S., Nakwacki, M. S., Démoulin, P., and Mandrini, C. H.: Progressive Transformation of a Flux Rope to an ICME, *Solar Phys.*, **244**, 115–137, doi:10.1007/s11207-007-9034-2, 2007.

de Toma, G., Holzer, T. E., Burkepile, J. T., and Gilbert, H. R.: Transient Coronal Holes as Seen in the He I 1083 nm MLSO Observations, *Astrophys. J.*, **621**, 1109–1120, doi:10.1086/426904, 2005.

Deforest, C. E.: On Re-sampling of Solar Images, *Solar Phys.*, **219**, 3–23, doi:10.1023/B:SOLA.0000021743.24248.b0, 2004.

Delaboudinière, J.-P., Artzner, G. E., Brunaud, J., Gabriel, A. H., Hochedez, J. F., Millier, F., Song, X. Y., Au, B., Dere, K. P., Howard, R. A., Kreplin, R., Michels, D. J., Moses, J. D., Defise, J. M., Jamar, C., Rochus, P., Chauvineau, J. P., Marioge, J. P., Catura, R. C., Lemen, J. R., Shing, L., Stern, R. A., Gurman, J. B., Neupert, W. M., Maucherat, A., Clette, F., Cugnon, P., and van Dessel, E. L.: EIT: Extreme-Ultraviolet Imaging Telescope for the SOHO Mission, *Solar Phys.*, **162**, 291–312, doi:10.1007/BF00733432, 1995.

Delannée, C.: Another View of the EIT Wave Phenomenon, *Astrophys. J.*, **545**, 512–523, doi:10.1086/317777, 2000.

Delannée, C. and Aulanier, G.: Cme Associated with Transequatorial Loops and a Bald Patch Flare, *Solar Phys.*, **190**, 107–129, 1999.

Delannée, C., Delaboudinière, J.-P., and Lamy, P.: Observation of the origin of CMEs in the low corona, *Astron. Astrophys.*, **355**, 725–742, 2000.

Delannée, C., Hochedez, J.-F., and Aulanier, G.: Stationary parts of an EIT and Moreton wave: a topological model, *Astron. Astrophys.*, **465**, 603–612, doi:10.1051/0004-6361:20065845, 2007.

Delannée, C., Török, T., Aulanier, G., and Hochedez, J.-F.: A New Model for Propagating Parts of EIT Waves: A Current Shell in a CME, *Solar Phys.*, **247**, 123–150, doi:10.1007/s11207-007-9085-4, 2008.

Démoulin, P.: Magnetic Topologies: where Will Reconnection Occur ?, in Chromospheric and Coronal Magnetic Fields, edited by D. E. Innes, A. Lagg, and S. A. Solanki, vol. 596 of *ESA Special Publication*, 2005.

Démoulin, P.: Extending the concept of separatrices to QSLs for magnetic reconnection, *Advances in Space Research*, **37**, 1269–1282, doi:10.1016/j.asr.2005.03.085, 2006.

Démoulin, P.: A review of the quantitative links between CMEs and magnetic clouds, *Annales Geophysicae*, **in press**, 2008.

Démoulin, P., Henoux, J. C., Priest, E. R., and Mandrini, C. H.: Quasi-Separatrix layers in solar flares. I. Method., *Astron. Astrophys.*, **308**, 643–655, 1996.

Dere, K. P., Brueckner, G. E., Howard, R. A., Koomen, M. J., Korendyke, C. M., Kreplin, R. W., Michels, D. J., Moses, J. D., Moulton, N. E., Socker, D. G., St. Cyr, O. C., Delaboudinière, J. P., Artzner, G. E., Brunaud, J., Gabriel, A. H., Hochedez, J. F., Millier, F., Song, X. Y., Chauvineau, J. P., Marioge, J. P., Defise, J. M., Jamar, C., Rochus, P., Catura, R. C., Lemen, J. R., Gurman, J. B., Neupert, W., Clette, F., Cugnon, P., van Dessel, E. L., Lamy, P. L., Llebaria, A., Schwenn, R., and Simnett, G. M.: EIT and LASCO Observations of the Initiation of a Coronal Mass Ejection, *Solar Phys.*, **175**, 601–612, doi:10.1023/A:1004907307376, 1997.

Dodson, H. W. and Hedeman, E. R.: The Proton Flare of August 28, 1966, *Solar Phys.*, **4**, 229–239, doi:10.1007/BF00148084, 1968.

Domingo, V., Fleck, B., and Poland, A. I.: The SOHO Mission: an Overview, *Solar Phys.*, **162**, 1–2, doi:10.1007/BF00733425, 1995.

Drazin, P. G. and Johnson, R. S.: Solitons: An Introduction, Cambridge Texts in Applied Matehmatics, No. 2, Cambridge University Press, 1989.

Driesman, A., Hynes, S., and Cancro, G.: The STEREO Observatory, *Space Science Reviews*, **136**, 17–44, doi:10.1007/s11214-007-9286-z, 2008.

Emslie, A. G.: Energy Release and Transport in Flare Plasmas, in NATO ASIC Proc. 373: The Sun: A Laboratory for Astrophysics, edited by J. T. Schmelz and J. C. Brown, p. 489, 1992.

Emslie, A. G., Kontar, E. P., Krucker, S., and Lin, R. P.: RHESSI Hard X-Ray Imaging Spectroscopy of the July 23, 2002 Solar Flare, in Bulletin of the American Astronomical Society, vol. 35 of *Bulletin of the American Astronomical Society*, p. 851, 2003.

Eto, S., Isobe, H., Narukage, N., Asai, A., Morimoto, T., Thompson, B., Yashiro, S., Wang, T., Kitai, R., Kurokawa, H., and Shibata, K.: Relation between a Moreton Wave and an EIT Wave Observed on 1997 November 4, *Pub. Astron. Soc. Japan*, **54**, 481–491, 2002.

Feldman, U., Widing, K. G., and Warren, H. P.: Morphology of the Quiet Solar Upper Atmosphere, *Astrophys. J.*, **522**, 1133–1147, doi:10.1086/307682, 1999.

Fisk, L. A.: The Open Magnetic Flux of the Sun. I. Transport by Reconnections with Coronal Loops, *Astrophys. J.*, **626**, 563–573, doi:10.1086/429957, 2005.

Fisk, L. A. and Schwadron, N. A.: The Behavior of the Open Magnetic Field of the Sun, *Astrophys. J.*, **560**, 425–438, doi:10.1086/322503, 2001.

Fisk, L. A. and Zurbuchen, T. H.: Distribution and properties of open magnetic flux outside of coronal holes, *Journal of Geophysical Research (Space Physics)*, **111**, 9115–9124, doi:10.1029/2005JA011575, 2006.

Fletcher, L. and Hudson, H. S.: Impulsive Phase Flare Energy Transport by Large-Scale Alfvén Waves and the Electron Acceleration Problem, *Astrophys. J.*, **675**, 1645–1655, doi:10.1086/527044, 2008.

Forbes, T. G.: A review on the genesis of coronal mass ejections, *J. Geophys. Res.*, **105**, 23 153–23 166, doi:10.1029/2000JA000005, 2000.

Forbes, T. G., Linker, J. A., Chen, J., Cid, C., Kóta, J., Lee, M. A., Mann, G., Mikić, Z., Potgieter, M. S., Schmidt, J. M., Siscoe, G. L., Vainio, R., Antiochos, S. K., and Riley, P.: CME Theory and Models, *Space Science Reviews*, **123**, 251–302, doi:10.1007/s11214-006-9019-8, 2006.

Gergely, T. E., Kundu, M. R., Erskine, III, F. T., Sawyer, C., Wagner, W. J., Illing, R., House, L. L., McCabe, M. K., Stewart, R. T., and Nelson, G. J.: Radio and visible-light observations of a coronal arcade transient, *Solar Phys.*, **90**, 161–176, 1984.

Gilbert, H. R. and Holzer, T. E.: Chromospheric Waves Observed in the He I Spectral Line (λ = 10830 Å): A Closer Look, *Astrophys. J.*, **610**, 572–587, doi:10.1086/421452, 2004.

Gilbert, H. R., Holzer, T. E., Thompson, B. J., and Burkepile, J. T.: A Comparison of CME-Associated Atmospheric Waves Observed in Coronal (Fe XII 195 Å) and Chromospheric (He I 10830 Å) Lines, *Astrophys. J.*, **607**, 540–553, doi:10.1086/383231, 2004.

Gold, T. and Hoyle, F.: On the origin of solar flares, *Mon. Not. Roy. Astron. Soc.*, **120**, 89, 1960.

Golub, L. and Pasachoff, J. M.: The Solar Corona, The Solar Corona, by Leon Golub and Jay M. Pasachoff, pp. 388. ISBN 0521480825. Cambridge, UK: Cambridge University Press, September 1997., 1997.

Gopalswamy, N. and Kaiser, M. L.: Solar eruptions and long wavelength radio bursts: The 1997 May 12 event, *Advances in Space Research*, **29**, 307–312, 2002.

Gopalswamy, N. and Thompson, B. J.: Early life of coronal mass ejections, *Journal of Atmospheric and Solar-Terrestrial Physics*, **62**, 1457–1469, 2000.

Gopalswamy, N., Kaiser, M. L., Sato, J., and Pick, M.: Shock Wave and EUV Transient During a Flare, in High Energy Solar Physics Workshop - Anticipating Hess!, edited by R. Ramaty and N. Mandzhavidze, vol. 206 of *Astronomical Society of the Pacific Conference Series*, p. 351, 2000.

Gosling, J. T., Pizzo, V., and Bame, S. J.: Anomalously low proton temperatures in the solar wind following interplanetary shock waves - evidence for magnetic bottles?, *J. Geophys. Res.*, **78**, 2001–2009, 1973.

Gosling, J. T., Hildner, E., MacQueen, R. M., Munro, R. H., Poland, A. I., and Ross, C. L.: Mass ejections from the sun - A view from SKYLAB, *J. Geophys. Res.*, **79**, 4581–4587, 1974.

Gosling, J. T., Hildner, E., MacQueen, R. M., Munro, R. H., Poland, A. I., and Ross, C. L.: The speeds of coronal mass ejection events, *Solar Phys.*, **48**, 389–397, 1976.

Grechnev, V. V., Chertok, I. M., Slemzin, V. A., Kuzin, S. V., Ignat'ev, A. P., Pertsov, A. A., Zhitnik, I. A., Delaboudinière, J.-P., and Auchère, F.: CORONAS-F/SPIRIT EUV observations of October-November 2003 solar eruptive events in combination with SOHO/EIT data, *Journal of Geophysical Research (Space Physics)*, **110**, 9–22, doi:10.1029/2004JA010931, 2005.

Green, L. M., Démoulin, P., Mandrini, C. H., and Van Driel-Gesztelyi, L.: How are Emerging Flux, Flares and CMEs Related to Magnetic Polarity Imbalance in Midi Data?, *Solar Phys.*, **215**, 307–325, 2003.

Green, L. M., Kliem, B., Török, T., van Driel-Gesztelyi, L., and Attrill, G. D. R.: Transient Coronal Sigmoids and Rotating Erupting Flux Ropes, *Solar Phys.*, **246**, 365–391, doi:10.1007/s11207-007-9061-z, 2007.

Hagenaar, H. J., Schrijver, C. J., Title, A. M., and Shine, R. A.: Dispersal of Magnetic Flux in the Quiet Solar Photosphere, *Astrophys. J.*, **511**, 932–944, doi:10.1086/306691, 1999.

Hagenaar, H. J., Schrijver, C. J., and Title, A. M.: The Properties of Small Magnetic Regions on the Solar Surface and the Implications for the Solar Dynamo(s), *Astrophys. J.*, **584**, 1107–1119, doi:10.1086/345792, 2003.

Hagenaar, H. J., DeRosa, M. L., and Schrijver, C. J.: The Dependence of Ephemeral Region Emergence on Local Flux Imbalance, *Astrophys. J.*, **678**, 541–548, doi:10.1086/533497, 2008.

Hannah, I. G., Hurford, G. J., Hudson, H. S., and Lin, R. P.: A new method of observing weak extended x-ray sources with RHESSI, *ArXiv Astrophysics e-prints*, 2007a.

Hannah, I. G., Hurford, G. J., Hudson, H. S., Lin, R. P., and van Bibber, K.: First Limits on the 3-200 keV X-Ray Spectrum of the Quiet Sun Using RHESSI, *Astrophys. J. Lett.*, **659**, L77–L80, doi:10.1086/516750, 2007b.

Hansen, R. T., Garcia, C. J., Hansen, S. F., and Yasukawa, E.: Abrupt Depletions of the Inner Corona, *Pub. Astron. Soc. Pac.*, **86**, 500–515, 1974.

Hara, H., Watanabe, T., Matsuzaki, K., Harra, L. K., Culhane, J. L., Cargill, P., Mariska, J. T., and Doschek, G. A.: 2006 December 17 Long Duration Flare Observed with the Hinode EUV Imaging Spectrometer, *Pub. Astron. Soc. Japan*, **60**, 275–284, 2008.

Harra, L. K. and Mason, K. O.: Space Science, Space Science, 2004.

Harra, L. K. and Sterling, A. C.: Material Outflows from Coronal Intensity "Dimming Regions" during Coronal Mass Ejection Onset, *Astrophys. J. Lett.*, **561**, L215–L218, doi:10.1086/324767, 2001.

Harra, L. K. and Sterling, A. C.: Imaging and Spectroscopic Investigations of a Solar Coronal Wave: Properties of the Wave Front and Associated Erupting Material, *Astrophys. J.*, **587**, 429–438, doi:10.1086/368079, 2003.

Harra, L. K., Crooker, N. U., Mandrini, C. H., van Driel-Gesztelyi, L., Dasso, S., Wang, J., Elliott, H., Attrill, G., Jackson, B. V., and Bisi, M. M.: How Does Large Flaring Activity from the Same Active Region Produce Oppositely Directed Magnetic Clouds?, *Solar Phys.*, **244**, 95–114, doi:10.1007/s11207-007-9002-x, 2007a.

Harra, L. K., Hara, H., Imada, S., Young, P., Williams, D. R., Sterling, A. C., Korendyke, C., and Attrill, G. D. R.: Coronal Dimmings Observed with Hinode: Outflows Related to a Coronal Mass Ejection, *Pub. Astron. Soc. Japan*, **59**, S801–S806, 2007b.

Harrison, R. A.: Soho observations relating to the association between flares and coronal mass ejections, *Advances in Space Research*, **32**, 2425–2437, doi:10.1016/j.asr.2003.03.016, 2003.

Harrison, R. A. and Lyons, M.: A spectroscopic study of coronal dimming associated with a coronal mass ejection, *Astron. Astrophys.*, **358**, 1097–1108, 2000.

Harrison, R. A., Sawyer, E. C., Carter, M. K., Cruise, A. M., Cutler, R. M., Fludra, A., Hayes, R. W., Kent, B. J., Lang, J., Parker, D. J., Payne, J., Pike, C. D., Peskett, S. C., Richards, A. G., Gulhane, J. L., Norman, K., Breeveld, A. A., Breeveld, E. R., Al Janabi, K. F., McCalden, A. J., Parkinson, J. H., Self, D. G., Thomas, P. D., Poland, A. I., Thomas, R. J., Thompson, W. T., Kjeldseth-Moe, O., Brekke, P., Karud, J., Maltby, P., Aschenbach, B., Bräuninger, H., Kühne, M., Hollandt, J., Siegmund, O. H. W., Huber, M. C. E., Gabriel, A. H., Mason, H. E., and Bromage, B. J. I.: The Coronal Diagnostic Spectrometer for the Solar and Heliospheric Observatory, *Solar Phys.*, **162**, 233–290, doi:10.1007/BF00733431, 1995.

Harvey, K. L., Martin, S. F., and Riddle, A. C.: Correlation of a Flare-Wave and Type II Burst, *Solar Phys.*, **36**, 151–155, doi:10.1007/BF00151556, 1974.

Hata, M.: Master's Dissertation at Science University of Tokyo (in Japanese), *Master's Dissertation at Science University of Tokyo (in Japanese)*, 2001.

Hildner, E., Gosling, J. T., Hansen, R. T., and Bohlin, J. D.: The sources of material comprising a mass ejection coronal transient, *Solar Phys.*, **45**, 363–376, 1975.

Hirayama, T.: Theoretical Model of Flares and Prominences. I: Evaporating Flare Model, *Solar Phys.*, **34**, 323–338, doi:10.1007/BF00153671, 1974.

Hirshberg, J. and Colburn, D. S.: Interplanetary field and geomagnetic variations-a unified view, *Planetary & Space Sci.*, **17**, 1183, 1969.

Howard, R. A., Michels, D. J., Sheeley, Jr., N. R., and Koomen, M. J.: The observation of a coronal transient directed at earth, *Astrophys. J. Lett.*, **263**, L101–L104, doi:10.1086/183932, 1982.

Howard, R. A., Sheeley, Jr., N. R., Michels, D. J., and Koomen, M. J.: Coronal mass ejections - 1979-1981, *J. Geophys. Res.*, **90**, 8173–8191, 1985.

Hoyng, P.: Mean Field Dynamo Theory, in NATO ASIC Proc. 373: The Sun: A Laboratory for Astrophysics, edited by J. T. Schmelz and J. C. Brown, p. 99, 1992.

Hudson, H. S. and Cliver, E. W.: Observing coronal mass ejections without coronagraphs, *J. Geophys. Res.*, **106**, 25 199–25 214, doi:10.1029/2000JA004026, 2001.

Hudson, H. S. and Warmuth, A.: Coronal Loop Oscillations and Flare Shock Waves, *Astrophys. J. Lett.*, **614**, L85–L88, doi:10.1086/425314, 2004.

Hudson, H. S. and Webb, D. F.: Soft X-ray signatures of coronal ejections, *AGU Monograph*, 1997.

Hudson, H. S., Acton, L. W., and Freeland, S. L.: A Long-Duration Solar Flare with Mass Ejection and Global Consequences, *Astrophys. J.*, **470**, 629–635, doi:10.1086/177894, 1996.

Hudson, H. S., Khan, J. I., Lemen, J. R., Nitta, N. V., and Uchida, Y.: Soft X-ray observation of a large-scale coronal wave and its exciter, *Solar Phys.*, **212**, 121–149, doi:10.1023/A:1022904125479, 2003.

Hundhausen, A. J.: Sizes and locations of coronal mass ejections - SMM observations from 1980 and 1984-1989, *J. Geophys. Res.*, **98**, 13 177, 1993.

Hundhausen, A. J., Sawyer, C. B., House, L., Illing, R. M. E., and Wagner, W. J.: Coronal mass ejections observed during the solar maximum mission - Latitude distribution and rate of occurrence, *J. Geophys. Res.*, **89**, 2639–2646, 1984.

Imada, S., Hara, H., Watanabe, T., Asai, A., Kamio, S., Matsuzaki, K., Harra, L. K., and Mariska, J. T.: Discovery of the Temperature-Dependent Upflow in the Plage Region During the Gradual Phase of the X-class Flare, *Pub. Astron. Soc. Japan*, **59**, S793–S799, 2007.

Ivanov, K. G., Belov, A. V., Kharshiladze, A. F., Romashets, E. P., Bothmer, V., Cargill, P. J., and Veselovsky, I. S.: Slow dynamics of photospheric regions of the open magnetic field of the Sun, solar activity phenomena, substructure of the interplanetary medium and near-Earth disturbances of the early 23rd cycle: March - June 1997 events, *Int. J. Geomag. Aeron.*, **4**, 91–109, doi:-, 2003.

Jian, L., Russell, C. T., Luhmann, J. G., and Skoug, R. M.: Properties of Interplanetary Coronal Mass Ejections at One AU During 1995 2004, *Solar Phys.*, **239**, 393–436, doi:10.1007/s11207-006-0133-2, 2006.

Jiang, Y., Yang, L., Li, K., and Ren, D.: Coronal and Chromospheric Dimmings during a Halo-Type CME Event, *Astrophys. J. Lett.*, **662**, L131–L134, doi:10.1086/519490, 2007.

Kahler, S. W. and Hudson, H. S.: Origin and development of transient coronal holes, *J. Geophys. Res.*, **106**, 29 239–29 248, doi:10.1029/2001JA000127, 2001.

Kai, K.: Expanding Arch Structure of a Solar Radio Outburst, *Solar Phys.*, **11**, 310–318, doi:10.1007/BF00155230, 1970.

Kaufmann, P., Giménez de Castro, C. G., Makhmutov, V. S., Raulin, J.-P., Schwenn, R., Levato, H., and Rovira, M.: Launch of solar coronal mass ejections and submillimeter pulse bursts, *Journal of Geophysical Research (Space Physics)*, **108**, 1280–1299, doi:10.1029/2002JA009729, 2003.

Khan, J. I. and Aurass, H.: X-ray observations of a large-scale solar coronal shock wave, *Astron. Astrophys.*, **383**, 1018–1031, doi:10.1051/0004-6361:20011707, 2002.

Khan, J. I. and Hudson, H. S.: Homologous sudden disappearances of transequatorial interconnecting loops in the solar corona, *Geophys. Res. Lett.*, **27**, 1083–1086, 2000.

Klassen, A., Aurass, H., Klein, K.-L., Hofmann, A., and Mann, G.: Radio evidence on shock wave formation in the solar corona, *Astron. Astrophys.*, **343**, 287–296, 1999.

Klassen, A., Aurass, H., Mann, G., and Thompson, B. J.: Catalogue of the 1997 SOHO-EIT coronal transient waves and associated type II radio burst spectra, *Astron. Astrophys. Suppl.*, **141**, 357–369, 2000.

Klein, L. W. and Burlaga, L. F.: Interplanetary magnetic clouds at 1 AU, *J. Geophys. Res.*, **87**, 613–624, 1982.

Kliem, B. and Török, T.: Torus Instability, *Physical Review Letters*, **96**, 255 002–255 006, doi:10.1103/PhysRevLett.96.255002, 2006.

Klimchuk, J. A.: Theory of Coronal Mass Ejections, *Space Weather (Geophysical Monograph 125), ed. P. Song, H. Singer, G. Siscoe (Washington: Am. Geophys. Un.), 143 (2001)*, **125**, 143, 2001.

Komm, R. W., Howard, R. F., and Harvey, J. W.: Torsional oscillation patterns in photospheric magnetic features, *Solar Phys.*, **143**, 19–39, 1993.

Kopp, R. A. and Pneuman, G. W.: Magnetic reconnection in the corona and the loop prominence phenomenon, *Solar Phys.*, **50**, 85–98, 1976.

Krasnoselskikh, V. and Podladchikova, O.: Are EIT waves slow mode blast waves?, *AGU Fall Meeting Abstracts*, p. A1047, 2007.

Krucker, S. and Benz, A. O.: Energy Distribution of Heating Processes in the Quiet Solar Corona, *Astrophys. J. Lett.*, **501**, L213–L216, doi:10.1086/311474, 1998.

Landau, L. D. and Lifshitz, E. M.: Fluid Mechanics, Course of Theoretical Physics, Vol 6., 2nd ed., Elsevier, New York., 1987.

Larson, D. E., Lin, R. P., McTiernan, J. M., McFadden, J. P., Ergun, R. E., McCarthy, M., Rème, H., Sanderson, T. R., Kaiser, M., Lepping, R. P., and Mazur, J.: Tracing the topology of the October 18-20, 1995, magnetic cloud with ˜0.1-10^{2}keV electrons, *Geophys. Res. Lett.*, **24**, 1911–1914, doi:10.1029/97GL01878, 1997.

Leamon, R. J., Canfield, R. C., and Pevtsov, A. A.: Properties of magnetic clouds and geomagnetic storms associated with eruption of coronal sigmoids, *Journal of Geophysical Research (Space Physics)*, **107**, 1234–1243, doi:10.1029/2001JA000313, 2002.

Lemen, J. R., Duncan, D. W., Edwards, C. G., Friedlaender, F. M., Jurcevich, B. K., Morrison, M. D., Springer, L. A., Stern, R. A., Wuelser, J.-P., Bruner, M. E., and Catura, R. C.: The solar x-ray imager for GOES, in Telescopes and Instrumentation for Solar Astrophysics. Edited by Fineschi, Silvano; Gummin, Mark A. Proceedings of the SPIE, Volume 5171, pp. 65-76 (2004)., edited by S. Fineschi and M. A. Gummin, vol. 5171 of *Presented at the Society of Photo-Optical Instrumentation Engineers (SPIE) Conference*, pp. 65–76, doi:10.1117/12.507566, 2004.

Lepping, R. P., Acũna, M. H., Burlaga, L. F., Farrell, W. M., Slavin, J. A., Schatten, K. H., Mariani, F., Ness, N. F., Neubauer, F. M., Whang, Y. C., Byrnes, J. B., Kennon, R. S., Panetta, P. V., Scheifele, J., and Worley, E. M.: The Wind Magnetic Field Investigation, *Space Science Reviews*, **71**, 207–229, doi:10.1007/BF00751330, 1995.

Lin, R. P., Anderson, K. A., Ashford, S., Carlson, C., Curtis, D., Ergun, R., Larson, D., McFadden, J., McCarthy, M., Parks, G. K., Rème, H., Bosqued, J. M., Coutelier, J., Cotin, F., D'Uston, C., Wenzel, K.-P., Sanderson, T. R., Henrion, J., Ronnet, J. C., and Paschmann, G.: A Three-Dimensional Plasma and Energetic Particle Investigation for the Wind Spacecraft, *Space Science Reviews*, **71**, 125–153, doi:10.1007/BF00751328, 1995.

Liu, C., Lee, J., Deng, N., Gary, D. E., and Wang, H.: Large-Scale Activities Associated with the 2003 October 29 X10 Flare, *Astrophys. J.*, **642**, 1205–1215, doi:10.1086/501000, 2006.

Liu, C., Lee, J., Yurchyshyn, V., Deng, N., Cho, K.-s., Karlický, M., and Wang, H.: The Eruption from a Sigmoidal Solar Active Region on 2005 May 13, *Astrophys. J.*, **669**, 1372–1381, doi:10.1086/521644, 2007.

Liu, Y. C.-M., Opher, M., Cohen, O., Liewer, P. C., and Gombosi, T. I.: A Simulation of a Coronal Mass Ejection Propagation and Shock Evolution in the Lower Solar Corona, *Astrophys. J.*, **680**, 757–763, doi:10.1086/587867, 2008.

Livingston, W., Harvey, J. W., Malanushenko, O. V., and Webster, L.: Sunspots with the Strongest Magnetic Fields, *Solar Phys.*, **239**, 41–68, doi:10.1007/s11207-006-0265-4, 2006.

Long, D. M., Gallagher, P. T., McAteer, R. T. J., and Bloomfield, D. S.: The Kinematics of a Globally Propagating Disturbance in the Solar Corona, *Astrophys. J. Lett.*, **680**, L81–L84, doi:10.1086/589742, 2008.

López Fuentes, M. C., Démoulin, P., Mandrini, C. H., Pevtsov, A. A., and van Driel-Gesztelyi, L.: Magnetic twist and writhe of active regions. On the origin of deformed flux tubes, *Astron. Astrophys.*, **397**, 305–318, doi:10.1051/0004-6361:20021487, 2003.

Lundquist, S.: Magnetohydrostatic fields, *Ark. Fys.*, **2**, 361–365, 1950.

Mackay, C. D.: Charge-coupled devices in astronomy, *Ann. Rev. Astron.*, **24**, 255–283, doi:10.1146/annurev.aa.24.090186.001351, 1986.

MacQueen, R. M., Eddy, J. A., Gosling, J. T., Hildner, E., Munro, R. H., Newkirk, Jr., G. A., Poland, A. I., and Ross, C. L.: The Outer Solar Corona as Observed from Skylab: Preliminary Results, *Astrophys. J. Lett.*, **187**, L85–L88, 1974.

Magdalenić, J., Vršnak, B., Pohjolainen, S., Temmer, M., Aurass, H., and Lehtinen, N.: Flare generated shock in the CME-flare event of 24 December 1996, *Solar Phys.*, **in press**, 2008.

Maia, D., Vourlidas, A., Pick, M., Howard, R., Schwenn, R., and Magalhães, A.: Radio signatures of a fast coronal mass ejection development on November 6, 1997, *J. Geophys. Res.*, **104**, 12 507–12 514, doi:10.1029/1999JA900033, 1999.

Malandraki, O. E., Lario, D., Lanzerotti, L. J., Sarris, E. T., Geranios, A., and Tsiropoula, G.: October/November 2003 interplanetary coronal mass ejections: ACE/EPAM solar energetic particle observations, *Journal of Geophysical Research (Space Physics)*, **110**, 09S06–A010 926, doi:10.1029/2004JA010926, 2005.

Mandrini, C. H., Pohjolainen, S., Dasso, S., Green, L. M., Démoulin, P., van Driel-Gesztelyi, L., Copperwheat, C., and Foley, C.: Interplanetary flux rope ejected from an X-ray bright point. The smallest magnetic cloud source-region ever observed, *Astron. Astrophys.*, **434**, 725–740, doi:10.1051/0004-6361:20041079, 2005.

Mandrini, C. H., Nakwacki, M. S., Attrill, G., van Driel-Gesztelyi, L., Démoulin, P., Dasso, S., and Elliott, H.: Are CME-Related Dimmings Always a Simple Signature of Interplanetary Magnetic Cloud Footpoints?, *Solar Phys.*, **244**, 25–43, doi:10.1007/s11207-007-9020-8, 2007.

Mann, G., Klassen, A., Estel, C., and Thompson, B. J.: Coronal Transient Waves and Coronal Shock Waves, in 8th SOHO Workshop: Plasma Dynamics and Diagnostics in the Solar Transition Region and Corona, edited by J.-C. Vial and B. Kaldeich-Schü, vol. 446 of *ESA Special Publication*, pp. 477–481, 1999.

Manoharan, P. K., van Driel-Gesztelyi, L., Pick, M., and Demoulin, P.: Evidence for Large-Scale Solar Magnetic Reconnection from Radio and X-Ray Measurements, *Astrophys. J. Lett.*, **468**, L73–L76, doi:10.1086/310221, 1996.

Marubashi, K.: Interplanetary Magnetic Flux Ropes and Solar Filaments, *Coronal Mass Ejections, Geophysical Monograph 99*, pp. 147.–156, 1997.

Matsuzaki, K., Hara, H., Watanabe, T., Dere, K. P., Brown, C. M., and Culhane, L.: Hot and Cool Loops Composing the Corona of the Quiet Sun, *Pub. Astron. Soc. Japan*, **59**, 683–687, 2007.

Matthews, S.: Space Weather, p. 157, Space Science, 2004.

McComas, D. J., Gosling, J. T., Phillips, J. L., Bame, S. J., Luhmann, J. G., and Smith, E. J.: Electron heat flux dropouts in the solar wind - Evidence for interplanetary magnetic field reconnection?, *J. Geophys. Res.*, **94**, 6907–6916, 1989.

McIntosh, S. W., Leamon, R. J., Davey, A. R., and Wills-Davey, M. J.: The Posteruptive Evolution of a Coronal Dimming, *Astrophys. J.*, **660**, 1653–1659, doi:10.1086/512665, 2007.

Melrose, D. B.: Plasma emission mechanisms, pp. 177–210, Solar Radiophysics: Studies of Emission from the Sun at Metre Wavelengths, 1985.

Moore, R. L., Sterling, A. C., Hudson, H. S., and Lemen, J. R.: Onset of the Magnetic Explosion in Solar Flares and Coronal Mass Ejections, *Astrophys. J.*, **552**, 833–848, doi:10.1086/320559, 2001.

Moore, R. L., Sterling, A. C., and Suess, S. T.: The Width of a Solar Coronal Mass Ejection and the Source of the Driving Magnetic Explosion: A Test of the Standard Scenario for CME Production, *Astrophys. J.*, **668**, 1221–1231, doi:10.1086/521215, 2007.

Moreton, G. E.: Hα Observations of Flare-Initiated Disturbances with Velocities ˜1000 km/sec., *Astronom. J.*, **65**, 494, doi:10.1086/108346, 1960.

Moreton, G. E. and Ramsey, H. E.: Recent Observations of Dynamical Phenomena Associated with Solar Flares, *Pub. Astron. Soc. Pac.*, **72**, 357, 1960.

Moreton, G. F.: Hα Shock Wave and Winking Filaments with the Flare of 20 September 1963., *Astronom. J.*, **69**, 145, doi:10.1086/109375, 1964.

Moses, D., Clette, F., Delaboudinière, J.-P., Artzner, G. E., Bougnet, M., Brunaud, J., Carabetian, C., Gabriel, A. H., Hochedez, J. F., Millier, F., Song, X. Y., Au, B., Dere, K. P., Howard, R. A., Kreplin, R., Michels, D. J., Defise, J. M., Jamar, C., Rochus, P., Chauvineau, J. P., Marioge, J. P., Catura, R. C., Lemen, J. R., Shing, L., Stern, R. A., Gurman, J. B., Neupert, W. M., Newmark, J., Thompson, B., Maucherat, A., Portier-Fozzani, F., Berghmans, D., Cugnon, P., van Dessel, E. L., and Gabryl, J. R.: EIT Observations of the Extreme Ultraviolet Sun, *Solar Phys.*, **175**, 571–599, doi:10.1023/A:1004902913117, 1997.

Narukage, N., Hudson, H. S., Morimoto, T., Akiyama, S., Kitai, R., Kurokawa, H., and Shibata, K.: Simultaneous Observation of a Moreton Wave on 1997 November 3 in Hα and Soft X-Rays, *Astrophys. J. Lett.*, **572**, L109–L112, doi:10.1086/341599, 2002.

Narukage, N., Morimoto, T., Kadota, M., Kitai, R., Kurokawa, H., and Shibata, K.: X-Ray Expanding Features Associated with a Moreton Wave, *Pub. Astron. Soc. Japan*, **56**, L5–L8, 2004.

Nelson, G. J. and Melrose, D. B.: Type II bursts, pp. 333–359, Solar Radiophysics: Studies of Emission from the Sun at Metre Wavelengths, 1985.

Ness, N. F.: Magnetometers for Space Research, *Space Science Reviews*, **11**, 459–554, doi:10.1007/BF00183028, 1970.

Neupert, W. M.: Transient coronal extreme ultraviolet emission before and during the impulsive phase of a solar flare, *Astrophys. J.*, **344**, 504–512, doi:10.1086/167819, 1989.

Odstrcil, D., Pizzo, V. J., and Arge, C. N.: Propagation of the 12 May 1997 interplanetary coronal mass ejection in evolving solar wind structures, *Journal of Geophysical Research (Space Physics)*, **110**, 2106–2121, doi:10.1029/2004JA010745, 2005.

Ofman, L. and Thompson, B. J.: Interaction of EIT Waves with Coronal Active Regions, *Astrophys. J.*, **574**, 440–452, doi:10.1086/340924, 2002.

Ogawara, Y., Takano, T., Kato, T., Kosugi, T., Tsuneta, S., Watanabe, T., Kondo, I., and Uchida, Y.: The Solar-A Mission - an Overview, *Solar Phys.*, **136**, 1–16, doi:10.1007/BF00151692, 1991.

Okamoto, T. J., Nakai, H., Keiyama, A., Narukage, N., UeNo, S., Kitai, R., Kurokawa, H., and Shibata, K.: Filament Oscillations and Moreton Waves Associated with EIT Waves, *Astrophys. J.*, **608**, 1124–1132, doi:10.1086/420838, 2004.

Parker, E. N.: Sweet's Mechanism for Merging Magnetic Fields in Conducting Fluids, *J. Geophys. Res.*, **62**, 509–520, 1957.

Parker, E. N.: Nanoflares and the solar X-ray corona, *Astrophys. J.*, **330**, 474–479, doi:10.1086/166485, 1988.

Parnell, C. E., Priest, E. R., and Golub, L.: The three-dimensional structures of X-ray bright points, *Solar Phys.*, **151**, 57–74, 1994.

Pauluhn, A. and Solanki, S. K.: A nanoflare model of quiet Sun EUV emission, *Astron. Astrophys.*, **462**, 311–322, doi:10.1051/0004-6361:20065152, 2007.

Petschek, H. E.: Magnetic Field Annihilation, in The Physics of Solar Flares, p. 425, 1964.

Pfaff, R. F., Borovsky, J. E., and Young, D. T., eds.: Measurement Techniques in Space Plasmas – Particles, 1998.

Phillips, K. J. H.: Guide to the sun, Cambridge, MA: Cambridge University Press, —c1992, 1992.

Phillips, K. J. H., Feldman, U., and Landi, E.: Ultraviolet and X-ray Spectroscopy of the Solar Atmosphere, Cambridge, MA: Cambridge University Press, —c2008, 2008.

Pick, M.: Radio Emissions from the Sun and the Interplanetary Medium, in Solar and Heliospheric Origins of Space Weather Phenomena, edited by J.-P. Rozelot, vol. 699 of *Lecture Notes in Physics, Berlin Springer Verlag*, p. 119, 2006.

Pick, M., Maia, D., Kerdraon, A., Howard, R., Brueckner, G. E., Michels, D. J., Paswaters, S., Schwenn, R., Lamy, P., Llebaria, A., Simnett, G., Lanzerotti, L. J., and Aurass, H.: Joint Nancay Radioheliograph and LASCO Observations of Coronal Mass Ejections - II. The 9 July 1996 Event, *Solar Phys.*, **181**, 455–468, 1998.

Pick, M., Malherbe, J.-M., Kerdraon, A., and Maia, D. J. F.: On the Disk Hα and Radio Observations of the 2003 October 28 Flare and Coronal Mass Ejection Event, *Astrophys. J. Lett.*, **631**, L97–L100, doi:10.1086/497137, 2005.

Plunkett, S. P., Thompson, B. J., Howard, R. A., Michels, D. J., St. Cyr, O. C., Tappin, S. J., Schwenn, R., and Lamy, P. L.: LASCO observations of an Earth-directed coronal mass ejection on May 12, 1997, *Geophys. Res. Lett.*, **25**, 2477–2480, doi:10.1029/98GL50307, 1998.

Podladchikova, O. and Berghmans, D.: Automated Detection Of Eit Waves And Dimmings, *Solar Phys.*, **228**, 265–284, doi:10.1007/s11207-005-5373-z, 2005a.

Podladchikova, O. and Berghmans, D.: Interaction of EIT Wave With Active Regions on the Sun, in Solar Wind 11/SOHO 16, Connecting Sun and Heliosphere, vol. 592 of *ESA Special Publication*, 2005b.

Pohjolainen, S., Maia, D., Pick, M., Vilmer, N., Khan, J. I., Otruba, W., Warmuth, A., Benz, A., Alissandrakis, C., and Thompson, B. J.: On-the-Disk Development of the Halo Coronal Mass Ejection on 1998 May 2, *Astrophys. J.*, **556**, 421–431, doi:10.1086/321577, 2001.

Pohjolainen, S., Vilmer, N., Khan, J. I., and Hillaris, A. E.: Early signatures of large-scale field line opening. Multi-wavelength analysis of features connected with a "halo" CME event, *Astron. Astrophys.*, **434**, 329–341, doi:10.1051/0004-6361:20041378, 2005.

Pomoell, J., Vainio, R., and Kissmann, R.: MHD Modeling of Coronal Large-Amplitude Waves Related to CME Lift-off, *Solar Phys.*, pp. 86–100, doi:10.1007/s11207-008-9186-8, 2008.

Priest, E. and Forbes, T.: Magnetic Reconnection, Magnetic Reconnection, by Eric Priest and Terry Forbes, pp. 612. ISBN 0521481791. Cambridge, UK: Cambridge University Press, 2000.

Priest, E. R.: Solar magneto-hydrodynamics, Dordrecht, Holland ; Boston : D. Reidel Pub. Co. ; Hingham, 1982.

Priest, E. R. and Démoulin, P.: Three-dimensional magnetic reconnection without null points. 1. Basic theory of magnetic flipping, *J. Geophys. Res.*, **100**, 23 443–23 464, doi:10.1029/95JA02740, 1995.

Priest, E. R. and Forbes, T. G.: The magnetic nature of solar flares, *Astron. Astrophys. Rev.*, **10**, 313–377, doi:10.1007/s001590100013, 2002.

Qiu, J., Hu, Q., Howard, T. A., and Yurchyshyn, V. B.: On the magnetic flux budget in low-corona magnetic reconnection and interplanetary coronal mass ejections, *Astrophys. J.*, **659**, 758–772, doi:10.1086/512060, 2007.

Reames, D. V.: Particle acceleration at the Sun and in the heliosphere, *Space Science Reviews*, **90**, 413–491, doi:10.1023/A:1005105831781, 1999.

Reinard, A. A. and Biesecker, D. A.: Coronal Mass Ejection-Associated Coronal Dimmings, *Astrophys. J.*, **674**, 576–585, doi:10.1086/525269, 2008.

Richardson, I. G., Farrugia, C. J., and Burlaga, L. F.: Energetic ion observations in the magnetic cloud of 14-15 January 1988 and their implications for the magnetic field topology, in International Cosmic Ray Conference, vol. 3 of *International Cosmic Ray Conference*, p. 597, 1991.

Riley, P., Gosling, J. T., and Crooker, N. U.: Ulysses Observations of the Magnetic Connectivity between Coronal Mass Ejections and the Sun, *Astrophys. J.*, **608**, 1100–1105, doi:10.1086/420811, 2004.

Robbrecht, E.: New techniques for the characterisation of dynamical phenomena in solar coronal images, Ph.D. thesis, Royal Observatory of Belgium, 2007.

Russell, J. S.: Report on Waves, *British Association for the Advancement of Science*, 1844.

Rust, D. M.: Coronal disturbances and their terrestrial effects /Tutorial Lecture/, *Space Science Reviews*, **34**, 21–36, 1983.

Rust, D. M. and Hildner, E.: Expansion of an X-ray coronal arch into the outer corona, *Solar Phys.*, **48**, 381–387, 1976.

Scherrer, P. H., Bogart, R. S., Bush, R. I., Hoeksema, J. T., Kosovichev, A. G., Schou, J., Rosenberg, W., Springer, L., Tarbell, T. D., Title, A., Wolfson, C. J., Zayer, I., and MDI Engineering Team: The Solar Oscillations Investigation - Michelson Doppler Imager, *Solar Phys.*, **162**, 129–188, 1995.

Schmieder, B., van Driel-Gesztelyi, L., Aulanier, G., Démoulin, P., Thompson, B., de Forest, C., Wiik, J. E., Saint Cyr, C., and Vial, J. C.: Relationships between CME's and prominences, *Advances in Space Research*, **29**, 1451–1460, 2002.

Schrijver, C. J. and Zwaan, C.: Solar and Stellar Magnetic Activity, Cambridge University Press, 2000.

Schrijver, C. J., Title, A. M., van Ballegooijen, A. A., Hagenaar, H. J., and Shine, R. A.: Sustaining the Quiet Photospheric Network: The Balance of Flux Emergence, Fragmentation, Merging, and Cancellation, *Astrophys. J.*, **487**, 424–436, doi:10.1086/304581, 1997.

Schwenn, R., dal Lago, A., Huttunen, E., and Gonzalez, W. D.: The association of coronal mass ejections with their effects near the Earth, *Annales Geophysicae*, **23**, 1033–1059, 2005.

Shibata, K., Masuda, S., Shimojo, M., Hara, H., Yokoyama, T., Tsuneta, S., Kosugi, T., and Ogawara, Y.: Hot-Plasma Ejections Associated with Compact-Loop Solar Flares, *Astrophys. J. Lett.*, **451**, L83–L85, doi:10.1086/309688, 1995.

Shodhan, S., Crooker, N. U., Kahler, S. W., Fitzenreiter, R. J., Larson, D. E., Lepping, R. P., Siscoe, G. L., and Gosling, J. T.: Counterstreaming electrons in magnetic clouds, *J. Geophys. Res.*, **105**, 27 261–27 268, doi:10.1029/2000JA000060, 2000.

Skoug, R. M., Gosling, J. T., Steinberg, J. T., McComas, D. J., Smith, C. W., Ness, N. F., Hu, Q., and Burlaga, L. F.: Extremely high speed solar wind: 29-30 October 2003, *Journal of Geophysical Research (Space Physics)*, **109**, 9102, doi:10.1029/2004JA010494, 2004.

Smith, C. W., L'Heureux, J., Ness, N. F., Acuña, M. H., Burlaga, L. F., and Scheifele, J.: The ACE Magnetic Fields Experiment, *Space Science Reviews*, **86**, 613–632, doi:10.1023/A:1005092216668, 1998.

Smith, S. F. and Harvey, K. L.: Observational Effects of Flare-Associated Waves, in Physics of the Solar Corona, vol. 27 of *Astrophysics and Space Science Library*, p. 156, 1971.

Sonnerup, B. U. O. and Scheible, M.: Analisys methods for multispacecraft data, Kluwer Academic, 1998.

Spiller, E., Barbee, T. W., Golub, L., Kalata, K., Nystrom, G. U., and Viola, A.: Results from the recent flights of the IBM/SAO x-ray telescopes, in Proc. SPIE Vol. 2011, p. 391-401, Multilayer and Grazing Incidence X-Ray/EUV Optics II, Richard B. Hoover; Arthur B. Walker; Eds., edited by R. B. Hoover and A. B. Walker, vol. 2011 of *Presented at the Society of Photo-Optical Instrumentation Engineers (SPIE) Conference*, pp. 391–401, 1994.

Spitzer, L.: Physics of Fully Ionized Gases, Physics of Fully Ionized Gases, New York: Interscience (2nd edition), 1962.

Srivastava, N. and Venkatakrishnan, P.: Solar and interplanetary sources of major geomagnetic storms during 1996-2002, *Journal of Geophysical Research (Space Physics)*, **109**, 10 103, doi:10.1029/2003JA010175, 2004.

St. Cyr, O. C., Howard, R. A., Sheeley, N. R. J., Plunkett, S. P., Michels, D. J., Paswaters, S. E., Koomen, M. J., Simnett, G. M., Thompson, B. J., Gurman, J. B., Schwenn, R., Webb, D. F., Hildner, E., and Lamy, P. L.: Properties of coronal mass ejections: SOHO LASCO observations from January 1996 to June 1998, *J. Geophys. Res.*, 2000.

Steinolfson, R. S., Wu, S. T., Dryer, M., and Tandberg-Hanssen, E.: Magnetohydrodynamic models of coronal transients in the meridional plane. I - The effect of the magnetic field, *Astrophys. J.*, **225**, 259–274, doi:10.1086/156489, 1978.

Sterling, A. C. and Hudson, H. S.: YOHKOH SXT Observations of X-Ray "Dimming" Associated with a Halo Coronal Mass Ejection, *Astrophys. J. Lett.*, **491**, L55–L58, doi:10.1086/311043, 1997.

Sterling, A. C. and Moore, R. L.: Internal and external reconnection in a series of homologous solar flares, *J. Geophys. Res.*, **106**, 25 227–25 238, doi:10.1029/2000JA004001, 2001.

Sturrock, P. A.: Model of the High-Energy Phase of Solar Flares, *Nature*, **211**, 695, 1966.

Sweet, P. A.: The Neutral Point Theory of Solar Flares, in Electromagnetic Phenomena in Cosmical Physics, edited by B. Lehnert, vol. 6 of *IAU Symposium*, p. 123, 1958.

Temmer, M., Veronig, A., Vršnak, B., Thalmann, J., and Hanslmeier, A.: Wave Phenomena Associated with the X3.8 Flare/cme of 17-JAN-2005, in The Dynamic Sun: Challenges for Theory and Observations, vol. 600 of *ESA Special Publication*, 2005.

Thompson, B. J. and Myers, D. C.: A Catalog of Coronal "EIT Wave" Transients, *Astrophys. J.*, 2009.

Thompson, B. J., Plunkett, S. P., Gurman, J. B., Newmark, J. S., St. Cyr, O. C., and Michels, D. J.: SOHO/EIT observations of an Earth-directed coronal mass ejection on May 12, 1997, *Geophys. Res. Lett.*, **25**, 2465–2468, doi:10.1029/98GL50429, 1998.

Thompson, B. J., Gurman, J. B., Neupert, W. M., Newmark, J. S., Delaboudinière, J.-P., St. Cyr, O. C., Stezelberger, S., Dere, K. P., Howard, R. A., and Michels, D. J.: SOHO/EIT Observations of the 1997 April 7 Coronal Transient: Possible Evidence of Coronal Moreton Waves, *Astrophys. J. Lett.*, **517**, L151–L154, doi:10.1086/312030, 1999.

Thompson, B. J., Cliver, E. W., Nitta, N., Delannée, C., and Delaboudinière, J.-P.: Coronal Dimmings and Energetic CMEs in April-May 1998, *Geophys. Res. Lett.*, **27**, 1431–1434, doi:10.1029/1999GL003668, 2000a.

Thompson, B. J., Reynolds, B., Aurass, H., Gopalswamy, N., Gurman, J. B., Hudson, H. S., Martin, S. F., and St. Cyr, O. C.: Observations of the 24 September 1997 Coronal Flare Waves, *Solar Phys.*, **193**, 161–180, 2000b.

Tomczyk, S., Card, G. L., Darnell, T., Elmore, D. F., Lull, R., Nelson, P. G., Streander, K. V., Burkepile, J., Casini, R., and Judge, P. G.: An Instrument to Measure Coronal Emission Line Polarization, *Solar Phys.*, **247**, 411–428, doi:10.1007/s11207-007-9103-6, 2008.

Török, T. and Kliem, B.: The evolution of twisting coronal magnetic flux tubes, *Astron. Astrophys.*, **406**, 1043–1059, doi:10.1051/0004-6361:20030692, 2003.

Török, T. and Kliem, B.: Confined and Ejective Eruptions of Kink-unstable Flux Ropes, *Astrophys. J. Lett.*, **630**, L97–L100, doi:10.1086/462412, 2005.

Török, T., Kliem, B., and Titov, V. S.: Ideal kink instability of a magnetic loop equilibrium, *Astron. Astrophys.*, **413**, L27–L30, doi:10.1051/0004-6361:20031691, 2004.

Tripathi, D. and Raouafi, N.-E.: On the relationship between coronal waves associated with a CME on 5 March 2000, *Astron. Astrophys.*, **473**, 951–957, doi:10.1051/0004-6361:20077255, 2007.

Tsuneta, S., Acton, L., Bruner, M., Lemen, J., Brown, W., Caravalho, R., Catura, R., Freeland, S., Jurcevich, B., and Owens, J.: The soft X-ray telescope for the SOLAR-A mission, *Solar Phys.*, **136**, 37–67, 1991.

Uchida, Y.: Propagation of Hydromagnetic Disturbances in the Solar Corona and Moreton's Wave Phenomenon, *Solar Phys.*, **4**, 30–44, doi:10.1007/BF00146996, 1968.

Uchida, Y.: Diagnosis of Coronal Magnetic Structure by Flare-Associated Hydromagnetic Disturbances, *Pub. Astron. Soc. Japan*, **22**, 341, 1970.

Uchida, Y.: Behavior of the flare produced coronal MHD wavefront and the occurrence of type II radio bursts, *Solar Phys.*, **39**, 431–449, 1974.

Uchida, Y., Tanaka, T., Hata, M., and Cameron, R.: Investigation of Coronal Mass Ejections I. Loop-type with Arcade Flare between the Fixed Legs, and Bubble-type Due to Flare Blast Waves, *Publications of the Astronomical Society of Australia*, **18**, 345–350, doi:10.1071/AS01043, 2001.

Ulmer, M. P., Nitta, N., and Stern, R. A.: Hard X-ray Focusing Optics for Solar Physics, in Bulletin of the American Astronomical Society, vol. 35 of *Bulletin of the American Astronomical Society*, p. 844, 2003.

Švestka, Z.: Varieties of Coronal Mass Ejections and Their Relation to Flares, *Space Science Reviews*, **95**, 135–146, 2001.

Vaiana, G. S., van Speybroeck, L., Zombeck, M. V., Krieger, A. S., Silk, J. K., and Timothy, A.: The S-054 X-ray telescope experiment on SKYLAB, *Space Sci. Instr.*, **3**, 19–76, 1977.

van Driel-Gesztelyi, L.: Emergence and loss of magnetic flux on the solar surface, in SOLMAG 2002. Proceedings of the Magnetic Coupling of the Solar Atmosphere Euroconference, edited by H. Sawaya-Lacoste, vol. 505 of *ESA Special Publication*, pp. 113–120, 2002.

van Driel-Gesztelyi, L.: An Introduction to Magnetohydrodynamics, p. 279, Space Science, 2004.

van Driel-Gesztelyi, L., Schmieder, B., Cauzzi, G., Mein, N., Hofmann, A., Nitta, N., Kurokawa, H., Mein, P., and Staiger, J.: X-Ray Bright Point Flares Due to Magnetic Reconnection, *Solar Phys.*, **163**, 145–170, doi:10.1007/BF00165462, 1996.

van Driel-Gesztelyi, L., Kovari, Z., Lopez-Fuentes, M., Mandrini, C. H., and Demoulin, P.: What Can we Learn Studying Long-Term Magnetic Evolution of Solar Active Regions?, in The Solar Cycle and Terrestrial Climate, Solar and Space weather, edited by A. Wilson, vol. 463 of *ESA Special Publication*, p. 451, 2000.

van Driel-Gesztelyi, L., Attrill, G. D. R., Démoulin, P., Mandrini, C. H., and Harra, L. K.: Why are CMEs large-scale coronal events: nature or nurture?, *Annales Geophysicae*, **26**, 3077–3088, 2008.

Veronig, A. M., Temmer, M., Vršnak, B., and Thalmann, J. K.: Interaction of a Moreton/EIT Wave and a Coronal Hole, *Astrophys. J.*, **647**, 1466–1471, doi:10.1086/505456, 2006.

Veronig, A. M., Temmer, M., and Vrsnak, B.: High cadence observations of a global coronal wave by EUVI/STEREO, *ArXiv e-prints*, **806**, 2008.

Vršnak, B.: Terminology of Large-Scale Waves in the Solar Atmosphere, *EOS Transactions*, **86**, 112–113, doi:10.1029/2005EO110004, 2005.

Vršnak, B. and Lulić, S.: Formation Of Coronal Mhd Shock Waves - I. The Basic Mechanism, *Solar Phys.*, **196**, 157–180, 2000a.

Vršnak, B. and Lulić, S.: Formation of coronal MHD shock waves - II. The Pressure Pulse Mechanism, *Solar Phys.*, **196**, 181–197, 2000b.

Vršnak, B., Warmuth, A., Brajša, R., and Hanslmeier, A.: Flare waves observed in Helium I 10 830 Å. A link between Hα Moreton and EIT waves, *Astron. Astrophys.*, **394**, 299–310, doi:10.1051/0004-6361:20021121, 2002.

Vršnak, B., Magdalenić, J., Temmer, M., Veronig, A., Warmuth, A., Mann, G., Aurass, H., and Otruba, W.: Broadband Metric-Range Radio Emission Associated with a Moreton/EIT Wave, *Astrophys. J. Lett.*, **625**, L67–L70, doi:10.1086/430763, 2005.

Wang, J., Zhou, G., Wang, Y., and Song, L.: Circular Polarization in a Solar Filament, *Solar Phys.*, **216**, 143–157, 2003.

Wang, J., Zhang, Y., Zhou, G., Harra, L. K., Williams, D. R., and Jiang, Y.: Solar Trans-equatorial Activity, *Solar Phys.*, **244**, 75–94, doi:10.1007/s11207-007-9038-y, 2007.

Wang, T., Yan, Y., Wang, J., Kurokawa, H., and Shibata, K.: The Large-Scale Coronal Field Structure and Source Region Features for a Halo Coronal Mass Ejection, *Astrophys. J.*, **572**, 580–597, doi:10.1086/340189, 2002.

Wang, Y.-M.: EIT Waves and Fast-Mode Propagation in the Solar Corona, *Astrophys. J. Lett.*, **543**, L89–L93, doi:10.1086/318178, 2000.

Warmuth, A.: Large-scale Waves and Shocks in the Solar Corona, in Lecture Notes in Physics, Berlin Springer Verlag, edited by K.-L. Klein and A. L. MacKinnon, vol. 725 of *Lecture Notes in Physics, Berlin Springer Verlag*, pp. 107–139, 2007.

Warmuth, A. and Mann, G.: A model of the Alfvén speed in the solar corona, *Astron. Astrophys.*, **435**, 1123–1135, doi:10.1051/0004-6361:20042169, 2005.

Warmuth, A., Vršnak, B., Aurass, H., and Hanslmeier, A.: Evolution of Two EIT/Hα Moreton Waves, *Astrophys. J. Lett.*, **560**, L105–L109, doi:10.1086/324055, 2001.

Warmuth, A., Vršnak, B., Aurass, H., and Hanslmeier, A.: Moreton waves and their relation with EIT waves, in Solspa 2001, Proceedings of the Second Solar Cycle and Space Weather Euroconference, edited by H. Sawaya-Lacoste, vol. 477 of *ESA Special Publication*, pp. 195–198, 2002.

Warmuth, A., Vršnak, B., Magdalenić, J., Hanslmeier, A., and Otruba, W.: A multiwavelength study of solar flare waves. I. Observations and basic properties, *Astron. Astrophys.*, **418**, 1101–1115, doi:10.1051/0004-6361:20034332, 2004a.

Warmuth, A., Vršnak, B., Magdalenić, J., Hanslmeier, A., and Otruba, W.: A multiwavelength study of solar flare waves. II. Perturbation characteristics and physical interpretation, *Astron. Astrophys.*, **418**, 1117–1129, doi:10.1051/0004-6361:20034333, 2004b.

Warmuth, A., Mann, G., and Aurass, H.: First Soft X-Ray Observations of Global Coronal Waves with the GOES Solar X-Ray Imager, *Astrophys. J. Lett.*, **626**, L121–L124, doi:10.1086/431756, 2005.

Webb, D. F., Kahler, S. W., McIntosh, P. S., and Klimchuck, J. A.: Large-scale structures and multiple neutral lines associated with coronal mass ejections, *J. Geophys. Res.*, **102**, 24 161–24 174, doi:10.1029/97JA01867, 1997.

Webb, D. F., Lepping, R. P., Burlaga, L. F., DeForest, C. E., Larson, D. E., Martin, S. F., Plunkett, S. P., and Rust, D. M.: The origin and development of the May 1997 magnetic cloud, *J. Geophys. Res.*, **105**, 27 251–27 260, doi:10.1029/2000JA000021, 2000.

Wen, Y., Wang, J., Maia, D. J. F., Zhang, Y., Zhao, H., and Zhou, G.: Spatial and Temporal Scales of Coronal Magnetic Restructuring in the Development of Coronal Mass Ejections, *Solar Phys.*, **239**, 257–276, doi:10.1007/s11207-006-0181-7, 2006.

White, S. M. and Thompson, B. J.: High-Cadence Radio Observations of an EIT Wave, *Astrophys. J. Lett.*, **620**, L63–L66, doi:10.1086/428428, 2005.

Wild, J. P. and McCready, L. L.: Observations of the Spectrum of High-Intensity Solar Radiation at Metre Wavelengths. I. The Apparatus and Spectral Types of Solar Burst Observed, *Australian Journal of Scientific Research A Physical Sciences*, **3**, 387–398, 1950.

Williams, D. R., Török, T., Démoulin, P., van Driel-Gesztelyi, L., and Kliem, B.: Eruption of a Kink-unstable Filament in NOAA Active Region 10696, *Astrophys. J. Lett.*, **628**, L163–L166, doi:10.1086/432910, 2005.

Wills-Davey, M. J.: Propagating disturbances in the lower solar corona, Ph.D. thesis, AA(MONTANA STATE UNIVERSITY), 2003.

Wills-Davey, M. J.: Tracking Large-Scale Propagating Coronal Wave Fronts (EIT Waves) using Automated Methods, *Astrophys. J.*, **645**, 757–765, doi:10.1086/504144, 2006.

Wills-Davey, M. J. and Thompson, B. J.: Observations of a Propagating Disturbance in TRACE, *Solar Phys.*, **190**, 467–483, doi:10.1023/A:1005201500675, 1999.

Wills-Davey, M. J., DeForest, C. E., and Stenflo, J. O.: Are "EIT Waves" Fast-Mode MHD Waves?, *Astrophys. J.*, **664**, 556–562, doi:10.1086/519013, 2007.

Wu, S. T., Zheng, H., Wang, S., Thompson, B. J., Plunkett, S. P., Zhao, X. P., and Dryer, M.: Three-dimensional numerical simulation of MHD waves observed by the Extreme Ultraviolet Imaging Telescope, *J. Geophys. Res.*, **106**, 25 089–25 102, doi:10.1029/2000JA000447, 2001.

Wuelser, J.-P., Lemen, J. R., Tarbell, T. D., Wolfson, C. J., Cannon, J. C., Carpenter, B. A., Duncan, D. W., Gradwohl, G. S., Meyer, S. B., Moore, A. S., Navarro, R. L., Pearson, J. D., Rossi, G. R., Springer, L. A., Howard, R. A., Moses, J. D., Newmark, J. S., Delaboudiniere, J.-P., Artzner, G. E., Auchere, F., Bougnet, M., Bouyries, P., Bridou, F., Clotaire, J.-Y., Colas, G., Delmotte, F., Jerome, A., Lamare, M., Mercier, R., Mullot, M., Ravet, M.-F., Song, X., Bothmer, V., and Deutsch, W.: EUVI: the STEREO-SECCHI extreme ultraviolet imager, in Telescopes and Instrumentation for Solar Astrophysics. Edited by Fineschi, Silvano; Gummin, Mark A. Proceedings of the SPIE, Volume 5171, pp. 111-122 (2004)., edited by S. Fineschi and M. A. Gummin, vol. 5171 of *Presented at the Society of Photo-Optical Instrumentation Engineers (SPIE) Conference*, pp. 111–122, doi:10.1117/12.506877, 2004.

Yashiro, S., Gopalswamy, N., Michalek, G., St. Cyr, O. C., Plunkett, S. P., Rich, N. B., and Howard, R. A.: A catalog of white light coronal mass ejections observed by the SOHO spacecraft, *Journal of Geophysical Research (Space Physics)*, **109**, 7105, doi:10.1029/2003JA010282, 2004.

Yurchyshyn, V., Liu, C., Abramenko, V., and Krall, J.: The May 13, 2005 Eruption: Observations, Data Analysis and Interpretation, *Solar Phys.*, **239**, 317–335, doi:10.1007/s11207-006-0177-3, 2006.

Zarro, D. M., Sterling, A. C., Thompson, B. J., Hudson, H. S., and Nitta, N.: SOHO EIT Observations of Extreme-Ultraviolet "Dimming" Associated with a Halo Coronal Mass Ejection, *Astrophys. J. Lett.*, **520**, L139–L142, doi:10.1086/312150, 1999.

Zhang, J., Dere, K. P., Howard, R. A., Kundu, M. R., and White, S. M.: On the Temporal Relationship between Coronal Mass Ejections and Flares, *Astrophys. J.*, **559**, 452–462, doi:10.1086/322405, 2001.

Zhang, J., Dere, K. P., Howard, R. A., and Vourlidas, A.: A Study of the Kinematic Evolution of Coronal Mass Ejections, *Astrophys. J.*, **604**, 420–432, doi:10.1086/381725, 2004.

Zhang, J., Ma, J., and Wang, H.: Comparison of Magnetic Flux Distribution between a Coronal Hole and a Quiet Region, *Astrophys. J.*, **649**, 464–469, doi:10.1086/506471, 2006.

Zhang, Y., Wang, J., Attrill, G. D. R., Harra, L. K., Yang, Z., and He, X.: Coronal Magnetic Connectivity and EUV Dimmings, *Solar Phys.*, **241**, 329–349, doi:10.1007/s11207-007-0229-3, 2007.

Zhitnik, I. A., Bougaenko, O. I., Delaboudiniere, J.-P., Ignatiev, A. P., Korneev, V. V., Krutov, V. V., Kuzin, S. V., Lisin, D. V., Mitrofanov, A. V., Oparin, S. N., Oraevsky, V. N., Pertsov, A. A., Slemzin, V. A., Sobelman, I. I., Stepanov, A. I., and Schwarz, J.: SPIRIT X-ray telescope/spectroheliometer results, in Solar Variability: From Core to Outer Frontiers, edited by J. Kuijpers, vol. 506 of *ESA Special Publication*, pp. 915–918, 2002.

Zhukov, A. N. and Auchère, F.: On the nature of EIT waves, EUV dimmings and their link to CMEs, *Astron. Astrophys.*, **427**, 705–716, doi:10.1051/0004-6361:20040351, 2004.

Zhukov, A. N. and Veselovsky, I. S.: Global Coronal Mass Ejections, *Astrophys. J. Lett.*, **664**, L131–L134, doi:10.1086/520928, 2007.

Zirin, H.: Solar Optical Instrumentation, in NATO ASIC Proc. 373: The Sun: A Laboratory for Astrophysics, edited by J. T. Schmelz and J. C. Brown, p. 379, 1992.